

---


Electronic Theses and Dissertations, 2004-2019

---

2006

## Predicting Surface Scatter Using A Linear Systems Formulation Of Non-paraxial Scalar Diffraction

Andrey Krywonos  
*University of Central Florida*

 Part of the [Electromagnetics and Photonics Commons](#), and the [Optics Commons](#)  
Find similar works at: <https://stars.library.ucf.edu/etd>  
University of Central Florida Libraries <http://library.ucf.edu>

This Doctoral Dissertation (Open Access) is brought to you for free and open access by STARS. It has been accepted for inclusion in Electronic Theses and Dissertations, 2004-2019 by an authorized administrator of STARS. For more information, please contact [STARS@ucf.edu](mailto:STARS@ucf.edu).

---

### STARS Citation

Krywonos, Andrey, "Predicting Surface Scatter Using A Linear Systems Formulation Of Non-paraxial Scalar Diffraction" (2006). *Electronic Theses and Dissertations, 2004-2019*. 1086.  
<https://stars.library.ucf.edu/etd/1086>

PREDICTING SURFACE SCATTER  
USING A LINEAR SYSTEMS FORMULATION  
OF NON-PARAXIAL SCALAR DIFFRACTION

by

ANDREY KRYWONOS

B.S. State University of New York Institute of Technology, 1995  
M.S. University of Central Florida, 2000

A dissertation submitted in partial fulfillment of the requirements  
for the degree of Doctor of Philosophy  
in the College of Optics and Photonics  
at the University of Central Florida  
Orlando, Florida

Fall Term  
2006

Major Professor: James E. Harvey

© 2006 Andrey Krywonos

## ABSTRACT

Scattering effects from rough surfaces are non-paraxial diffraction phenomena resulting from random phase variations in the reflected wavefront. The ability to predict these effects is important in a variety of applications including x-ray and EUV imaging, the design of stray light rejection systems, and reflection modeling for rendering realistic scenes and animations of physical objects in computer graphics.

Rayleigh-Rice (small perturbation method) and Beckmann-Kirchhoff (Kirchhoff approximation) theories are commonly used to predict surface scatter effects. In addition, Harvey and Shack developed a linear systems formulation of surface scatter phenomena in which the scattering behavior is characterized by a surface transfer function. This treatment provided insight and understanding not readily gleaned from the two previous theories, and has been incorporated into a variety of computer software packages (ASAP, Zemax, Tracepro). However, smooth surface and paraxial approximations have severely limited the range of applicability of each of the above theoretical treatments.

In this dissertation, a linear systems formulation of non-paraxial scalar diffraction theory is first developed and then applied to sinusoidal phase gratings, resulting in diffraction efficiency predictions far more accurate than those provided by classical scalar theories. The application of the theory to these gratings was motivated by the fact that rough surfaces are frequently modeled as a superposition of sinusoidal surfaces of different amplitudes, periods, and orientations.

The application of the non-paraxial scalar diffraction theory to surface scatter phenomena resulted first in a modified Beckmann-Kirchhoff surface scattering model,

then a generalized Harvey-Shack theory, both of which produce accurate results for rougher surfaces than the Rayleigh-Rice theory and for larger incident and scattering angles than the classical Beckmann-Kirchhoff theory. These new developments enable the analysis and simplify the understanding of wide-angle scattering behavior from rough surfaces illuminated at large incident angles. In addition, they provide an improved *BRDF* (Bidirectional Reflectance Distribution Function) model, particularly for the smooth surface inverse scattering problem of determining surface power spectral density (*PSD*) curves from *BRDF* measurements.

This work is dedicated to the memory of my brother

Volodimir Krywonos  
(1969-1985)

You left us far too soon, and I miss you.

## ACKNOWLEDGMENTS

There have been a number of people throughout my career as a graduate student who have helped me, inspired me, and generally made it all worthwhile. To these people, I give my heartfelt thanks.

First I thank my advisor, James Harvey, for the opportunity to work with you over these many years on many interesting projects. It was truly an honor. Your insight, enthusiasm, patience, and dedication to your students are but a few of your numerous qualities. I have thoroughly enjoyed all of our discussions, both technical and not, and am grateful that your door was always open. I could not have done this without you.

I would also like to offer thanks to each of the members of my committee, both for agreeing to serve as members and because each of them has had an impact on me during my time here:

- Glenn Boreman - without a doubt the best classroom teacher I have ever had.
- Jannick Rolland - because the things you taught me I have used a thousand times (maybe a million!)
- Richard Eastes - for the opportunity to work on an extremely interesting project, and for all of your support.

I thank John Stover for generously providing some of the scattering measurements used in this dissertation.

I give enormous thanks to my parents, Very Rev. Mykola and Rita Krywonos, who have always supported me whether they agreed with me or not. They have always done their best to be the best parents they could be, and they have truly succeeded.

I thank the following people for their friendship and support:

- Dan Durfey - because if you hadn't, I probably wouldn't have either, and because you're the best friend a person could ever hope to have.
- Javier Gonzalez - for all of your advice, for your tennis lessons, and for making it bearable when it didn't seem bearable.
- Larry D. Davis, Jr. - for letting me beat you at racquetball, for Epic Gatherings, and for being someone I can always count on.
- Gabriel Popescu - for road trips to Boston, for your movie making skills, and for making things interesting.
- Ferenc Szipőcs - for Ali G, Monty P, and for lots of interesting conversations.
- Cindi Vernold - for all of your help early on

Thanks to Caroline for your endless supply of smiles. You may have slowed me down a little bit, but it was worth every minute.

Last, but most of all, I thank my wonderful wife Betsy for all of her love, support, patience, and understanding. And for putting up with all of my illustrated explanations. I don't know how you do it, but you do it so well, and I'm eternally grateful.



## TABLE OF CONTENTS

LIST OF FIGURES .....	xi
LIST OF TABLES .....	xviii
TABLE OF ACRONYMS/ABBREVIATIONS.....	xix
CHAPTER 1: INTRODUCTION .....	1
1.1 Surface Scatter Phenomena.....	1
1.2 Motivation And Goals For This Research .....	5
1.3 Organization Of This Dissertation .....	7
CHAPTER 2: HISTORICAL BACKGROUND .....	9
2.1 Scalar Diffraction Theory .....	9
2.1.1 Fresnel And Fraunhofer Diffraction .....	15
2.1.1.1 The Fresnel Approximation .....	15
2.1.1.2 The Fraunhofer Approximation .....	16
2.1.2 Fourier Treatment Of Non-Paraxial Scalar Diffraction Theory .....	18
2.1.2.1 The Angular Spectrum Of Plane Waves .....	19
2.1.2.2 The Diffracted Wave Field As A Superposition Of Spherical Waves.....	23
2.1.2.3 Aberrations Of Diffracted Wave Fields.....	26
2.2 Surface Scatter Theory.....	28
2.2.1 The Bidirectional Reflectance Distribution Function (BRDF).....	31
2.2.2 Rayleigh-Rice (Small Perturbation) Surface Scatter Theory .....	34
2.2.3 Beckmann-Kirchhoff Surface Scatter Theory .....	38
2.2.4 Harvey-Shack Surface Scatter Theory.....	49

CHAPTER 3: A LINEAR SYSTEMS FORMULATION OF NON-PARAXIAL SCALAR DIFFRACTION THEORY .....	57
3.1 Radiometric Terminology .....	61
3.2 Diffracted Radiance – A Fundamental Quantity .....	63
3.3 Renormalization Conserves Energy In The Presence Of Evanescent Waves.....	66
3.4 Application To Sinusoidal Phase Gratings .....	72
3.4.1 Paraxial Model Of Sinusoidal Phase Gratings.....	73
3.4.2 Wide-Angle Behavior Of Sinusoidal Phase Gratings.....	78
3.4.3 Prediction Of Diffraction Efficiency .....	88
CHAPTER 4: MODIFIED BECKMANN-KIRCHHOFF SURFACE SCATTER THEORY .....	100
4.1 Non-Intuitive Surface Scatter Measurements .....	100
4.2 Qualitative Explanation Of Non-Intuitive Effects .....	104
4.3 Empirical Modification Of The Beckmann-Kirchhoff Theory.....	109
4.4 Comparison With Experimental Measurements For Rough Surfaces .....	112
4.5 Comparison With The Rayleigh-Rice Theory For Smooth Surfaces .....	116
4.6 Range Of Validity Of The Modified Beckmann-Kirchhoff Equations .....	123
4.6.1 Smooth Surface Approximation .....	124
4.6.2 Moderately Rough Surfaces.....	127
4.6.3 Very Rough Approximation .....	132
CHAPTER 5: GENERALIZED HARVEY-SHACK SURFACE SCATTER THEORY .....	136
5.1 The Original Harvey-Shack Theory.....	136
5.2 The Modified Harvey-Shack Formulation.....	138
5.2.1 Smooth Surface Approximation .....	143

5.2.2 Rough Surfaces .....	154
5.3 The Generalized Harvey-Shack Formulation .....	162
5.3.1 Smooth Surface Approximation .....	166
5.3.2 Quasi-Vectorizing The Harvey-Shack Theory For Smooth Surfaces.....	177
5.3.3 Inverse Scattering For Smooth Surfaces.....	178
5.3.4 Numerical Calculations For Rough Surfaces.....	189
5.3.5 Comparison With The Modified Beckman-Kirchhoff Theory .....	200
CHAPTER 6: SUMMARY AND CONCLUSIONS .....	211
6.1 Dissertation Summary.....	211
6.2 Areas For Future Work .....	214
LIST OF REFERENCES .....	216

## LIST OF FIGURES

Figure 1-1: Light incident on an imperfect optical surface.....	2
Figure 1-2: Schematic diagram of a surface profile and its relevant statistical parameters.....	3
Figure 1-3: Illustration of the relationship between relevant surface parameters.....	3
Figure 2-1: Geometry of the Kirchhoff formulation of diffraction by a plane screen .....	12
Figure 2-2: Geometry of the Rayleigh-Sommerfeld diffraction integral.....	14
Figure 2-3: Regions of validity of the Fraunhofer, Fresnel, and Rayleigh-Sommerfeld diffraction integrals.....	18
Figure 2-4: Geometry of propagation from plane $P_0$ to plane $P$ .....	19
Figure 2-5: Unit circle in direction cosine space .....	22
Figure 2-6: Diffraction geometry when observation space is a hemisphere centered on the diffracting aperture.....	25
Figure 2-7: Illustration of the geometry used in defining the BRDF.....	32
Figure 2-8: Scattering geometry and coordinate system for the Beckmann-Kirchhoff theory .....	39
Figure 2-9: Polished and aluminized fused quartz sample: a) Scattered intensity as a function of scattering angle, b) Scattered radiance as a function of $\beta-\beta_0$ .....	50
Figure 3-1: Converging incident beam striking a diffracting aperture at an arbitrary angle .....	60
Figure 3-2: Geometrical configuration used to demonstrate the fundamental theorem of radiometry, from which the quantity radiance is obtained.....	62
Figure 3-3: (a) Profile of an on-axis Gaussian radiance distribution in direction cosine space. (b) Profile of the on-axis intensity distribution corresponding to (a) as a function of diffraction angle. (c) Off-axis (normalized) radiance distribution resulting from a $64^\circ$ incident angle. (d) The off-axis intensity distribution in direction cosine space corresponding to (c). (e) Off-axis intensity distribution as a function of the diffraction angle.....	71

Figure 3-4: Diffracted intensity profile as predicted by the paraxial model for a sinusoidal reflection grating of period $d = 20\lambda$ operating at normal incidence .....	75
Figure 3-5: Diffracted intensity distribution profile as predicted by the paraxial model for a sinusoidal reflection grating of period $1.3\lambda$ (invalid operating regime).....	78
Figure 3-6: Diffracted radiance distribution profile (in direction cosine space) predicted by our non-paraxial model for a sinusoidal reflection grating with a period of $d = 1.95\lambda$ .....	83
Figure 3-7: Diffracted intensity distribution profile predicted by our non-paraxial model for a sinusoidal reflection grating with a period of $d = 1.95\lambda$ .....	84
Figure 3-8: Comparison of wide-angle diffraction behavior of a sinusoidal reflection grating with a period of $d = 1.95\lambda$ , and a groove depth of $h = 0.5\lambda$ as predicted by scalar theory with and without a paraxial approximation. ....	86
Figure 3-9: Diffracted radiance in direction cosine space as a function of grating period for a sinusoidal reflection grating of groove depth $h = 0.25\lambda$ as predicted by our non-paraxial model .....	87
Figure 3-10: Diffracted intensity corresponding to the radiance distribution in Figure 3-9.....	88
Figure 3-11: Diffraction grating efficiency of the first order for a sinusoidal phase grating ( $h/d = 0.2$ ) in the Littrow condition as predicted by the Beckmann-Kirchhoff theory, the paraxial scalar theory, and a rigorous integral vector theory.....	90
Figure 3-12: Illustration of the peak-to-peak phase variation introduced into a given diffracted order by reflection from a sinusoidal surface.....	94
Figure 3-13: Diffraction grating efficiency of the first order for a perfectly conducting sinusoidal phase grating with $h/d = 0.2$ used in the Littrow condition as predicted by the Beckmann-Kirchhoff theory, the paraxial scalar theory, our non-paraxial scalar theory, and a rigorous integral vector theory .....	95
Figure 3-14: Diffraction grating efficiency of the first order for a perfectly conducting sinusoidal phase grating with $h/d = 0.05$ used in the Littrow condition as predicted by the Beckmann-Kirchhoff theory, the paraxial scalar theory, our non-paraxial scalar theory, and a rigorous integral vector theory .....	96

Figure 3-15: Diffraction grating efficiency of the first order for a perfectly conducting sinusoidal phase grating with $h/d = 0.15$ used in the Littrow condition as predicted by the Beckmann-Kirchhoff theory, the paraxial scalar theory, our non-paraxial scalar theory, and a rigorous integral vector theory .....	97
Figure 3-16: Diffraction grating efficiency of the first order for a perfectly conducting sinusoidal phase grating with $h/d = 0.30$ used in the Littrow condition as predicted by the Beckmann-Kirchhoff theory, the paraxial scalar theory, our non-paraxial scalar theory, and a rigorous integral vector theory .....	98
Figure 4-1: Classical Beckmann-Kirchhoff theory compared to O'Donnell-Mendez experimental data for $\lambda = 10.6 \mu\text{m}$ , $\theta_i = 20^\circ$ .....	102
Figure 4-2: Classical Beckmann-Kirchhoff theory compared to O'Donnell-Mendez experimental data for $\lambda = 10.6 \mu\text{m}$ , $\theta_i = 70^\circ$ .....	103
Figure 4-3: Classical Beckmann-Kirchhoff theory compared to O'Donnell-Mendez experimental data for $\lambda = 0.6328 \mu\text{m}$ and $\theta_i = 70^\circ$ .....	104
Figure 4-4: $ACV$ of equation 4.3 with $\sigma_s = 2.27 \mu\text{m}$ and $\ell_c = 20.9 \mu\text{m}$ .....	106
Figure 4-5: Harvey-Shack prediction of the scattered radiance and intensity distributions for the O'Donnell-Mendez surface with $\theta_i = 0^\circ$ and $\lambda = 10.6 \mu\text{m}$ .....	107
Figure 4-6: Harvey-Shack prediction of the scattered radiance and intensity distributions for the O'Donnell-Mendez surface with $\theta_i = 0^\circ$ and $\lambda = 10.6 \mu\text{m}$ .....	108
Figure 4-7: BK and MBK compared to experimental data for $\lambda = 10.6 \mu\text{m}$ and $\theta_i = 20^\circ$ .....	113
Figure 4-8: BK and MBK compared to experimental data for $\lambda = 10.6 \mu\text{m}$ and $\theta_i = 70^\circ$ .....	114
Figure 4-9: BK and MBK compared to experimental data for $\lambda = 0.6328 \mu\text{m}$ and $\theta_i = 70^\circ$ .....	115
Figure 4-10: BK, MBK, and RR compared for a smooth surface at normal incidence and with small scattering angles .....	118
Figure 4-11: BK, MBK, and RR compared for a smooth surface at normal incidence and with large scattering angles .....	118

Figure 4-12: BK and MBK compared to RR for $\theta_i = 20^\circ$ , $\sigma_s/\lambda = 0.02$ , and $\ell_c/\lambda = 5$ , 1, 0.5, and 0.25.....	120
Figure 4-13: BK and MBK compared to RR for $\theta_i = 50^\circ$ , $\sigma_s/\lambda = 0.02$ , and $\ell_c/\lambda = 5$ , 1, 0.5, and 0.25.....	121
Figure 4-14: BK and MBK compared to RR for $\theta_i = 70^\circ$ , $\sigma_s/\lambda = 0.02$ , and $\ell_c/\lambda = 5$ , 1, 0.5, and 0.25.....	122
Figure 4-15: Comparison between the general MBK solution using 50 terms in equation 4.12 and the MBK smooth surface approximation of using only one term in equation 4.12 for $g = 2, 0.5, .1$ , and $0.01$ .....	125
Figure 4-16: Maximum error between the general MBK solution using 50 terms in equation 4.12 and the MBK smooth approximation using 1 term in equation 4.12 as a function of $g$ for $\theta_i = 0^\circ, 50^\circ$ , and $70^\circ$ .....	126
Figure 4-17: Term Importance as a function of scattering angle in the plane of incidence for $\theta_i = 0^\circ$ , $\ell_c/\lambda = 10$ , $g = 50$ , $n = 45$ , and $m = 400$ .....	128
Figure 4-18: Average Term Importance as a function of term number for $\theta_i = 0^\circ$ , $\ell_c/\lambda = 10$ , $g = 50$ , and $m = 400$ .....	130
Figure 4-19: Average Term Importance as a function of term number for $\theta_i = 0^\circ$ , $\ell_c/\lambda = 10$ , $g = 300$ , and $m = 500$ .....	130
Figure 4-20: Number of terms needed to calculate the general MBK result of equation 4.12 as a function of $g$ for $\theta_i = 0^\circ, 50^\circ$ , and $70^\circ$ .....	131
Figure 4-21: Comparison between the general MBK solution of equation 4.12 with an appropriate number of terms, and the MBK very rough surface approximation of equation 4.14 for $g = 5, 20, 100$ , and $400$ .....	133
Figure 4-22: Maximum error between the general MBK solution and the MBK very rough approximation as a function of $g$ for $\theta_i = 0^\circ, 50^\circ$ , and $70^\circ$ .....	134
Figure 5-1: Illustration of the OPD for a specularly reflected ray .....	139
Figure 5-2: OHS and MHS compared to RR for $\theta_i = 0^\circ$ and $\ell_c/\lambda = 5$ .....	146
Figure 5-3: OHS and MHS compared to RR for $\theta_i = 0^\circ$ and $\ell_c/\lambda = 0.5$ .....	147
Figure 5-4: OHS and MHS compared to RR for $\theta_i = 5^\circ$ and $\ell_c/\lambda = 5$ .....	148
Figure 5-5: OHS and MHS compared to RR for $\theta_i = 40^\circ$ and $\ell_c/\lambda = 5$ .....	149

Figure 5-6: MHS compared to RR for $\theta_i = 20^\circ$ and $\ell_c/\lambda = 40, 10, 5$ , and 1 .....	151
Figure 5-7: MHS compared to RR for $\theta_i = 50^\circ$ and $\ell_c/\lambda = 40, 10, 5$ , and 1 .....	152
Figure 5-8: MHS compared to RR for $\theta_i = 70^\circ$ and $\ell_c/\lambda = 40, 10, 5$ , and 1 .....	153
Figure 5-9: MHS surface transfer function for a scattering surface with a Gaussian <i>ACV</i> function. $\lambda = 10.6 \mu\text{m}$ , $\theta_i = 70^\circ$ , $\sigma_s = 2.27 \mu\text{m}$ , $\ell_c = 20.9 \mu\text{m}$ .....	155
Figure 5-10: The <i>ASF</i> calculated by taking the Fourier transform of the transfer function in Figure 5-9 .....	155
Figure 5-11: Truncated and renormalized <i>ASF</i> of Figure 5-10 .....	156
Figure 5-12: Plane-of-incidence profile of the diffusely scattered portion of the <i>ASF</i> in Figure 5-10 both before and after renormalization .....	157
Figure 5-13: Scattered intensity in the plane of incidence as a function of scattering angle for the diffusely scattered portion of the <i>ASF</i> of Figure 5-10 .....	158
Figure 5-14: MHS compared to OHS and OM experimental data for $\sigma_s/\lambda = 0.214$ , $\ell_c/\lambda = 1.97$ , and $\theta_i = 0^\circ, 20^\circ, 50^\circ$ , and $70^\circ$ .....	160
Figure 5-15: MHS compared to OHS and OM experimental data for $\sigma_s/\lambda = 3.59$ , $\ell_c/\lambda = 33.0$ , and $\theta_i = 70^\circ$ .....	162
Figure 5-16: Illustration of the OPD for a ray scattered at an arbitrary angle $\theta_s$ .....	163
Figure 5-17: GHS and MHS compared to RR for $\theta_i = 0^\circ$ and $\ell_c/\lambda = 5$ .....	169
Figure 5-18: GHS and MHS compared to RR for $\theta_i = 0^\circ$ and $\ell_c/\lambda = 0.5$ .....	170
Figure 5-19: GHS and MHS compared to RR for $\theta_i = 20^\circ$ and $\ell_c/\lambda = 10, 5, 1$ , and 0.5 .....	171
Figure 5-20: GHS and MHS compared to RR for $\theta_i = 50^\circ$ and $\ell_c/\lambda = 10, 5, 1$ , and 0.5 .....	172
Figure 5-21: GHS and MHS compared to RR for $\theta_i = 70^\circ$ and $\ell_c/\lambda = 10, 5, 1$ , and 0.5 .....	173
Figure 5-22: GHS and RR for a K-Correlation <i>PSD</i> with $a = 1.5\text{E}5$ , $b = 300$ , $c = 1.4$ , $\lambda = 0.6328\mu\text{m}$ for $\theta_i = 0^\circ, 20^\circ, 50^\circ$ , and $70^\circ$ .....	176
Figure 5-23: Measured <i>BRDF</i> of molybdenum mirror for $\theta_i = -5^\circ$ and $\lambda = 0.488 \mu\text{m}$ .....	181



Figure 5-24: Reflectance of the molybdenum mirror as a function of angle.....	181
Figure 5-25: Predicted <i>PSD</i> of the molybdenum mirror using the Rayleigh-Rice theory and measured <i>BRDF</i> data for $\theta_i = -5^\circ$ and $\lambda = 0.488 \mu\text{m}$ .....	183
Figure 5-26: Predicted <i>PSD</i> of the molybdenum mirror using the generalized Harvey-Shack theory and measured <i>BRDF</i> data for $\theta_i = -5^\circ$ and $\lambda = 0.488 \mu\text{m}$ .....	183
Figure 5-27: GHS and RR predictions of <i>BRDF</i> for a K-Correlation <i>PSD</i> with $a = 1.5\text{E}5$ , $b = 300$ , $c = 1.4$ , and $\lambda = 0.6328 \mu\text{m}$ for normal incidence. ....	184
Figure 5-28: K-correlation fit to the <i>PSD</i> prediction shown in Figure 5-26.....	185
Figure 5-29: GHS and RR predictions of the <i>BRDF</i> for the molybdenum mirror compared to experimental data for $\theta_i = -5^\circ$ and $\lambda = 0.488$ .....	186
Figure 5-30: GHS and RR predictions of the <i>BRDF</i> for the molybdenum mirror compared to experimental data for $\theta_i = -45^\circ$ and $\lambda = 0.488$ .....	187
Figure 5-31: GHS and RR predictions of the <i>BRDF</i> for the molybdenum mirror compared to experimental data for $\theta_i = -75^\circ$ and $\lambda = 0.488$ .....	188
Figure 5-32: Grid of $\alpha$ , $\beta$ values with unit circle representing the observation space....	190
Figure 5-33: GHS surface transfer function for a surface with a Gaussian <i>ACV</i> function. $\lambda = 10.6 \mu\text{m}$ , $\sigma_s = 2.27 \mu\text{m}$ , $\ell_c = 20.9 \mu\text{m}$ , $\theta_i = 45^\circ$ , $\alpha_s = -0.88$ , $\beta_s = 0$ .....	192
Figure 5-34: Intermediate <i>ASF</i> calculated from the surface transfer function in Figure 5-33 where $\alpha_s = -0.88$ , $\beta_s = 0$ .....	193
Figure 5-35: One-dimensional profile along the $\beta = 0$ axis for the intermediate <i>ASF</i> of Figure 5-34. The single data point being extracted is circled.....	194
Figure 5-36: Final <i>ASF</i> predicted by the GHS theory for a surface with a Gaussian <i>ACV</i> function. $\lambda = 10.6 \mu\text{m}$ , $\sigma_s = 2.27 \mu\text{m}$ , $\ell_c = 20.9 \mu\text{m}$ , and $\theta_i = 45^\circ$ .....	195
Figure 5-37: Profile of the <i>ASF</i> in Figure 5-36 in the plane-of-incidence.....	195
Figure 5-38: GHS compared to MHS and OM experimental data for $\sigma_s/\lambda = 0.214$ , $\ell_c/\lambda = 1.97$ , and $\theta_i = 0^\circ, 20^\circ, 50^\circ$ , and $70^\circ$ .....	197
Figure 5-39: GHS compared to MHS and OM experimental data for $\sigma_s/\lambda = 3.59$ , $\ell_c/\lambda = 33.0$ , and $\theta_i = 70^\circ$ .....	199

Figure 5-40: GHS and MBK scattering functions compared for a moderately rough surface with a Gaussian $ACV$ function. $\ell_c = 2$ , $\sigma_s = 0.1$ , $\lambda = 0.6328$ , and $\theta_i = 50^\circ$ .....	202
Figure 5-41: The same comparison as Figure 5-40, except that the MBK result has been divided by $\lambda^2$ .....	203
Figure 5-42: GHS and MBK angle spread functions compared for a very rough surface with a Gaussian $ACV$ function. $\ell_c = 20$ , $\sigma_s = 2.74$ , $\lambda = 0.6328$ , and $\theta_i = 50^\circ$ .....	203
Figure 5-43: The same comparison as Figure 5-42, except that the MBK result has been divided by $\lambda^2$ .....	204

## LIST OF TABLES

Table 1: Diffraction efficiencies for a coarse (paraxial regime) sinusoidal phase grating optimized for maximum efficiency in the $\pm 1$ diffracted orders. ....	76
---	----

## TABLE OF ACRONYMS/ABBREVIATIONS

ACV	Autocovariance (function)
ASF	Angle Spread Function
BK	Beckmann-Kirchhoff
BRDF	Bidirectional Reflectance Distribution Function
BSDF	Bidirectional Scattering Distribution Function
BTDF	Bidirectional Transmittance Distribution Function
FFT	Fast Fourier Transform
GHS	Generalized Harvey-Shack
MBK	Modified Beckmann-Kirchhoff
MHS	Modified Harvey-Shack
OHS	Original Harvey-Shack
OM	O'Donnell-Mendez
OPD	Optical Path Difference
PSD	Power Spectral Density
PSF	Point Spread Function
RMS	Root Mean Square
RR	Rayleigh-Rice
SPM	Small Perturbation Method
TIS	Total Integrated Scatter

## **CHAPTER 1: INTRODUCTION**

Scattering from rough surfaces has been an area of intense study over the last century, and is an important issue in a large number of scientific areas including optics, geophysics, acoustics, oceanography, communications, and remote sensing. It is also of great importance in the area of computer graphics, where efficient scattering models are needed to create photorealistic images of synthetic scenes and environments.

### **1.1 Surface Scatter Phenomena**

Surface scatter effects can be considered to be merely diffraction phenomena resulting from random phase variations induced upon a reflected wavefront by microtopographic surface features. Most natural surfaces have an inherent roughness that results in scattered light. Machined and otherwise processed surfaces also exhibit characteristic surface features or roughness. Even the smoothest optically polished surfaces have a small residual roughness due to the imperfect optical fabrication process.

When light is reflected from an imperfect optical surface, the reflected radiation consists of a specularly reflected component and a diffusely reflected component as illustrated in Figure 1-1. The light scattered from optical surface irregularities degrades optical performance in several different ways: (i) it reduces optical throughput since some of the scattered radiation will not even reach the focal plane, (ii) the wide-angle scatter will produce a veiling glare which reduces image contrast or the signal-to-noise ratio, and (iii) the small-angle scatter will decrease resolution by producing an image blur.

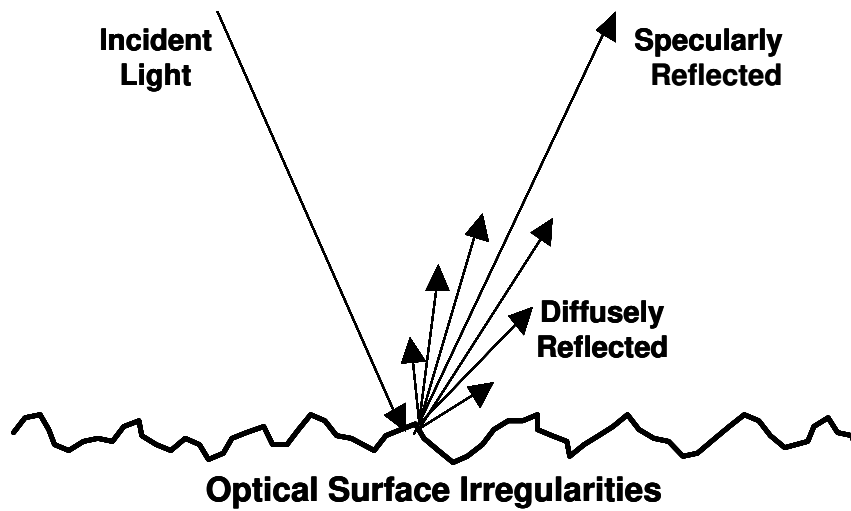


Figure 1-1: Light incident on an imperfect optical surface

The behavior of light scattered from randomly rough surfaces is dictated by the statistical surface characteristics. Consider the surface profile illustrated in Figure 1-2. The surface has a zero mean with the surface height,  $h$ , illustrated as a function of position along a one-dimensional trace of finite length. The two relevant statistical surface characteristics are the surface height distribution function and the surface autocovariance (*ACV*) function. Fortunately, for many cases of interest, the surface heights are normally distributed (i.e., the surface height distribution is Gaussian). The root-mean-square (RMS) surface roughness,  $\sigma_s$ , is the standard deviation of that normal distribution. The autocovariance length,  $\ell$ , is defined as the half-width of the autocovariance function at the  $1/e$  height. It would be convenient, at least mathematically, if the surface autocovariance function were also Gaussian, however that is not usually the case. Instead, the autocovariance function is material and process dependent.

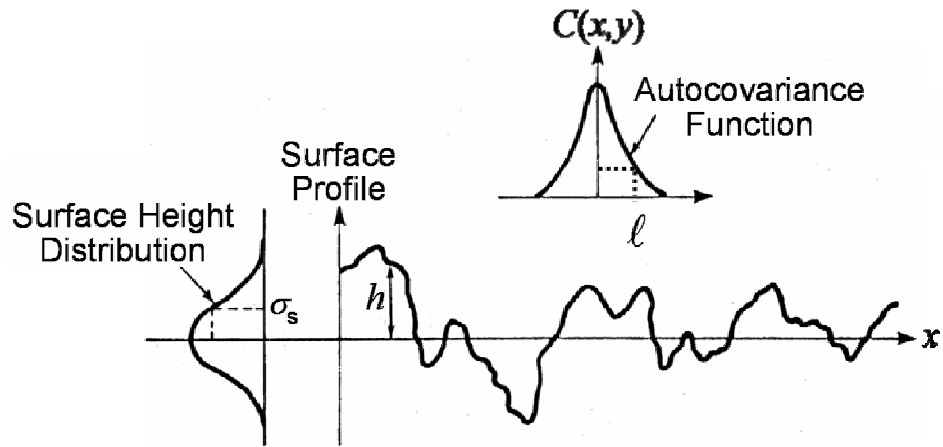


Figure 1-2: Schematic diagram of a surface profile and its relevant statistical parameters

The surface power spectral density (*PSD*) function and the surface *ACV* function form a Fourier transform pair, and therefore Figure 1-3 further illustrates the surface characteristics relevant to scattered light behavior.

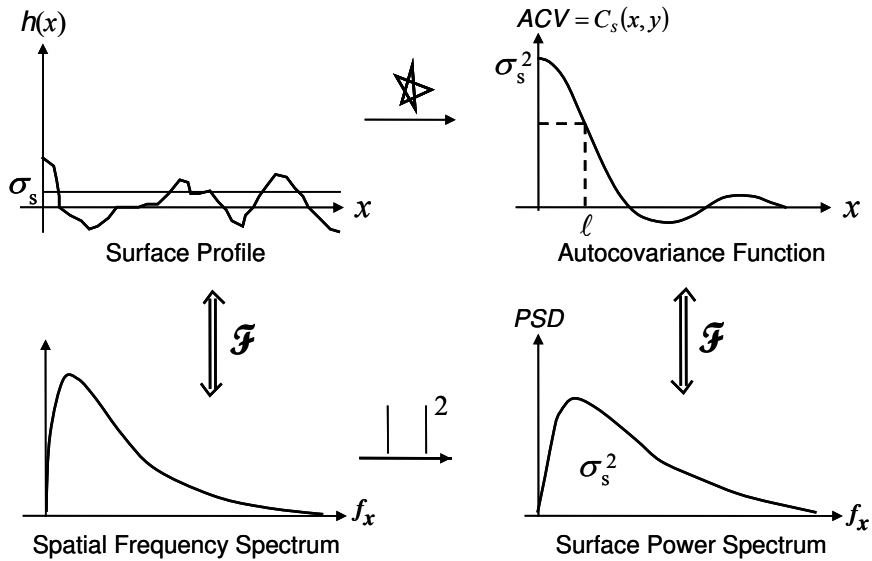


Figure 1-3: Illustration of the relationship between relevant surface parameters

Note that the value of the surface autocovariance function at the origin is equal to the surface variance  $\sigma_s^2$ . From the central ordinate theorem of Fourier transform theory [1], we therefore know that the volume under the two-dimensional surface *PSD* is also equal to the surface variance. The surface *PSD* can be thought of as a plot of surface variance as a function of the spatial frequency of the surface irregularities.

There is clearly a relationship between the surface roughness and the amount of light scattered out of the specular beam upon reflection from a surface. In fact, scattered light measurements are an excellent way to infer surface characteristics. The total integrated scatter (*TIS*) is defined as that fraction of the total reflected radiant power that is scattered out of the specular beam. In 1954, Davies reported the following relationship for total integrated scatter from smooth, clean, conductive surfaces [2]

$$TIS = \frac{P_s}{RP_i} = \frac{P_s}{P_o + P_s} \approx \left( \frac{4\pi\sigma_s \cos\theta_i}{\lambda} \right)^2. \quad (1.1)$$

In the above equation,  $P_i$  is the incident power,  $R$  is the (power) reflectance of the surface,  $P_s$  is the scattered power,  $P_o$  is the power remaining in the specularly reflected beam,  $\sigma_s$  is the rms surface roughness,  $\theta_i$  is the incident angle, and  $\lambda$  is the wavelength of the incident radiation. In addition to the smooth surface requirement ( $\sigma_s/\lambda \ll 1$ ), Davies also assumed that the surface height distribution was Gaussian and that most of the scattered light was restricted to angles close to the specular beam ( $\theta_s \approx \theta_o$ ).

The conditions of Davies' derivation resulting in equation 1.1 were somewhat more restrictive than necessary. A more general expression for the *TIS* is given by [3]



$$TIS = 1 - \exp\left[-\left(4\pi \cos \theta_i \sigma_s / \lambda\right)^2\right]. \quad (1.2)$$

Equation 1.2 is valid for moderately rough surfaces and does not require that the surface have a Gaussian surface height distribution function. In addition, for the special case of smooth surfaces, retaining only the first term of a binomial expansion of the exponential causes equation 1.2 to reduce to the more restrictive equation 1.1.

## 1.2 Motivation And Goals For This Research

In many optics applications, it is not only the *amount* of scattered light, but also the *direction* of the scattered radiation that plays a crucial role in the performance of an optical system. This is particularly true for three distinct types of applications: (i) the design and analysis of stray light rejection systems required by optical systems used to view a relatively faint target in the vicinity of a much brighter object, (ii) the fabrication of “super-smooth” surfaces for high resolution X-ray and extreme ultraviolet (EUV) imaging systems, and (iii) remote sensing applications where scattered light signatures are used to remotely infer target characteristics. For these applications, as well as many others, the ability to predict scattered light distributions from surface topography (or vice versa) is extremely important.

The two oldest approaches to the problem of surface scattering are also the most widely used. The Rayleigh-Rice vector perturbation theory agrees well with experimental wide-angle scatter measurements from “smooth” ( $\sigma_s/\lambda \ll 1$ ) surfaces for arbitrary incident and scattering angles. However, not all applications of interest satisfy

the smooth surface approximation. The Beckmann-Kirchhoff scattering theory is valid for rougher surfaces, but contains a paraxial (small-angle) assumption that limits its ability to accurately handle wide-angle scattering and large angles of incidence. The linear systems approach to scattering developed by Harvey and Shack in the 1970s, while intuitive, also contains a small-angle assumption that limits its usefulness.

There have been a number of alternative approaches to solving the problem of scattering from rough surfaces. In 2004, Elfouhaily and Guérin published a critical survey of approximate theories of scattering from random rough surfaces [4]. They attempted to classify and characterize over thirty different approximate methods. They were all variants of the small perturbation method (Rayleigh-Rice), the Kirchhoff approach, or the so-called unified methods which attempt to bridge the gap between the two classical theories. The authors concluded that “there does not seem to be universal method that is to be preferred systematically. All methods represent a compromise between versatility, simplicity, numerical efficiency, accuracy, and robustness”. Their final statement was “There is still room for improvement in the development of approximate scattering methods”.

The goal of the research leading to this dissertation was the development of a surface scatter model that combined the advantages of the Rayleigh-Rice and Beckmann-Kirchhoff theories (without their disadvantages in terms of roughness and angular coverage), while retaining the intuitive nature of the Harvey-Shack linear systems treatment.

### 1.3 Organization Of This Dissertation

This dissertation consists of six chapters, including the present one. The remainder of the dissertation is organized in the following manner:

Chapter two gives a historical background of both scalar diffraction theory, and surface scatter theory. Particular emphasis is placed on the theories and models which will be built upon in this dissertation.

In chapter three a linear-systems approach to non-paraxial scalar diffraction theory is developed. By incorporating proper radiometric terminology and choosing an appropriate parameter space, it is shown that *diffracted radiance* is shift-invariant in direction cosine space, and therefore the fundamental quantity predicted by scalar diffraction theory. In addition, it is shown that the proper application of Parseval's theorem allows the theory to model the redistribution of energy from evanescent waves to propagating waves, ensuring conservation of energy. Finally, this non-paraxial scalar diffraction theory is applied to sinusoidal phase gratings, and is shown to be more accurate at predicting diffraction efficiencies than classical scalar theory.

In chapter four, the insight and understanding of non-paraxial scalar diffraction obtained in the previous chapter is utilized to make an empirical modification to the classical Beckmann-Kirchhoff scattering theory. This modified Beckmann-Kirchhoff model agrees with the Rayleigh-Rice theory for smooth surfaces with large incident and scattering angles, while at the same time agreeing with experimental rough surface measurements at large incident and scattering angles.

In chapter five, the Harvey-Shack surface scatter theory is generalized to account for large incident and scattering angles. This leads to a new two-parameter family of surface transfer functions, which allows numerical calculation of surface scatter behavior that agrees well with the Rayleigh-Rice theory for smooth surfaces with large incident and scattering angles. In addition, this linear systems formulation of surface scatter theory agrees well with experimental data from rough surfaces at large incident and scattering angles. A smooth-surface approximation to the generalized Harvey-Shack scattering theory is also shown to provide an improved *BRDF* model for solving the inverse scattering problem to obtain surface characteristics from measured *BRDF* data. Finally, it is shown that the modified Beckmann-Kirchhoff model and generalized Harvey-Shack theories are in fact identical

Chapter six consists of a summary of the dissertation and identifies areas for future work.

## **CHAPTER 2: HISTORICAL BACKGROUND**

### **2.1 Scalar Diffraction Theory**

The discovery of diffraction phenomena is usually credited to Francesco Grimaldi, a professor at the Jesuit college in Bologna, Italy, and in fact it was Grimaldi who invented the term “diffraction” [5]. He was among the first to observe and study the gradual transition from light to dark in the shadow region behind an aperture. A detailed study of his work, including a description of bands of light (fringes) within the shadow of a rod illuminated with a small source was given in his book, *De Lumine*, published in 1665.

Robert Hooke, curator of experiments for the Royal Society in London also observed the effects of diffraction. His study of the colored interference patterns generated by thin films was detailed in his book *Micrographia*, published in 1665. In it, he correctly concluded that the patterns were due to an interaction between the light reflected from the front and back surfaces [6].

James Gregory, best known for the telescope design that bears his name, effectively discovered the diffraction grating during his tenure at the University of St. Andrews in Scotland (1668-1674) [7]. By illuminating a bird feather with sunlight passing through a small hole, he was able to observe a central white spot surrounded by diffracted orders made up of a spectrum of colors [8].

In 1678, the Dutch physicist Christian Huygens wrote a treatise on the wave theory of light called *Traite de la Lumiere* (published in 1690), in which he expressed the

idea that every point on a wavefront serves as the source of spherical secondary wavelets such that the primary wavefront at some later time is the envelope of these wavelets [9]. This principle is a precise description of the convolution of a spherical wavelet with the complex amplitude distribution representing the primary wavefront. Using this principle, Huygens was able to derive the laws of reflection and refraction.

In 1704, Isaac Newton published *Opticks*, in which he strongly advocated for the corpuscular theory of light over the wave theory [10]. Because of Newton's prestige, most scientific opinion at the time sided with him. As a result, not much was done to advance the wave theory of light during the 18th century.

In 1802, Thomas Young provided indisputable evidence that light exhibits a wave-like nature when he presented the results of his now-famous experiments on the interference of light that he had carried out in Cambridge between 1797 and 1799. On July 1, 1802 and again on November 24, 1803 he presented papers before the Royal Society advocating the wave theory of light, and introducing the fundamental concept of interference [11]. With the wave theory, Young was able to explain the colored fringes of thin films, and determined the wavelengths of various colors using Newton's own data. Other scientists found Young's results to be counter-intuitive, however, and it did not gain widespread acceptance at the time.

In 1818 Augustin Fresnel submitted a paper to a competition sponsored by the French Academy of Sciences for the best work on diffraction. In it, he outlined a wave theory of light and showed that it was able to account for a number of phenomena including reflection, refraction, diffraction, and interference. Fresnel's work was essentially an extension of Huygens' work. He postulated that the Huygens' secondary

wavelets mutually interfere, and by making some arbitrary assumptions about their amplitudes and phases, he was able to accurately predict diffraction patterns. Most of the members of the judging committee, including Jean Biot, Siméon Poisson, and Pierre Laplace, were proponents of the corpuscular theory of light. Poisson used Fresnel's theory to show the seemingly absurd result that if light were incident on a circular obscuration, a bright spot would occur at the center of the shadow region behind the obscuration. The committee chairman, Dominique Arago, quickly set up an experiment and showed that Poisson's prediction was correct, and Fresnel won the competition.

The *Huygens-Fresnel principle*, as it has come to be known, is given by a superposition of spherical wavelets emanating from each point within a diffracting aperture, where each spherical wave exhibits a  $\pi/2$  phase delay, a cosine obliquity factor, and an amplitude that is inversely proportional to the wavelength of the radiation [12]. This is expressed mathematically by

$$U(x, y) = \frac{1}{i\lambda} \iint_{\Sigma} U_o(x_1, y_1) \frac{\exp(ikr)}{r} \cos(\vec{n}, \vec{r}) dx_1 dy_1, \quad (2.1)$$

where the integral is over the two-dimensional diffraction aperture,  $U_o(x_1, y_1)$  is the optical disturbance emerging from the aperture, and since  $\exp(i\pi/2) = i$ , the  $i$  in the denominator represents a  $\pi/2$  phase delay.

In 1882, Gustav Kirchhoff added some mathematical rigor to the ideas of Huygens and Fresnel by showing that the amplitudes and phases ascribed to the secondary wavelets were logical consequences of the wave nature of light. He did this by choosing an appropriate Green's function that satisfied the differential wave equation.

Figure 2-1, borrowed from Goodman [13], illustrates the geometry of the Kirchhoff formulation of diffraction by a plane screen. Monochromatic radiation is assumed to be incident from the left on an aperture  $\Sigma$  in an infinite opaque screen.

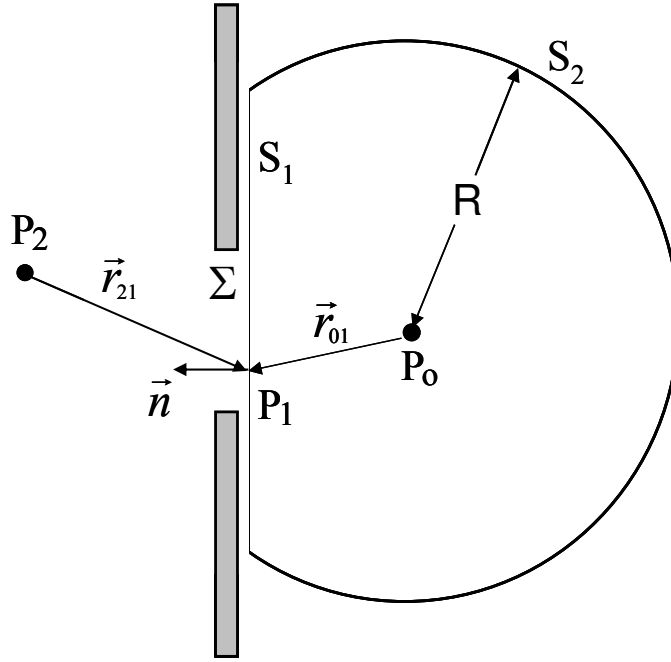


Figure 2-1: Geometry of the Kirchhoff formulation of diffraction by a plane screen

The diffracted wave field at the point  $P_o$  is calculated by applying the *integral theorem of Helmholtz and Kirchhoff* [14], and the result is given by [13]

$$U(P_o) = \frac{A}{i\lambda} \iint_{\Sigma} \frac{\exp[ik(r_{21} + r_{01})]}{r_{21} r_{01}} \left[ \frac{\cos(\vec{n}, \vec{r}_{01}) - \cos(\vec{n}, \vec{r}_{21})}{2} \right] ds. \quad (2.2)$$



The Kirchhoff formulation, however, was based upon the following inconsistent boundary conditions:

- (i) The field distribution  $U$  and its derivative  $\partial U/\partial n$  are the same across the aperture as they would be in the absence of the screen.
- (ii) The field distribution  $U$  and its derivative  $\partial U/\partial n$  are identically zero over the portion of  $S_1$  that lies in the geometrical shadow of the screen.

It can be shown that if the field and its normal derivative vanish together on any finite surface element, then the field must vanish everywhere. Therefore, the two Kirchhoff boundary conditions together require the field to be zero everywhere behind the aperture.

In 1896 [15], Sommerfeld eliminated the need for imposing boundary conditions upon both the field and its normal derivative simultaneously, thereby removing the inconsistencies in the Fresnel-Kirchhoff formulation. The resulting Rayleigh-Sommerfeld diffraction theory is a rigorous treatment limited only in that it is a scalar theory that neglects the fact that the various components of the electric and magnetic fields are coupled through Maxwell's equations. The general form of the Rayleigh-Sommerfeld diffraction formula is valid throughout the entire observation space, right down to the aperture, and is given by [16]

$$U_2(x_2, y_2) = \frac{A}{\lambda} \int_{-\infty}^{\infty} \int_{-\infty}^{\infty} U_1(x_1, y_1) \left( \frac{1}{k\ell} - i \right) \frac{\exp(ik\ell)}{\ell} \cos(\vec{n}, \vec{\ell}) dx_1 dy_1. \quad (2.3)$$

The more common form of the Rayleigh-Sommerfeld diffraction formula is an

approximation valid for  $z \gg \lambda$ , and is given by

$$U_2(x_2, y_2) = \frac{A}{i\lambda} \int_{-\infty}^{\infty} \int_{-\infty}^{\infty} U_1(x_1, y_1) \frac{\exp(ik\ell)}{\ell} \cos(\vec{n}, \vec{\ell}) dx_1 dy_1. \quad (2.4)$$

The quantity  $U_1(x_1, y_1)$  is the complex amplitude distribution emerging from the diffracting aperture  $\Sigma$ , and

$$\ell = \sqrt{z^2 + (x_2 - x_1)^2 + (y_2 - y_1)^2} \quad (2.5)$$

is the distance from an arbitrary point in the diffracting aperture to an arbitrary point in the observation plane as shown in Figure 2-2.

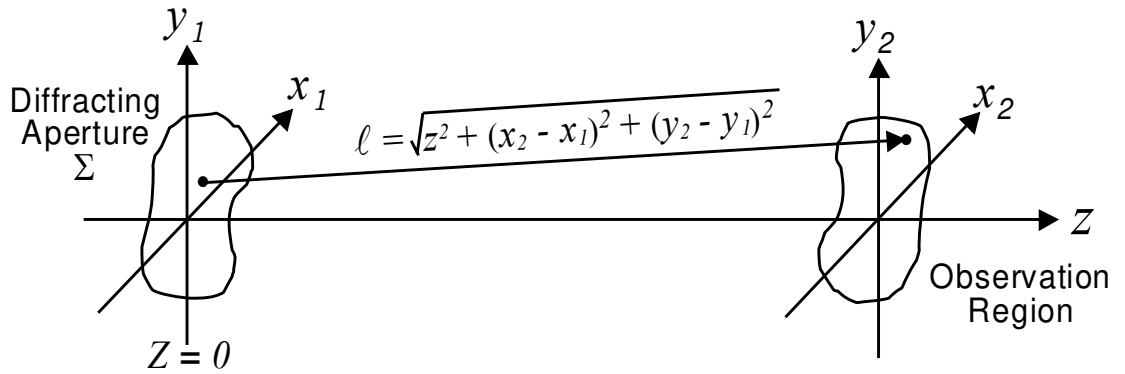


Figure 2-2: Geometry of the Rayleigh-Sommerfeld diffraction integral

### 2.1.1 Fresnel And Fraunhofer Diffraction

The Rayleigh-Sommerfeld diffraction integral is rather difficult to solve in closed form for most problems of practical interest. Certain approximations can be made, however, that will allow relatively simple calculation of diffraction patterns.

For applications where only paraxial diffraction angles are involved, the  $\ell$  in the denominator of the integrand in equation 2.4 can be approximated by the quantity  $z$ , and the cosine obliquity factor is approximately unity. However, the  $\ell$  in the exponent is multiplied by a very large number,  $k = 2\pi/\lambda$ , and even small changes in phase can change the value of the exponential significantly.

#### 2.1.1.1 The Fresnel Approximation

The Fresnel approximation is obtained by making a binomial expansion of the quantity  $\ell$  in the Rayleigh-Sommerfeld integral of equation 2.4, and retaining only the first two terms of the expansion in the exponent, while at the same time replacing the  $\ell$  in the denominator with  $z$ . The resulting expression for the complex amplitude distribution in the observation plane is given by [13]

$$U_2(x_2, y_2) = \frac{\exp(ikz)}{i\lambda z} \int_{-\infty}^{\infty} \int_{-\infty}^{\infty} U_1(x_1, y_1) \exp\left\{\frac{ik}{2z} \left[(x_2 - x_1)^2 + (y_2 - y_1)^2\right]\right\} dx_1 dy_1. \quad (2.6)$$

The approximation leading to equation 2.6 will be valid provided the following *Fresnel criterion* is met:

$$z^3 \gg \frac{\pi}{4\lambda} \left[ (x_2 - x_1)^2 + (y_2 - y_1)^2 \right]_{\max}^2. \quad (2.7)$$

The Fresnel diffraction integral in equation 2.6 is readily seen to be a convolution integral that can be expressed in the form

$$U_2(x_2, y_2) = \int_{-\infty}^{\infty} \int_{-\infty}^{\infty} U_1(x_1, y_1) h(x_2 - x_1, y_2 - y_1) dx_1 dy_1, \quad (2.8)$$

where the convolution kernel (impulse response of the Fresnel diffraction process) is merely a parabolic approximation to a spherical Huygens' wavelet given by

$$h(x_1, y_1) = \frac{\exp(ikz)}{i\lambda z} \exp\left[\frac{ik}{2z}(x_1^2 + y_1^2)\right]. \quad (2.9)$$

Equation 2.6 can also be written as a Fourier transform integral given by

$$\begin{aligned} U_2(x_2, y_2) &= \frac{\exp(ikz)}{i\lambda z} \exp\left[\frac{ik}{2z}(x_2^2 + y_2^2)\right] \\ &\times \int_{-\infty}^{\infty} \int_{-\infty}^{\infty} \left\{ U_1(x_1, y_1) \exp\left[\frac{ik}{2z}(x_1^2 + y_1^2)\right] \right\} \exp\left[-\frac{i2\pi}{\lambda z}(x_2x_1 + y_2y_1)\right] dx_1 dy_1. \end{aligned} \quad (2.10)$$

### 2.1.1.2 The Fraunhofer Approximation

The Fraunhofer approximation is obtained from the Fresnel approximation by additionally imposing the stricter *Fraunhofer criterion*

$$z \gg \frac{k(x_1^2 + y_1^2)_{\max}}{2}. \quad (2.11)$$

When this inequality is true, the quadratic phase factor in the integrand of the Fresnel diffraction formula of equation 2.10 is approximately equal to unity over the entire aperture. The resulting expression for the complex amplitude distribution in the observation plane is given (with the exception of a multiplicative phase factor) directly by the Fourier transform of complex amplitude emerging from the aperture, evaluated at spatial frequencies  $\xi = x_2 / \lambda z$  and  $\eta = y_2 / \lambda z$  [13]:

$$U_2(x_2, y_2) = \frac{\exp(ikz)}{i\lambda z} \exp\left[\frac{ik}{2z}(x_2^2 + y_2^2)\right] \times \int_{-\infty}^{\infty} \int_{-\infty}^{\infty} U_1(x_1, y_1) \exp\left[-\frac{i2\pi}{\lambda z}(x_2 x_1 + y_2 y_1)\right] dx_1 dy_1 . \quad (2.12)$$

When the Fraunhofer criterion is satisfied, the irradiance distribution in the observation plane is given by the following well-known expression:

$$E_2(x_2, y_2) = |U_2(x_2, y_2)|^2 = \frac{1}{\lambda^2 z^2} \left| \mathcal{F}\{U_1(x_1, y_1)\} \Big|_{\substack{\xi=x_2/\lambda z \\ \eta=y_2/\lambda z}} \right|^2, \quad (2.13)$$

where  $\mathcal{F}$  represents the Fourier transform operation.

Figure 2-3 illustrates the axial regions of space in which the Fraunhofer, Fresnel, and Rayleigh-Sommerfeld diffraction formulas are valid. Note that the Fraunhofer region is contained in the Fresnel region, and both the Fraunhofer and Fresnel regions are contained in the Rayleigh-Sommerfeld region. The far field is widely understood to be synonymous with the Fraunhofer region; however there is less agreement in the literature upon the definition of the near field. We define the near field to be that region of space

that does not satisfy even the Fresnel criterion. The near field and the far field are therefore mutually exclusive, but not all inclusive.

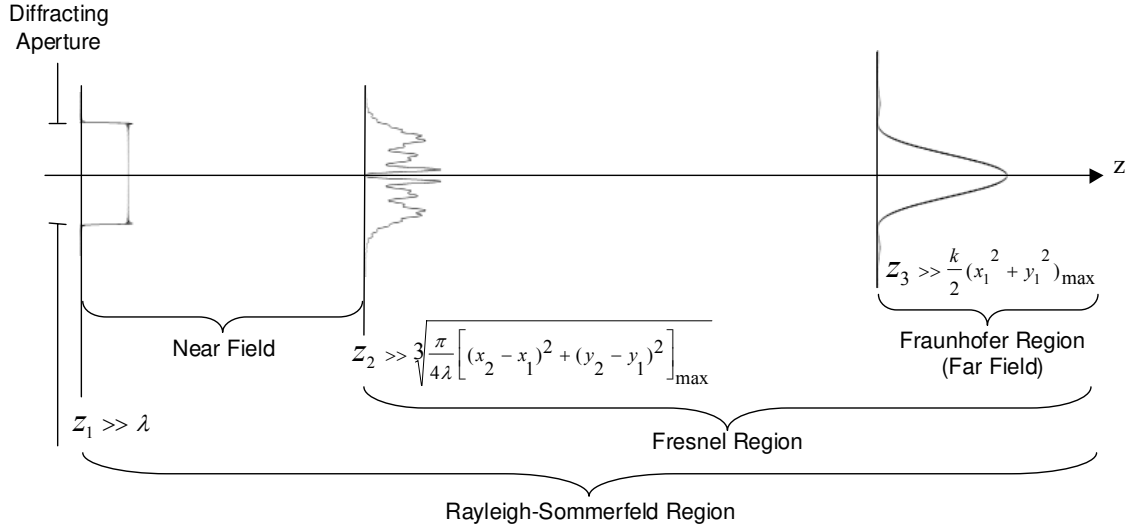


Figure 2-3: Regions of validity of the Fraunhofer, Fresnel, and Rayleigh-Sommerfeld diffraction integrals.

### 2.1.2 Fourier Treatment Of Non-Paraxial Scalar Diffraction Theory

It is also possible to formulate scalar diffraction theory using an approach based on the concepts of linear systems theory. This method, known as the *angular spectrum* approach, was first proposed by Booker and Clemmow in 1950 [17], and later treated in detail by others [13,18,19]

Harvey generalized the Fourier treatment of scalar diffraction to include new insight into the phenomenon of diffraction throughout the whole space in which it occurs

[20]. Since we will expand upon Harvey's treatment in this dissertation, we will present it now in some detail. The discussion that follows comes directly from [20,21].

### 2.1.2.1 The Angular Spectrum Of Plane Waves

The diffraction problem can be considered to consist of two parts: (i) determining the effect on the wave field that comes from introducing a diffracting screen or aperture and (ii) determining how it affects the field at some point beyond the aperture due to propagation. We will consider the propagation problem first.

The geometry for the problem is shown in Figure 2-4. Let the complex amplitude distribution in plane  $P_o$  be given by the scalar function  $U_o(\hat{x}, \hat{y}; 0)$ , which will be assumed to be the only radiation contributing to the complex amplitude distribution  $U(\hat{x}, \hat{y}; \hat{z})$  in plane  $P$ . Note that a scaled coordinate system is used in which  $\hat{x} = x / \lambda$ ,  $\hat{y} = y / \lambda$ , and  $\hat{z} = z / \lambda$ .



Figure 2-4: Geometry of propagation from plane  $P_o$  to plane  $P$

It will be assumed that the complex amplitude of any monochromatic optical disturbance propagating through free space must obey the time-independent (Helmoltz) wave equation, and that Fourier transforms of both  $U_o(\hat{x}, \hat{y}; 0)$  and  $U(\hat{x}, \hat{y}; z)$  exist.

In plane  $P_o$ , the relationship between the complex amplitude  $U_o$  and its Fourier transform, which we will call  $A_o$ , is given by

$$A_o(\alpha, \beta; 0) = \int_{-\infty}^{\infty} \int_{-\infty}^{\infty} U_o(\hat{x}, \hat{y}; 0) \exp[-i2\pi(\alpha\hat{x} + \beta\hat{y})] d\hat{x} d\hat{y} \quad (2.14)$$

and

$$U_o(\hat{x}, \hat{y}; 0) = \int_{-\infty}^{\infty} \int_{-\infty}^{\infty} A_o(\alpha, \beta; 0) \exp[i2\pi(\alpha\hat{x} + \beta\hat{y})] d\alpha d\beta. \quad (2.15)$$

Similarly, in the plane  $P$ , the complex amplitude  $U$ , and its Fourier transform,  $A$ , are related by

$$A(\alpha, \beta; \hat{z}) = \int_{-\infty}^{\infty} \int_{-\infty}^{\infty} U(\hat{x}, \hat{y}; \hat{z}) \exp[-i2\pi(\alpha\hat{x} + \beta\hat{y})] d\hat{x} d\hat{y} \quad (2.16)$$

and

$$U(\hat{x}, \hat{y}; \hat{z}) = \int_{-\infty}^{\infty} \int_{-\infty}^{\infty} A(\alpha, \beta; \hat{z}) \exp[i2\pi(\alpha\hat{x} + \beta\hat{y})] d\alpha d\beta. \quad (2.17)$$

Equations 2.14 and 2.16 indicate that the complex amplitude distribution in planes  $P_o$  and  $P$  can be decomposed into a set of plane-wave components whose amplitudes are functions of the direction cosines of the propagation vector.  $A_o(\alpha, \beta; 0)$  and  $A(\alpha, \beta; z)$  are referred to as the *angular spectrum* of  $U_o(\hat{x}, \hat{y}; 0)$  and  $U(\hat{x}, \hat{y}; z)$  respectively.



In the scaled coordinate system, the Helmholtz wave equation can be written as

$$\left[ \hat{\nabla}^2 + (2\pi)^2 \right] U(\hat{x}, \hat{y}; \hat{z}) = 0. \quad (2.18)$$

By applying 2.18 to 2.17, the angular spectrum in plane  $P_o$  can be shown to be related to the angular spectrum in plane  $P$  by

$$A(\alpha, \beta; \hat{z}) = A_o(\alpha, \beta; 0) \exp(i2\pi \gamma \hat{z}), \quad (2.19)$$

where 
$$\gamma = \sqrt{1 - (\alpha^2 + \beta^2)}. \quad (2.20)$$

The transfer function of a linear system relates the spectrum of the input to the spectrum of the output, and if we consider  $U_o(\hat{x}, \hat{y}; 0)$  to be our system input and  $U(\hat{x}, \hat{y}; z)$  to be the output, equation 2.19 can be rewritten in terms of a transfer function relationship as

$$H(\alpha, \beta; \hat{z}) = \frac{A(\alpha, \beta; \hat{z})}{A_o(\alpha, \beta; \hat{z})} = \exp(i2\pi \gamma \hat{z}), \quad (2.21)$$

where  $H(\alpha, \beta; \hat{z})$  is the transfer function for free space propagation.

No restrictions have been applied on  $\gamma$ , but it is obvious from equation 2.20 that  $\gamma$  can be either real (when  $\alpha^2 + \beta^2 \leq 1$ ) or imaginary (when  $\alpha^2 + \beta^2 > 1$ ). Figure 2-5 shows a unit circle in the  $\alpha$ - $\beta$  plane in direction cosine space. Inside the circle,  $\gamma$  is real and the corresponding part of the optical disturbance will propagate and contribute to the wave field in plane  $P$ . However, those components of the spectrum which lie outside of the

unit circle have imaginary values of  $\gamma$  and are rapidly attenuated by the propagation phenomena. These components are known as evanescent waves and do not contribute to the wave field in plane P.

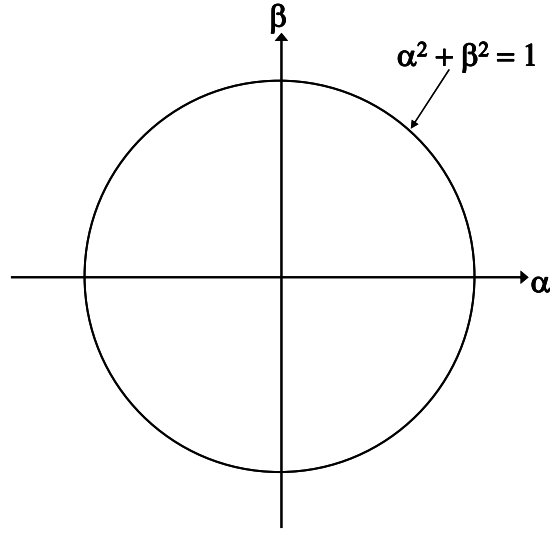


Figure 2-5: Unit circle in direction cosine space

The entire process can be summarized as follows. The known complex amplitude distribution  $U_o$  in a plane  $P_o$  is Fourier transformed to obtain its angular spectrum. The angular spectrum is then multiplied by the transfer function of free space to account for propagation along the  $z$  axis from  $P_o$  to  $P$ . Finally, the inverse Fourier transform (of the angular spectrum-transfer function product) is performed to yield the complex amplitude distribution in the second plane. The process can be expressed as

$$U(\hat{x}, \hat{y}; \hat{z}) = \int_{-\infty}^{\infty} \int_{-\infty}^{\infty} A_o(\alpha, \beta; 0) \exp(i2\pi\gamma\hat{z}) \exp[i2\pi(\alpha\hat{x} + \beta\hat{y})] d\alpha d\beta. \quad (2.22)$$

### 2.1.2.2 The Diffracted Wave Field As A Superposition Of Spherical Waves

If we take the inverse Fourier transform of the angular spectrum given by equation 2.19 we obtain

$$\mathcal{F}^{-1}\{A(\alpha, \beta; \hat{z})\} = \mathcal{F}^{-1}\{A_o(\alpha, \beta; 0) \exp(i2\pi \gamma \hat{z})\}. \quad (2.23)$$

Using the convolution theorem of Fourier transform theory [1], as well as the Fourier transform relationships given by equations 2.15 and 2.17, equation 2.23 can be rewritten as

$$U(\hat{x}, \hat{y}; \hat{z}) = U_o(\hat{x}, \hat{y}; 0) ** \mathcal{F}^{-1}\{\exp(i2\pi \gamma \hat{z})\}, \quad (2.24)$$

where \*\* represents the two-dimensional convolution operation.

The complex amplitude distribution in the observation plane can therefore be expressed as a convolution of the original disturbance with the impulse response of the diffraction (or propagation) process. The impulse response is obtained by taking the inverse Fourier transform of the transfer function of free space (equation 2.21), and is given by [20]:

$$h(\hat{x}, \hat{y}; \hat{z}) = \mathcal{F}^{-1}\{\exp(i2\pi \gamma \hat{z})\} = \left( \frac{1}{2\pi \hat{r}} - i \right) \frac{\hat{z}}{\hat{r}} \frac{\exp(i2\pi \hat{r})}{\hat{r}}. \quad (2.25)$$

Using the impulse response in equation 2.25, we can rewrite the convolution operation of equation 2.24 in integral form as

$$U(\hat{x}, \hat{y}; \hat{z}) = \int_{-\infty}^{\infty} \int_{-\infty}^{\infty} U_o(\hat{x}', \hat{y}'; 0) \left( \frac{1}{2\pi\hat{\ell}} - i \right) \frac{\hat{z}}{\hat{\ell}} \frac{\exp(i2\pi\hat{\ell})}{\hat{\ell}} d\hat{x}' d\hat{y}', \quad (2.26)$$

where 
$$\hat{\ell}^2 = (\hat{x} - \hat{x}')^2 + (\hat{y} - \hat{y}')^2 + \hat{z}^2. \quad (2.27)$$

Note that  $\hat{x}'$  and  $\hat{y}'$  are dummy variables of integration in the original plane ( $z = 0$ ). Equation 2.26 expresses the complex amplitude in the observation plane as a superposition of spherical waves. Comparing equation 2.26 to equation 2.3, we can see that equation 2.26 is the *general Rayleigh-Sommerfeld diffraction integral*. This result has been obtained purely from a linear systems Fourier treatment, with no knowledge of the Huygens-Fresnel principle necessary.

No approximations have been made in obtaining 2.26, and therefore it is valid throughout the entire space in which the diffraction occurs. If we require that  $\hat{z} \gg 1$ , and use the algebraic substitutions  $\hat{\ell} = \hat{z}(1 + \delta)$ ,  $\delta = (\hat{\ell} - \hat{z})/\hat{z}$ , equation 2.26 can be written as

$$U(\hat{x}, \hat{y}; \hat{z}) = \frac{\exp(i2\pi\hat{z})}{i\hat{z}} \int_{-\infty}^{\infty} \int_{-\infty}^{\infty} U_o(\hat{x}', \hat{y}'; 0) \frac{1}{(1 + \delta)^2} \exp[i2\pi(\hat{\ell} - \hat{z})] d\hat{x}' d\hat{y}'. \quad (2.28)$$

No restrictions have been placed on the size of the aperture or the size of the observation space in equation 2.28. The only requirement is that the observation plane must be many wavelengths from the aperture.

The Rayleigh-Sommerfeld diffraction integrals above are given in terms of an observation *plane*, however the observation space is not limited to this geometry. We can use an observation hemisphere centered on the diffracting aperture as our observation space, as well. This is illustrated in Figure 2-6.

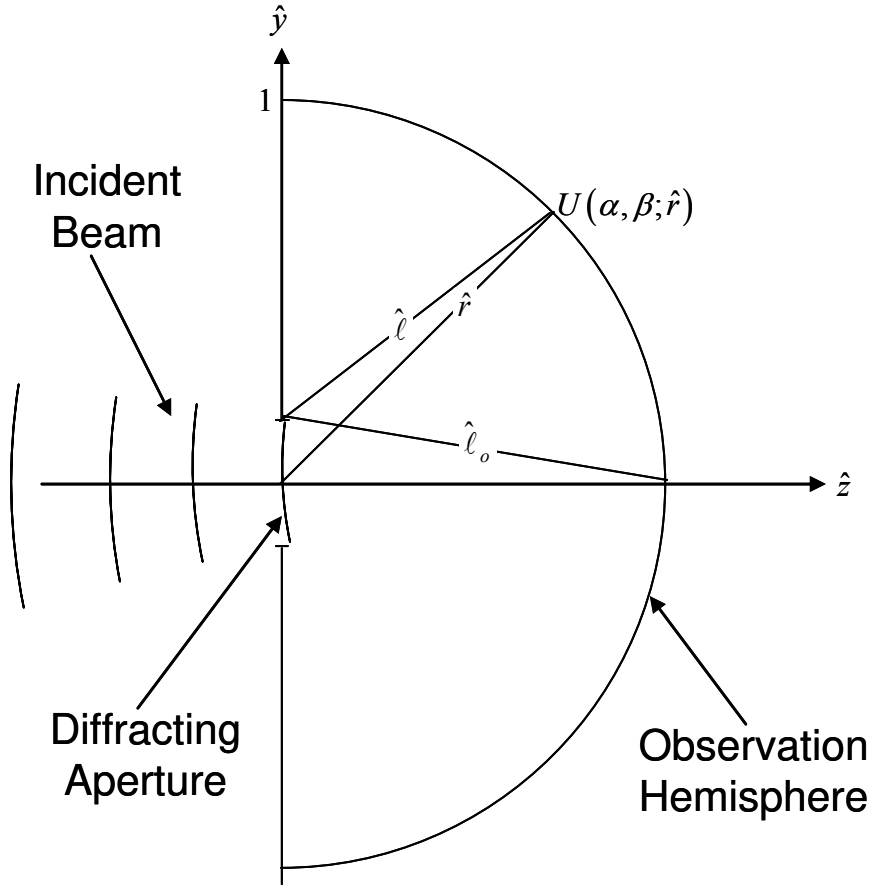


Figure 2-6: Diffraction geometry when observation space is a hemisphere centered on the diffracting aperture

The position of an arbitrary observation point on a hemisphere of radius  $\hat{r}$  will be specified by the direction cosines  $\alpha$  and  $\beta$  of its position vector, given by

$$\alpha = \hat{x} / \hat{r}, \quad \beta = \hat{y} / \hat{r}, \quad \gamma = \hat{z} / \hat{r}, \quad (2.29)$$

where 
$$\hat{r}^2 = \hat{x}^2 + \hat{y}^2 + \hat{z}^2. \quad (2.30)$$

Using the above equations and the algebraic substitution

$$\begin{aligned}\hat{\ell} &= \hat{r}(1 + \varepsilon) \\ \varepsilon &= (\hat{\ell} - \hat{r}) / \hat{r}\end{aligned}\tag{2.31}$$

allows the Rayleigh-Sommerfeld integral of equation 2.26 to be written as

$$\begin{aligned}U(\alpha, \beta; \hat{r}) &= \gamma \frac{\exp(i2\pi\hat{r})}{\hat{r}} \int_{-\infty}^{\infty} \int_{-\infty}^{\infty} U_o(\hat{x}', \hat{y}'; 0) \left( \frac{1}{2\pi\hat{r}(1+\varepsilon)} - i \right) \\ &\quad \times \frac{1}{(1+\varepsilon)^2} \exp[i2\pi(\hat{\ell} - \hat{r})] d\hat{x}' d\hat{y}' .\end{aligned}\tag{2.32}$$

When  $\hat{r} \gg 1$ , equation 2.32 reduces to

$$U(\alpha, \beta; \hat{r}) = \gamma \frac{\exp(i2\pi\hat{r})}{\hat{r}} \int_{-\infty}^{\infty} \int_{-\infty}^{\infty} U_o(\hat{x}', \hat{y}'; 0) \frac{1}{(1+\varepsilon)^2} \exp[i2\pi(\hat{\ell} - \hat{r})] d\hat{x}' d\hat{y}' .\tag{2.33}$$

### 2.1.2.3 Aberrations Of Diffracted Wave Fields

The Rayleigh-Sommerfeld diffraction integrals are generally difficult to solve for most practical cases of interest. It is for this reason that the Fresnel and Fraunhofer approximations are usually applied. The Fresnel diffraction formula can be obtained by replacing the quantity  $\hat{\ell}$  with the quantity  $\hat{z}$  (or  $\hat{r}$ ) in the denominator of the Rayleigh-Sommerfeld integral, and retaining only the first two terms of the binomial expansion for the quantity  $\hat{\ell}$  in the exponent. The Fraunhofer diffraction formula is similarly obtained by making the same Fresnel approximations, but additionally requiring the *Fraunhofer criterion* of equation 2.11 to be met.

Making the above approximations puts severe restrictions on both the size of the aperture and the region over which the calculations are valid in the observation plane.

The region of space usually referred to as the *near field* is excluded from consideration, and a *paraxial limitation* is imposed. In order to avoid these restrictions, all of the terms of the binomial expansion of  $\hat{\ell}$  need to be retained.

Harvey showed [20,22] that this could be accomplished by rewriting the Rayleigh-Sommerfeld diffraction integral given in equation 2.33 as a Fourier transform integral given by

$$U(\alpha, \beta; \hat{r}) = \gamma \frac{\exp(i2\pi\hat{r})}{i\hat{r}} \int_{-\infty}^{\infty} \int_{-\infty}^{\infty} \mathbf{u}_o(\hat{x}', \hat{y}'; \alpha, \beta) \exp[-i2\pi(\alpha\hat{x}' + \beta\hat{y}')] d\hat{x}' d\hat{y}', \quad (2.34)$$

where the complex quantity

$$\mathbf{u}_o(\hat{x}', \hat{y}'; \alpha, \beta) = T_o(\hat{x}', \hat{y}'; 0) \frac{1}{(1+\mathcal{E})^2} \exp(i2\pi\hat{W}) \quad (2.35)$$

can be regarded as a *generalized pupil function*.  $T_o(\hat{x}, \hat{y}; 0)$  is the complex amplitude transmittance of the aperture (or aperture function), and all of the terms from the binomial expansion for the quantity  $\hat{\ell}$ , except for the term which was extracted for use as the Fourier kernel, are contained in the quantity  $\hat{W}$ .

The quantity  $\hat{W}$  represents phase variations in the diffracted wavefront emerging from the aperture. Any departures of the actual diffracted wave from that predicted by the Fourier transform of the aperture function are shown to have the same functional form as the conventional wavefront aberrations of imaging systems. These aberrations, which are inherent to the diffraction process, are precisely the effects ignored when making the

usual Fresnel and Fraunhofer approximations. Near-field diffraction patterns are therefore aberrated Fraunhofer diffraction patterns.

When a spherical wave is incident upon a diffracting aperture and the observation space is a hemisphere, the phase variations mentioned above are frequently negligible. When that is the case, equation 2.34 can be written as [20]

$$U(\alpha, \beta; \hat{r}) = \gamma \left[ \frac{\exp(i2\pi\hat{r})}{(i\hat{r})} \right] \mathfrak{F}\{U_o(\hat{x}, \hat{y}; 0)\}, \quad (2.36)$$

where  $U_o(\hat{x}, \hat{y}; 0)$  is the complex amplitude distribution function emanating from the aperture.

Equation 2.36 will be the starting point for our further development of non-paraxial scalar diffraction theory in chapter three.

## 2.2 Surface Scatter Theory

The first investigations into scattering from a rough surface were probably those of Lord Rayleigh. In 1896 he published a book on the theory of sound, in which he investigated the reflection of acoustic waves [23]. He later noted the effects of poorly polished surfaces on optical performance and examined the effects of surface roughness and angle of incidence on reflected light [24]. In 1907, Lord Rayleigh published an extensive vector perturbation theory of scattering from periodically corrugated reflection gratings [25] which was an extension of his previous work on the theory of sound.



In 1919, Chenmoganadam [26] derived a theory of scattered light based on the phase shift of a reflected beam due to a rough surface. Fano [27] expanded the Rayleigh approach to explain anomalous diffraction gratings and quasi-stationary waves on metallic surfaces. However it was the problem of radar scatter from the sea associated with the detection of naval targets that motivated Rice (1951) [28,29] and others [30-36] to attempt to solve the scattering problem for random rough surfaces. Considerable work was also done during the 1960s in attempting to explain radar reflection from the moon [37-39]. Church introduced the vector perturbation theory to the optics literature [40,41] and published a myriad of papers throughout his career on the application of the theory to the specific problem of light scattering from optical surfaces [42-46].

Surface scatter effects can also be described as merely diffraction phenomena resulting from random phase variations induced upon the reflected wavefront by microtopographic surface features. The Kirchhoff (or tangent plane) approximation was first introduced in the context of scattering in 1952 by Brekhovskikh [47,48], and applied by Isakovich (1952) [49] to statistically rough surfaces. It was later treated in English by Eckart (1953) [50] and Davies (1954) [2]; however it is the monograph by Beckmann and Spizzichino (1963) [51] that is the most common reference in the western world.

In 1970, Nicodemus [52] introduced the four-dimensional bi-directional reflectance distribution function (*BRDF*), defined as reflected *radiance* divided by incident *irradiance* in an attempt to (geometrically) characterize the scattering properties of a surface.

In the late 1970s, Harvey and Shack [21,53] developed a linear systems formulation of surface scatter phenomena in which the scattering behavior is

characterized by a *surface transfer function*. The Fourier transform of this surface transfer function yielded a scattered *radiance* distribution function closely related to the *BRDF*. The transfer function characterization of scattering surfaces was modified in the 1980s to account for grazing incidence effects in X-ray telescopes and “mid” spatial frequency errors that span the gap between “figure” and “finish” errors [54]. This allowed accurate predictions of image degradation due to scattering effects from residual optical fabrication errors on NASA’s Chandra Observatory and NOAA’s Solar X-Ray Imager (SXI) [55,56].

The two classical approaches, the Rayleigh-Rice (small perturbation method) and Beckmann-Kirchhoff (Kirchhoff approximation) have regions of validity that do not greatly overlap. The Rayleigh-Rice theory agrees well with experimental wide-angle scatter measurements from “smooth” ( $\sigma_s/\lambda \ll 1$ ) surfaces for arbitrary incident and scattering angles. The Beckmann-Kirchhoff scattering theory is valid for rougher surfaces; but contains a paraxial (small-angle) assumption that limits its ability to accurately handle wide-angle scattering and large angles of incidence. Neither theory is able to handle cases involving rougher surfaces with large incident and scattering angles. For this reason, much of the more recent work in the theoretical scattering community has focused on “unifying” methods that attempt to bridge the gap between the two classical approaches.

Some of these unifying approaches are the phase perturbation method [57-59], the small slope approximation method [60,61], the operator expansion method [62-67], and the integral equation method [68-71]. This list of methods and references is by no means

complete. The recent survey of approximate scattering theories by Elfouhaily and Guérin [4] is an excellent overview of the more recent approaches.

We will now take a more detailed look at some of the items from the preceding discussion, as they will either be used or modified in this dissertation. In particular, we will look at the concept of the *BRDF*, the classical Rayleigh-Rice and Beckmann-Kirchhoff theories, and the Harvey-Shack theory.

### 2.2.1 The Bidirectional Reflectance Distribution Function (*BRDF*)

One special quantity that has been used to quantify scattering measurements is the bi-directional reflectance distribution function (*BRDF*). The *BRDF* was defined and described by Nicodemus [52] who put a lot of effort into examining the problem of defining and measuring the reflectance of optical surfaces that are neither completely specular nor completely diffuse (i.e., all real optics). The resulting *BRDF* is a fundamental quantity that completely describes (geometrically) the scattering properties of a differential surface element. It is defined in radiometric terms as the *reflected* (scattered) *radiance* divided by the *incident irradiance*, given by

$$BRDF = f(\theta_s, \phi_s, \theta_i, \phi_i) = \frac{dL(\theta_s, \phi_s, \theta_i, \phi_i)}{dE(\theta_i, \phi_i)}, \quad (2.37)$$

where  $(\theta_i, \phi_i)$  and  $(\theta_s, \phi_s)$  are the incident angle and scattered angle in conventional spherical coordinates as shown in Figure 2-7. The units of the *BRDF* are 1/sr.

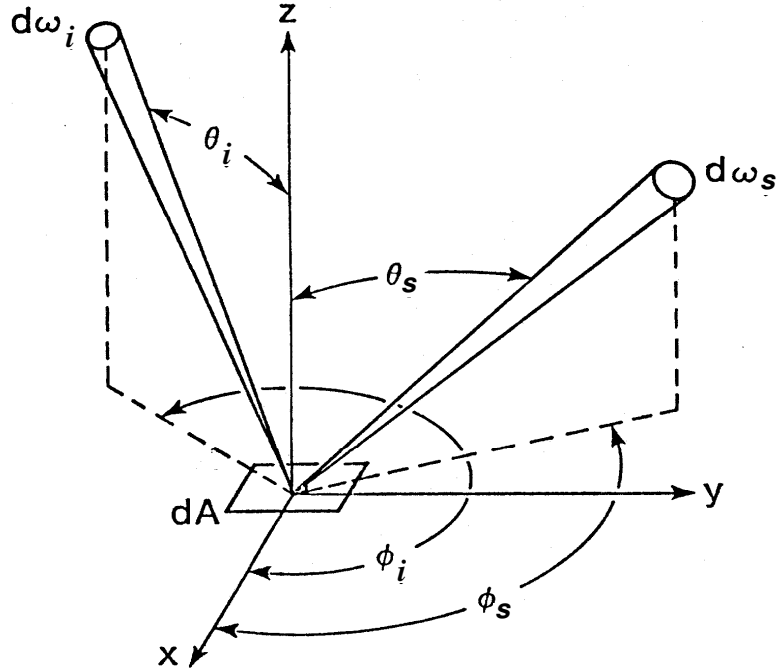


Figure 2-7: Illustration of the geometry used in defining the BRDF

We can envision illuminating a small differential area element of a reflecting surface,  $dA$ , with a narrow beam of light at a fixed angle of incidence and measuring the radiant power by scanning a small collecting aperture over a hemisphere centered upon the normal to the surface element. Under these conditions, we can approximate the *BRDF* by dropping the differentials in equation 2.37, leading to

$$BRDF \Big|_{\theta_i, \phi_i} = \frac{L_r(\theta_s, \phi_s; \theta_i, \phi_i)}{E_i(\theta_i, \phi_i)} = \frac{dP_s(\theta_s, \phi_s) / d\Omega_s dA \cos \theta_s}{P_i / dA} \approx \frac{P_s / \Omega}{P_i \cos \theta_s}, \quad (2.38)$$

where  $dP_s$  is the radiant power scattered into the solid angle  $d\Omega_s$  subtended by the collecting aperture, and  $P_i$  is the incident radiant power falling on the area element  $dA$ .

The total *BRDF* would consist of an infinite family of these two-dimensional scattered light distribution functions; one for every possible incident angle. The *BRDF* is also a function of the wavelength and the state of polarization of both the incident and scattered radiation.

The *BRDF* definition and nomenclature has been extended to describe diffuse scattering from transmissive optical elements, in which case it is called the bi-directional transmittance distribution function (*BTDF*) [72]. Both the *BRDF* and the *BTDF* have been included in the more general bi-directional scatter distribution function (*BSDF*) [73].

Unfortunately, there has been a lack of standardization in the definitions of radiometric quantities and in scatter measurement instrumentation and procedures, and it has been difficult to directly compare scattering results from different laboratories and facilities. The U.S. Air Force at Rome Air Development Center therefore sponsored a *BRDF* round robin measurement program whereby several specific scattering surfaces were measured at several government, industrial, and university laboratories [74]. In addition, an ASTM standard (E1392-90) was eventually produced to govern *BRDF* measurement practices [75].

Since the *BRDF* is for the most part a quantity used for representing scattering measurements, it is not generally referred to in the theoretical literature. It is used extensively, however, by optical engineers when attempting to determine the effect of scattering on image quality. It is also used extensively by the computer graphics community in rendering photo-realistic images.

### 2.2.2 Rayleigh-Rice (Small Perturbation) Surface Scatter Theory

The Rayleigh-Rice theory, also known as the small perturbation method (SPM) is the oldest theory dealing with scattering from rough surfaces, and is probably the most widely used. In this approach, the surface roughness is considered to be a small perturbation to the case of a perfectly smooth surface, which requires that the roughness is small compared to the wavelength of the incident radiation. There are a number of different methods that have been used to derive the scattered fields using this approach [28,34,76-86], all yielding identical results, at least up to the fifth order of the perturbation expansion [87]. Due to the mathematical complexity involved for higher order terms, only the first order term of the expansion is usually used for two-dimensional rough surfaces.

A derivation of the Rayleigh-Rice theory is beyond the scope of this historical background, however detailed derivations are available in, for instance, [30,88,89]. In the following discussion, we will only present the result of the theory for first order as applied to two-dimensional rough surfaces.

Using Stover's notation for the Rayleigh-Rice theory [3], the scattered intensity normalized by the incident radiant power is given by

$$\frac{I}{P_i} = \frac{(dP/d\Omega_s)}{P_i} = \left( \frac{16\pi^2}{\lambda^4} \right) \cos \theta_i \cos^2 \theta_s Q \text{ PSD}(f_x, f_y). \quad (2.39)$$

The dimensionless quantity  $Q$  is the polarization dependent reflectance of the surface. For an s-polarized (TE) source, and measurements made in the plane of incidence,  $Q$  is given exactly (at least for the first order perturbation expansion) by the geometric mean

of the sample specular reflectances at  $\theta_i$  and  $\theta_s$  [3]:

$$Q = \sqrt{R_s(\theta_i) R_s(\theta_s)}. \quad (2.40)$$

For highly reflective surfaces, this means that  $Q$  is very nearly equal to a constant for all scatter angles.  $PSD(f_x, f_y)$  is the two-sided, two-dimensional surface power spectral density function expressed in terms of the sample spatial frequencies given by [3]

$$f_x = \frac{\sin \theta_s \cos \phi_s - \sin \theta_i}{\lambda} \quad \text{and} \quad f_y = \frac{\sin \theta_s \sin \phi_s}{\lambda}, \quad (2.41)$$

which are obtained from the conical diffraction grating equations.

From the definition of the  $BRDF$  given in equation 2.38, the Rayleigh-Rice result can be written as

$$BRDF = \frac{dP / d\Omega_s}{P_i \cos \theta_s} = \left( \frac{16\pi^2}{\lambda^4} \right) \cos \theta_i \cos \theta_s Q PSD(f_x, f_y). \quad (2.42)$$

In addition, the Rayleigh-Rice theory can also be used to solve the inverse scattering problem for smooth surfaces by inverting equation 2.42 and solving for the surface  $PSD$  function:

$$PSD(f_x, f_y) = \frac{10^8 \lambda^4 BRDF}{16\pi^2 \cos \theta_i \cos \theta_s Q}. \quad (2.43)$$

The factor of  $10^8$  in equation 2.43 has been added to give the surface  $PSD$  units of  $\text{\AA}^2 \mu\text{m}^2$  when the wavelength is expressed in micrometers.

Recall that the quantity  $Q$  was referred to as the polarization dependent reflectance of the surface. It is a dimensionless real number that relates the effect of the surface material properties (as opposed to the surface shape) on the  $BRDF$  [3]. Its value depends on the sample dielectric constant,  $\varepsilon$ , as well the incident and scattering angles. It also depends on the polarization of the incident beam, as well as the state of polarization allowed to reach the detector.

For the special case of an  $s$ -polarized source and a sensor that only receives  $s$ -polarized light,  $Q$  is given by [3,42]

$$Q_{ss} = \left| \frac{(\varepsilon - 1) \cos \phi_s}{\left( \cos \theta_i + \sqrt{\varepsilon - \sin^2 \theta_i} \right) \left( \cos \theta_s + \sqrt{\varepsilon - \sin^2 \theta_s} \right)} \right|^2. \quad (2.44)$$

For an  $s$ -polarized source and a sensor that only receives  $p$ -polarized light,  $Q$  is given by

$$Q_{sp} = \left| \frac{(\varepsilon - 1) \sqrt{\varepsilon - \sin^2 \theta_s} \sin \phi_s}{\left( \cos \theta_i + \sqrt{\varepsilon - \sin^2 \theta_i} \right) \left( \varepsilon \cos \theta_s + \sqrt{\varepsilon - \sin^2 \theta_s} \right)} \right|^2. \quad (2.45)$$

For a  $p$ -polarized source and a sensor that only receives  $s$ -polarized light,  $Q$  is given by

$$Q_{ps} = \left| \frac{(\varepsilon - 1) \sqrt{\varepsilon - \sin^2 \theta_i} \sin \phi_s}{\left( \varepsilon \cos \theta_i + \sqrt{\varepsilon - \sin^2 \theta_i} \right) \left( \cos \theta_s + \sqrt{\varepsilon - \sin^2 \theta_s} \right)} \right|^2. \quad (2.46)$$

And finally, for a  $p$ -polarized source and a sensor that only receives  $p$ -polarized light,  $Q$  is given by



$$Q_{pp} = \left| \frac{(\varepsilon - 1) \left( \sqrt{\varepsilon - \sin^2 \theta_s} \sqrt{\varepsilon - \sin^2 \theta_i} \cos \phi_s - \varepsilon \sin \theta_i \sin \theta_s \right)}{\left( \varepsilon \cos \theta_i + \sqrt{\varepsilon - \sin^2 \theta_i} \right) \left( \varepsilon \cos \theta_s + \sqrt{\varepsilon - \sin^2 \theta_s} \right)} \right|^2. \quad (2.47)$$

In the above equations,  $\varepsilon = \varepsilon_2/\varepsilon_1$  is the relative permittivity (or dielectric constant) of the interface where the subscripts 1 and 2 denote the incident and refracting side, respectively. If one considers reflective scattering at an air-material interface and takes  $\varepsilon = 1$  for air, then  $\varepsilon = \varepsilon_2$  for scattering of the air side, and  $\varepsilon = 1/\varepsilon_1$  for scattering on the material side. In general  $\varepsilon$  is complex and equals the square of the complex index of refraction.

It follows that for  $s$ -polarized light incident upon the scattering surface and no polarization discrimination from the sensor,  $Q$  is given by

$$Q = Q_{ss} + Q_{sp}, \quad (2.48)$$

And for  $p$ -polarized incident light with no polarization discrimination for the sensor,  $Q$  is given by

$$Q = Q_{ps} + Q_{pp}. \quad (2.49)$$

Likewise, for unpolarized light incident upon the scattering surface and a sensor that only receives  $s$ -polarized light,  $Q$  is given by

$$Q = Q_{ss} + Q_{ps}, \quad (2.50)$$

and for unpolarized incident light and a sensor that only receives  $p$ -polarized light,  $Q$  is given by

$$Q = Q_{sp} + Q_{pp} . \quad (2.51)$$

Finally, for unpolarized incident light, and no polarization discrimination of the sensor,  $Q$  is given by

$$Q = Q_{ss} + Q_{sp} + Q_{ps} + Q_{pp} . \quad (2.52)$$

Note that for scattering measurements made in the plane of incidence ( $\phi_s = 0$ ), the cross-polarization terms ( $Q_{sp}$  and  $Q_{ps}$ ) are equal to zero. And in the specular direction ( $\theta_s = \theta_o$ ), equations 2.44 and 2.47 reduce to the well-known Fresnel reflection coefficients for radiant power [3].

It is important to remember that the Rayleigh-Rice theory is only applicable to “smooth” surfaces for which the RMS roughness is much smaller than the wavelength of the incident light, as this was the condition under which it was derived. It is also only applicable to clean, front surface reflecting surfaces as it does not take into account particulate scattering or bulk (subsurface) scattering. In addition, the first order solution does not account for multiple scattering.

### ***2.2.3 Beckmann-Kirchhoff Surface Scatter Theory***

While the Rayleigh-Rice approach works well for smooth surfaces, it is not readily applicable to rough surfaces, as explained in the previous section. For this reason, Beckmann (as well as others) used the Kirchhoff method to approach the scattering problem [90]. Instead of satisfying the exact boundary conditions, as is done in the Rayleigh-Rice theory, the field and its normal derivative are approximated on the

scattering surface. This approximation, while causing the loss of some generality, allows one to calculate scattering for surfaces much rougher than the Rayleigh-Rice theory allows. Since we will be discussing a modification to the Beckmann-Kirchhoff theory in chapter four, we will examine the theory here in some detail. The following discussion comes directly from [90], albeit with less detail.

Figure 2-8 illustrates the scattering geometry and coordinate system of the Beckmann-Kirchhoff approach.

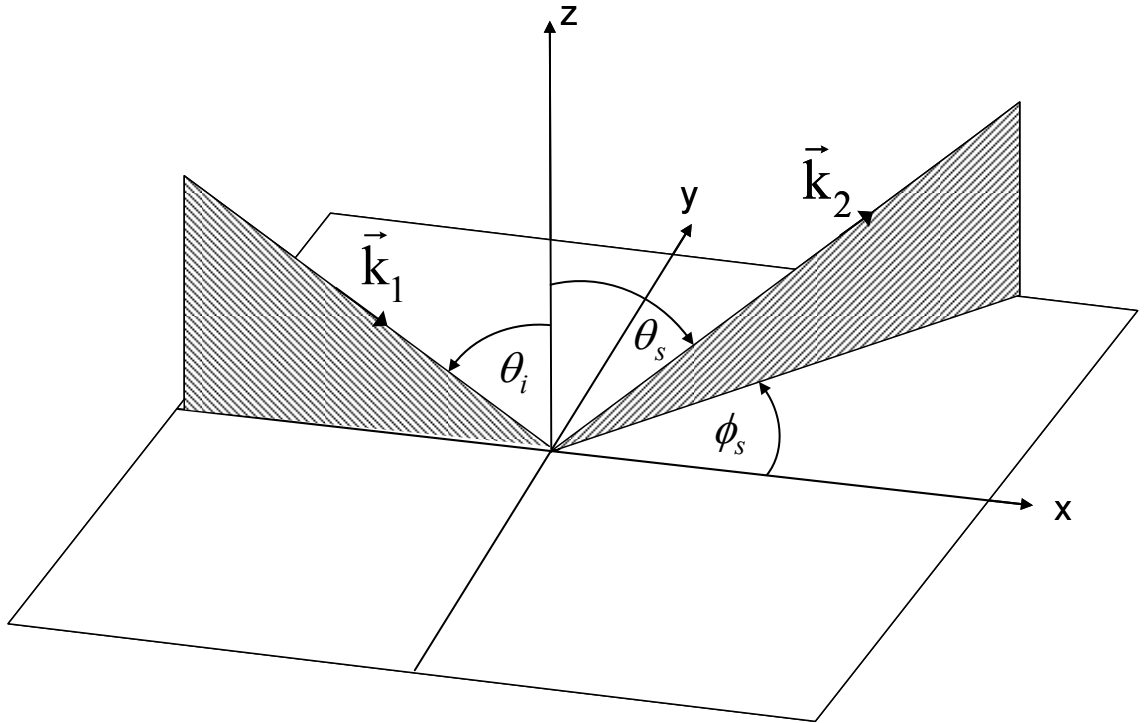


Figure 2-8: Scattering geometry and coordinate system for the Beckmann-Kirchhoff theory

The surface  $S$  is described by the function  $h(x,y)$ , where  $h$  is the height deviation from the mean  $xy$  plane. The surface height irregularities,  $h(x,y)$ , may be an arbitrary deterministic function, a periodic function, as in the case of a diffraction grating, or it may be a random process, as in the case of a statistically rough surface. The quantity  $\vec{k}_1$  is the propagation vector of a plane electromagnetic wave incident on the surface  $S$ . The  $xz$  plane is assumed to be the plane of incidence, and  $\theta_i$  is the angle of incidence. Finally,  $\vec{k}_2$  is the propagation vector of radiation scattered into the direction given by the conventional spherical coordinates  $\theta_s$  and  $\phi_s$ .

At an observation point  $P$ , the scattered field  $E_2$  is given by the Helmholtz integral (Appendix A in [90])

$$E_2(P) = \frac{1}{4\pi} \iint_S \left( E \frac{\partial \psi}{\partial n} - \psi \frac{\partial E}{\partial n} \right) dS, \quad (2.53)$$

where

$$\psi = \frac{\exp(ik_2 R_2)}{R_2}. \quad (2.54)$$

Here  $R_2$  is the distance from a point on the surface to the observation point  $P$ ,  $E$  is the field on the surface, and  $\partial/\partial n$  indicates the derivative along the surface normal.

It is at this point that Beckmann makes use of the Kirchhoff (or tangent plane) approximation. He assumes that the radii of curvature of the surface are much larger than the wavelength  $\lambda$ , and approximates the field and its normal derivative at any point on a surface by the field and its derivative that would be present on the tangent plane at that

point (pg. 20 of [90]). With this assumption, the field and its normal derivative on the surface are given by the boundary conditions

$$(E)_s = (1 + R)E_1 \quad (2.55)$$

and

$$\left(\frac{\partial E}{\partial n}\right)_s = (1 - R)E_1(\vec{k}_1 \cdot \vec{n}), \quad (2.56)$$

where  $\vec{n}$  is the surface normal,  $R$  is the local reflection coefficient, and  $E_1$  is the incident field given by

$$E_1 = E_o \exp[i(\vec{k}_1 \cdot \vec{r} - \omega t)], \quad (2.57)$$

where

$$\vec{r} = x\vec{x} + y\vec{y} + z\vec{z} \quad (2.58)$$

is a position vector in terms of the unit vectors  $(\vec{x}, \vec{y}, \vec{z})$  of the coordinate system.

Beckmann then defines a dimensionless quantity which he calls the *scattering coefficient*, given by

$$\rho = \frac{E_2}{E_{20}}, \quad (2.59)$$

where  $E_2$  is the scattered field and  $E_{20}$  is the field that would be reflected in the specular direction by a perfectly reflecting smooth planar surface given the same incident angle and the same distance. Given the geometry shown in Figure 2-8, and using equations 2.53-2.58, it can be shown (chapter three in [90]) that for a perfectly reflecting surface with the observation point  $P$  in the Fraunhofer zone, the scattering coefficient is given by

$$\rho = \frac{F(\theta_i, \theta_s, \phi)}{A} \iint_A \exp(i\vec{v} \cdot \vec{r}) \, dx \, dy, \quad (2.60)$$

where

$$F(\theta_i, \theta_s, \phi) = \frac{1 + \cos \theta_i \cos \theta_s - \sin \theta_i \sin \theta_s \cos \phi_s}{\cos \theta_i (\cos \theta_i + \cos \theta_s)} \quad (2.61)$$

is called the *geometrical factor* (or *obliquity factor*),  $A$  is the area of surface  $S$  in the  $xy$  plane,  $\vec{v}$  is given by

$$\vec{v} = \vec{k}_1 - \vec{k}_2 = k \left[ (\sin \theta_i - \sin \theta_s \cos \phi) \vec{x} - \sin \theta_s \sin \phi \vec{y} - (\cos \theta_i + \cos \theta_s) \vec{z} \right], \quad (2.62)$$

and

$$\vec{r} = x\vec{x} + y\vec{y} + h(x, y)\vec{z} \quad (2.63)$$

is the position vector describing the rough surface. Equation 2.60 is the general Kirchhoff solution to the scattering problem.

For a randomly rough surface, the surface height  $h(x, y)$  is not a known function, but is a random function of position on the surface  $S$ ; i.e.,  $h$  is a random variable that assumes heights  $z$  with a probability density  $p(z)$ . The joint probability density is  $p_2(z_1, z_2)$  where  $z_1$  and  $z_2$  are the surface heights assumed by  $h$  at the points  $(x_1, y_1)$  and  $(x_2, y_2)$ . It will be assumed that  $h(x, y)$  is stationary, so that its two-dimensional probability density does not depend on the points  $(x_1, y_1)$  and  $(x_2, y_2)$ , but only on the distance between them, given by

$$\tau = \sqrt{(x_2 - x_1)^2 + (y_2 - y_1)^2}. \quad (2.64)$$

The one dimensional characteristic function associated with the distribution  $p(z)$  is given by

$$\chi(t) = \langle \exp(itz) \rangle = \int_{-\infty}^{\infty} p(z) \exp(itz) dz, \quad (2.65)$$

and the two-dimensional characteristic function associated with  $p_2(z_1, z_2)$  is given by

$$\chi_2(t_1, t_2) = \langle \exp(it_1 z_1 + it_2 z_2) \rangle = \int_{-\infty}^{\infty} \int_{-\infty}^{\infty} p_2(z_1, z_2) \exp(it_1 z_1 + it_2 z_2) dz_1 dz_2, \quad (2.66)$$

where  $\langle \rangle$  denotes the ensemble mean.

Combining equations 2.60 and 2.66, the mean scattered field in any direction is given by

$$\begin{aligned} \langle \rho \rangle &= \frac{F}{A} \int_{-X}^X \int_{-Y}^Y \exp(iv_x x + iv_y y) \langle \exp(iv_z z) \rangle dx dy \\ &= \frac{F}{A} \chi(v_z) \int_{-X}^X \int_{-Y}^Y \exp(iv_x x + iv_y y) dx dy \end{aligned} \quad (2.67)$$

for a surface stretching from  $-X$  to  $X$  in the  $x$ -direction and from  $-Y$  to  $Y$  in the  $y$ -direction. Integrating 2.67 yields

$$\langle \rho \rangle = \frac{F}{A} \chi(v_z) \rho_o, \quad (2.68)$$

where

$$\rho_o = \frac{\sin(v_x X)}{v_x X} \frac{\sin(v_y Y)}{v_y Y} \quad (2.69)$$

is the scattering coefficient of a plane surface of area  $A = XY$ .

It can be seen from equation 2.69, that as long as  $X \gg \lambda$ ,  $Y \gg \lambda$ ,  $\rho_o$  will equal unity in the specular direction where  $v_x = v_y = 0$ , but will rapidly tend to zero elsewhere. Therefore, the mean scattering coefficient  $\langle \rho \rangle$  will equal zero everywhere except in the neighborhood of the specular direction.

The mean square of equation 2.60 is given by

$$\langle |\rho|^2 \rangle = \langle \rho \rho^* \rangle = \left\langle \left| \frac{E_2}{E_{20}} \right|^2 \right\rangle, \quad (2.70)$$

which according to Beckmann is proportional to the mean scattered power (or mean optical intensity).

Using equations 2.60 and 2.66, transforming to polar coordinates, and assuming  $X$  and  $Y$  to be much greater than the correlation distance of the surface height variation  $h(x,y)$ , it can be shown (pg. 78 of [90]) that

$$\langle \rho \rho^* \rangle = \frac{2\pi F^2}{A} \int_0^\infty J_0(v_{xy}\tau) \chi_2(v_z, -v_z; \tau) \tau d\tau, \quad (2.71)$$

where 
$$v_{xy} = \sqrt{v_x^2 + v_y^2}, \quad (2.72)$$

and  $v_x$  and  $v_y$  are the  $x$  and  $y$  components of  $\vec{v}$  in equation 2.62.

The quantity  $\langle \rho \rho^* \rangle$  can also be expressed in terms of  $\langle \rho \rangle$  and the variance of  $\rho$  (denoted by  $D\{\rho\}$ ) by (Appendix C in [90])

$$\langle \rho \rho^* \rangle = D\{\rho\} + \langle \rho \rangle \langle \rho^* \rangle. \quad (2.73)$$



The first term on the right side of equation 2.73 represents the diffusely scattered radiation, while the second term represents the specular beam. Using equations 2.68, 2.71, and 2.73, we can write the diffuse scattered portion of equation 2.73 as

$$D\{\rho\} = \frac{2\pi F^2}{A} \int_0^\infty J_o(v_{xy}\tau) \left[ \chi_2(v_z, -v_z; \tau) - \chi(v_z) \chi^*(v_z) \right] \tau d\tau. \quad (2.74)$$

Equation 2.74 is used to calculate the scattering from random rough surfaces, but in order to do so a specific type of distribution for  $h(x,y)$  must be assumed, as this determines the characteristic functions  $\chi$  and  $\chi_2$ . This distribution alone is not enough to uniquely describe the surface, as it gives no information about the density of the surface irregularities (separation between the peaks and valleys on the surface). This information is given by the autocorrelation function of the surface, and therefore a specific autocorrelation function must also be assumed.

Beckmann chose the normal (Gaussian) distribution, describing it as “the most important and typical of a rough surface” (pg. 80 of [90]), and a Gaussian autocorrelation function which he calls “sufficiently general” (pg. 81 of [90]) in order to arrive at a closed form solution.

If  $h(x,y)$  is a normal process with a zero mean and a standard deviation of  $\sigma_s$ , the normal distribution (probability density) is given by

$$p(z) = \frac{1}{\sigma\sqrt{2\pi}} \exp\left(-\frac{z^2}{2\sigma^2}\right). \quad (2.75)$$

The standard deviation describes the roughness of the surface, and because  $h$  has a zero

mean, the standard deviation is also the RMS value of  $h$ .

The one-dimensional characteristic function associated with the normal distribution is given, from equation 2.65, by

$$\chi(v) = \exp\left(-\frac{1}{2}\sigma^2 v_z^2\right). \quad (2.76)$$

The Gaussian autocorrelation function is given by

$$C(\tau) = \exp\left(-\frac{\tau^2}{\ell_c^2}\right), \quad (2.77)$$

where  $\ell_c$  is the correlation distance, at which  $C(\tau)$  falls to the value  $1/e$ .

The two-dimensional normal distribution (joint probability density) of two random variables  $h_1$  and  $h_2$ , with zero means, variances of  $\sigma^2$ , and correlated by a correlation function  $C$ , is given by

$$p_2(z_1, z_2) = \frac{1}{2\pi\sigma^2\sqrt{1-C^2}} \exp\left(-\frac{z_1^2 - 2Cz_1z_2 + z_2^2}{2\sigma^2(1-C^2)}\right), \quad (2.78)$$

and the two-dimensional characteristic function associated with the normal distribution in equation 2.78 is given, from equation 2.66, by

$$\chi_2(v_z, -v_z; \tau) = \exp\left[-\sigma^2 v_z^2 (1-C)\right]. \quad (2.79)$$

Substituting the autocorrelation function of equation 2.77 into equation 2.79 and expanding the result in a MacLaurin series yields

$$\chi_2(v_z, -v_z; \tau) = \exp(-v_z^2 \sigma^2) \sum_{m=0}^{\infty} \frac{v_z^{2m} \sigma^{2m}}{m!} \exp\left(-\frac{m\tau^2}{\ell_c^2}\right). \quad (2.80)$$

Substituting equations 2.76 and 2.79 into equation 2.74 yields

$$D\{\rho\} = \frac{2\pi F^2 \exp(-g)}{A} \sum_{m=1}^{\infty} \frac{g^m}{m!} \int_0^{\infty} J_0(v_{xy} \tau) \exp\left(-\frac{m\tau^2}{\ell_c^2}\right) \tau d\tau, \quad (2.81)$$

where

$$g = v_z^2 \sigma^2 = \left(\frac{2\pi\sigma}{\lambda}\right)^2 (\cos\theta_i + \cos\theta_s)^2, \quad (2.82)$$

and, as stated previously

$$v_{xy} = \sqrt{v_x^2 + v_y^2} = \left(\frac{2\pi}{\lambda}\right) \sqrt{\sin^2\theta_i - 2\sin\theta_i \sin\theta_s \cos\phi_s + \sin^2\theta_s}. \quad (2.83)$$

Since (Appendix C of [90])

$$\int_0^{\infty} J_0(v\tau) \exp(-m\tau^2) \tau d\tau = \frac{1}{2m} \exp\left(-\frac{v^2}{4m}\right), \quad (2.84)$$

equation 2.81 finally yields Beckmann's general expression for the diffusely scattered portion of the scattered light distribution:

$$D\{\rho\} = \frac{\pi \ell_c^2 F^2 \exp(-g)}{A} \sum_{m=1}^{\infty} \frac{g^m}{m! m} \exp\left(-\frac{v_{xy}^2 \ell_c^2}{4m}\right). \quad (2.85)$$

The quantity  $g$  in equation 2.85 is the local phase variation (relative to a perfectly plane surface) of the radiation scattered in to a given angle  $\theta_s$ . This quantity is primarily driven by the surface roughness,  $\sigma/\lambda$ , but is also affected by both the incident and

scattering angles. We will now look at three special cases: (i)  $g \ll 1$  (scattering from slightly rough surfaces), (ii)  $g \approx 1$  (scattering from moderately rough surfaces), and (iii)  $g \gg 1$  (scattering from very rough surfaces).

(i) *Slightly rough surfaces* ( $g \ll 1$ ): When  $g$  is much less than unity, the series in equation 2.85 will converge very rapidly. We can therefore discard all but the first term in the series. In this case, equation 2.85 reduces to

$$D\{\rho\} = \frac{\pi g \ell_c^2 F^2}{A} \exp\left[-\left(g + \frac{v_{xy}^2 \ell_c^2}{4}\right)\right], \quad (g \ll 1). \quad (2.86)$$

(ii) *Moderately rough surfaces* ( $g \approx 1$ ): Equation 2.85 can be used in this regime as long as enough terms are used to guarantee convergence of the series. As  $g$  increases, the number of terms necessary to include in the calculation also increases.

(iii) *Very rough surfaces* ( $g \gg 1$ ): When  $g$  is much larger than unity, the series in equation 2.85 will converge very slowly and will not be of much use. In this case, we need to go back to the integral in equation 2.74. From equations 2.68, 2.76, and 2.82, we can see that when  $g \gg 1$ , the intensity of the specular beam becomes vanishingly small, i.e.,  $\langle \rho \rangle \langle \rho^* \rangle \rightarrow 0$ , so that

$$D\{\rho\} = \langle \rho \rho^* \rangle - \langle \rho \rangle \langle \rho^* \rangle \approx \langle \rho \rho^* \rangle. \quad (2.87)$$

Therefore, substituting equations 2.77, 2.79, and 2.82 into equation 2.74 yields

$$D\{\rho\} \approx \langle \rho \rho^* \rangle = \frac{2\pi F^2}{A} \int_0^\infty J_0(v_{xy}\tau) \exp\left\{-g\left[1 - \exp\left(\frac{\tau^2}{\ell_c^2}\right)\right]\right\} \tau d\tau. \quad (2.88)$$

It can be shown (pg. 87 of [90]) that for  $g \gg 1$ , the integral in equation 2.88 only receives significant contributions in the neighborhood of  $\tau = 0$ . Therefore, we can keep only the first two terms of the expansion of  $\exp(\tau^2 / \ell_c^2) \approx 1 - \tau^2 / \ell_c^2$  and write equation 2.88 as

$$D\{\rho\} \approx \langle \rho \rho^* \rangle = \frac{2\pi F^2}{A} \int_0^\infty J_o(v_{xy}\tau) \exp\left(-\frac{g\tau^2}{\ell_c^2}\right) \tau d\tau. \quad (2.89)$$

From equation 2.84, this reduces to

$$D\{\rho\} \approx \langle \rho \rho^* \rangle = \frac{\pi F^2 T^2}{Ag} \exp\left(-\frac{v_{xy} \ell_c^2}{4g}\right). \quad (2.90)$$

This is consistent with a geometrical optics approach in which the scattered light distribution is proportional to the slope distribution of the surface.

#### ***2.2.4 Harvey-Shack Surface Scatter Theory***

As part of his dissertation research, Harvey measured scattering from various reflecting surfaces [21]. When the scattered intensity was plotted versus scattering angle, the curves were extremely asymmetrical. However, when the intensity was divided by the scattering angle (to convert to radiance) and plotted versus  $\beta - \beta_0$  (sine of the scattering angle minus the sine of the angle of specular reflection), the curves coincided almost perfectly. An example of this is shown in Figure 2-9 for a polished and aluminized fused quartz sample for incident angles ranging from zero to 60 degrees.

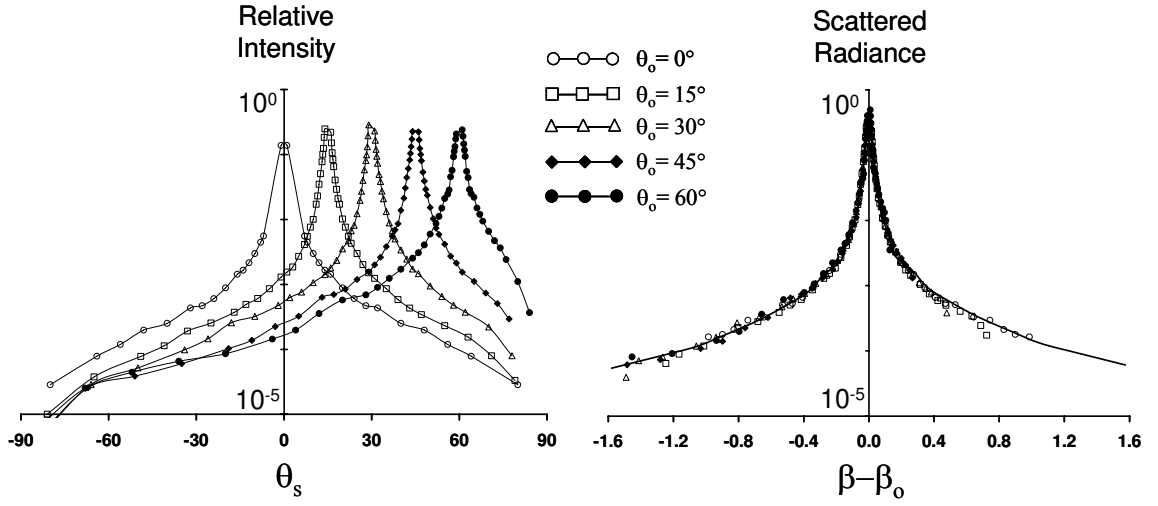


Figure 2-9: Polished and aluminized fused quartz sample: a) Scattered intensity as a function of scattering angle, b) Scattered radiance as a function of  $\beta - \beta_o$

Based upon the above empirical experimental observation that scattered radiance is shift-invariant in direction cosine space, Harvey and Shack developed a linear systems formulation of surface scatter phenomena in which the scattering behavior is characterized by a *surface transfer function* [21,53]. Since we will be building upon this linear systems formulation later in this dissertation, we will now provide a detailed review. The discussion that follows come directly from [21].

Using equation 2.36 and Rayleigh's theory from Fourier transform theory[1], the total radiant power reflected from a scattering surface can be written as

$$P = \int_{-\infty}^{\infty} \int_{-\infty}^{\infty} \frac{\hat{r}^2}{\gamma^2} |U(\alpha, \beta; \hat{r})|^2 d\alpha d\beta = \int_{-\infty}^{\infty} \int_{-\infty}^{\infty} |U_o(\hat{x}, \hat{y}; 0)|^2 d\hat{x} d\hat{y}. \quad (2.91)$$

Noting that  $d\omega = d\alpha d\beta / \gamma$ , the radiant intensity can be written as

$$I(\alpha, \beta) = \frac{dP}{d\omega} = \frac{\hat{r}^2}{\gamma} |U(\alpha, \beta; \hat{r})|^2 = \gamma \left| \mathcal{F}\{U_o(\hat{x}, \hat{y}; 0)\} \right|^2. \quad (2.92)$$

Utilizing the autocorrelation theorem of Fourier transform theory, this is equivalent to

$$I(\alpha, \beta) = \gamma \mathcal{F} \left\{ \int_{-\infty}^{\infty} \int_{-\infty}^{\infty} U_o(\hat{x}', \hat{y}'; 0) U_o^*(\hat{x}' - \hat{x}, \hat{y}' - \hat{y}; 0) d\hat{x}' d\hat{y}' \right\}. \quad (2.93)$$

Harvey then derived an analytical expression for the surface transfer function by following the same procedure used in image formation. The effective transfer function of the scattering system is defined as the normalized autocorrelation of the pupil function

$$H_{eff}(\hat{x}, \hat{y}; 0) = \frac{\int_{-\infty}^{\infty} \int_{-\infty}^{\infty} U_o(\hat{x}', \hat{y}'; 0) U_o^*(\hat{x}' - \hat{x}, \hat{y}' - \hat{y}; 0) d\hat{x}' d\hat{y}'}{\int_{-\infty}^{\infty} \int_{-\infty}^{\infty} |U_o(\hat{x}', \hat{y}')|^2 d\hat{x}' d\hat{y}'}. \quad (2.94)$$

The effective (angle) spread function of the scattering system is then defined in the usual way as the Fourier transform of this effective transfer function

$$ASF(\alpha, \beta) = \mathcal{F}\{H_{eff}(\hat{x}, \hat{y}; 0)\} = \frac{\mathcal{F} \left\{ \int_{-\infty}^{\infty} \int_{-\infty}^{\infty} U_o(\hat{x}', \hat{y}'; 0) U_o^*(\hat{x}' - \hat{x}, \hat{y}' - \hat{y}; 0) d\hat{x}' d\hat{y}' \right\}}{\int_{-\infty}^{\infty} \int_{-\infty}^{\infty} |U_o(\hat{x}', \hat{y}')|^2 d\hat{x}' d\hat{y}'}. \quad (2.95)$$

Direct substitution from equations 2.91 and 2.92 results in the following expression for the angle spread function in terms of the radiant intensity of the scattered light

$$ASF(\alpha, \beta) = \frac{1}{\gamma P} I(\alpha, \beta), \quad \gamma = \sqrt{1 - \alpha^2 - \beta^2}. \quad (2.96)$$

The pupil function of the beam emerging from the scattering surface,  $U_o(\hat{x}, \hat{y}; 0)$ , referred to in equation 2.94 is given by

$$U_o(\hat{x}, \hat{y}; 0) = \left\{ a(\hat{x}, \hat{y}; 0) \exp \left[ i 2 \pi \hat{W}(\hat{x}, \hat{y}; 0) \right] \right\} \left\{ a_s(\hat{x}, \hat{y}; 0) \exp \left[ i 2 \pi \hat{h}(\hat{x}, \hat{y}; 0) \right] \right\}. \quad (2.97)$$

The first term in the above equation is the deterministic part of the pupil function where  $a(\hat{x}, \hat{y}; 0)$  represents the amplitude variations and  $\hat{W}(\hat{x}, \hat{y}; 0)$  represents the aberrations in the exit pupil of the optical system producing the incident beam. The second term is the random component of the pupil function caused by reflection from the residual surface roughness. For most mirror surfaces  $a_s(\hat{x}, \hat{y}; 0) = \sqrt{R}$  is the (constant) Fresnel reflection coefficient of the scattering surface and

$$\phi(\hat{x}, \hat{y}; 0) = (2\pi / \lambda) OPD = 4\pi \hat{h}(\hat{x}, \hat{y}; 0) \quad (2.98)$$

is the random phase variation introduced by reflection from the scattering surface. Note that this expression is restricted to normal incidence where the height variations on the reflected wavefront are twice as large as the actual variations on the reflecting surface.

Harvey made the following assumptions about the scattering surface and the surface height distribution  $\hat{h}$ : i) The power reflectance,  $R$ , is constant over the entire surface, ii) The surface height distribution,  $\hat{h}(\hat{x}, \hat{y}; 0)$ , is Gaussian, iii)  $\hat{h}(\hat{x}, \hat{y}; 0)$  is locally stationary in the statistical sense, iv) The random variables  $\hat{h}(\hat{x}_1, \hat{y}_1; 0)$  and  $\hat{h}(\hat{x}_2, \hat{y}_2; 0)$ , produced by any two fixed pairs of spatial coordinates, are jointly normal, and v)  $\hat{h}(\hat{x}, \hat{y}; 0)$  is weakly ergodic.



Substituting equation 2.97 into 2.94, we obtain

$$H_{eff}(\hat{x}, \hat{y}; 0) = \frac{\int_{-\infty}^{\infty} \int_{-\infty}^{\infty} a_1 a_2 \exp[i2\pi(\hat{W}_1 - \hat{W}_2)] \exp[i4\pi(\hat{h}_1 - \hat{h}_2)] d\hat{x}' d\hat{y}'}{\int_{-\infty}^{\infty} \int_{-\infty}^{\infty} |a_1|^2 d\hat{x}' d\hat{y}'}, \quad (2.99)$$

$$\begin{aligned} \text{where} \quad a_1 &= a(\hat{x}', \hat{y}'; 0) & a_2 &= a(\hat{x}' - \hat{x}, \hat{y}' - \hat{y}; 0) \\ \hat{W}_1 &= \hat{W}(\hat{x}', \hat{y}'; 0) & \hat{W}_2 &= \hat{W}(\hat{x}' - \hat{x}, \hat{y}' - \hat{y}; 0) \\ \hat{h}_1 &= \hat{h}(\hat{x}', \hat{y}'; 0) & \hat{h}_2 &= \hat{h}(\hat{x}' - \hat{x}, \hat{y}' - \hat{y}; 0). \end{aligned} \quad (2.100)$$

The above expression for the transfer function contains the random variables  $\hat{h}_1$  and  $\hat{h}_2$ . If we take the expected value we obtain

$$\mathcal{E}\{H_{eff}(\hat{x}, \hat{y}; 0)\} = \frac{\int_{-\infty}^{\infty} \int_{-\infty}^{\infty} a_1 a_2 \exp[i2\pi(\hat{W}_1 - \hat{W}_2)] \mathcal{E}\left[\exp[i4\pi(\hat{h}_1 - \hat{h}_2)]\right] d\hat{x}' d\hat{y}'}{\int_{-\infty}^{\infty} \int_{-\infty}^{\infty} |a_1|^2 d\hat{x}' d\hat{y}'}. \quad (2.101)$$

If we assume the random variables to be stationary, the expected value under the integral is independent of  $\hat{x}'$  and  $\hat{y}'$  and can be taken outside the integral yielding

$$\mathcal{E}\{H_{eff}(\hat{x}, \hat{y}; 0)\} = \mathcal{E}\left[\exp[i4\pi(\hat{h}_1 - \hat{h}_2)]\right] \frac{\int_{-\infty}^{\infty} \int_{-\infty}^{\infty} a_1 a_2 \exp[i2\pi(\hat{W}_1 - \hat{W}_2)] d\hat{x}' d\hat{y}'}{\int_{-\infty}^{\infty} \int_{-\infty}^{\infty} |a_1|^2 d\hat{x}' d\hat{y}'}. \quad (2.102)$$

We now see that the effective transfer function is just the product of the transfer function of the scattering surface with the transfer function of the optical system producing the incident beam:

$$H_{eff}(\hat{x}, \hat{y}; 0) = H_s(\hat{x}, \hat{y}; 0) H(\hat{x}, \hat{y}; 0). \quad (2.103)$$

The surface transfer function is merely the joint characteristic function of the two random variables  $\hat{h}_1$  and  $\hat{h}_2$ , given by

$$H_s(\hat{x}, \hat{y}; 0) = \mathcal{E} \left\{ \exp \left[ i4\pi (\hat{h}_1 - \hat{h}_2) \right] \right\}. \quad (2.104)$$

Since  $\hat{h}_1$  and  $\hat{h}_2$  are jointly normal random variables, it can be shown that [91]

$$\mathcal{E} \left\{ \exp \left[ i4\pi (\hat{h}_1 - \hat{h}_2) \right] \right\} = \exp \left[ i4\pi (\eta_1 - \eta_2) \right] \exp \left[ -8\pi^2 (\hat{\sigma}_1^2 - 2\hat{C}_{12} + \hat{\sigma}_2^2) \right], \quad (2.105)$$

where

$$C_{12} = \mathcal{E} \left\{ (\hat{h}_1 - \eta_1)(\hat{h}_2 - \eta_2) \right\} \quad (2.106)$$

is the covariance function of the random variables  $\hat{h}_1$  and  $\hat{h}_2$ . But  $\hat{h}_1$  and  $\hat{h}_2$  are identical functions merely displaced from each other, and therefore

$$\sigma_1 = \sigma_2 = \sigma_s, \text{ and } \eta_1 = \eta_2. \quad (2.107)$$

The surface transfer function can therefore be written as

$$H_s(\hat{x}, \hat{y}) = \exp \left\{ - (4\pi \sigma_s)^2 \left[ 1 - \frac{C_s(\hat{x}, \hat{y})}{\sigma_s^2} \right] \right\}, \quad (2.108)$$

where  $C_s(\hat{x}, \hat{y}) \equiv C_{12}$  is the two-dimensional autocovariance function of the surface and  $\sigma_s^2$  is the variance of the surface height distribution function. The scattered light distribution, in the form of the *angle spread function* is given by the Fourier transform of equation 2.108.

The transfer function in equation 2.108 can also be rewritten in the form of

$$H(\hat{x}, \hat{y}) = A + B G(\hat{x}, \hat{y}), \quad (2.109)$$

where

$$A = \exp\left[-(4\pi\hat{\sigma}_s)^2\right], \quad (2.110)$$

$$B = 1 - \exp\left[-(4\pi\hat{\sigma}_s)^2\right], \quad (2.111)$$

and

$$G(\hat{x}, \hat{y}) = \frac{\exp\left[(4\pi)^2 \hat{C}(\hat{x}, \hat{y})\right] - 1}{\exp(4\pi\hat{\sigma}_s)^2 - 1}. \quad (2.112)$$

From equation 2.109, we see that the surface transfer function can be written as the sum of two separate components. The angle spread function can therefore be written as the sum of the Fourier transforms of the two components making up the transfer function:

$$ASF(\alpha, \beta) = \mathcal{F}\{H(\hat{x}, \hat{y})\} = A\delta(\alpha, \beta) + S(\alpha, \beta), \quad (2.113)$$

where

$$S(\alpha, \beta) = B \mathcal{F}\{G(\hat{x}, \hat{y})\}. \quad (2.114)$$

Therefore the scattering surface reflects an incident beam of light as a specularly reflected beam of diminished intensity surrounded by a halo of scattered light.

Note that the value of the surface transfer function is unity at the origin since  $A + B = 1$ . The central ordinate theorem of Fourier transform theory [1] therefore requires that the angle spread function have unit volume. Furthermore,  $A$  and  $B$  correspond to the fraction of the total reflected radiant power contained in the specular and the scattered components of the angle spread function, respectively (i.e.,  $B$  is identical to the total integrated scatter,  $B \equiv TIS$ ).

From equation 2.96 and Lambert's Cosine Law, it is clear that the angle spread function is a scattered *radiance* function ( $\gamma = \cos \theta_s$ ), albeit a normalized one. The ASF is related to classical radiance,  $L$ , by

$$ASF = \frac{L A_s}{P}, \quad (2.115)$$

where  $A_s$  is the illuminated area of the scattering surface, and  $P$  is the total scattered power.

The four-dimensional *BRDF* is made up of a superposition of these two-dimensional angle spread functions, one for every possible angle of incidence:

$$BRDF = \sum_{\theta_i, \phi_i} R \cdot ASF(\alpha, \beta). \quad (2.116)$$

Alternatively, for a given angle of incidence, the BRDF is related to the ASF by

$$BRDF|_{\theta_i, \phi_i} = R \cdot ASF(\alpha, \beta), \quad (2.117)$$

where  $R$  is the reflectance of the scattering surface.

### CHAPTER 3: A LINEAR SYSTEMS FORMULATION OF NON-PARAXIAL SCALAR DIFFRACTION THEORY

Most textbook treatments of diffraction include a paraxial (small-angle) limitation. For instance, it is well known that the irradiance distribution in the far field (Fraunhofer region) of a diffracting aperture is given by the squared modulus of the Fourier transform of the complex amplitude distribution emerging from the diffracting aperture [1,13]:

$$E(x_2, y_2) = \frac{1}{\lambda^2 z^2} \left| \mathcal{F}\{U_o^+(x_1, y_1)\} \Big|_{\xi=\frac{x_2}{\lambda z}, \eta=\frac{y_2}{\lambda z}} \right|^2, \quad (3.1)$$

where 
$$U_o^+(x_1, y_1) = U_o^-(x_1, y_1) t_1(x_1, y_1) \quad (3.2)$$

is the complex amplitude distribution emerging from a diffracting aperture with a complex amplitude transmittance given by  $t_1(x_1, y_1)$ .  $\mathcal{F}\{\dots\}$  denotes the Fourier transform operation given by

$$\mathcal{F}\{U_o^+(x_1, y_1)\} = \int_{-\infty}^{\infty} \int_{-\infty}^{\infty} U_o^+(x_1, y_1) \exp[-i2\pi(x_1\xi + y_1\eta)] dx_1 dy_1, \quad (3.3)$$

where the reciprocal Fourier transform variables are the spatial frequencies  $\xi$  and  $\eta$ .

The Fresnel diffraction integral can be written as the Fourier transform of the product of the aperture function with a quadratic phase factor [1,13]:

$$E(x_2, y_2) = \frac{1}{\lambda^2 z^2} \left| \mathcal{F} \left\{ U_o^+(x_1, y_1) \exp \left[ \frac{i\pi}{\lambda z} (x_1^2 + y_1^2) \right] \right\} \right|_{\xi=\frac{x_2}{\lambda z}, \eta=\frac{y_2}{\lambda z}}^2. \quad (3.4)$$

The Fraunhofer and Fresnel approximations expressed in equations 3.1 and 3.4 , however, contain an implicit paraxial limitation that severely restricts the conditions under which diffraction phenomena are adequately described [13]. Diffraction gratings, for instance, are inherently wide-angle devices and their behavior cannot be accurately modeled using paraxial diffraction theory. Scattering from surface roughness is also not limited to the paraxial region, and since predicting it is the goal of this dissertation, we will need a model of diffraction theory that is not limited by a paraxial approximation.

As discussed in section 2.1.2 of chapter 2, Harvey generalized the angular spectrum approach to scalar diffraction theory to include new insight into the phenomenon of diffraction throughout the whole space in which it occurs. The Rayleigh-Sommerfeld diffraction integral was rewritten as a Fourier transform integral of a generalized pupil function that includes phase variations resembling conventional wavefront aberrations of imaging systems. These aberrations, which are inherent to the diffraction process, are precisely the effects that are ignored when making the usual Fresnel and Fraunhofer approximations.

When a spherical wave is incident upon a diffracting aperture and the observation space is a hemisphere centered on the aperture, the phase variations mentioned above are frequently negligible [20]. The diffracted wave field on the hemisphere is then given by the Fourier transform of the aperture function:

$$U(\alpha, \beta; \hat{r}) = \gamma \left[ \frac{\exp(i2\pi\hat{r})}{(i\hat{r})} \right] \mathcal{F}\{U_o(\hat{x}, \hat{y}; 0)\}. \quad (3.5)$$

Recall that a scaled coordinate system is used in which the spatial variables are normalized by the wavelength of light, e.g.,  $\hat{x} = x/\lambda$ , and the reciprocal Fourier transform variables are the direction cosines of the propagation vectors. This Fourier transform relation is valid not only over a small region about the optical axis, as it is in the case of the Fraunhofer or Fresnel approximations, but over the entire observation hemisphere (with certain restrictions, depending on the residual phase variations [22]).

When radiation is incident upon the diffracting aperture at an angle  $\theta_i$ , as shown in Figure 3-1, it is equivalent to introducing a linear phase variation across the aperture and attenuating the irradiance in the plane of the aperture by a factor of  $\gamma_i = \cos\theta_i$ . The shift theorem of Fourier transform theory [1] can be applied to equation 3.5 yielding

$$U(\alpha, \beta - \beta_o; \hat{r}) = \gamma \left[ \frac{\exp(i2\pi\hat{r})}{(i\hat{r})} \right] \mathcal{F}\{U'_o(\hat{x}, \hat{y}; 0) \exp(i2\pi\beta_o\hat{y})\}, \quad (3.6)$$

where 
$$U'_o(\hat{x}, \hat{y}; 0) = \sqrt{\gamma_i} U_o(\hat{x}, \hat{y}; 0), \quad (3.7)$$

$\beta$  is the direction cosine of the position vector of the observation point, and  $\beta_o$  is the direction cosine of the undiffracted beam. The direction cosines can be obtained by simply projecting the respective points on the hemisphere into the plane of the aperture and normalizing to a unit radius. From equation 3.6, we can see that the complex amplitude distribution at an arbitrary point on the hemisphere can be expressed as a function of the distance of the observation point from the undiffracted beam in direction

cosine space. The quantity  $\gamma = \cos\theta$  in equations 3.5 and 3.6 is a cosine obliquity factor. Equations 3.5 and 3.6 will be used as the starting point for our further development of a non-paraxial model of scalar diffraction theory.

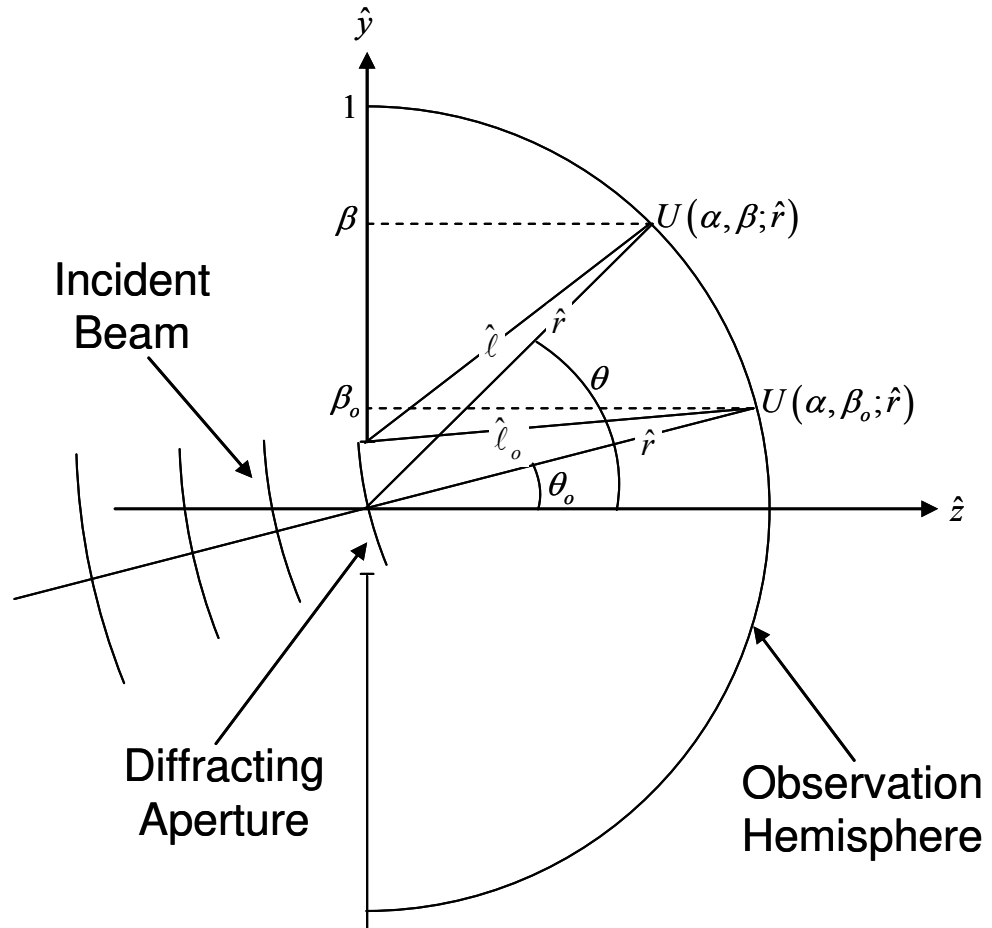


Figure 3-1: Converging incident beam striking a diffracting aperture at an arbitrary angle



### 3.1 Radiometric Terminology

Before proceeding in the development of our non-paraxial formulation of scalar diffraction, we will briefly review the definitions of a few radiometric quantities.

In the past, scientists have generally used the word *intensity* to mean *the flow of energy per unit area per unit time*. However, by international, if not universal, agreement, that term is being replaced by the term *irradiance* [92]:

$$Irradiance \equiv E = \frac{\partial P}{\partial A_c} \left( \frac{\text{power}}{\text{area}} \right). \quad (3.8)$$

Irradiance is defined as the radiant power density incident upon a collecting surface, noted by the subscript  $c$  on the differential area element in equation 3.8. Radiant intensity, on the other hand, is defined as the power per unit solid angle radiated from a source (particularly a point source or a source that has negligible area compared with the square of the viewing distance) [93,94]:

$$Radiant\ Intensity \equiv I = \frac{\partial P}{\partial \omega_c} \left( \frac{\text{power}}{\text{solid angle}} \right). \quad (3.9)$$

And radiance, the radiometric analog to the more familiar photometric term brightness, is defined as radiant power per unit solid angle per unit projected source area. Radiance is used to characterize an extended source (one that has an appreciable area compared with the square of the viewing distance) [93,94]. In differential form, radiance is given by

$$Radiance \equiv L = \frac{\partial^2 P}{\partial \omega_c \partial A_s \cos \theta_s} \left( \frac{\text{power}}{\text{solid angle - projected area}} \right). \quad (3.10)$$

The radiance of a source is, in general, a function of position on the source and a function of the two angular variables  $\theta$  and  $\phi$  in conventional spherical coordinates.

Noting that  $\partial\omega_c = \partial A_c \cos\theta_c / r^2$  and  $\partial\omega_s = \partial A_s \cos\theta_s / r^2$ , we can rearrange equation 3.10 to obtain the double differential

$$\begin{aligned}\partial^2 P &= L(\theta_s, \phi_s, x, y) \partial A_s \cos\theta_s \partial\omega_c \\ &= L(\theta_s, \phi_s, x, y) \partial A_s \cos\theta_s \frac{\partial A_c \cos\theta_c}{r^2} \\ &= L(\theta_s, \phi_s, x, y) \partial\omega_s \partial A_c \cos\theta_c ,\end{aligned}\tag{3.11}$$

where  $r$  is the distance between the source and the collector as shown in Figure 3-2. Equation 3.11 can be considered to be the fundamental theorem of radiometry as it describes the radiant power transfer between an elemental source and an elemental collector.

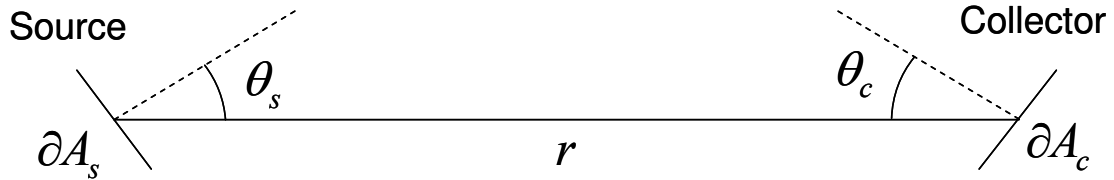


Figure 3-2: Geometrical configuration used to demonstrate the fundamental theorem of radiometry, from which the quantity radiance is obtained

### 3.2 Diffracted Radiance – A Fundamental Quantity

If we consider the diffracting aperture of Figure 3-1 to be the source, and the observation hemisphere to be the collector, we can integrate equation 3.11 once with respect to the projected source area to obtain the diffracted intensity:

$$I(\theta, \phi) = \frac{\partial P}{\partial \omega_c} = \int_{A_s} L(\theta, \phi, x, y) \cos \theta_s \partial A_s. \quad (3.12)$$

We can also integrate equation 3.11 once with respect to the source solid angle to obtain the irradiance

$$E = \frac{\partial P}{\partial A_c} = \int_{\omega_s} L(\theta, \phi, x, y) \cos \theta_c \partial \omega_s. \quad (3.13)$$

Since  $\partial \omega_s = \partial A_s \cos \theta_s / r^2$ , and  $\theta_c = 0$  on the observation hemisphere, equation 3.13 can be written as

$$E(\theta, \phi) = \frac{\cos \theta_s}{r^2} \int_{A_s} L(\theta, \phi, x, y) \partial A_s. \quad (3.14)$$

The direction cosines  $\alpha$ ,  $\beta$ , and  $\gamma$  are related to the angular variables  $\theta$  and  $\phi$  in conventional spherical coordinates by

$$\begin{aligned} \alpha &= \sin \theta \cos \phi \\ \beta &= \sin \theta \sin \phi \\ \gamma &= \cos \theta \\ \alpha^2 + \beta^2 + \gamma^2 &= 1. \end{aligned} \quad (3.15)$$

Since the integral in equation 3.14 is over the differential source area and is not affected by the  $\theta, \phi$  dependence, equations 3.15 can be used to rewrite equation 3.14 in terms of direction cosines as

$$E(\alpha, \beta) = \frac{\gamma}{r^2} \int_{A_s} L(\alpha, \beta, x, y) dA_s, \quad (3.16)$$

and after rearranging, we obtain

$$\int_{A_s} L(\alpha, \beta, x, y) dA_s = r^2 \frac{E_c(\alpha, \beta)}{\gamma}. \quad (3.17)$$

The irradiance on an observation plane parallel to the plane of the aperture is given by  $|U(\alpha, \beta; \hat{r})|^2$ , however the irradiance on the hemisphere is given by  $|U(\alpha, \beta; \hat{r})|^2 / \gamma$  and equation 3.17 can therefore be rewritten as

$$\int_{A_s} L(\alpha, \beta, x, y) dA_s = r^2 \frac{|U(\alpha, \beta; \hat{r})|^2}{\gamma^2}. \quad (3.18)$$

Substituting equation 3.5 into equation 3.18 yields

$$\int_{A_s} L(\alpha, \beta, x, y) dA_s = \lambda^2 \left| \mathcal{F}\{U_o(\hat{x}, \hat{y}; 0)\} \right|^2. \quad (3.19)$$

If the source is a uniformly illuminated diffracting aperture, the radiance does not depend upon the position in the aperture and the left hand side of equation 3.19 is given by

$$\int_{A_s} L(\alpha, \beta, x, y) \partial A_s = L(\alpha, \beta) \int_{A_s} \partial A_s \approx L(\alpha, \beta) A_s. \quad (3.20)$$

Substituting equation 3.20 into 3.19 and dividing by the area of the diffracting aperture gives the following expression for diffracted radiance:

$$L(\alpha, \beta) = \frac{\lambda^2}{A_s} \left| \mathcal{F} \left\{ U_o(\hat{x}, \hat{y}; 0) \right\} \right|^2. \quad (3.21)$$

We have therefore shown that the squared modulus of the Fourier transform of the complex amplitude distribution emerging from a diffracting aperture yields the diffracted radiance and *not* the irradiance or the intensity. In addition, equation 3.21, unlike the more familiar expression of equation 3.1, is not restricted to small diffraction angles.

For radiation incident upon the diffracting aperture at an angle, equation 3.6 can be substituted into 3.18, and if the aperture is uniformly illuminated we obtain

$$L(\alpha, \beta - \beta_o) = \gamma_o \frac{\lambda^2}{A_s} \left| \mathcal{F} \left\{ U_o(\hat{x}, \hat{y}; 0) \exp(i2\pi\beta_o\hat{y}) \right\} \right|^2. \quad (3.22)$$

From equation 3.22, we can see that changes in the angle of incidence of the radiation illuminating the diffracting aperture will merely result in a shift of the radiance function in direction cosine space and an attenuation by the factor  $\gamma_o = \cos\theta_o$ . However, because the functional form does not change, the diffracted radiance can be considered to be shift invariant in direction cosine space (with respect to incident angle), and the simple Fourier techniques that have previously been used in paraxial applications can be used for non-paraxial applications as well.

### 3.3 Renormalization Conserves Energy In The Presence Of Evanescent Waves

Rayleigh's (Parseval's) theorem from Fourier transform theory states that the integral over all space of the squared modulus of any function is equal to the integral over all space of the squared modulus of its Fourier transform [13]. We can therefore write

$$\int_{-\infty}^{\infty} \int_{-\infty}^{\infty} |U'_o(\hat{x}, \hat{y}; 0) \exp(i2\pi\beta_o \hat{y})|^2 d\hat{x} d\hat{y} = \int_{-\infty}^{\infty} \int_{-\infty}^{\infty} |\mathcal{F}\{U'_o(\hat{x}, \hat{y}; 0) \exp(i2\pi\beta_o \hat{y})\}|^2 d\alpha d\beta. \quad (3.23)$$

Substituting equation 3.22 into equation 3.23 gives

$$\int_{-\infty}^{\infty} \int_{-\infty}^{\infty} |U'_o(\hat{x}, \hat{y}; 0) \exp(i2\pi\beta_o \hat{y})|^2 d\hat{x} d\hat{y} = \frac{A_s}{\lambda^2} \int_{-\infty}^{\infty} \int_{-\infty}^{\infty} L(\alpha, \beta - \beta_o) d\alpha d\beta. \quad (3.24)$$

Recall that only those plane wave components that lie inside the unit circle in direction cosine space ( $\alpha^2 + \beta^2 \leq 1$ ) are real and propagate. Those that lie outside of the unit circle are imaginary and are referred to as *evanescent* waves (and thus do not propagate) [13,20]. All (real) space is therefore represented by the unit circle in the two-dimensional direction cosine space. All of the radiant power emanating from the diffracting aperture is contained in that portion of the diffracted radiance distribution function lying inside the unit circle in direction cosine space (the direction cosines of a vector must satisfy the equation  $\alpha^2 + \beta^2 + \gamma^2 = 1$ ). Therefore equation 3.24 can also be written as

$$\int_{-\infty}^{\infty} \int_{-\infty}^{\infty} |U'_o(\hat{x}, \hat{y}; 0) \exp(i2\pi\beta_o \hat{y})|^2 d\hat{x} d\hat{y} = \frac{A_s}{\lambda^2} \int_{-1}^1 \int_{-\sqrt{1-\alpha^2}}^{\sqrt{1-\alpha^2}} L'(\alpha, \beta - \beta_o) d\alpha d\beta. \quad (3.25)$$

where we have used  $L'(\alpha, \beta - \beta_o)$  to indicate the real diffracted radiance distribution

that lies inside of the unit circle. Note that the left side of equation 3.25 is merely the integral of the radiant exitance over the (scaled) aperture. It is therefore proportional to the total radiant power transmitted through the diffracting aperture, which diminishes with the cosine of the incident angle:

$$\int_{-\infty}^{\infty} \int_{-\infty}^{\infty} \left| U'_o(\hat{x}, \hat{y}; 0) \exp(i2\pi\beta_o \hat{y}) \right|^2 d\hat{x} d\hat{y} = \frac{P_T(\theta_i)}{\lambda^2} = \frac{E_o A_s \gamma_i}{\lambda^2}. \quad (3.26)$$

If we substitute equation 3.26 into equations 3.24 and 3.25, it is evident that, for the case of a uniformly illuminated diffracting aperture, the total radiant power diffracted from the aperture is just the area of the aperture times the integral of the diffracted radiance in direction cosine space:

$$P_T = A_s \int_{-\infty}^{\infty} \int_{-\infty}^{\infty} L(\alpha, \beta - \beta_o) d\alpha d\beta = A_s \int_{-1}^1 \int_{-\sqrt{1-\alpha^2}}^{\sqrt{1-\alpha^2}} L'(\alpha, \beta - \beta_o) d\alpha d\beta, \quad (3.27)$$

where  $L(\alpha, \beta - \beta_o)$  is given by equation 3.22 and

$$L'(\alpha, \beta - \beta_o) = K L(\alpha, \beta - \beta_o). \quad (3.28)$$

The real radiance distribution function,  $L'(\alpha, \beta - \beta_o)$ , is thus merely a renormalized version of the original radiance distribution function,  $L(\alpha, \beta - \beta_o)$ . The renormalization constant,  $K$ , is given by the ratio of the integral of  $L(\alpha, \beta - \beta_o)$  over infinite limits to the integral of  $L(\alpha, \beta - \beta_o)$  over the unit circle in direction cosine space:

$$K = \frac{\int_{-\infty}^{\infty} \int_{-\infty}^{\infty} L(\alpha, \beta - \beta_o) d\alpha d\beta}{\int_{-1}^1 \int_{-\sqrt{1-\alpha^2}}^{\sqrt{1-\alpha^2}} L(\alpha, \beta - \beta_o) d\alpha d\beta} . \quad (3.29)$$

For those cases where the diffracted radiance distribution function, given by equation 3.22, extends beyond the unit circle in direction cosine space, the real (propagating) radiance distribution is thus given by

$$L'(\alpha, \beta - \beta_o) = \begin{cases} K \frac{\lambda^2}{A_s} \left| \mathcal{F}\{U'_o(\hat{x}, \hat{y}; 0) \exp(i2\pi\beta_o \hat{y})\} \right|^2 & \text{for } \alpha^2 + \beta^2 \leq 1 \\ 0 & \text{for } \alpha^2 + \beta^2 > 1 \end{cases} . \quad (3.30)$$

The re-normalization constant,  $K$ , differs from unity only if the radiance distribution function extends beyond the unit circle in direction cosine space (i.e., only if evanescent waves are produced), and this renormalization process is consistent with the law of conservation of energy. However, it is significant that this linear systems formulation of non-paraxial scalar diffraction theory has been derived by the application of Rayleigh's (Parseval's) theorem and not by merely heuristically imposing the law of conservation of energy. The physics has not changed from the Rayleigh-Sommerfeld theory, but we have re-formulated it into a Fourier treatment which can be easily solved for a wide variety of non-paraxial applications.

In order to calculate radiant intensity to compare with experimental measurements (since radiance is not a measurable quantity), one can use equation 3.12 (i.e., multiply the radiance by  $\gamma = \cos\theta$  and integrate over the source area). In terms of direction cosines this is given by



$$I(\alpha, \beta) = \int_{A_s} \gamma L(\alpha, \beta, x, y) dA. \quad (3.31)$$

Again, if the source is a uniformly illuminated diffracting aperture, the radiance does not depend on the position in the source, and we obtain the diffracted intensity by multiplying equation 3.30 by  $\gamma A_s$ :

$$I(\alpha, \beta - \beta_o) = \begin{cases} K \gamma_o \gamma \lambda^2 \left| \mathcal{F}\{U_o(\hat{x}, \hat{y}; 0) \exp(i2\pi\beta_o \hat{y})\} \right|^2 & \text{for } \alpha^2 + \beta^2 \leq 1 \\ 0 & \text{for } \alpha^2 + \beta^2 > 1 \end{cases}. \quad (3.32)$$

Although the diffracted radiance can exhibit a discontinuity at the edge of the unit circle (for a Lambertian emitter the radiance is constant and drops discontinuously to zero at the edge of the unit circle), the cosine factor ( $\gamma = \cos\theta$ ) in equation 3.32 assures that the diffracted intensity never exhibits such discontinuities.

The radiant power can be calculated by integrating the intensity over the solid angle of the collector as indicated by equation 3.9, and in spherical coordinates, the differential solid angle  $\partial\omega_c$  is given by  $\sin\theta_s d\theta_s d\phi_s$  [94], allowing us to write

$$P = \int_{\omega_c} I \partial\omega_c = \iint_B I(\theta, \phi) \sin\theta d\theta d\phi. \quad (3.33)$$

For the coordinate transformation defined by equations 3.15, the Jacobian determinant in the well known change of variables [95] theorem is given by

$$\left| \frac{\partial(\alpha, \beta)}{\partial(\theta, \phi)} \right| = \sin\theta \cos\theta, \quad (3.34)$$

and the differential solid angle can be written as

$$d\omega_c = \sin \theta \, d\theta \, d\phi = \frac{d\alpha \, d\beta}{\gamma}. \quad (3.35)$$

Using equations 3.15, 3.34, and 3.35, we can apply the change of variables theorem to equation 3.33 and obtain the total radiant power in the diffracted intensity distribution:

$$P_T = \int_{-1}^1 \int_{-\sqrt{1-\alpha^2}}^{\sqrt{1-\alpha^2}} \frac{I(\alpha, \beta)}{\gamma} d\alpha \, d\beta. \quad (3.36)$$

To illustrate the renormalization process described above, consider the example of a rotationally symmetric, on-axis Gaussian radiance distribution function given by

$$L(\alpha, \beta) = \exp\left[-\frac{\alpha^2 + \beta^2}{b^2}\right]. \quad (3.37)$$

A profile of this radiance distribution is shown in Figure 3-3a for  $b = 0.2$ . The diffracted intensity can be calculated through the use of equation 3.31 yielding

$$I(\alpha, \beta) = \gamma A_s \exp\left[-\frac{\alpha^2 + \beta^2}{b^2}\right]. \quad (3.38)$$

A profile of the diffracted intensity as a function of diffraction angle ( $\theta = \sin^{-1}\beta$ ) is shown in Figure 3-3b. Both the radiance and intensity are centered on the optic axis and are clearly contained entirely within the unit circle.

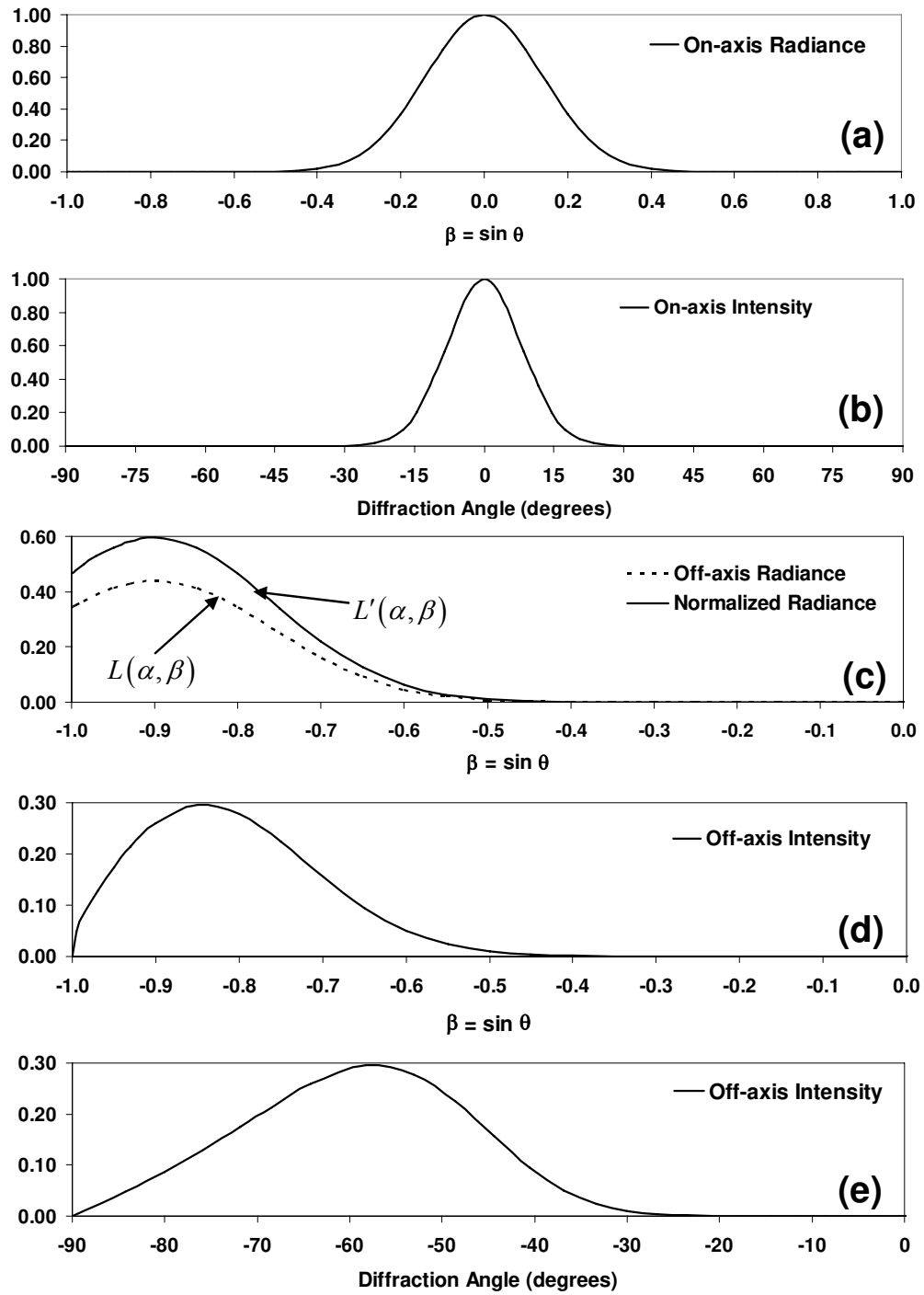


Figure 3-3: (a) Profile of an on-axis Gaussian radiance distribution in direction cosine space. (b) Profile of the on-axis intensity distribution corresponding to (a) as a function of diffraction angle. (c) Off-axis (normalized) radiance distribution resulting from a  $64^\circ$  incident angle. (d) The off-axis intensity distribution in direction cosine space corresponding to (c). (e) Off-axis intensity distribution as a function of the diffraction angle.

If we introduce a rather large incident angle of 64 degrees ( $\beta_i = 0.9$ ), the radiance distribution function,  $L(\alpha, \beta)$ , is shifted until it is centered on  $\beta = -0.9$ , and attenuated by the constant  $\gamma_i = \cos \theta_i$  as shown in Figure 3-3c. A significant portion of this shifted radiance distribution function,  $L(\alpha, \beta - \beta_0)$ , extends beyond the unit circle in direction cosine space. However, only that portion that lies inside the unit circle is real and contains radiant power or energy, and the radiance needs to be renormalized through the use of equations 3.28 and 3.29. The renormalized radiance distribution function,  $L'(\alpha, \beta - \beta_0)$ , for the current example is also shown in Figure 3-3c.

The diffracted intensity can again be calculated using equation 3.31 and is shown as a function of  $\beta$  in Figure 3-3d, and as a function of the diffraction angle,  $\theta$ , in Figure 3-3e. Note the asymmetry in this intensity profile that is characteristic of diffraction patterns at large incident angles.

### 3.4 Application To Sinusoidal Phase Gratings

Diffraction gratings are inherently wide-angle devices, and are frequently used with large oblique incident angles. Paraxial diffraction theory therefore cannot adequately model the behavior of diffraction gratings, except in cases where the paraxial approximation holds. For this reason, scalar diffraction theory is frequently considered to be inadequate for predicting diffraction efficiencies for grating applications when the ratio of the wavelength of the incident radiation to the period of the grating ( $\lambda/d$ ) is greater than 0.1[96-98]. It has also been stated that scalar theory *imposes* energy on the evanescent diffracted orders [96]. These notions are driven more by the unnecessary

paraxial limitation in the traditional Fourier treatment of scalar diffraction theory than by the scalar limitation itself.

Since the late 1960s, holographic gratings, fabricated by the exposure of photoresist by a stationary sinusoidal interference fringe field, have become commonplace. The photoresist substrate is chemically developed after exposure to produce a master holographic grating with sinusoidal groove profiles. These master holographic gratings are routinely coated and replicated, as are master ruled gratings.

Prior to the widespread use of holographic gratings, the diffraction characteristics of sinusoidal phase gratings were of interest primarily because other groove profiles (lamellar and blazed gratings) can be Fourier analyzed into a superposition of sinusoidal profiles[99]. Likewise, arbitrary scattering surfaces are routinely modeled as a superposition of sinusoidal surfaces of different amplitudes, periods, and orientations[3,90,100]. For these reasons, the sinusoidal phase grating is a logical choice of an example with which to test our non-paraxial model of scalar diffraction theory.

### ***3.4.1 Paraxial Model Of Sinusoidal Phase Gratings***

Goodman [13] discusses sinusoidal phase gratings, and using the Fraunhofer approximation derives the following expression for the diffracted irradiance distribution in the far field when one has a square grating of width  $L$ , period  $d$ , and peak-to-peak phase excursion  $a$ , illuminated with the uniform irradiance  $E_o$ :

$$E(x, y) = E_o \left( \frac{L^2}{\lambda z} \right)^2 \sum_{-\infty}^{\infty} J_m^2 \left( \frac{a}{2} \right) \text{sinc}^2 \left[ \frac{L}{\lambda z} \left( x - \frac{m\lambda z}{d} \right) \right] \text{sinc}^2 \left( \frac{Ly}{\lambda z} \right), \quad (3.39)$$

where

$$\text{sinc}(u) = \frac{\sin(\pi u)}{(\pi u)}, \quad (3.40)$$

This expression results in the well-known fact that, within the paraxial approximation, the diffraction efficiency of the  $m^{\text{th}}$  diffracted order is given by  $J_m^2(a/2)$ , where  $J_m$  is the  $m^{\text{th}}$  order Bessel function of the first kind.

Following Goodman's derivation, the expression for the diffracted irradiance when the aperture is illuminated by a Gaussian beam of width  $b$  (radius at which the field drops to  $e^{-\pi}$  of its peak value) instead of a uniformly illuminated square aperture can be written as

$$E(x, y) = E_o \left( \frac{b^2}{\lambda z} \right)^2 \sum_{-\infty}^{\infty} J_m^2 \left( \frac{a}{2} \right) \text{Gaus}^2 \left[ \frac{b}{\lambda z} \left( x - \frac{m\lambda z}{d}, y \right) \right], \quad (3.41)$$

where

$$\text{Gaus}(u, v) = \exp \left[ -\pi (u^2 + v^2) \right]. \quad (3.42)$$

Since equation 3.41 is specifically limited to the far field of the diffracting aperture, and the paraxial approximation is implicit in the far field (or Fraunhofer) approximation, we can write

$$\theta_x = \tan^{-1}(x/z) \approx x/z, \quad \theta_y = \tan^{-1}(y/z) \approx y/z, \quad (3.43)$$

and since the radiant intensity is equal to the irradiance divided by the square of the viewing distance [94], we can rewrite equation 3.41 in terms of the intensity as

$$I(\theta, \phi) = E_o \left( \frac{b^2}{\lambda} \right)^2 \sum_{-\infty}^{\infty} J_m^2 \left( \frac{a}{2} \right) \text{Gaus}^2 \left[ \frac{b}{\lambda} \left( \theta_x - \frac{m\lambda}{d}, \theta_y \right) \right]. \quad (3.44)$$

The diffracted intensity profile predicted using the paraxial model of equation 3.44 is shown in Figure 3-4 as a function of the diffraction angle,  $\theta_x$ , and the groove depth,  $h$ , for a sinusoidal reflection grating with period  $d = 20\lambda$  operating at normal incidence. For a sinusoidal reflection grating, the peak-to-peak phase excursion for normally incident radiation is given by  $a = 4\pi h/\lambda$ .

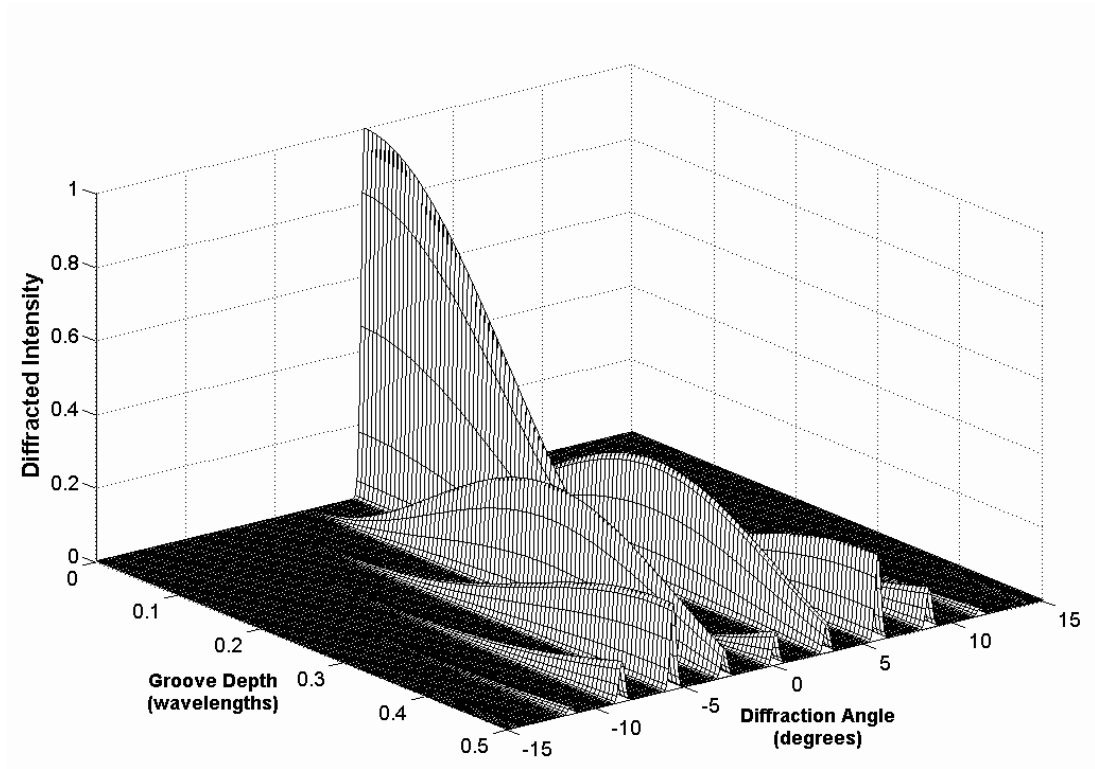


Figure 3-4: Diffracted intensity profile as predicted by the paraxial model for a sinusoidal reflection grating of period  $d = 20\lambda$  operating at normal incidence

Figure 3-4 represents a valid regime for the paraxial model, as almost all of the energy is contained within the first few orders, which are diffracted at small angles ( $<12^\circ$ ). The maximum value of  $J_1^2(a/2)$ , which is the diffraction efficiency of the 1<sup>st</sup>

order, is equal to 0.3386 and occurs when  $a = 3.68$  ( $h = 0.293\lambda$ ). The diffraction efficiencies of the first few orders for this value of  $a$  are tabulated in Table 1. Note that the energy falls off rapidly, with 99.88% of the energy contained in diffracted orders  $|m| \leq 3$ .

Table 1: Diffraction efficiencies for a coarse (paraxial regime) sinusoidal phase grating optimized for maximum efficiency in the  $\pm 1$  diffracted orders.

Diffracted Order	Diffraction Efficiency
0	$1.003 \times 10^{-1}$
$\pm 1$	$3.386 \times 10^{-1}$
$\pm 2$	$9.970 \times 10^{-2}$
$\pm 3$	$1.093 \times 10^{-2}$
$\pm 4$	$6.320 \times 10^{-4}$

The paraxial model of equation 3.44 is only accurate for very coarse gratings ( $d \gg \lambda$ ), and only when  $h/\lambda$  is small enough to ensure that almost all of the energy is contained in orders that diffract at small angles. In addition, the paraxial model leads to the common misconception that it is impossible to get more than 33.86% of the incident energy into the first diffracted order with a sinusoidal phase grating.

A simple thought experiment can prove this misconception to be false. Suppose that we have a grating with a period such that only three orders are propagating (-1,0,+1).



If we choose an angle of incidence such that the -1 order goes evanescent, there will be only two propagating orders (0,+1). We can then choose a groove depth such that there is no energy in the 0<sup>th</sup> order (i.e.  $J_0(a/2) = 0$ ). Since there are only two propagating orders, and there is no energy in the 0<sup>th</sup> order, *all* of the energy has to be contained in the +1 order. The maximum diffraction efficiency of the 1<sup>st</sup> order for a sinusoidal phase grating is therefore equal to unity, not 0.3386 as predicted by the paraxial model.

If we use equation 3.44 to model the behavior of fine (small spatial period) gratings whose diffracted orders do not fall within the paraxial region, we will obtain incorrect results that lead to a variety of other misconceptions. For example, the diffracted intensity profile predicted using the paraxial model of equation 3.44 is shown in Figure 3-4 as a function of the diffraction angle,  $\theta_x$ , and the groove depth,  $h$ , for a sinusoidal reflection grating with period  $d = 1.3\lambda$  operating at normal incidence.

There are several features of the predicted intensity distribution in Figure 3-4 that are inaccurate: (i) The small angle approximation to the grating equation inherent in equation 3.44 leads to the erroneous prediction of equally spaced diffracted orders (in diffraction angle). (ii) When a diffracted order of finite width is located near  $\pm 90$  degrees, the predicted diffracted intensity (or irradiance) exhibits a discontinuity that is an unacceptable non-physical phenomenon. (iii) The predicted angular width of the diffracted orders does not indicate the broadening that occurs with increasing diffraction angle [101]. (iv) The diffraction efficiencies of the propagating orders are not adjusted to account for the Wood's anomaly effect of redistributing the energy associated with evanescent orders among the remaining propagating orders[102].

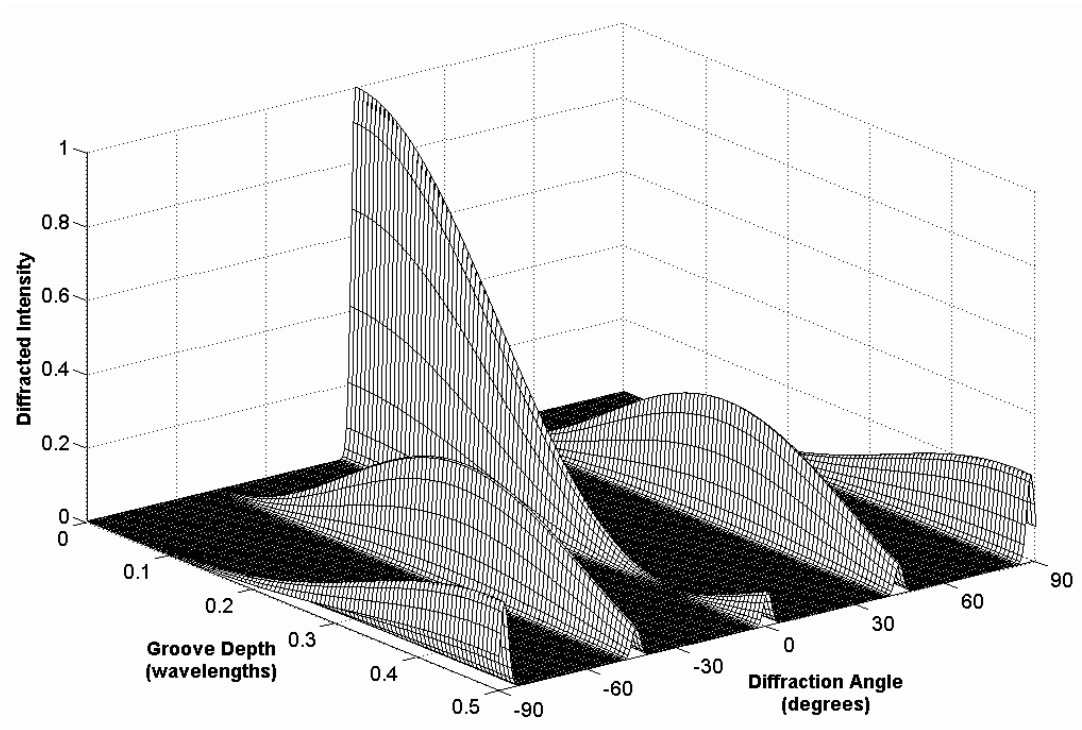


Figure 3-5: Diffracted intensity distribution profile as predicted by the paraxial model for a sinusoidal reflection grating of period  $1.3\lambda$  (invalid operating regime)

### *3.4.2 Wide-Angle Behavior Of Sinusoidal Phase Gratings*

We will now apply our non-paraxial model of scalar diffraction developed in sections 3.2 and 3.3 to the case of the sinusoidal phase (reflection) grating, and show that the inaccuracies outlined above for the paraxial model are due to the paraxial limitation, and not due to the scalar limitation.

The complex amplitude transmittance of a sinusoidal phase grating can be written as

$$t(\hat{x}, \hat{y}) = \exp \left[ i \frac{a}{2} \sin \left( 2\pi \frac{\hat{x}}{\hat{d}} \right) \right], \quad (3.45)$$

where  $\hat{x} = x/\lambda$ ,  $\hat{y} = y/\lambda$ , and  $\hat{d} = d/\lambda$ . The complex amplitude distribution emerging from the grating is given by

$$U_o^+(\hat{x}, \hat{y}) = U_o^-(\hat{x}, \hat{y}) t(\hat{x}, \hat{y}), \quad (3.46)$$

where  $U_o^-(\hat{x}, \hat{y})$  is the complex amplitude distribution of the converging spherical wavefront incident upon the grating. Recall again that we have scaled the spatial variables by the wavelength of the incident radiation so the reciprocal variables in Fourier transform space will be the direction cosines of the propagation vectors of the resulting plane wave components. Note also that we have dropped a factor representing the average phase delay in passing through the grating, and that the parameter  $a$  represents the peak-to-peak excursion of the phase delay.

The diffraction grating analysis can be simplified by use of the following mathematical identity [13]

$$\exp \left[ i \frac{a}{2} \sin \left( 2\pi \frac{\hat{x}}{\hat{d}} \right) \right] = \sum_{m=-\infty}^{\infty} J_m \left( \frac{a}{2} \right) \exp \left( i 2\pi \frac{m\hat{x}}{\hat{d}} \right). \quad (3.47)$$

We know from equation 3.19 that the integral of the diffracted radiance over the diffracting aperture is proportional to the squared modulus of the Fourier transform of the complex amplitude distribution emerging from the aperture:

$$\int_{A_s} L(\alpha, \beta, x, y) dA_s = \lambda^2 \left| \mathcal{F} \{ U_o(\hat{x}, \hat{y}; 0) \} \right|^2. \quad (3.48)$$

Assuming that a narrow Gaussian beam of width  $b$  (radius at which the field drops to  $e^{-\pi}$  of its peak value) is incident upon the sinusoidal phase grating at normal incidence, we can write the radiance as the product of two separable functions:

$$L(\alpha, \beta, x, y) = L(\alpha, \beta) \text{Gaus}^2 \left( \frac{x}{b}, \frac{y}{b} \right), \quad (3.49)$$

where the Gaus function is again defined by equation 3.42.  $L(\alpha, \beta)$  can therefore be brought outside of the integral in equation 3.48, and since  $b$  is small relative to the radius of the observation hemisphere,  $\cos \theta_s$  can also be brought outside of the integral, yielding

$$L(\alpha, \beta) \cos \theta_s \int_{A_s} \text{Gaus}^2 \left( \frac{x}{b}, \frac{y}{b} \right) dx dy = \gamma \lambda^2 \left| \mathcal{F} \{ U_o^+(\hat{x}, \hat{y}; 0) \} \right|^2. \quad (3.50)$$

The integral of the Gaus function in equation 3.50 is equal to  $b^2/2$ , and since  $\gamma = \cos \theta_s$ , the diffracted radiance is given by

$$L(\alpha, \beta) = \frac{2}{b^2} \left| \mathcal{F} \{ U_o^+(\hat{x}, \hat{y}; 0) \} \right|^2. \quad (3.51)$$

$U_o^+(\hat{x}, \hat{y})$  is the complex amplitude distribution emerging from the grating, given by

$$U_o^+(\hat{x}, \hat{y}) = U_o^- \text{Gaus} \left( \frac{\hat{x}}{b}, \frac{\hat{y}}{b} \right) t(\hat{x}_1, \hat{y}_1) = U_o^- \text{Gaus} \left( \frac{\hat{x}}{b}, \frac{\hat{y}}{b} \right) \sum_{m=-\infty}^{\infty} J_m \left( \frac{a}{2} \right) \exp \left( i 2\pi \frac{m\hat{x}}{d} \right). \quad (3.52)$$

Applying the convolution theorem of Fourier transform theory [1] to equation 3.52, we

can write

$$\mathcal{F}\{U_o^+(\hat{x}, \hat{y})\} = U_o^- \hat{b}^2 \text{Gaus}[\hat{b}(\alpha, \beta)] ** \mathcal{F}\left\{\sum_{m=-\infty}^{\infty} J_m\left(\frac{a}{2}\right) \exp\left(i2\pi \frac{m\hat{x}}{\hat{d}}\right)\right\}, \quad (3.53)$$

where the symbol  $**$  represents a two-dimensional convolution operation. Performing the Fourier transform on the right hand side of equation 3.53 yields

$$\mathcal{F}\{U_o^+(\hat{x}, \hat{y})\} = U_o^- \hat{b}^2 \text{Gaus}[\hat{b}(\alpha, \beta)] ** \sum_{m=-\infty}^{\infty} J_m\left(\frac{a}{2}\right) \delta\left(\alpha - \frac{m}{\hat{d}}, \beta\right), \quad (3.54)$$

and since any function convolved with a delta function merely replicates that function at the location of the delta function, we obtain

$$\mathcal{F}\{U_o^+(\hat{x}, \hat{y})\} = U_o^- \hat{b}^2 \sum_{m=-\infty}^{\infty} J_m\left(\frac{a}{2}\right) \text{Gaus}\left[\hat{b}\left(\alpha - \frac{m}{\hat{d}}, \beta\right)\right]. \quad (3.55)$$

Substituting equation 3.55 into equation 3.51, and noting that the peak irradiance in the incident beam is given by  $E_o = |U_o^-|^2$  yields

$$L(\alpha, \beta) = 2 E_o \hat{b}^2 \left| \sum_{m=-\infty}^{\infty} J_m\left(\frac{a}{2}\right) \text{Gaus}\left[\hat{b}\left(\alpha - \frac{m}{\hat{d}}, \beta\right)\right] \right|^2. \quad (3.56)$$

If we assume that  $b \gg d$ , there will be negligible overlap between the various diffracted orders (i.e., no cross terms), and the diffracted radiance distribution is given by

$$L(\alpha, \beta) = 2 E_o \hat{b}^2 \sum_{m=-\infty}^{\infty} J_m^2\left(\frac{a}{2}\right) \text{Gaus}^2\left[\hat{b}\left(\alpha - \frac{m}{\hat{d}}, \beta\right)\right]. \quad (3.57)$$

As explained in section 3.3, if there are any evanescent diffracted orders, the diffracted

radiance distribution of equation 3.57 must be renormalized using equations 3.28 and 3.29. Therefore, for those cases where evanescent waves exist, the diffracted radiance can be expressed as

$$L'(\alpha, \beta) = \begin{cases} K^2 E_o^2 \hat{b}^2 \sum_{m=-\infty}^{\infty} J_m^2\left(\frac{a}{2}\right) \text{Gaus}^2\left[\hat{b}\left(\alpha - \frac{m}{\hat{d}}, \beta\right)\right] & \text{for } \alpha^2 + \beta^2 \leq 1 \\ 0 & \text{for } \alpha^2 + \beta^2 > 1 \end{cases} \quad (3.58)$$

Using equation 3.58 for a sinusoidal reflection grating with a period of  $d = 1.95\lambda$  and normally incident radiation results in the predicted radiance distribution profile illustrated in Figure 3-6. The radiance profile is plotted as a function of both groove depth and the direction cosine of the diffraction angle. This distribution is very similar to the one shown in Figure 3-5, except that we are plotting the diffracted radiance in direction cosine space. Note that the diffracted orders are equally spaced and have equal widths in direction cosine space. This is consistent with previous work highlighting the advantages of describing diffraction grating behavior in direction cosine space [103]. The distribution exhibits discontinuities at  $\alpha = \pm 1$  ( $\theta = \pm 90^\circ$ ), however radiance is allowed to exhibit such discontinuities. In addition, the diffracted radiance distribution has been renormalized in accordance with equations 3.28 and 3.29. This renormalization ensures that all of the transmitted energy is contained in the propagating plane-wave components.

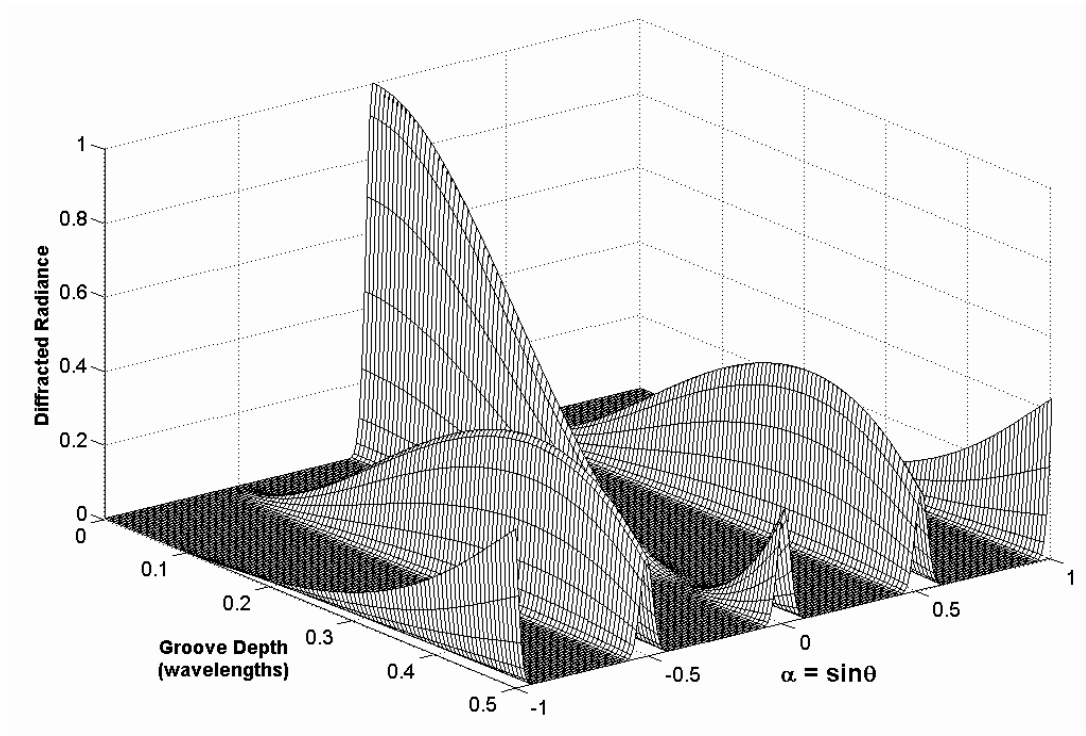


Figure 3-6: Diffracted radiance distribution profile (in direction cosine space) predicted by our non-paraxial model for a sinusoidal reflection grating with a period of  $d = 1.95\lambda$

To calculate the diffracted intensity, we merely need to apply equation 3.31 to the diffracted radiance distribution (i.e., we multiply the radiance by  $\gamma = \cos\theta$  and integrate over the source area):

$$\begin{aligned}
 I(\alpha, \beta) &= \int_{A_s} L(\alpha, \beta, x, y) \cos\theta \, dA \\
 &= \int_{A_s} L'(\alpha, \beta) \text{Gaus}^2\left(\frac{x}{b}, \frac{y}{b}\right) \cos\theta \, dA \\
 &= L'(\alpha, \beta) \cos\theta \int_{A_s} \text{Gaus}^2\left(\frac{x}{b}, \frac{y}{b}\right) \, dA \\
 &= \frac{b^2}{2} L'(\alpha, \beta) \cos\theta .
 \end{aligned} \tag{3.59}$$

The diffracted intensity distribution for the sinusoidal phase grating is therefore given by

$$I(\alpha, \beta) = \begin{cases} K \gamma E_o \hat{b}^4 \lambda^2 \sum_{m=-\infty}^{\infty} J_m^2\left(\frac{a}{2}\right) \text{Gaus}^2\left[\hat{b}\left(\alpha - \frac{m}{\hat{d}}, \beta\right)\right] & \text{for } \alpha^2 + \beta^2 \leq 1 \\ 0 & \text{for } \alpha^2 + \beta^2 > 1 \end{cases} \quad (3.60)$$

Figure 3-7 shows the diffracted intensity profile, predicted using equation 3.60, as a function of groove depth and diffraction angle for a sinusoidal reflection grating with period  $d = 1.95\lambda$ .

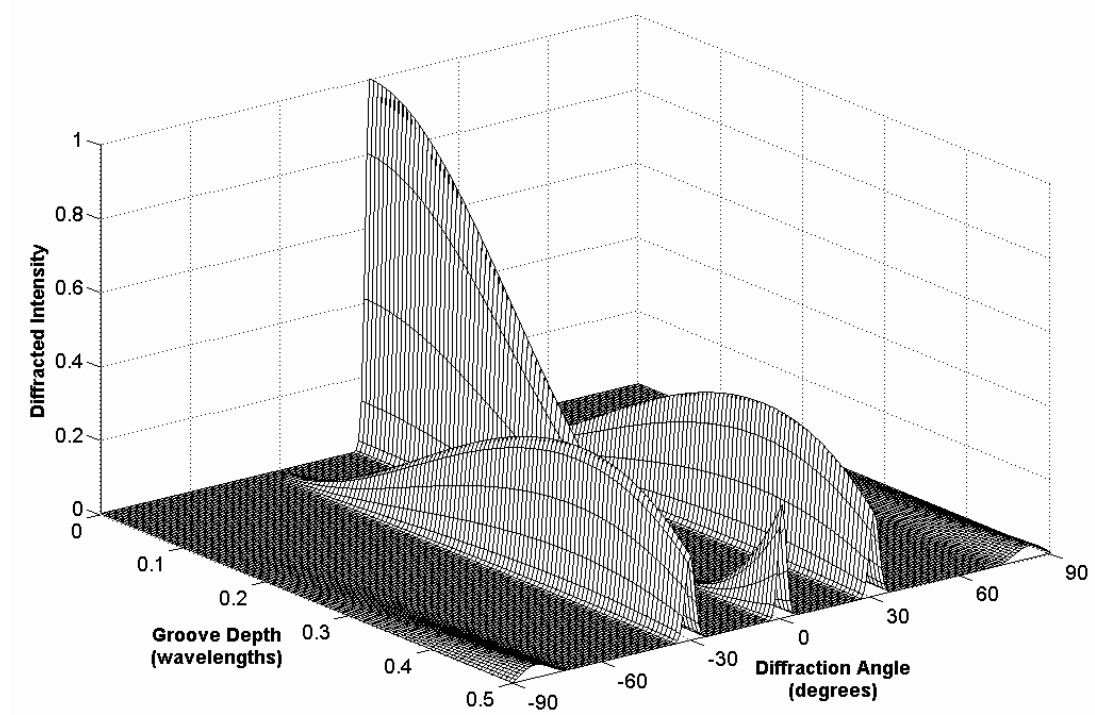


Figure 3-7: Diffracted intensity distribution profile predicted by our non-paraxial model for a sinusoidal reflection grating with a period of  $d = 1.95\lambda$



As Figure 3-7 shows, when plotted as a function of diffraction angle, the diffracted orders are no longer equally spaced, and they become progressively wider with increasing diffraction angle. In fact, for large diffraction angles the peak (or centroid) of the diffracted order is shifted from the position that is predicted by the grating equation, an effect that has been observed experimentally [101]. In addition, unlike the paraxial model, our non-paraxial model for diffracted intensity exhibits no discontinuities at  $\pm 90$  degrees. This is due to the factor  $\gamma = \cos\theta$  in equation 3.60, which causes the intensity to fall gracefully to zero as the diffraction angle approaches  $\pm 90$  degrees.

The paraxial and non paraxial models are compared directly in Figure 3-8 for a sinusoidal reflection grating with a period of  $d = 1.95\lambda$ , a groove depth of  $h = 0.5\lambda$ , and a normally incident Gaussian beam of radius  $b = 12\lambda$ . Note that the paraxial limitation inherent in equation 3.44 results in the prediction of seven propagating orders which are evenly spaced and of equal widths in angular space. This behavior violates the well-known grating equation. In addition, the paraxial intensity prediction exhibits a discontinuity at  $\pm 90$  degrees, and does not account for the redistribution of energy from evanescent orders to propagating orders. The non-paraxial scalar diffraction model does agree with the grating equation, exhibits a broadening of the high-angle diffracted orders (an experimentally observed reality), has a discontinuity at  $\pm 90$  degrees in the diffracted radiance, but not in the diffracted intensity, and redistributes energy from evanescent to propagating orders. Even the rather subtle shift of large-angle diffracted orders from the position predicted by the grating equation is readily observed.

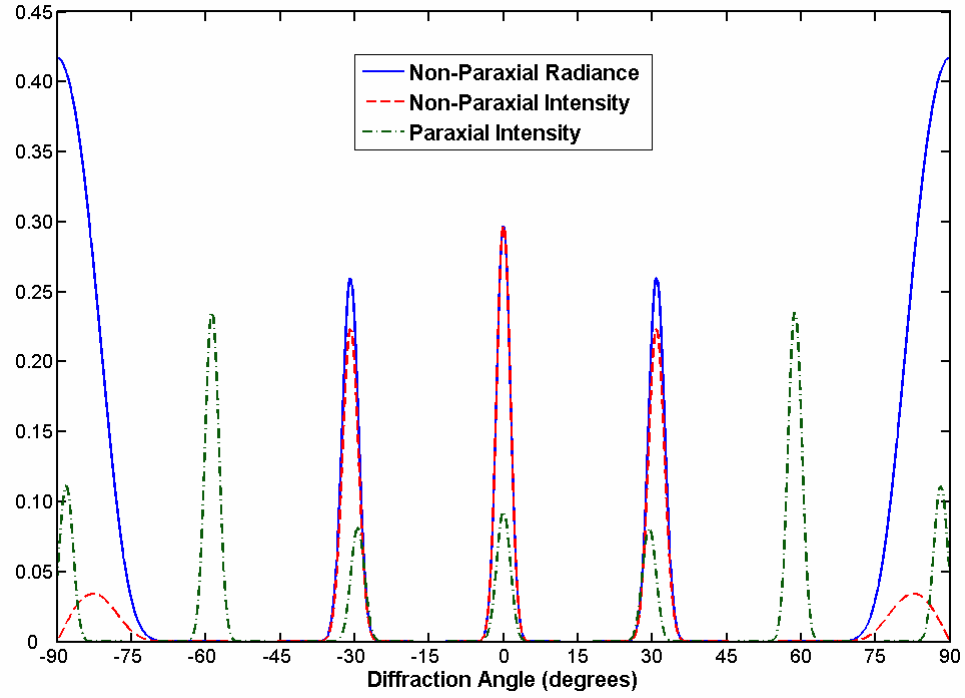


Figure 3-8: Comparison of wide-angle diffraction behavior of a sinusoidal reflection grating with a period of  $d = 1.95\lambda$ , and a groove depth of  $h = 0.5\lambda$  as predicted by scalar theory with and without a paraxial approximation.

Additional insight into the wide-angle behavior of sinusoidal phase gratings can be obtained by plotting the diffracted radiance profile as a function of grating period for a fixed groove depth. Figure 3-9 clearly illustrates the redistribution of energy from the evanescent orders into the propagating orders as the grating period varies from three wavelengths to one wavelength for a groove depth of  $h = 0.25\lambda$ . Note the modest increase in the zero order and the  $\pm 1$  orders when the  $\pm 2$  orders go evanescent. The rather bizarre spike in the diffracted radiance of the  $\pm 1$  orders is due to the finite width of the diffracted orders. The diffracted order does not go evanescent instantaneously (due to its finite width), but in a piecewise manner, one plane-wave component at a time. As

each plane-wave component goes evanescent, the diffracted radiance distribution function is re-normalized, and some of its energy gets redistributed back into the remaining propagating plane-wave components of that same diffracted order.

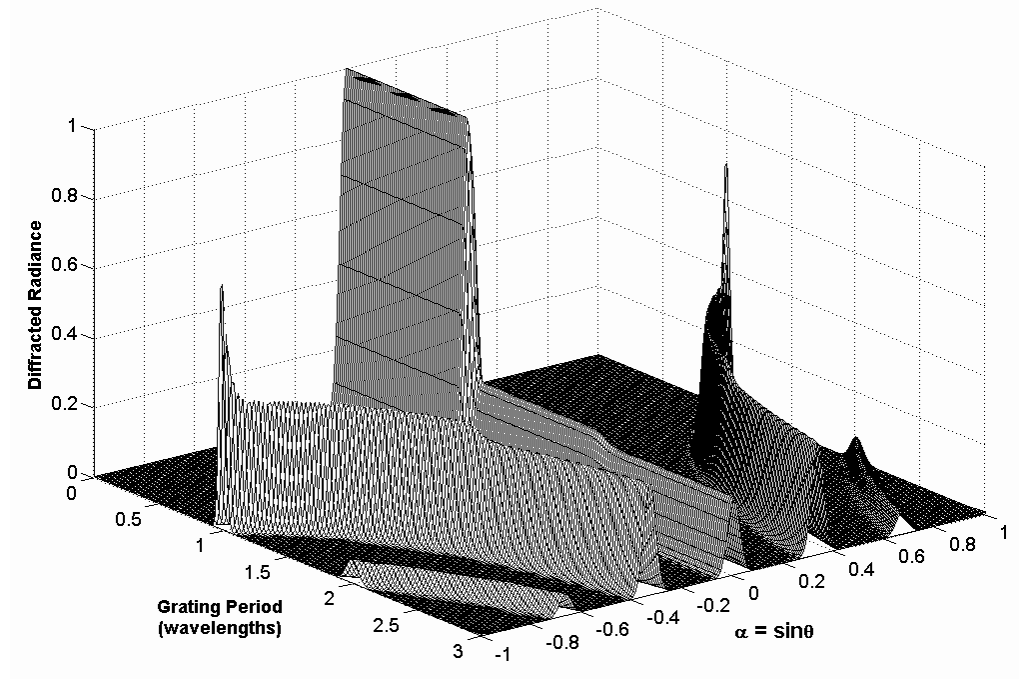


Figure 3-9: Diffracted radiance in direction cosine space as a function of grating period for a sinusoidal reflection grating of groove depth  $h = 0.25\lambda$  as predicted by our non-paraxial model

As shown in Figure 3-10, the corresponding intensity does not exhibit these spikes because of the effect of the factor  $\gamma = \cos \theta$  in equation 3.60, which always causes the intensity to fall to zero as the diffraction angle approaches  $\pm 90$  degrees.

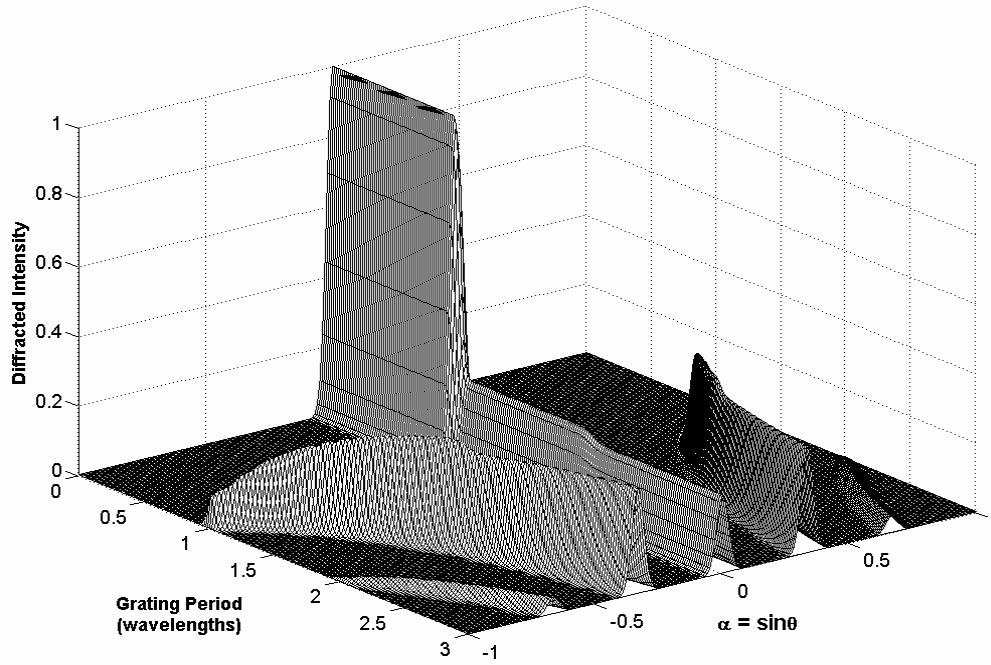


Figure 3-10: Diffracted intensity corresponding to the radiance distribution in Figure 3-9

### 3.4.3 Prediction Of Diffraction Efficiency

In the last section, we discussed the qualitative nature of radiance and intensity distributions as predicted by our non-paraxial diffraction model. We will now use the non-paraxial scalar theory to make quantitative predictions of diffraction efficiency for perfectly conducting sinusoidal phase gratings.

In a review article [104] on diffraction gratings, Maystre discussed a variety of rigorous vector theories including the Rayleigh method, the Waterman method, his own integral vector method, and other differential and modal methods. He presented a comparison of the diffraction efficiency (for TE polarization) of the first diffracted order for a perfectly conducting sinusoidal grating with  $h/d = 0.20$  in the Littrow condition (diffracted order propagating back along the direction of incident radiation) as calculated

by the classical Beckmann-Kirchhoff theory and his own rigorous integral vector theory. For this special case ( $\theta_m = -\theta_i$  in Maystre's sign convention), the Beckmann geometric factor [90] reduces to

$$F = \sec \theta_m \frac{1 + \cos(\theta_i + \theta_m)}{\cos \theta_i + \cos \theta_m} \approx \frac{1}{\cos^2 \theta_m}, \quad (3.61)$$

and the classical Beckmann-Kirchhoff theory predicts a diffraction efficiency of

$$\eta_m \approx \frac{J_m^2(2\pi h \cos \theta_m / \lambda)}{\cos^4 \theta_m}, \quad (3.62)$$

where  $h$  is the peak-to-peak amplitude of the sinusoidal grating surface profile.

The comparison between Maystre's rigorous vector theory and the Beckmann-Kirchhoff theory has been recreated in Figure 3-11. We have also added the paraxial scalar prediction of diffraction efficiency for sinusoidal phase gratings given by [13,105-107]

$$\eta_m = J_m^2\left(\frac{a}{2}\right) = J_m^2\left(\frac{2\pi h \cos \theta_i}{\lambda}\right). \quad (3.63)$$

The format of Figure 3-11 is commonly used to display diffraction efficiency data because the Littrow condition ( $\theta_m = \theta_i$  in our standard sign convention) allows one to leave the detector and the source fixed and to merely rotate the grating between measurements. Every data point in Figure 3-11 therefore requires a different incident angle. An angular deviation of 2-8 degrees between the source and detector is often used for convenience, thus not strictly satisfying the Littrow condition [108].

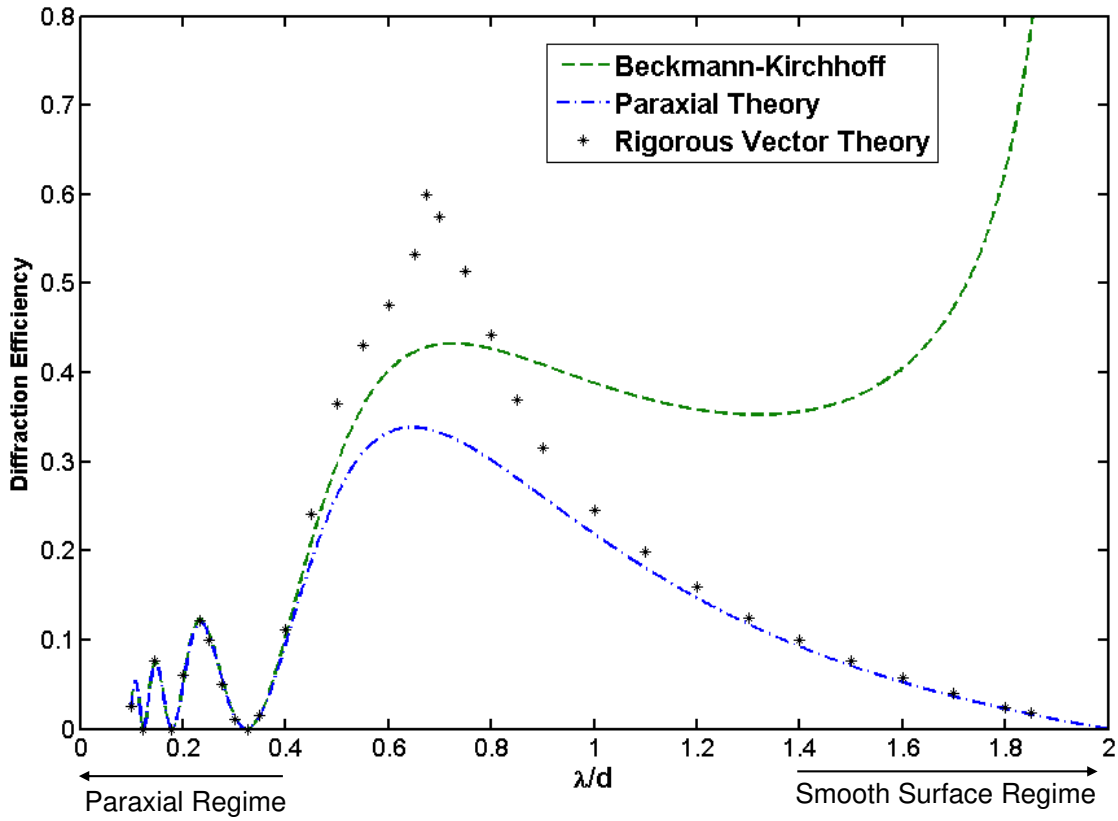


Figure 3-11: Diffraction grating efficiency of the first order for a sinusoidal phase grating ( $h/d = 0.2$ ) in the Littrow condition as predicted by the Beckmann-Kirchhoff theory, the paraxial scalar theory, and a rigorous integral vector theory.

For small values of  $\lambda/d$  in Figure 3-11, there are many diffracted orders, but those containing a significant amount of energy are diffracted at small angles as long as the groove depth is not too large. Therefore, the left edge of the curve is the paraxial regime. As the grating is rotated to increase  $\lambda/d$ , both the angle of incidence and the diffraction angles increase, and the higher diffracted orders start going evanescent. For the right two-thirds of the curves in Figure 3-11, there can be at most only two propagating orders, the zero order and the +1 order. All other orders are evanescent.

Note that all three theories in Figure 3-11 agree well for  $\lambda/d < 0.4$ , i.e. in the paraxial regime. The Beckmann-Kirchhoff theory is better than the paraxial theory for  $\lambda/d < 0.8$ , but diverges for values of  $\lambda/d > 1.5$ . The paraxial scalar theory agrees well not only in the paraxial regime, but also in the long wavelength region, i.e. the smooth surface regime. Although many authors state categorically that scalar theory can only be applied when  $\lambda/d < 0.1$ , they would probably concede that in the smooth surface regime, the higher orders of a sinusoidal phase grating contain a negligible fraction of the energy and the predicted efficiency is not significantly affected when those orders go evanescent. It is the central region of the diffraction efficiency curve for which the traditional paraxial scalar diffraction theory is totally inadequate.

To calculate diffraction efficiencies with our non-paraxial scalar theory, we can model either a uniformly illuminated grating of finite size, or we can model a small beam of some specific size and shape underfilling a large grating. In the first case the total radiant power being transmitted through the aperture is reduced by  $\cos\theta_i$ , while in the second case, the total transmitted radiant power remains the same, but the beam footprint in the plane of the grating is increased by  $\cos\theta_i$  and the radiant exitance emerging from the plane of the grating is reduced by  $\cos\theta_i$ . Both cases should yield the same results for diffraction efficiency, defined as the ratio of the radiant power in a given diffracted order to the radiant power in the incident beam, except for some minor discrepancies when diffracted orders of finite size go evanescent. Since we have already modeled the second case in the previous section, we will use that result as our starting point here.

Recall that the diffracted intensity predicted by our non-paraxial scalar model for a sinusoidal phase grating illuminated by a Gaussian beam of width  $b$ , period  $d$ , and peak-to-peak phase excursion  $a$  operating at normal incidence is given by equation 3.60 as

$$I(\alpha, \beta) = \begin{cases} K \gamma E_o \hat{b}^4 \lambda^2 \sum_{m=-\infty}^{\infty} J_m^2\left(\frac{a}{2}\right) \text{Gaus}^2\left[\hat{b}\left(\alpha - \frac{m}{\hat{d}}, \beta\right)\right] & \text{for } \alpha^2 + \beta^2 \leq 1 \\ 0 & \text{for } \alpha^2 + \beta^2 > 1 \end{cases} \quad (3.64)$$

For an arbitrary incident angle  $\theta_i$ , the propagating portion of the intensity distribution can be written as

$$I(\alpha - \alpha_o, \beta) = K \gamma E_o \hat{b}^4 \lambda^2 \sum_{m=-\infty}^{\infty} J_m^2\left(\frac{a}{2}\right) \text{Gaus}^2\left[\hat{b}\left(\alpha + \alpha_i - \frac{m}{\hat{d}}, \beta\right)\right], \quad (3.65)$$

where  $\alpha_i = \sin \theta_i$ . (3.66)

Using equation 3.36, the total power in the diffracted intensity distribution is given by

$$P_T = K E_o b^2 \sum_{m=\min}^{\max} J_m^2\left(\frac{a}{2}\right) \int_{-1}^1 \int_{-\sqrt{1-\alpha^2}}^{\sqrt{1-\alpha^2}} \hat{b}^2 \text{Gaus}^2\left[\hat{b}\left(\alpha + \alpha_i - \frac{m}{\hat{d}}, \beta\right)\right] d\alpha d\beta, \quad (3.67)$$

where the summation is taken only over the diffracted orders lying inside the unit circle in direction cosine space (i.e., the propagating diffracted orders). The quantity in the integral is simply a unit volume  $\text{Gaus}^2$  function. If  $\hat{b} \gg 1$ , the  $\text{Gaus}^2$  function is very narrow and we will assume that it lies entirely inside the unit circle, even for large



diffraction angles. The integral in equation 3.67 is therefore equal to unity and the total diffracted power can be written as

$$P_T = K E_o b^2 \sum_{m=\min}^{\max} J_m^2 \left( \frac{a}{2} \right). \quad (3.68)$$

The radiant power in a given diffracted order is therefore given by

$$P_m = K E_o b^2 J_m^2 \left( \frac{a}{2} \right). \quad (3.69)$$

Since we are assuming a perfectly conducting grating, the total diffracted power is equal to the total incident power, and the diffraction efficiency of the  $m^{\text{th}}$  diffracted order for our non-paraxial model is given by

$$\eta_m = \frac{P_m}{P_T} = \frac{J_m^2 \left( \frac{a}{2} \right)}{\sum_{m=\min}^{\max} J_m^2 \left( \frac{a}{2} \right)}. \quad (3.70)$$

Recall that the quantity  $a$  in 3.70 is the peak-to-peak phase variation introduced by the sinusoidal grating. Figure 3-12 illustrates that  $a$  varies not only with the angle of incidence but with the diffraction angle as well. It can therefore be written as

$$a = \frac{2\pi}{\lambda} (h_1 + h_2) = \frac{2\pi h}{\lambda} (\cos \theta_i + \cos \theta_m). \quad (3.71)$$

Equations 3.70 and 3.71 can now be used to calculate the diffraction efficiency of a perfectly conducting sinusoidal reflection grating.

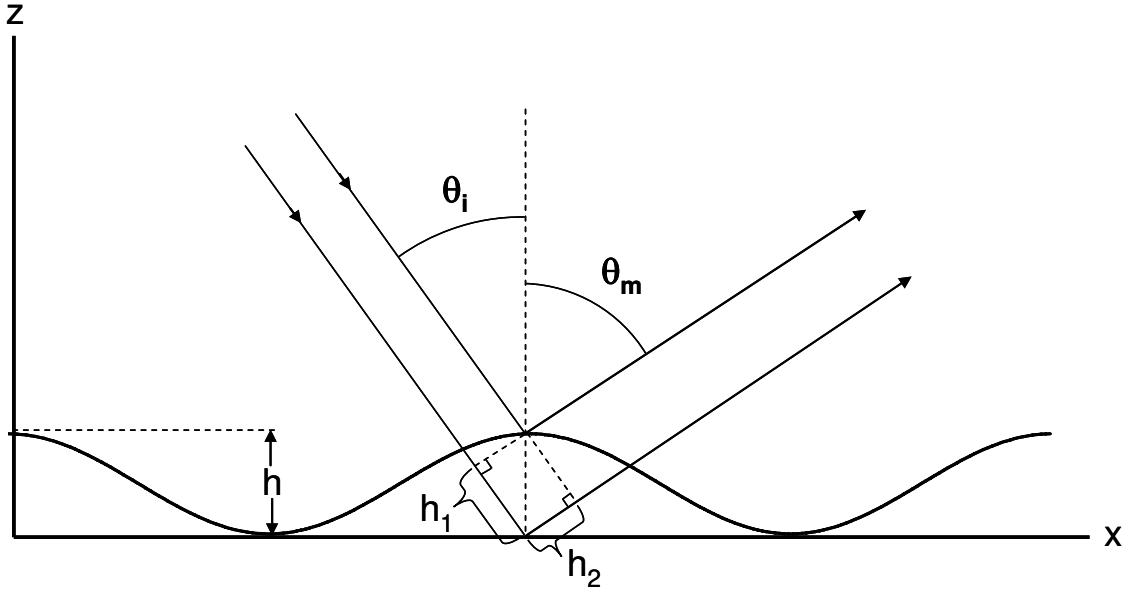


Figure 3-12: Illustration of the peak-to-peak phase variation introduced into a given diffracted order by reflection from a sinusoidal surface

The diffracted efficiency predicted by our non-paraxial model for a sinusoidal reflection grating with  $h/d = 0.2$  used in the Littrow condition is shown in Figure 3-13, where it is compared to the predictions previously shown in Figure 3-11. The non-paraxial scalar model provides remarkably good agreement with the rigorous vector theory, not merely in the paraxial regime and the smooth surface (shallow grating) regime, but over the entire range of  $\lambda/d$ .

Similar predictions for sinusoidal reflection gratings with  $h/d$  values of 0.05, 0.15, and 0.30 are shown in Figures 3-14, 3-15, and 3-16 respectively. The values for the rigorous vector theory in these figures were obtained from [99].

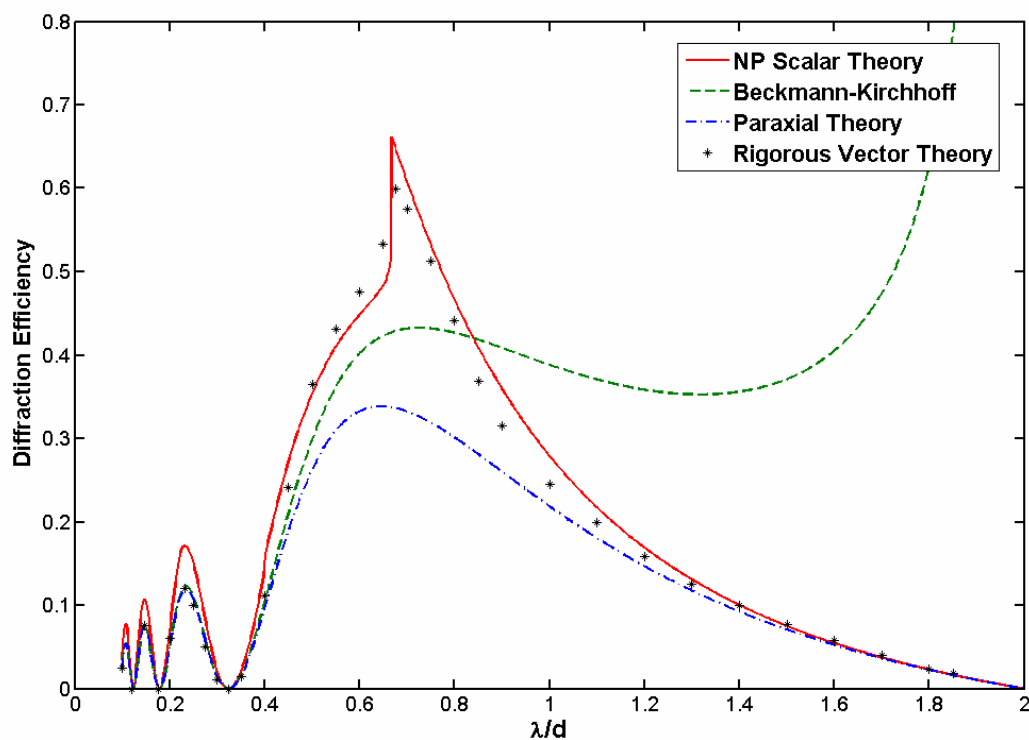


Figure 3-13: Diffraction grating efficiency of the first order for a perfectly conducting sinusoidal phase grating with  $h/d = 0.2$  used in the Littrow condition as predicted by the Beckmann-Kirchhoff theory, the paraxial scalar theory, our non-paraxial scalar theory, and a rigorous integral vector theory

As one would expect, Figure 3-14 shows that all of the theories agree quite well with the rigorous vector predictions for small values of  $h/d$ . The lone exception is the Beckmann-Kirchhoff theory which begins to depart from the other theories at around  $\lambda/d = 0.4$ , and exhibits rather bizarre behavior as  $\lambda/d$  approaches 2 due to the factor of  $\cos^4 \theta_m$  in equation 3.62.

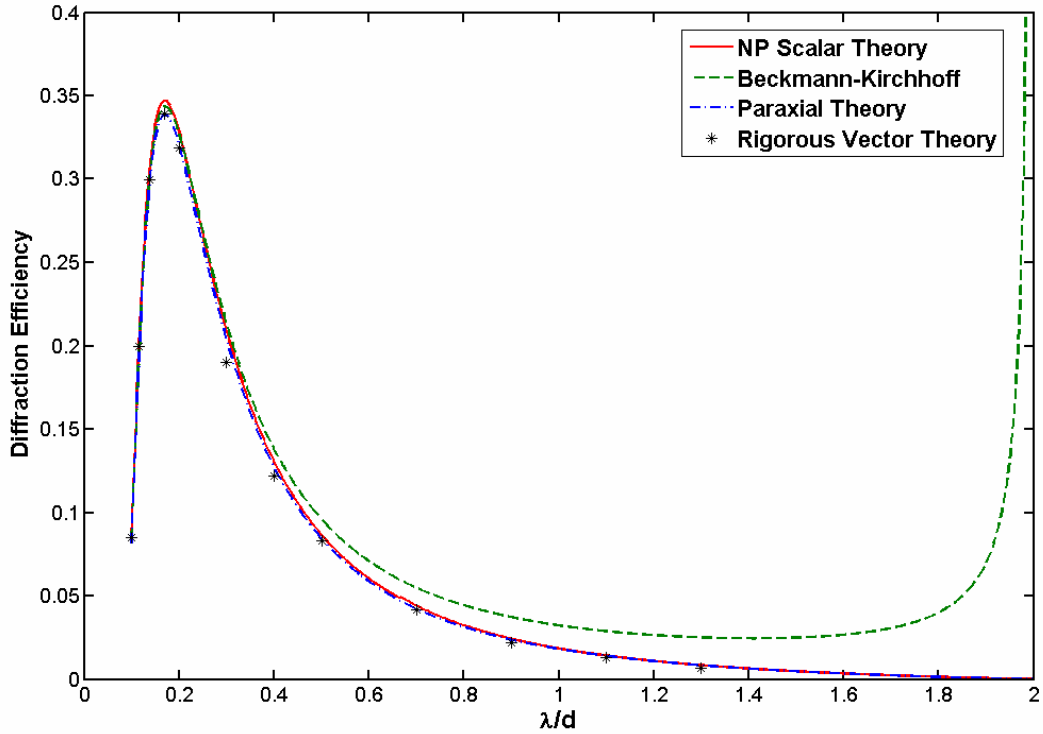


Figure 3-14: Diffraction grating efficiency of the first order for a perfectly conducting sinusoidal phase grating with  $h/d = 0.05$  used in the Littrow condition as predicted by the Beckmann-Kirchhoff theory, the paraxial scalar theory, our non-paraxial scalar theory, and a rigorous integral vector theory

Figure 3-15 continues to show good agreement between our non-paraxial scalar theory and the rigorous vector theory, but it also demonstrates that our non-paraxial model indeed predicts the Rayleigh anomalies[97,99,109] that occur when a propagating order goes evanescent. Note the abrupt increase in diffraction efficiency at  $\lambda/d = 0.67$ . This is precisely the value at which the -1 and +2 diffracted orders go evanescent.

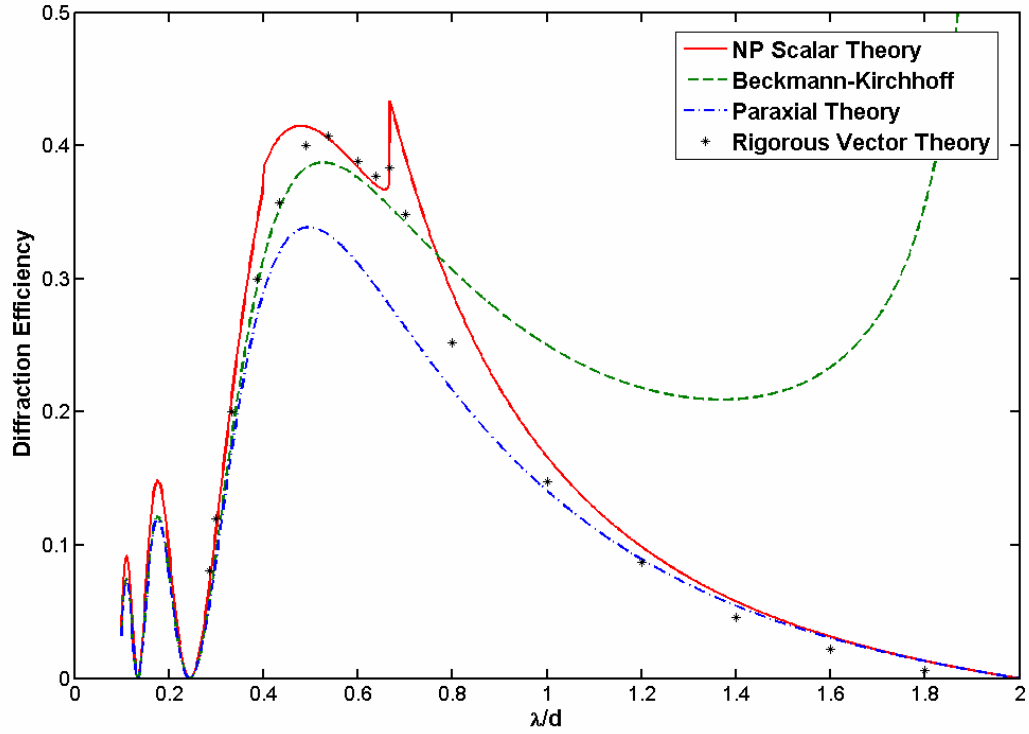


Figure 3-15: Diffraction grating efficiency of the first order for a perfectly conducting sinusoidal phase grating with  $h/d = 0.15$  used in the Littrow condition as predicted by the Beckmann-Kirchhoff theory, the paraxial scalar theory, our non-paraxial scalar theory, and a rigorous integral vector theory

Figure 3-16 shows that our non-paraxial scalar model continues to predict the major features of the diffraction efficiency curve even for an  $h/d$  value of 0.30. The diminishing agreement over the middle part of the  $\lambda/d$  range may be due to the fact that our model does not account for shadowing and multiple scattering effects. However, our non-paraxial model is still a large improvement over the classical paraxial theory. Note that both our non-paraxial model and the rigorous theory predict a maximum diffraction efficiency that approaches unity while the maximum of the paraxial theory is 0.3386.

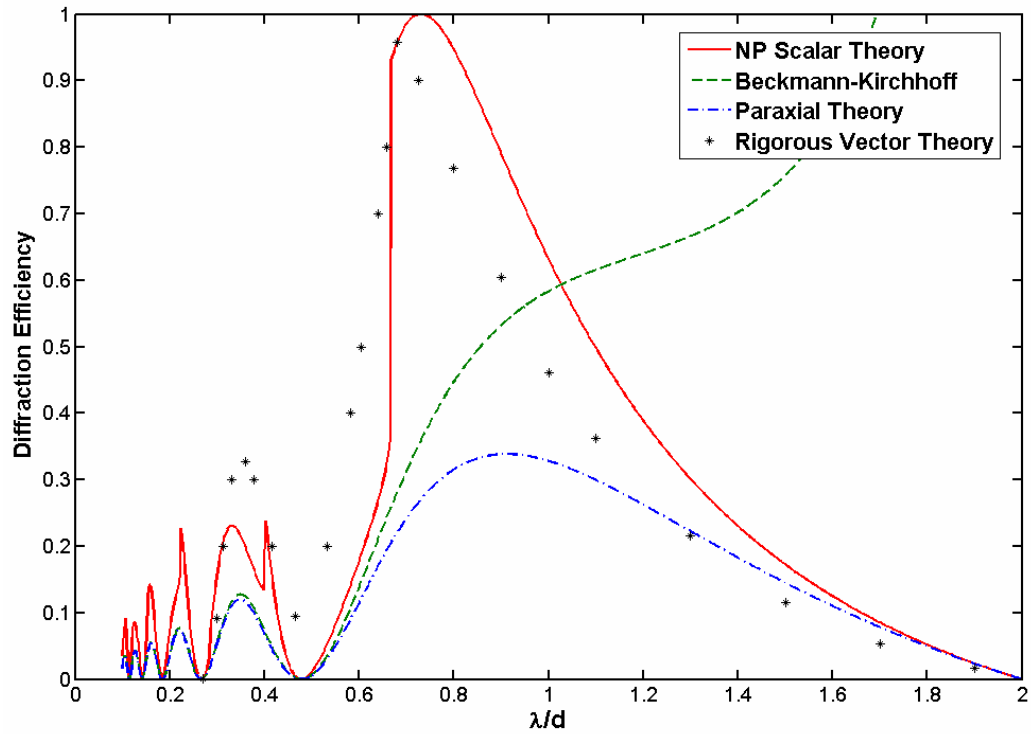


Figure 3-16: Diffraction grating efficiency of the first order for a perfectly conducting sinusoidal phase grating with  $h/d = 0.30$  used in the Littrow condition as predicted by the Beckmann-Kirchhoff theory, the paraxial scalar theory, our non-paraxial scalar theory, and a rigorous integral vector theory

There is a substantial difference in the peak values of the oscillatory behavior in the paraxial regime as predicted by the paraxial and the non-paraxial scalar theories in Figures 3-13, 3-15, and 3-16. The diffraction efficiency predicted by the non-paraxial scalar theory is given by equation 3.70. As  $\lambda/d$  becomes very small (paraxial regime), the number of diffracted orders becomes very large and the denominator of equation 3.70 approaches unity resulting in the well known paraxial result given by equation 3.63. Clearly for a finite number of propagating orders, the denominator is less than unity. This results in a higher value for the non-paraxial prediction compared to the paraxial result. Our non-paraxial model assumes that the energy previously contained in the evanescent orders is distributed uniformly over the remaining propagating orders. This may or may not be an accurate assumption. Additional rigorous data, or experimental results, are needed to quantitatively evaluate the deviation between the non-paraxial scalar theory and the rigorous theory in the paraxial regime.

## **CHAPTER 4: MODIFIED BECKMANN-KIRCHHOFF SURFACE SCATTER THEORY**

The development of a linear systems formulation of non-paraxial scalar diffraction phenomena discussed in chapter three indicating that *diffracted radiance* is a fundamental quantity predicted by scalar diffraction theory, and the fact that it was *scattered radiance* that was shown to exhibit shift-invariant behavior when presented in the proper format has led to a re-examination of the classical Beckmann-Kirchhoff scattering theory. In this chapter, we will demonstrate an empirically modified Beckmann-Kirchhoff theory that accurately predicts non-intuitive experimental scatter data for rough surfaces at large incident and large scatter angles, yet also agrees with Rayleigh-Rice predictions within its domain of applicability for smooth surfaces.

### **4.1 Non-Intuitive Surface Scatter Measurements**

A detailed experimental investigation of light scattering from well-characterized random surfaces was reported by O'Donnell and Mendez in 1987 [110]. The surfaces were made by first exposing photoresist to a laser speckle pattern, and then applying a gold coating. The surface autocovariance (ACV) function was almost a perfect Gaussian. The measured root-mean-square (RMS) surface roughness was  $\sigma_s = 2.27 \mu\text{m}$  and the measured autocovariance length ( $e^{-1}$  half-width of the ACV function) was  $\ell_c = 20.9 \mu\text{m}$ . For the small slopes represented by these parameters, multiple scattering effects are negligible. Conventional high angular resolution scattering data was measured for two wavelengths,  $\lambda = 0.6328 \mu\text{m}$  and  $\lambda = 10.6 \mu\text{m}$ , and two angles of incidence,  $\theta_i = 20$



degrees and  $\theta_i = 70$  degrees. At these wavelengths and incident angles, this surface is too rough to satisfy the Rayleigh-Rice smooth-surface requirement.

When the experimental scattered intensity measurements were compared with classical Beckmann-Kirchhoff scattering theory, several puzzling effects were observed. For a wavelength of  $10.6 \mu\text{m}$  and small angles of incidence, the Beckmann-Kirchhoff solution agrees quite well with the experimental data; however, the authors noticed a persistent tendency for the data to be narrower than the theoretical predictions. This can be seen in Figure 4-1, where the Beckmann-Kirchhoff theory is compared to experimental data obtained from [110]. This behavior is non-intuitive, as the presence of experimental error sources (jitter, turbulence effects, etc.) would tend to make the experimental curve broader than the theoretical curve. It was suggested by the authors that this minor departure might be due to a resonance effect since  $\ell \sim \lambda$ ; however, this was not verified. The total integrated scatter is given by [3]

$$TIS = 1 - \exp\left[-\left(4\pi \cos \theta_i \sigma_s / \lambda\right)^2\right]. \quad (4.1)$$

From equation 4.1, we find that there is no discernable specular beam for an incident angle of 20 degrees with a wavelength of  $10.6 \mu\text{m}$  as the total integrated scatter is almost unity.

For angles of incidence greater than 50 degrees, substantial disagreement between the theoretical predictions and experimental measurements was observed. For a wavelength of  $10.6 \mu\text{m}$  and an incident angle of 70 degrees, there is a specular beam containing over 40% of the reflected radiant power. The data points representing the

specular beam have been omitted from the experimental data shown in Figure 4-2. The peak of the measured scattering function does not lie in the specular direction, but instead lies approximately 10 degrees inside of the specular beam. The Beckmann-Kirchhoff theoretical prediction no longer exhibits symmetry about the specular direction, and shows a similar shift of the peak of the diffuse component of the scattered light distribution. The Beckmann-Kirchhoff prediction also contains an unphysical discontinuity at 90 degrees. The authors offered no explanation for this non-intuitive behavior.

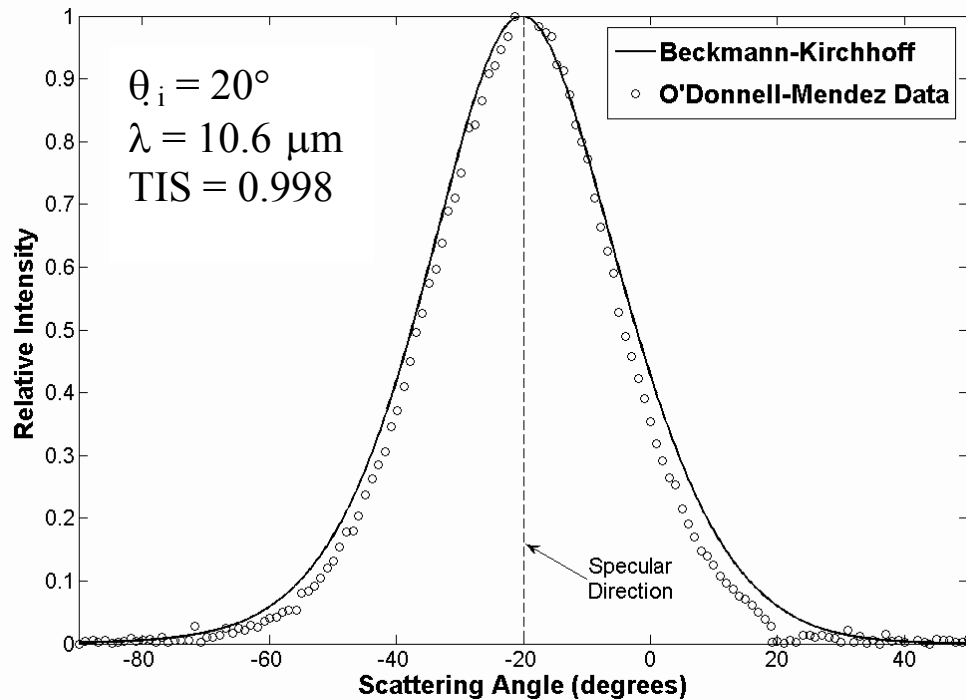


Figure 4-1: Classical Beckmann-Kirchhoff theory compared to O'Donnell-Mendez experimental data for  $\lambda = 10.6 \mu\text{m}$ ,  $\theta_i = 20^\circ$

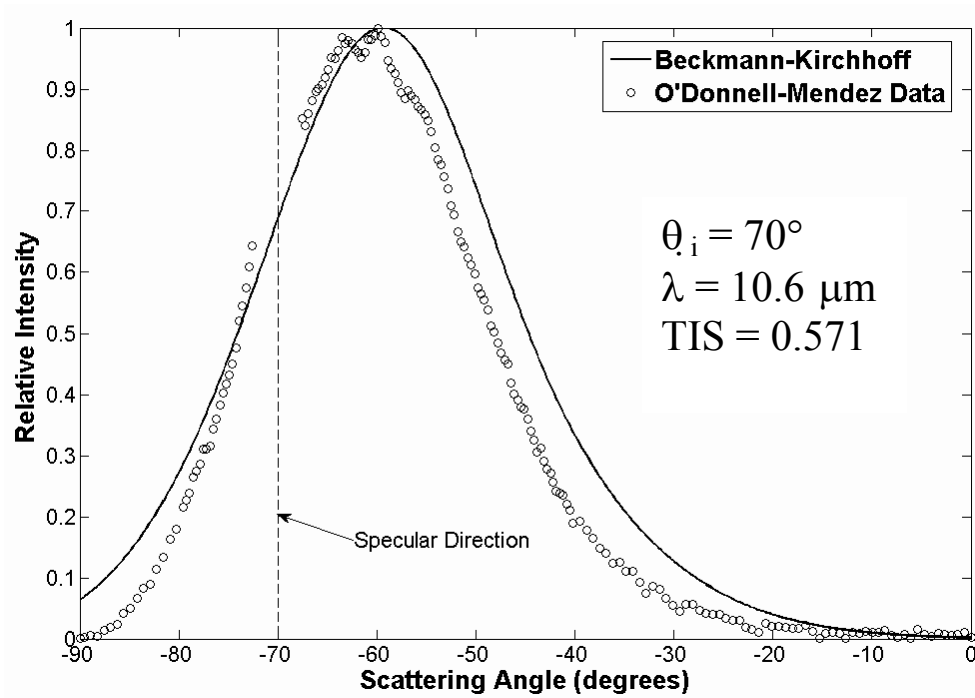


Figure 4-2: Classical Beckmann-Kirchhoff theory compared to O'Donnell-Mendez experimental data for  $\lambda = 10.6 \mu\text{m}$ ,  $\theta_i = 70^\circ$

In Figure 4-3 the Beckmann-Kirchhoff prediction is compared to experimental data for a wavelength of  $0.6328 \mu\text{m}$  and an incident angle of  $70^\circ$ . The experimental data is highly asymmetrical about the specular direction. There is no specular beam, however, as all of the light is diffusely scattered. The experimental data drops smoothly to zero at  $-90$  degrees. The classical B-K theory predicts a symmetrical intensity distribution about the specular direction, though it is unphysical in that it exhibits a discontinuity at  $-90$  degrees. The authors suggested that the failure of the Beckmann-Kirchhoff theory at this angle of incidence and wavelength is perhaps due to shadowing and multiple scattering

effects, and stated that they are unaware of any available theory that compares to their measured data.

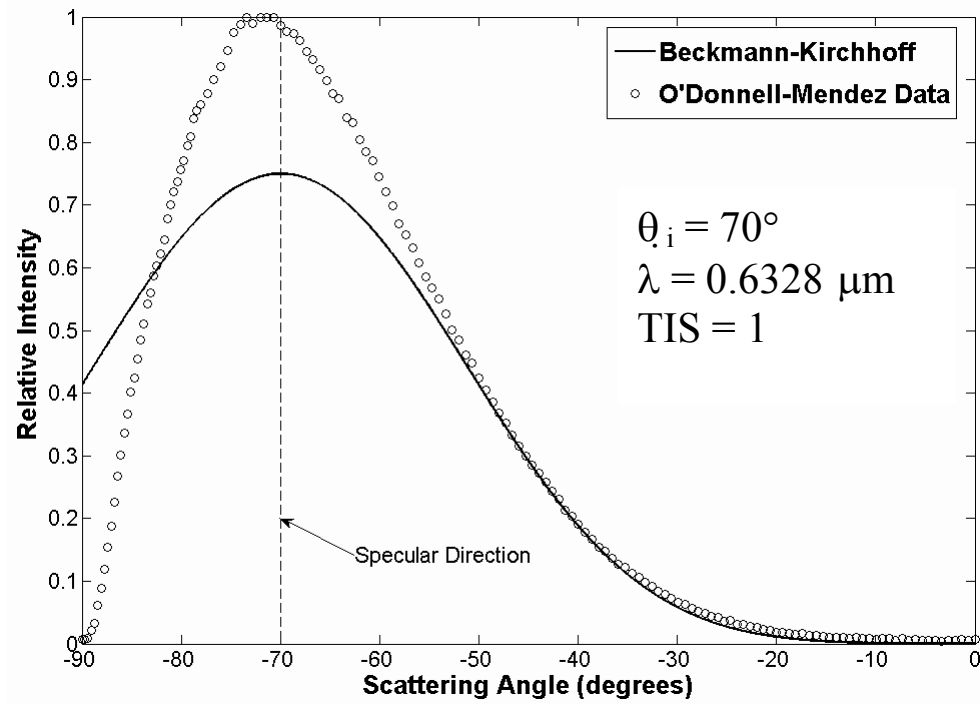


Figure 4-3: Classical Beckmann-Kirchhoff theory compared to O'Donnell-Mendez experimental data for  $\lambda = 0.6328 \mu\text{m}$  and  $\theta_i = 70^\circ$

## 4.2 Qualitative Explanation Of Non-Intuitive Effects

The Harvey-Shack surface scatter theory was discussed in section 2.2.4 of chapter two, and will be further elaborated on in chapter five. It will be used here briefly, however, to attempt to qualitatively explain the non-intuitive surface scatter measurements discussed in section 4.1.

The Harvey-Shack surface transfer function modified to account for radiation incident at an arbitrary angle is given by

$$H_s(\hat{x}, \hat{y}) = \exp \left\{ - \left( 4\pi \cos \theta_i \hat{\sigma}_s \right)^2 \left[ 1 - C_s(\hat{x}, \hat{y}) / \sigma_s^2 \right] \right\}, \quad (4.2)$$

where the “hats” indicate scaling by the wavelength, e.g.  $\hat{x} = x / \lambda$ , and  $C_s$  is the surface autocovariance function. For the surface described in section 4.1, the autocovariance function is Gaussian and is given by

$$C_s(\hat{x}, \hat{y}) = \sigma_s^2 \exp \left[ - \left( \frac{\hat{x}^2 + \hat{y}^2}{\ell_c^2} \right) \right], \quad (4.3)$$

with  $\sigma_s = 2.27 \text{ } \mu\text{m}$  and  $\ell_c = 20.9 \text{ } \mu\text{m}$  as stated previously. A radial plot of the autocovariance function is shown in Figure 4-4. As discussed in chapter two, the Fourier transform of the surface transfer function yields the angle spread function

$$ASF(\alpha, \beta) = \mathcal{F} \left\{ H_s(\hat{x}, \hat{y}; \gamma_i) \right\}, \quad (4.4)$$

which includes both the specular reflection and the diffuse scattering from the surface. The surface transfer function in equation 4.2 is defined as the normalized autocorrelation of the complex pupil function. From the autocorrelation theorem of Fourier transform theory [1], the angle spread function is therefore also given by the squared modulus of the Fourier transform of the complex pupil function. From equation 3.21, we thus know that the angle spread function is a scattered *radiance* distribution function. If any of the radiance distribution falls outside of the unit circle in direction cosine space, the radiance needs to be truncated and re-normalized as dictated by equation 3.29. To convert the

scattered radiance to intensity, we use equation 3.31, multiplying the radiance by  $\cos\theta$  and integrating over the illuminated area of the scattering surface:

$$I(\alpha, \beta) = \int_{A_s} L(\alpha, \beta) \cos\theta \, dA = L(\alpha, \beta) A_s \cos\theta. \quad (4.5)$$

Equations 4.2 through 4.5 can be used to predict the scattered radiance and intensity for the scattering surface described in section 4.1.

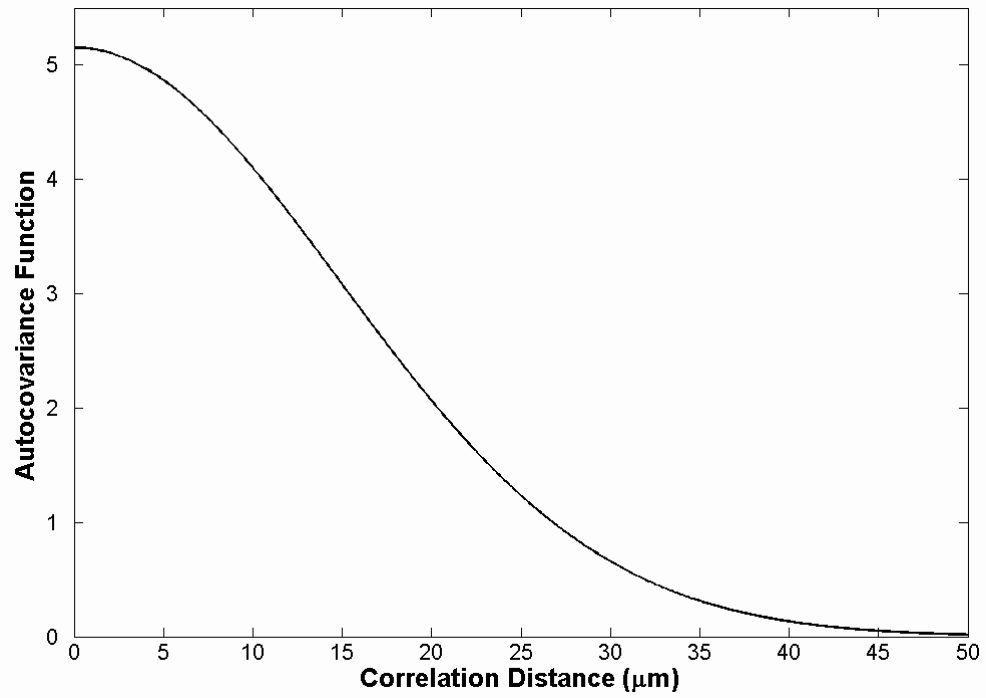


Figure 4-4:  $ACV$  of equation 4.3 with  $\sigma_s = 2.27 \, \mu\text{m}$  and  $\ell_c = 20.9 \, \mu\text{m}$

For small angles of incidence, applying equation 4.5 to the scattered radiance distribution will always result in an intensity distribution that is slightly narrower than the radiance distribution. An example of this is shown in Figure 4-5, which shows a comparison between scattered radiance and scattered intensity as predicted by the H-S theory for a  $10.6\text{ }\mu\text{m}$  wavelength beam normally incident upon the surface characterized by the autocovariance function of Figure 4-4. This behavior is similar to the persistent effect, noted by O'Donnell and Mendez, of the experimental scattering data being narrower than the Beckmann-Kirchhoff prediction for small incident angles.

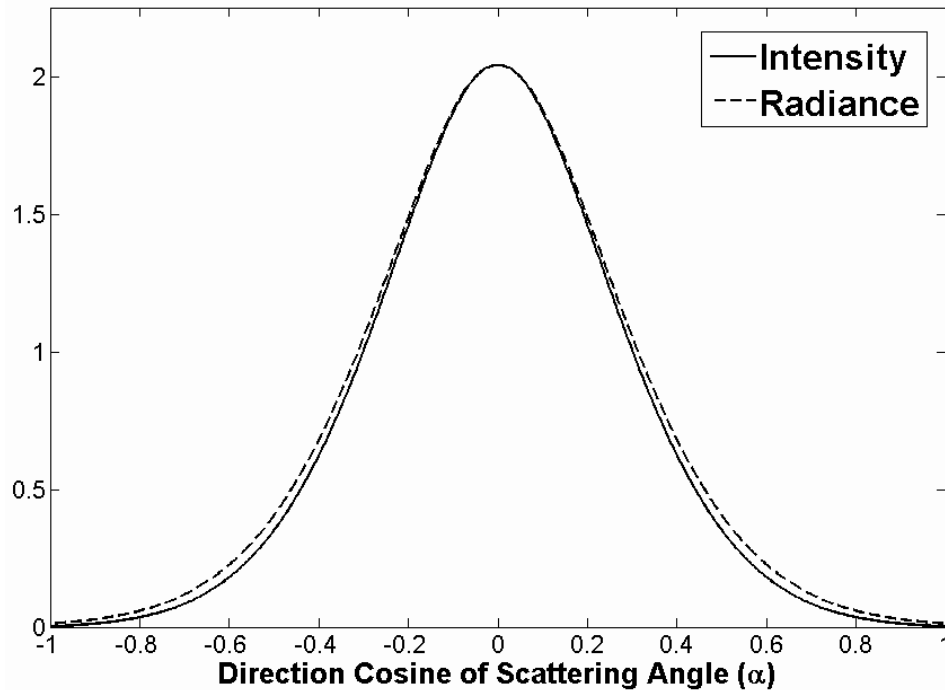


Figure 4-5: Harvey-Shack prediction of the scattered radiance and intensity distributions for the O'Donnell-Mendez surface with  $\theta_i = 0^\circ$  and  $\lambda = 10.6\text{ }\mu\text{m}$

For large angles of incidence, the Harvey-Shack scattered radiance function is substantially shifted, and abruptly truncated by the unit circle in direction cosine space. The scattered radiance and intensity as predicted by the Harvey-Shack theory are compared in Figure 4-6 for a  $10.6\text{ }\mu\text{m}$  wavelength beam at an incident angle of 70 degrees reflected from the scattering surface characterized by the autocovariance function of Figure 4-4. The scattered radiance distribution is discontinuous at  $-90$  degrees, as was the B-K prediction, but the application of equation 4.5 causes the scattered intensity to fall gracefully to zero at that angle. Applying equation 4.5 to the radiance also causes the peak of the intensity distribution to shift inside of the specular beam, similar to the experimental data in Figure 4-2.

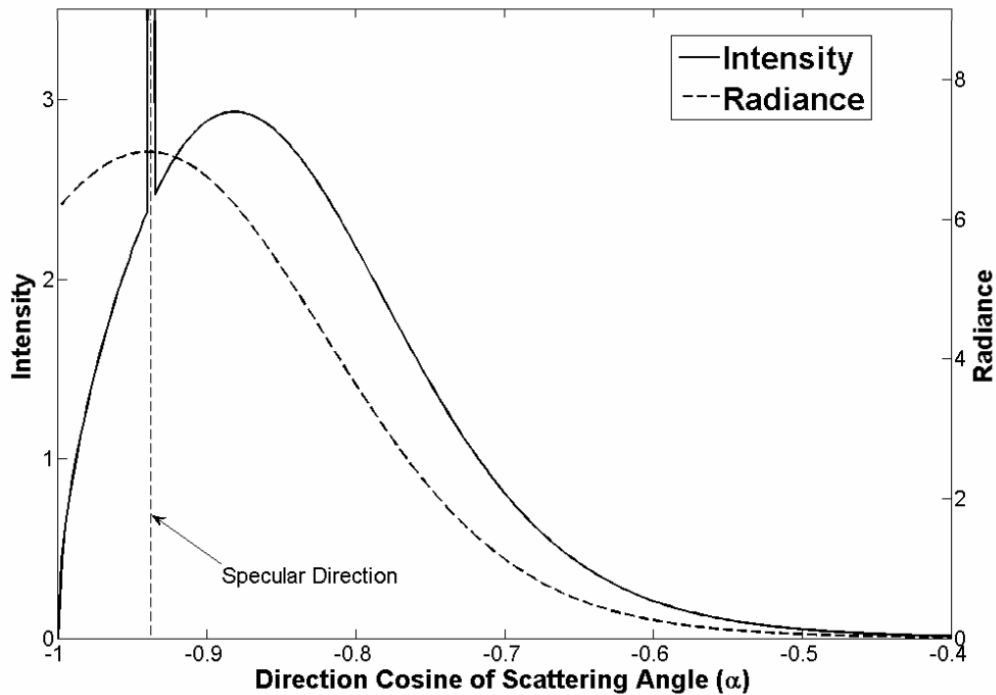


Figure 4-6: Harvey-Shack prediction of the scattered radiance and intensity distributions for the O'Donnell-Mendez surface with  $\theta_i = 0^\circ$  and  $\lambda = 10.6\text{ }\mu\text{m}$



The Harvey-Shack scattering predictions, at least qualitatively, seem to explain the non-intuitive scattering results of Figures 4-1, 4-2, and 4-3. Since the solid angle subtended by the collecting aperture of the scatterometer used by O'Donnell and Mendez was constant as they scanned the observation hemisphere, the voltage signal received from their instrument is indeed proportional to scattered intensity. However, the predictions from the Beckmann-Kirchhoff theory appear to be a better representation of scattered *radiance* than scattered *intensity*. This leads us to believe that the non-intuitive results of Figures 4-1, 4-2, and 4-3 might be the result of inappropriately comparing different radiometric quantities.

### 4.3 Empirical Modification Of The Beckmann-Kirchhoff Theory

The classical B-K theory that O'Donnell and Mendez used to predict the scattering in Figure 4-1 and Figure 4-2 was the closed-form solution valid only for Gaussian surface autocovariance functions given in [90] and outlined in section 2.2.3 of this dissertation. From equation 2.85, this closed-form solution is given by

$$D\{\rho\} = \frac{\pi \ell_c^2 F^2 \exp(-g)}{A_s} \sum_{m=1}^{\infty} \frac{g^m}{m!m} \exp\left(-\frac{v_{xy}^2 \ell_c^2}{4m}\right), \quad (4.6)$$

where  $A_s$  is the illuminated area of the scattering surface,  $\ell_c$  is the correlation length, and  $F$  is a geometrical factor defined in terms of incident and scattering angles in the spherical coordinate system as

$$F(\theta_i, \theta_s, \phi_s) = \frac{1 + \cos \theta_i \cos \theta_s - \sin \theta_i \sin \theta_s \cos \phi_s}{\cos \theta_i (\cos \theta_i + \cos \theta_s)}. \quad (4.7)$$

The function  $g$  in equation 4.6 is a measure of the phase variation introduced by an RMS surface roughness,  $\sigma_s$ , and is given by

$$g = \left( \frac{2\pi\sigma_s}{\lambda} \right)^2 (\cos \theta_i + \cos \theta_s)^2, \quad (4.8)$$

while  $v_{xy}$  is given by

$$v_{xy} = \left( \frac{2\pi}{\lambda} \right) \sqrt{\sin^2 \theta_i - 2 \sin \theta_i \sin \theta_s \cos \phi_s + \sin^2 \theta_s}. \quad (4.9)$$

If  $g \ll 1$ , the surface can be classified as smooth, and only the first term of the series in equation 4.6 needs to be used. For larger values of  $g$ , equation 4.6 needs to be used with enough terms to ensure that the series converges. If  $g \gg 1$ , the surface can be classified as very rough, and the series will converge very slowly. When this is the case, equation 2.90 can be used instead:

$$D\{\rho\} = \frac{\pi F^2 \ell_c^2}{A_s g} \exp\left(-\frac{v_{xy} \ell_c^2}{4g}\right), \quad (4.10)$$

where  $A_s$ ,  $\ell_c$ ,  $F$ ,  $g$ , and  $v_{xy}$  are the same as for the general case above.

The quantity  $D\{\rho\}$  in equations 4.6 and 4.9, which corresponds to the diffusely scattered light, is proportional to the time average of the squared modulus of the electric field vector and is called the mean scattered power by Beckmann and Spizzichino [90]. Many physicists would interpret this quantity to be proportional to radiant power density

on the collecting surface, and perhaps call it *intensity*. The geometrical factor  $F$  is an attempt to account for the fact that the local surface normal and mean surface normal of the scattering surface are not the same.

The insight provided by equations 3.30 and 3.29, in which diffracted radiance is presented as the fundamental quantity predicted by scalar diffraction theory, as well as the successful application of the non-paraxial scalar diffraction theory of chapter three to the calculation of diffraction grating efficiencies, and the qualitative success of the Harvey-Shack surface scatter theory in explaining the non-intuitive scattering behavior described in section 4.1 have all led to an empirical modification of the Beckmann-Kirchhoff scattering theory [111]. Three explicit modifications include: (i) eliminating the geometrical factor  $F^2$ ; (ii) introducing a renormalization factor, analogous to  $K$  in equation 3.29, which accounts for the re-distribution of radiant energy from the evanescent waves into the propagating waves; and (iii) equating the right side of equations 4.6 and 4.9 to scattered radiance.

Applying the modifications above to equation 4.6 results in the following expression of the *modified Beckmann-Kirchhoff scatter theory* for smooth or moderately rough surfaces with Gaussian autocovariance functions:

$$L(\theta_s, \phi_s) = K \frac{\pi \ell_c^2 \exp(-g)}{A_s} \sum_{m=1}^{\infty} \frac{g^m}{m!m} \exp\left(-\frac{v_{xy}^2 \ell_c^2}{4m}\right). \quad (4.11)$$

To obtain the scattered intensity distribution, we merely use equation 4.5, yielding

$$I(\theta_s, \phi_s) = K \pi \ell_c^2 \cos \theta_s \exp(-g) \sum_{m=1}^{\infty} \frac{g^m}{m!m} \exp\left(-\frac{v_{xy}^2 \ell_c^2}{4m}\right). \quad (4.12)$$

For very rough surfaces with Gaussian autocovariance functions, the *modified Beckmann-Kirchhoff scatter theory* is given by

$$L(\theta_s, \phi_s) = K \frac{\pi \ell_c^2}{A_s g} \exp\left(-\frac{v_{xy} \ell_c^2}{4g}\right). \quad (4.13)$$

Using equation 4.5 to convert from radiance to intensity yields:

$$I(\theta_s, \phi_s) = K \frac{\pi \ell_c^2}{g} \cos \theta_s \exp\left(-\frac{v_{xy} \ell_c^2}{4g}\right). \quad (4.14)$$

#### 4.4 Comparison With Experimental Measurements For Rough Surfaces

We will now use the modified Beckmann-Kirchhoff theory given by equations 4.12 and 4.14 to predict the scattering from the surface discussed in section 4.1 and compare it to both the classical Beckmann-Kirchhoff theory and the O'Donnell-Mendez experimental results.

Recall from section 4.1 that for a wavelength of 10.6  $\mu\text{m}$  and an incident angle of 20 degrees, almost all of the reflected light is scattered ( $TIS = 0.998$ ) and there is virtually no specular beam. In Figure 4-7, scattered intensity predictions from the modified Beckmann-Kirchhoff theory expressed by equation 4.12 are compared with the classical Beckmann-Kirchhoff theory and the experimental data from Figure 4-1. Since we only have one-dimensional experimental scattering profile data, we merely normalize the peak of the scattering function to unity, and label the curve relative intensity. For this modest 20 degree incident angle, the departure of the predictions from the classical Beckmann-

Kirchhoff and the modified Beckmann-Kirchhoff theories are not severe; however, the modified theory does more closely match the experimental data.

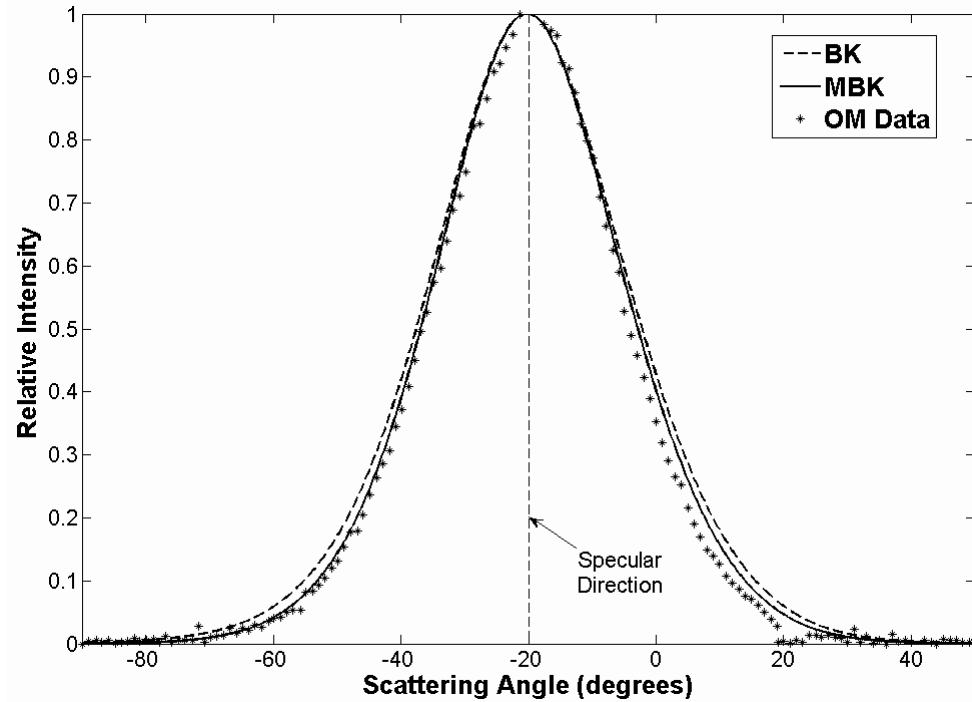


Figure 4-7: BK and MBK compared to experimental data for  $\lambda = 10.6 \mu\text{m}$  and  $\theta_i = 20^\circ$

For a 70 degree incident angle and a wavelength of  $10.6 \mu\text{m}$ , the departure between the experimental data and the prediction of the classical Beckmann-Kirchhoff theory in Figure 4-2 was significant. In addition, there was a particularly bothersome (non-physical) discontinuity in the predicted curve at a scattering angle of  $-90$  degrees. At this large incident angle, almost half of the reflected radiant power resides in the specular beam ( $TIS = 0.571$ ) and, as previously noted, the peak of the scattering function

is shifted approximately ten degrees from the specular direction. As seen in Figure 4-8, the modified Beckmann-Kirchhoff theory given by equation 4.12 once again more closely matches the experimental measurements, and it does not exhibit the non-physical discontinuity at a scattering angle of  $-90$  degrees.

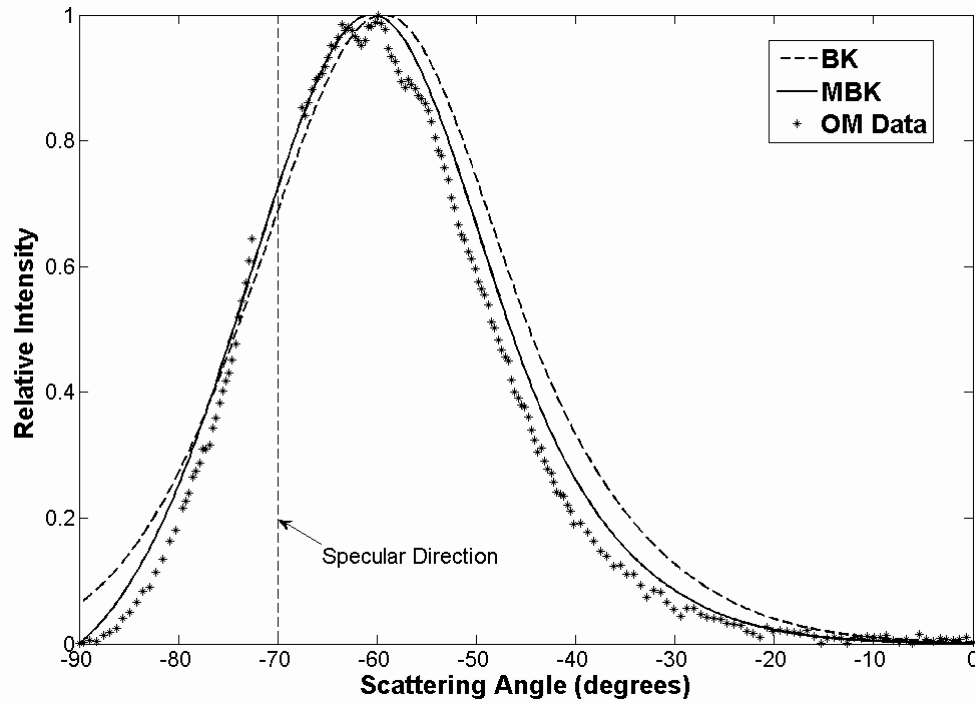


Figure 4-8: BK and MBK compared to experimental data for  $\lambda = 10.6 \mu\text{m}$  and  $\theta_i = 70^\circ$

For the much shorter wavelength of  $0.6328 \mu\text{m}$ , the O'Donnell-Mendez surface must be categorized as very rough as  $\sigma_s/\lambda = 3.59$ , and for  $\theta_i = 70$  degrees, the maximum value of  $g$  is approximately equal to 915. For such a rough surface, all of the incident light is scattered and there is no specular beam. Equation 4.12 will converge very slowly for this situation, and we can instead use the rough surface expression of equation 4.14.

In Figure 4-9, scattered intensity predictions from the modified Beckmann-Kirchhoff theory expressed by equation 4.14 are compared with the classical Beckmann-Kirchhoff theory and experimental data from Figure 4-3. We again normalized the peak of the modified Beckmann-Kirchhoff scattering profile to unity. For this short wavelength and a 70 degree incident angle, the departure between the predictions of the classical and the modified theory is quite dramatic. The classical Beckmann-Kirchhoff theory indicates a very significant (non-physical) discontinuity at a scattering angle of  $-90$  degrees and is clearly not capable of making accurate surface scatter predictions for very rough surfaces at these large incident angles. The empirically modified Beckmann-Kirchhoff theory, however, agrees extremely well with the experimental data.

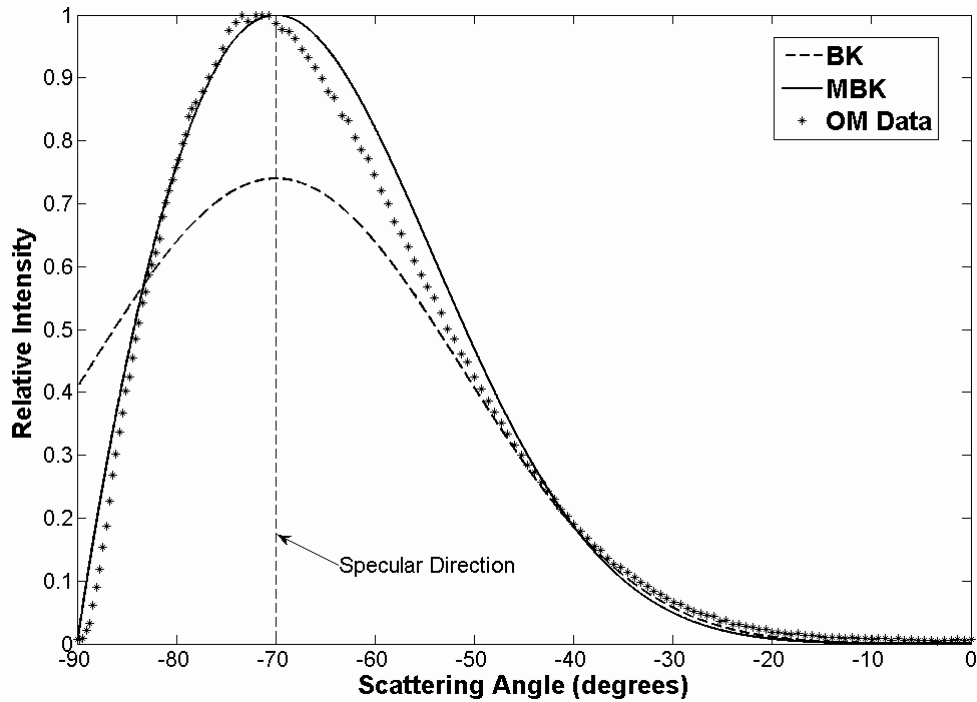


Figure 4-9: BK and MBK compared to experimental data for  $\lambda = 0.6328 \mu\text{m}$  and  $\theta_i = 70^\circ$

#### 4.5 Comparison With The Rayleigh-Rice Theory For Smooth Surfaces

The Rayleigh-Rice surface scatter theory discussed in section 2.2.2 has been widely accepted and extensively validated for smooth surfaces ( $\sigma_s/\lambda \ll 1$ ) even for large incident and scattering angles. We will therefore compare the modified Beckmann-Kirchhoff surface scatter theory with predictions from the Rayleigh-Rice theory for smooth surfaces.

From equation 2.39, the Rayleigh-Rice prediction of scattered intensity can be written as

$$I_{RR}(\theta_s, \phi_s; \theta_i) = P_i \frac{16\pi^2}{\lambda^4} \cos \theta_i \cos^2 \theta_s \mathcal{Q} PSD(f_x, f_y). \quad (4.15)$$

The dimensionless quantity  $\mathcal{Q}$  in equation 4.15 is the polarization dependent reflectance of the surface as discussed in section 2.2.2. For an infinitely conducting surface,  $\mathcal{Q} = 1$  in the plane of incidence. The  $PSD$  is the two-dimensional power spectral density of the scattering surface expressed in terms of spatial frequencies  $f_x$  and  $f_y$ . These spatial frequencies are related to incident and scattering angles in the spherical coordinate system by

$$f_x = \frac{\sin \theta_s \cos \phi_s - \sin \theta_i}{\lambda}, \quad f_y = \frac{\sin \theta_s \sin \phi_s}{\lambda}. \quad (4.16)$$

If we assume a Gaussian autocovariance function given by

$$ACV = \sigma_s^2 \exp\left[-(r/\ell_c^2)\right], \quad (4.17)$$



then the *PSD*, which is the two-dimensional Fourier transform of the *ACV*, is given by

$$PSD(f_x, f_y) = \pi \sigma_s^2 \ell_c^2 \exp \left[ -\pi^2 \ell_c^2 (f_x^2 + f_y^2) \right]. \quad (4.18)$$

Using equation 4.16, we can write the x-profile of equation 4.18 as

$$PSD(f_x) = \pi \sigma_s^2 \ell_c^2 \exp \left[ -\frac{\pi^2 \ell_c^2}{\lambda^2} (\sin \theta_s - \sin \theta_o)^2 \right]. \quad (4.19)$$

The intensity in the plane of incidence, as predicted by the Rayleigh-Rice theory is therefore given by

$$I_{RR}(\theta_s, \phi_s; \theta_i) = P_i \left( \frac{16\pi^3 \sigma_s^2 \ell_c^2}{\lambda^4} \right) \cos \theta_i \cos^2 \theta_s Q \exp \left[ -\frac{\pi^2 \ell_c^2}{\lambda^2} (\sin \theta_s - \sin \theta_o)^2 \right]. \quad (4.20)$$

We will assume a perfectly conducting surface so that  $Q = 1$ , and use equations 4.6, 4.12, and 4.20 to compare the classical Beckmann-Kirchhoff theory, the modified Beckmann-Kirchhoff theory, and the Rayleigh-Rice theory for several cases.

Figure 4-10 shows a comparison of the three theories for a smooth surface at normal incidence, and with  $\ell_c/\lambda = 2$ . This surface will produce a fairly narrow scattering function and, as the figure shows, all three theories predict essentially the same results.

In Figure 4-11, we retained the same RMS roughness and wavelength, but reduced the correlation length by a factor of five. These changes yield fairly wide-angle scattering, and the classical Beckmann-Kirchhoff theory starts to break down, exhibiting a non-physical discontinuity at  $\pm 90$  degrees. The modified Beckmann-Kirchhoff theory, on the other hand, continues to agree extremely well with the Rayleigh-Rice theory.

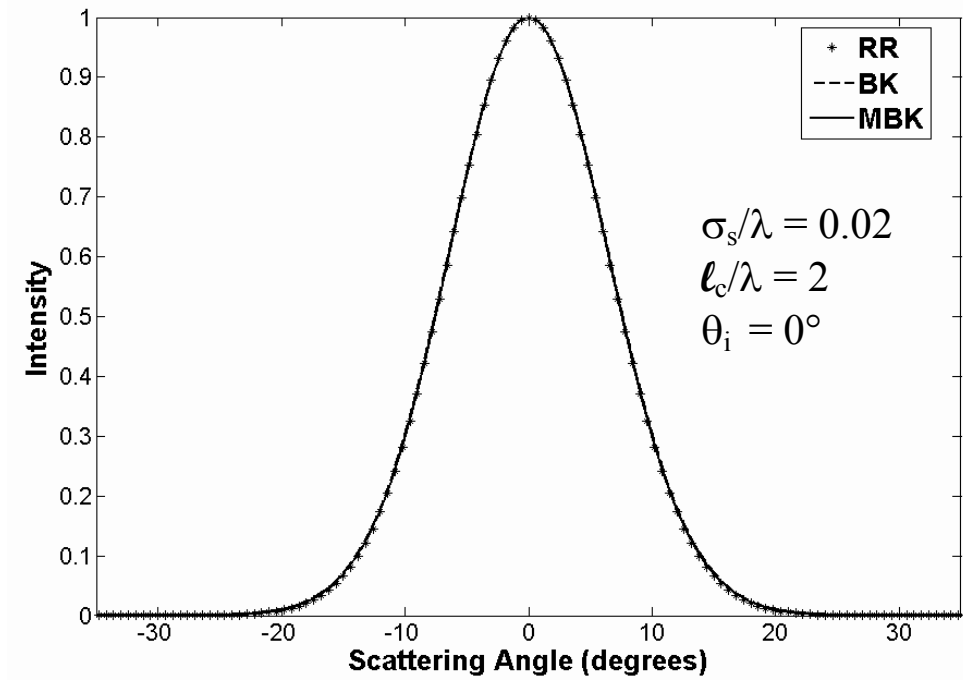


Figure 4-10: BK, MBK, and RR compared for a smooth surface at normal incidence and with small scattering angles

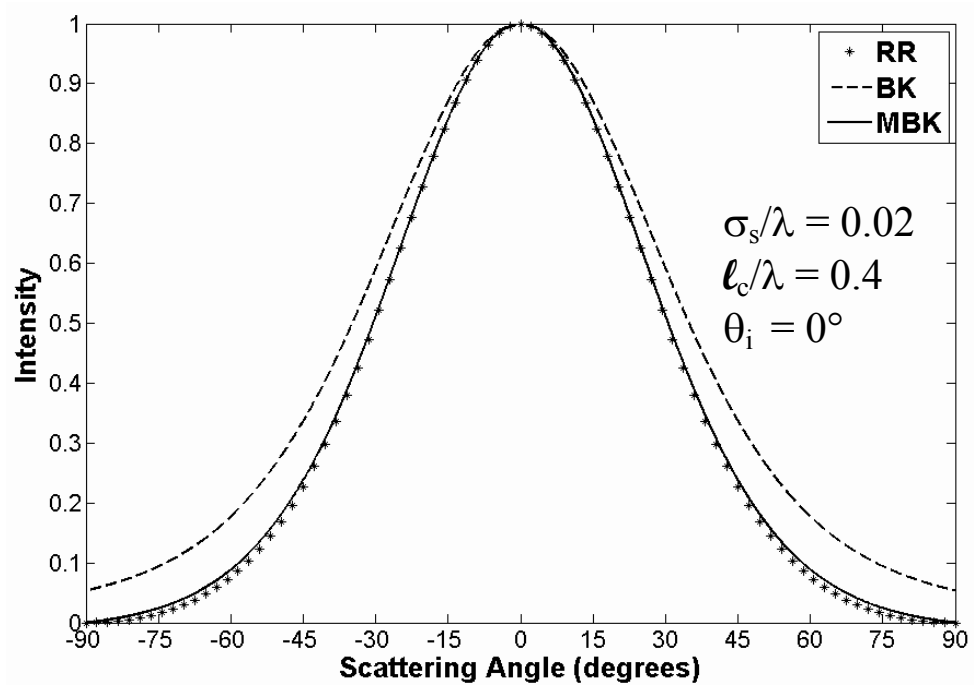


Figure 4-11: BK, MBK, and RR compared for a smooth surface at normal incidence and with large scattering angles

In Figures 4-12, 4-13, and 4-14, the classical Beckmann-Kirchhoff, modified Beckmann-Kirchhoff, and Rayleigh-Rice theories are compared for incident angles of 20, 50, and 70 degrees and  $\ell_c/\lambda$  ratios of 5, 1, 0.5, and 0.25.

For the 20 degree angle of incidence in Figure 4-12, all three theories agree very well for  $\ell_c/\lambda = 5$  and  $\ell_c/\lambda = 1$ . For  $\ell_c/\lambda = 0.5$ , the departure of the classical Beckmann-Kirchhoff theory from the others becomes significant, and it exhibits a discontinuity at  $-90$  degrees. For  $\ell_c/\lambda = 0.25$ , the disagreement between the classical Beckmann-Kirchhoff and the other two theories is quite severe, with discontinuities at both  $\pm 90$  degrees. The peak of the classical Beckmann-Kirchhoff theory is also shifted slightly away from the peaks of the other two theories and towards zero degrees. The modified Beckmann-Kirchhoff and Rayleigh-Rice theories agree extremely well at this incident angle for all values of  $\ell_c/\lambda$ , except for very small differences at larger scattering angles for the smaller correlation lengths. Note that the peaks of all three theories shift away from the specular beam and towards zero degrees as  $\ell_c/\lambda$  decreases.

For the 50 degree incident angle in Figure 4-13, all three theories again yield virtually identical results for  $\ell_c/\lambda = 5$ . The disagreement between the classical Beckmann-Kirchhoff theory and the other two theories is more significant for the rest of the values of  $\ell_c/\lambda$  than it was for the 20 degree incident angle. We can also see that the peak of the classical Beckmann-Kirchhoff prediction increasingly shifts away from the peaks of the other two theories as the correlation length is decreased. The agreement between the modified Beckmann-Kirchhoff theory and the Rayleigh-Rice theory continues to be excellent, again except for some very small differences at larger angles.

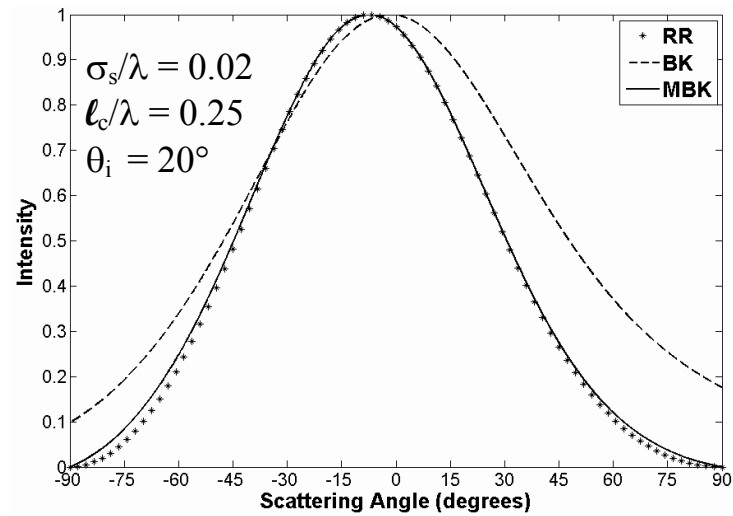
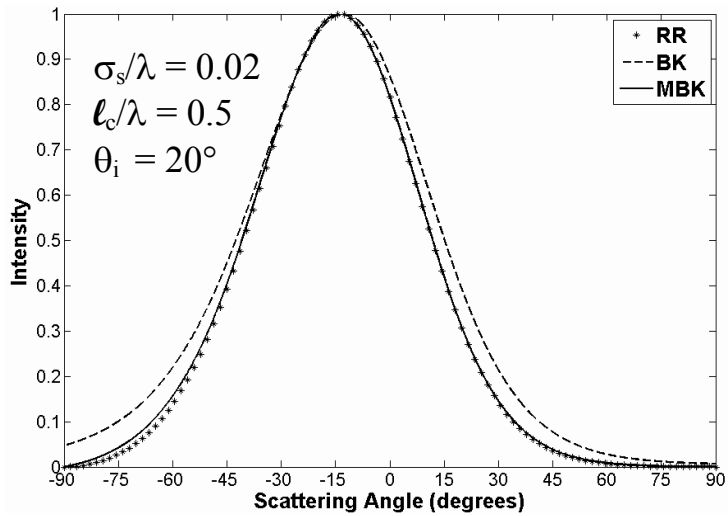
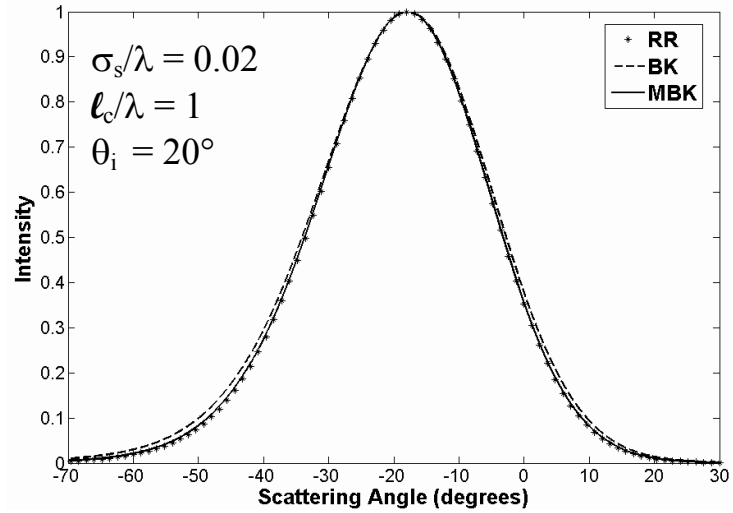
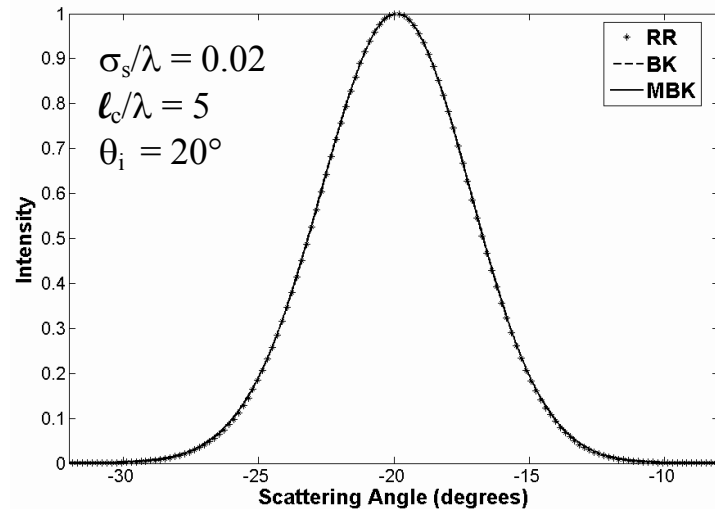


Figure 4-12: BK and MBK compared to RR for  $\theta_i = 20^\circ$ ,  $\sigma_s/\lambda = 0.02$ , and  $\ell_c/\lambda = 5, 1, 0.5$ , and  $0.25$

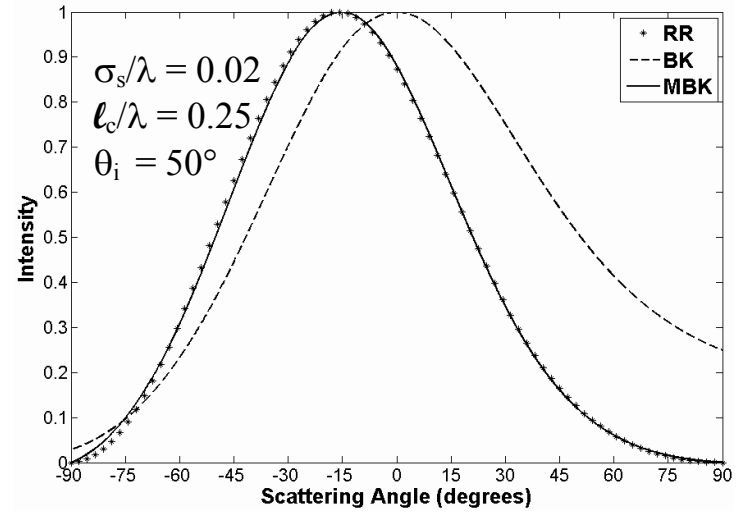
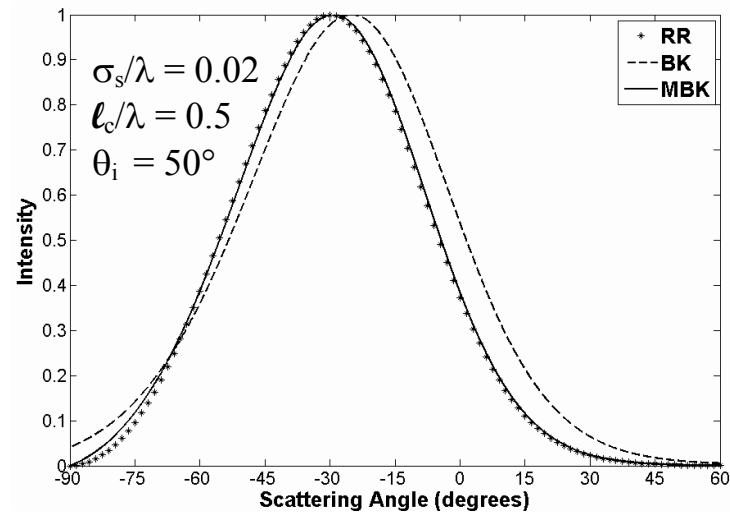
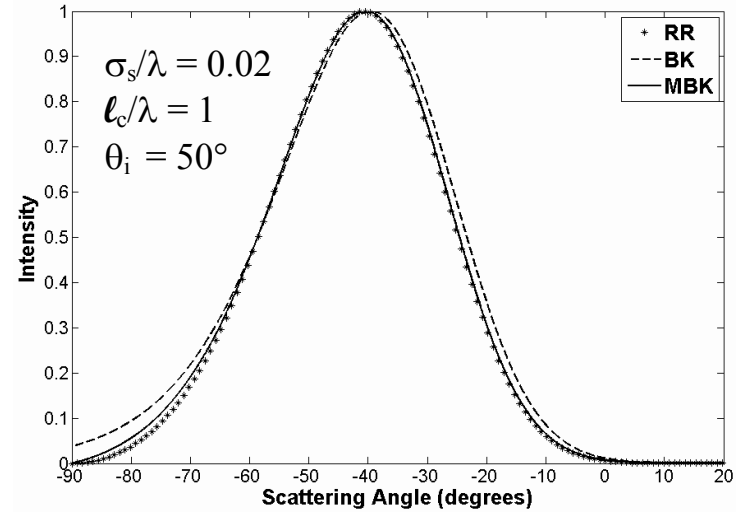
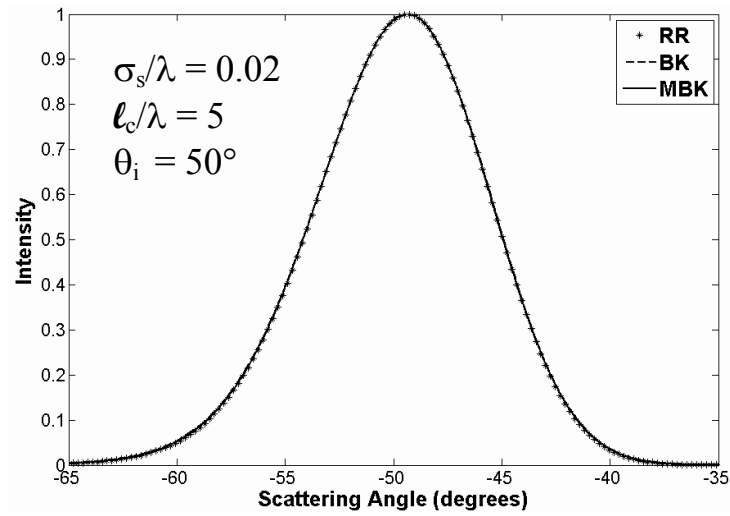


Figure 4-13: BK and MBK compared to RR for  $\theta_i = 50^\circ$ ,  $\sigma_s/\lambda = 0.02$ , and  $\ell_c/\lambda = 5, 1, 0.5$ , and  $0.25$

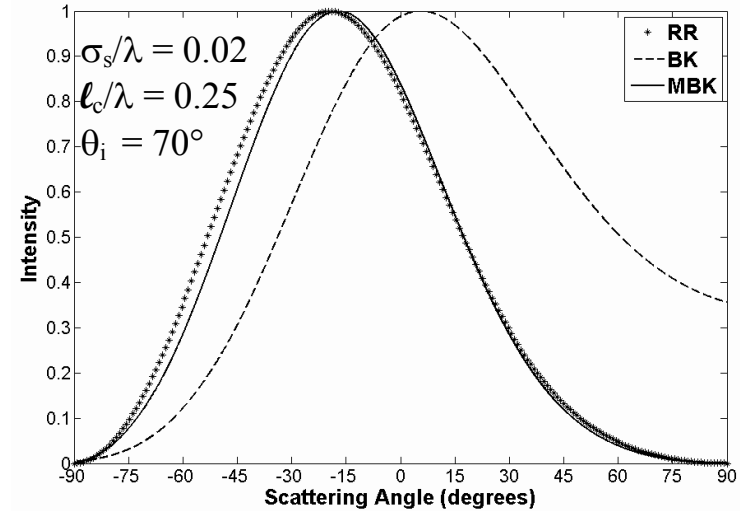
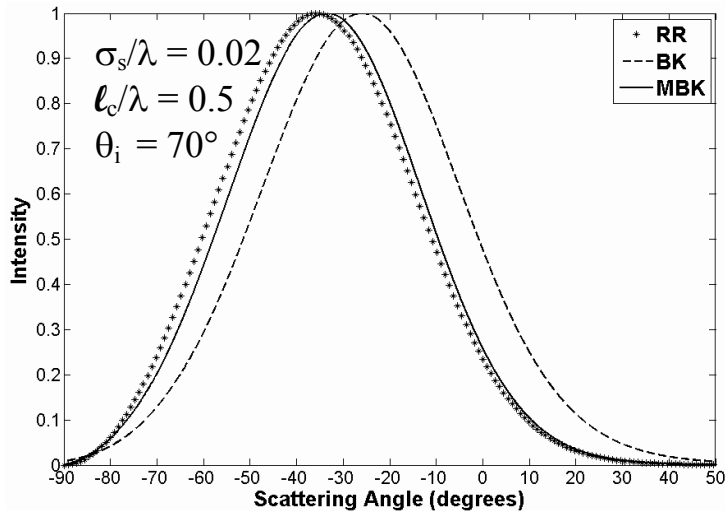
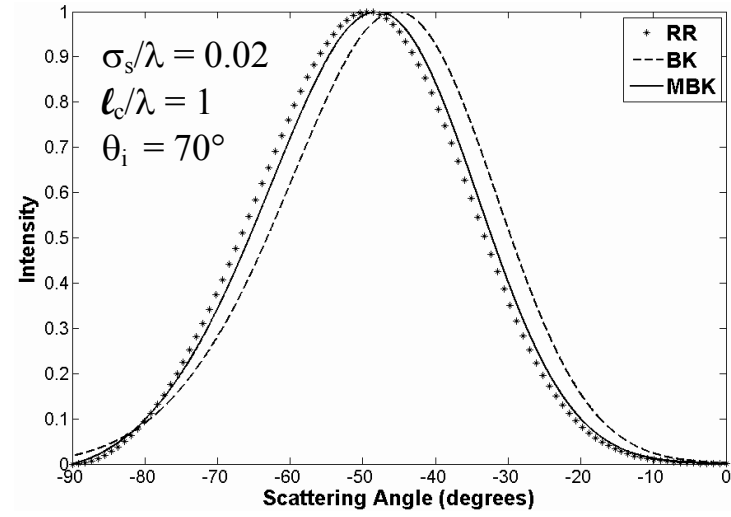
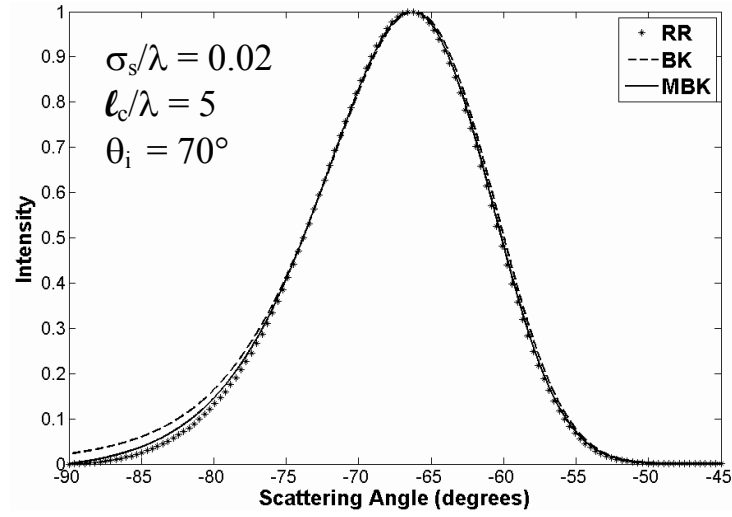


Figure 4-14: BK and MBK compared to RR for  $\theta_i = 70^\circ$ ,  $\sigma_s/\lambda = 0.02$ , and  $\ell_c/\lambda = 5, 1, 0.5$ , and  $0.25$

For the 70 degree angle of incidence in Figure 4-14, the disagreement between the classical Beckmann-Kirchhoff theory and the other two theories is worse than it was for the smaller incident angles. For  $\ell_c/\lambda = 5$ , it agrees fairly well with the predictions of the other two theories, except for small differences at large negative scattering angles and a discontinuity at  $-90$  degrees. The disagreement of the classical Beckmann-Kirchhoff theory with the other two theories becomes increasingly worse as  $\ell_c/\lambda$  is decreased. The modified Beckmann-Kirchhoff theory again agrees extremely well with the Rayleigh-Rice theory for this angle of incidence. For  $\ell_c/\lambda$  values of 1, 0.5, and 0.25 the modified Beckmann-Kirchhoff prediction is shifted slightly from the Rayleigh-Rice prediction. Compared to the shift of the classical Beckmann-Kirchhoff theory, however, the shift of the modified Beckmann-Kirchhoff theory is relatively minor.

The modified Beckmann-Kirchhoff theory is obviously a significant improvement over the classical Beckmann-Kirchhoff theory. The disagreement between the classical theory and the Rayleigh-Rice theory becomes increasingly significant with both decreasing correlation length and increasing incident angle. The modified theory, on the other hand, agrees extremely well with the Rayleigh-Rice theory for both large incident angles and large scattering angles (i.e. small correlation lengths).

#### **4.6 Range Of Validity Of The Modified Beckmann-Kirchhoff Equations**

In the derivation of his scattering theory, Beckmann provided [90] some general criteria for when to use each of the closed-form equations. When  $g \ll 1$  (smooth surfaces), he suggested that one need only use the first term of the infinite series in

equation 4.6. For  $g \approx 1$  (moderately rough surfaces), he stated that equation 4.6 could be used with an appropriate number of terms. And for  $g \gg 1$  (very rough surfaces), he derived the approximation given by equation 4.9.

But how much smaller than one does  $g$  need to be in order for a surface to be considered smooth? How much larger than one does  $g$  need to be in order for a surface to be rough? And for moderately rough surfaces, what constitutes an appropriate number of terms? We will now take a closer look at these roughness regimes and try to gain a better understanding of when it is appropriate to use each of the equations that make up the Beckmann-Kirchhoff theory. Note from equation 4.8 that for a given incident angle,  $g$  is actually a function of the scattering angle. When we discuss  $g$  as a parameter in the following analysis, we refer to its maximum value which always occurs at a scattering angle of zero degrees.

#### ***4.6.1 Smooth Surface Approximation***

For smooth surfaces, only the first term of equation 4.12 needs to be used, as all higher terms should be negligible. To determine what constitutes a “smooth” surface, we can compare predictions using equation 4.12 with many terms to predictions using equation 4.12 with only one term for various values of the parameter  $g$ . Examples of this are shown in Figure 4-15 for four values of  $g$ . The angle of incidence was assumed to be zero degrees, the quantity  $\ell/\lambda$  was assumed to be unity, and the RMS roughness,  $\sigma_s$ , was varied to obtain the different values of  $g$ . The smooth approximation is the result of using one term in equation 4.12, while 50 terms were used to obtain the general result.



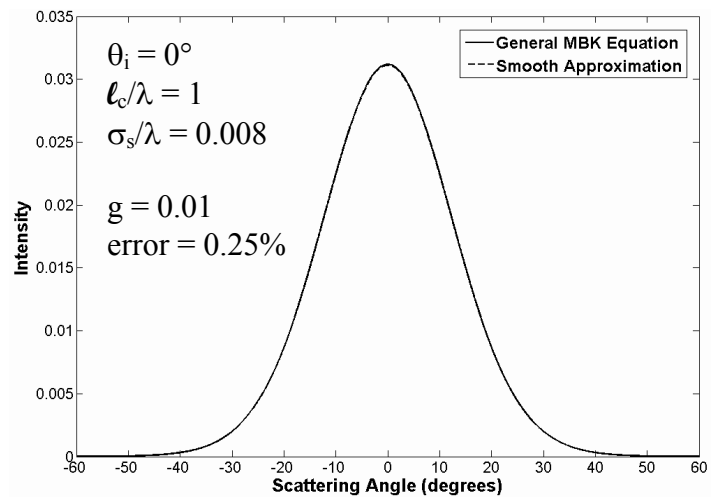
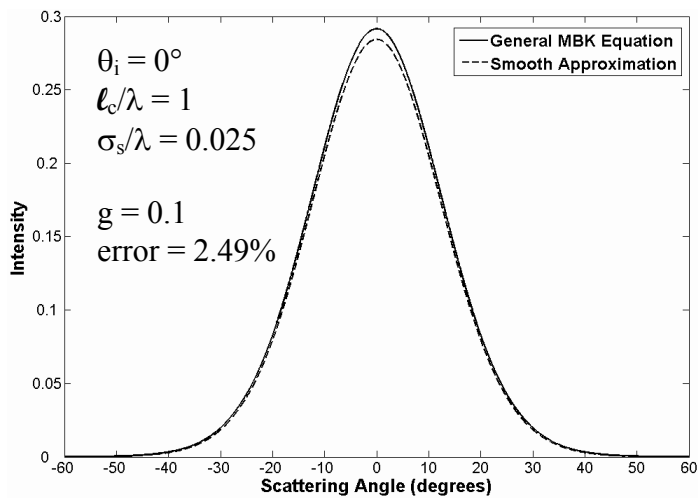
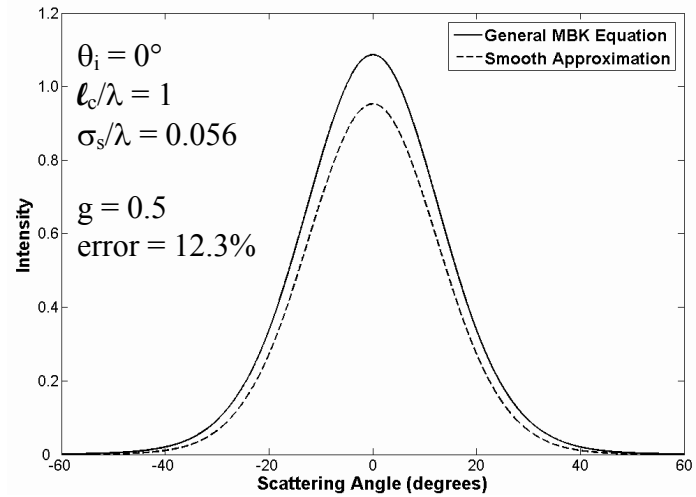
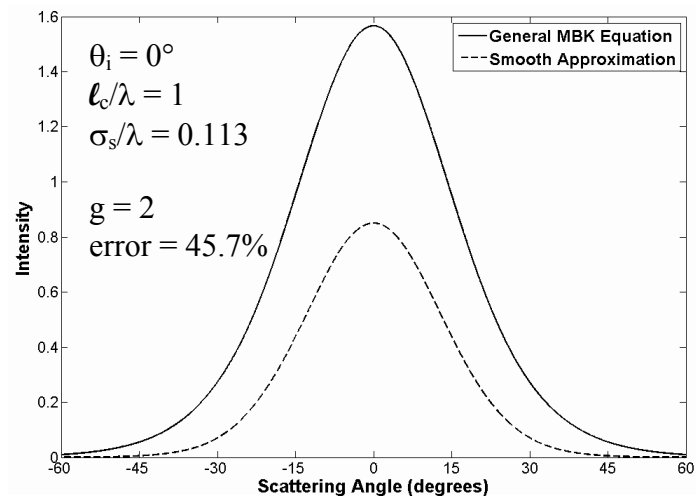


Figure 4-15: Comparison between the general MBK solution using 50 terms in equation 4.12 and the MBK smooth surface approximation of using only one term in equation 4.12 for  $g = 2, 0.5, .1$ , and  $0.01$

We can see from Figure 4-15, that as  $g$  is decreased and the smooth surface approximation gets closer to the general result, the largest discrepancy between the two results occurs at their peaks. Because of this behavior, we decided that the maximum error between the two predictions was a better measure of the validity of the approximation than some other quantity, such as RMS error. The maximum error in Figure 4-15 ranges from 45.7% for  $g = 2$  to 0.25% for  $g = 0.01$ . Calculations of the maximum error were performed over a range of  $g$  values from 0 to 0.5 for several incident angles. These results are shown in Figure 4-16.

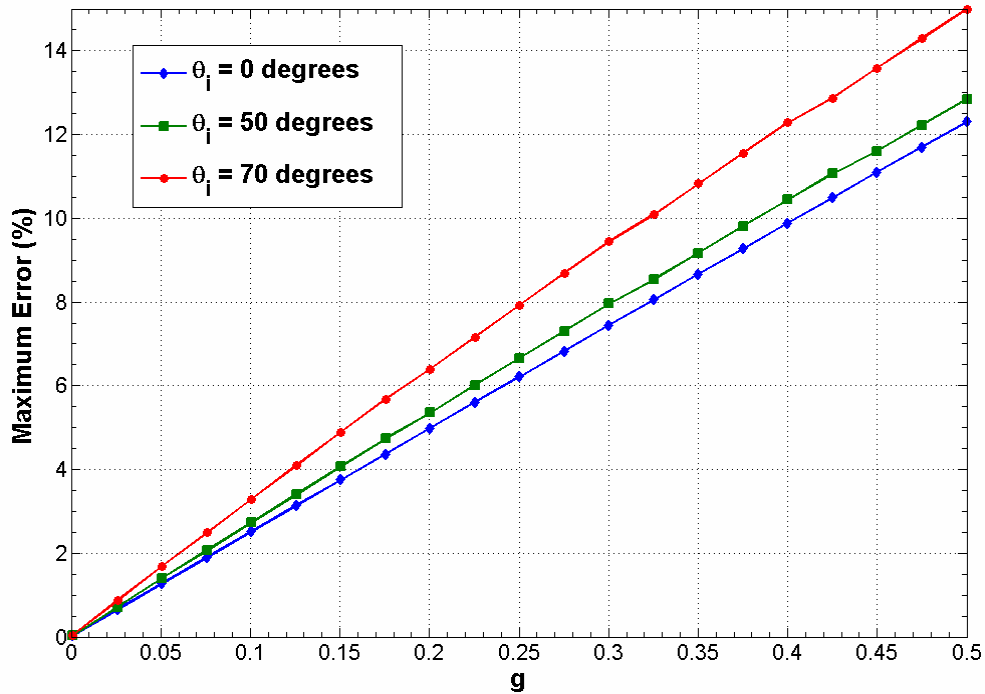


Figure 4-16: Maximum error between the general MBK solution using 50 terms in equation 4.12 and the MBK smooth approximation using 1 term in equation 4.12 as a function of  $g$  for  $\theta_i = 0^\circ$ ,  $50^\circ$ , and  $70^\circ$

As seen in Figure 4-16, the maximum error between the general solution of the modified Beckmann-Kirchhoff theory and the smooth surface approximation varies linearly with the parameter  $g$ . We can also see that the slope of this linear relationship increases with increasing incident angle. Determining the value of  $g$  for which the smooth approximation is valid depends on how much error can be tolerated. A tolerance of 2% on the maximum error, for instance, would allow one to use the smooth surface approximation when  $g$  is less than 0.05 for incident angles less than 70 degrees.

#### ***4.6.2 Moderately Rough Surfaces***

For surfaces that cannot be classified as either smooth ( $g \ll 1$ ) or very rough ( $g \gg 1$ ), the general modified Beckmann-Kirchhoff solution of equation 4.12 needs to be used with an appropriate number of terms. We therefore want to determine how the number of terms needed varies with the parameter  $g$ .

We will first create a quantity we call Term Importance (TI), which will be defined as the value of a single term of equation 4.12 divided by the sum of all terms in equation 4.12. In other words, the Term Importance of the  $n^{\text{th}}$  term is given by

$$TI(\theta_s, \phi_s, n) = \frac{\frac{g^n}{n!n} \exp\left(-\frac{v_{xy}^2 \ell_c^2}{4n}\right)}{\sum_{m=1}^{\infty} \frac{g^m}{m!m} \exp\left(-\frac{v_{xy}^2 \ell_c^2}{4m}\right)}. \quad (4.21)$$

Note that since  $v_{xy}$  is a function of scattering angle, Term Importance is also a function of scattering angle. Therefore equation 4.21 represents the fraction of the total scattered

intensity contributed by the  $n^{\text{th}}$  term for a given scattering angle. It is important to realize that the number of terms ( $m$ ) used to calculate the denominator of equation 4.21 needs to be large enough to assure convergence of the series.

An example of the Term Importance is shown in Figure 4-17 as a function of the scattering angle. The light was assumed to be normally incident on the surface, and  $g$  was set equal to 50. A total of 400 terms were used to calculate the denominator of equation 4.21, and the Term Importance plotted in Figure 4-17 is that of the 45<sup>th</sup> term. From this plot, we can see, for instance, that this term accounts for approximately 5% of the total scatter distribution at a scattering angle of zero degrees and roughly 7.5% at a scattering angle of 52 degrees.

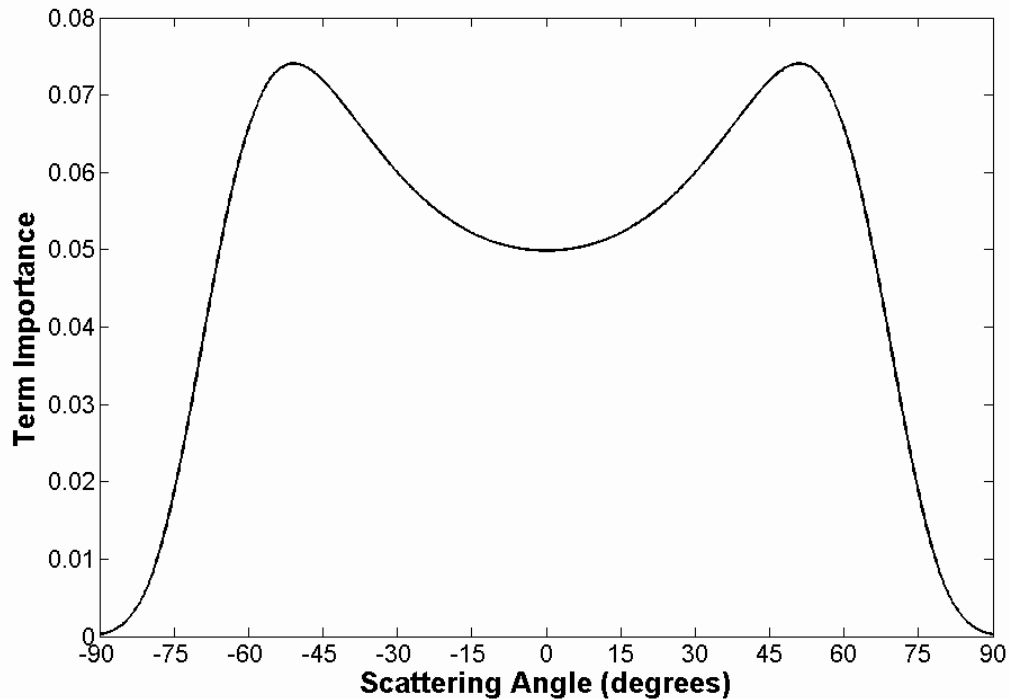


Figure 4-17: Term Importance as a function of scattering angle in the plane of incidence for  $\theta_i = 0^\circ$ ,  $\ell_c/\lambda = 10$ ,  $g = 50$ ,  $n = 45$ , and  $m = 400$

We next define a quantity we call the Average Term Importance. This quantity is given by the average of the Term Importance for a given term over all scattering angles. It is therefore a measure of how much each term contributes to the total scatter distribution for all scattering angles. For the example shown in Figure 4-17, the average term importance is 0.0489. If we calculate the Average Term Importance for each term used to calculate the total distribution and plot it against the term number, we obtain a visual tool showing us approximately how important each term is to the total scattering distribution.

For the above example where  $g = 50$ , the Average Term Importance (normalized to a peak of 1) is shown in Figure 4-18. From this figure we can immediately see that the first 20 terms hardly contribute at all to the scatter distribution, and neither do terms higher than the 70<sup>th</sup> term. Using 400 terms to calculate the scattering function when  $g = 50$  is obviously not necessary. If we had not used enough terms to calculate the denominator of equation 4.21, the plot of the Average Term Importance would exhibit a discontinuity at the maximum term number.

Figure 4-19 shows another example of the Average Term Importance, this time for  $g = 300$ . From the figure, we can see that the highest average contribution to the scattering distribution comes from the 284<sup>th</sup> term, but that all terms from around  $n = 60$  to  $n = 360$  are important to the calculation of the scattering distribution.

We then decided that the number of terms needed for a given value of  $g$  would be determined by the point at which the Average Term Importance drops to  $1/1000^{\text{th}}$  of its maximum value. Based on this criterion, we calculated the number of terms needed as a function of  $g$  for several angles of incidence. The results are shown in Figure 4-20.

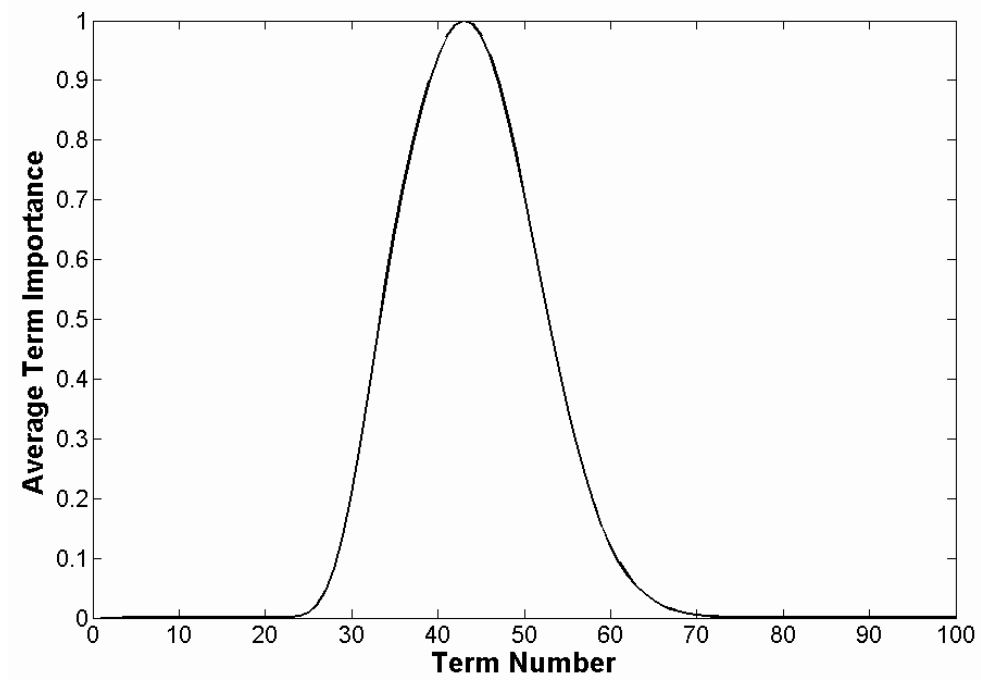


Figure 4-18: Average Term Importance as a function of term number for  $\theta_i = 0^\circ$ ,  $\ell_c/\lambda = 10$ ,  $g = 50$ , and  $m = 400$

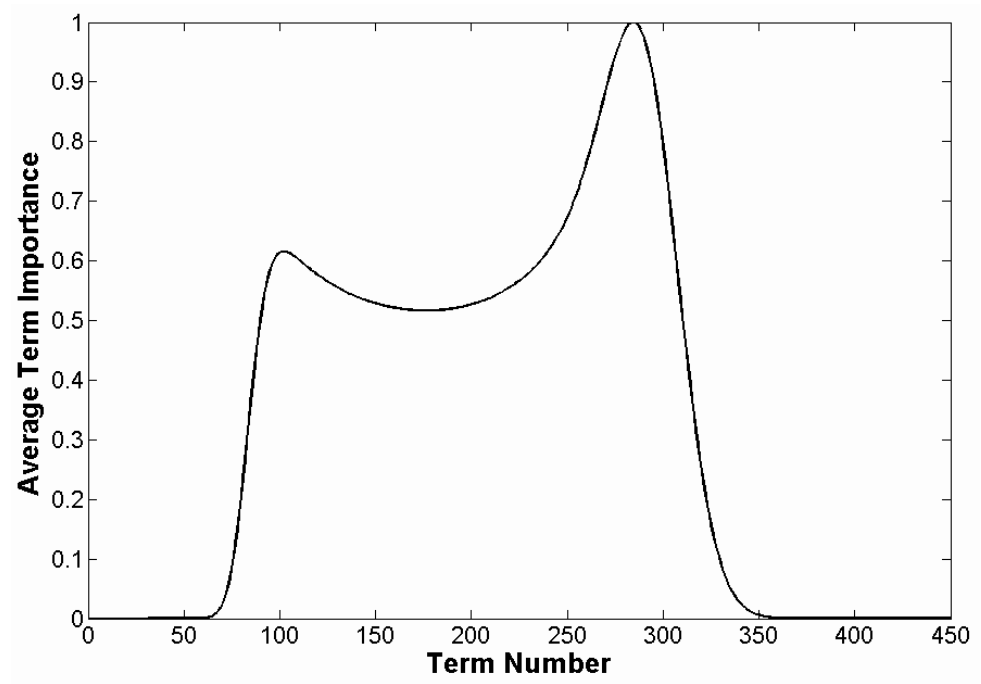


Figure 4-19: Average Term Importance as a function of term number for  $\theta_i = 0^\circ$ ,  $\ell_c/\lambda = 10$ ,  $g = 300$ , and  $m = 500$

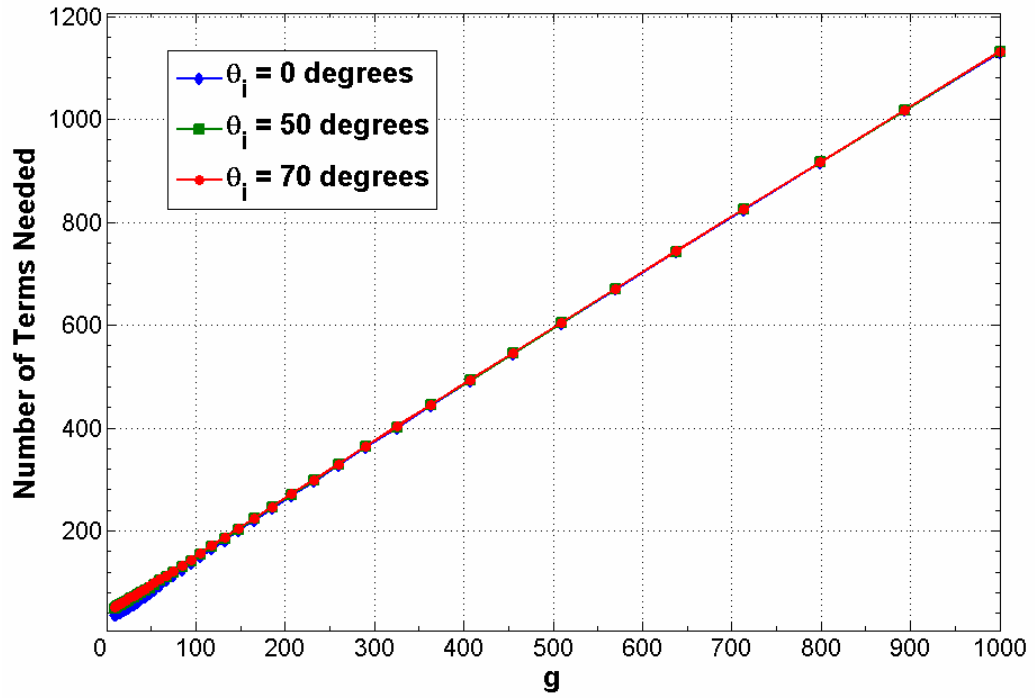


Figure 4-20: Number of terms needed to calculate the general MBK result of equation 4.12 as a function of  $g$  for  $\theta_i = 0^\circ$ ,  $50^\circ$ , and  $70^\circ$

As Figure 4-20 shows, the relationship between the number of terms needed to calculate the general modified Beckmann Kirchhoff scattering distribution of equation 4.12 is linear in nature, and does not depend on the angle of incidence. Based on a linear fit to the data points in Figure 4-20, the number of terms needed to calculate equation 4.12 as a function of  $g$  is given by

$$\text{Number of Terms} = 1.10 \times g + 40. \quad (4.22)$$

Equation 4.22 can easily be made part of any numerical routine used to calculate the modified Beckmann-Kirchhoff theory when using equation 4.12. As a final comment, it is important to realize for large values of  $m$  in equation 4.12, some of the

intermediate steps, such as the factorial, result in very large numbers, even though the final result may not be large. This can be a problem when using some software packages to do the calculations. MATLAB®, for instance, can only accurately calculate factorials of up to 25 since it uses double precision, and above values of 170 it gives the result as infinity. MATHEMATICA®, on the other hand, is able to use arbitrary precision, and can therefore better handle a larger number of terms. For the calculations above and in the next section as well, we used a combination of the two programs. The majority of the calculations were performed in MATLAB®, and a linking program was used to call MATHEMATICA® to perform the calculations requiring arbitrary precision. These results were then returned to MATLAB® where the calculations were completed.

#### ***4.6.3 Very Rough Approximation***

For very rough surfaces, the approximate expression of equation 4.14 can be used to calculate the scattered intensity distribution. This can be extremely useful because using equation 4.12 for these surfaces can involve a rather large number of terms and require a great deal more computation. To determine what constitutes a “very rough” surface, we can compare predictions calculated using equation 4.12 (with an appropriate number of terms given by equation 4.22) with predictions from the very rough approximation of equation 4.14. Examples of this are shown in Figure 4-21 for four values of  $g$ . The angle of incidence was assumed to be zero degrees, the quantity  $\ell/\lambda$  was assumed to be 10, and the RMS roughness,  $\sigma_s$ , was varied to obtain the different values of  $g$ .



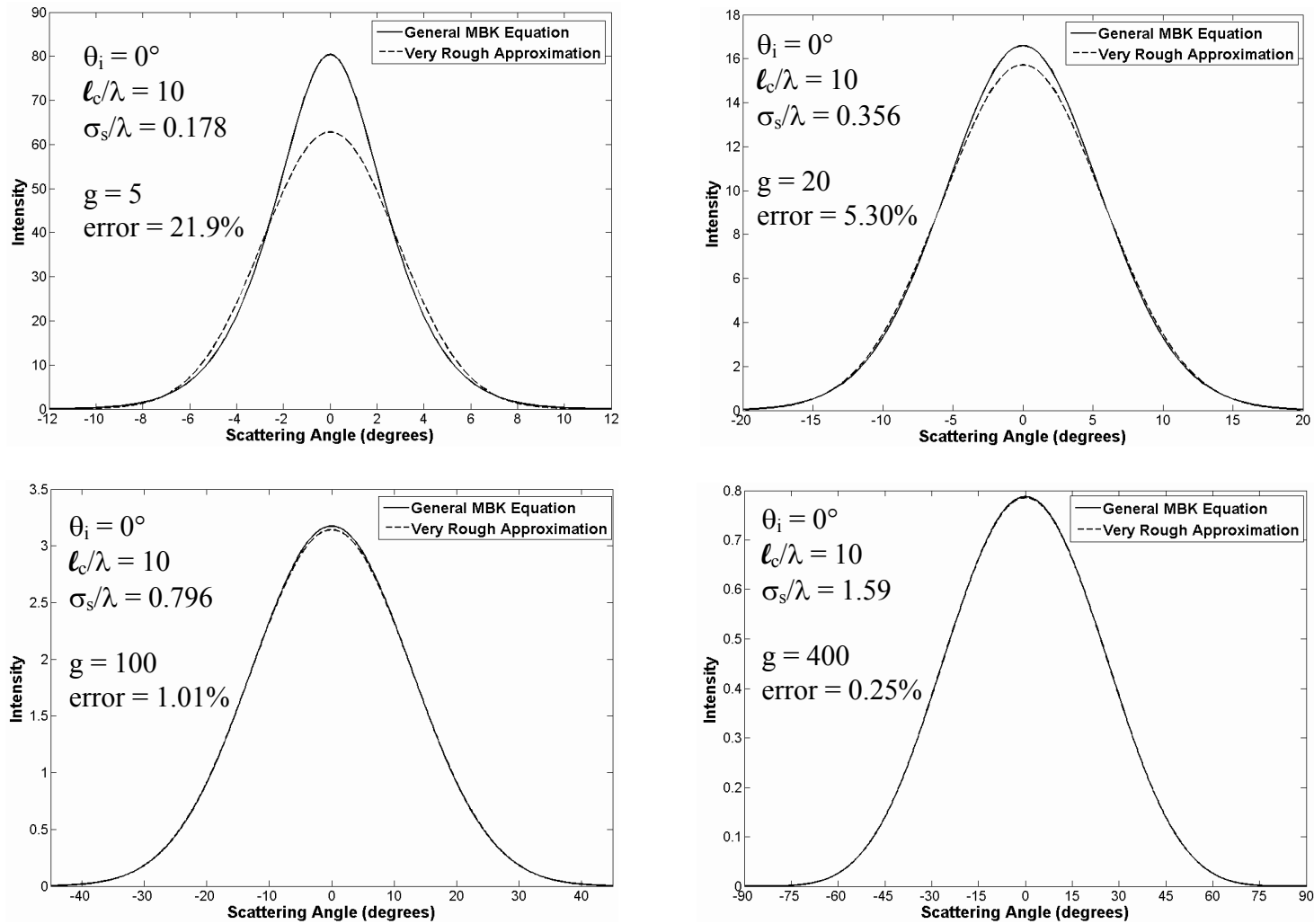


Figure 4-21: Comparison between the general MBK solution of equation 4.12 with an appropriate number of terms, and the MBK very rough surface approximation of equation 4.14 for  $g = 5, 20, 100$ , and  $400$

As was the case for the smooth surface approximation, the largest discrepancy between the general Beckmann-Kirchhoff solution and the very rough approximation also occurs at the peaks of the two functions. The maximum error is therefore again a good measure of the validity of the approximation. The maximum error for the example in Figure 4-21 varies from 21.9% for  $g = 5$  to 0.25% for  $g = 400$ . Calculations of the maximum error were performed over a range of  $g$  values from 0 to 0.5 for several incident angles. These results are shown in Figure 4-22.

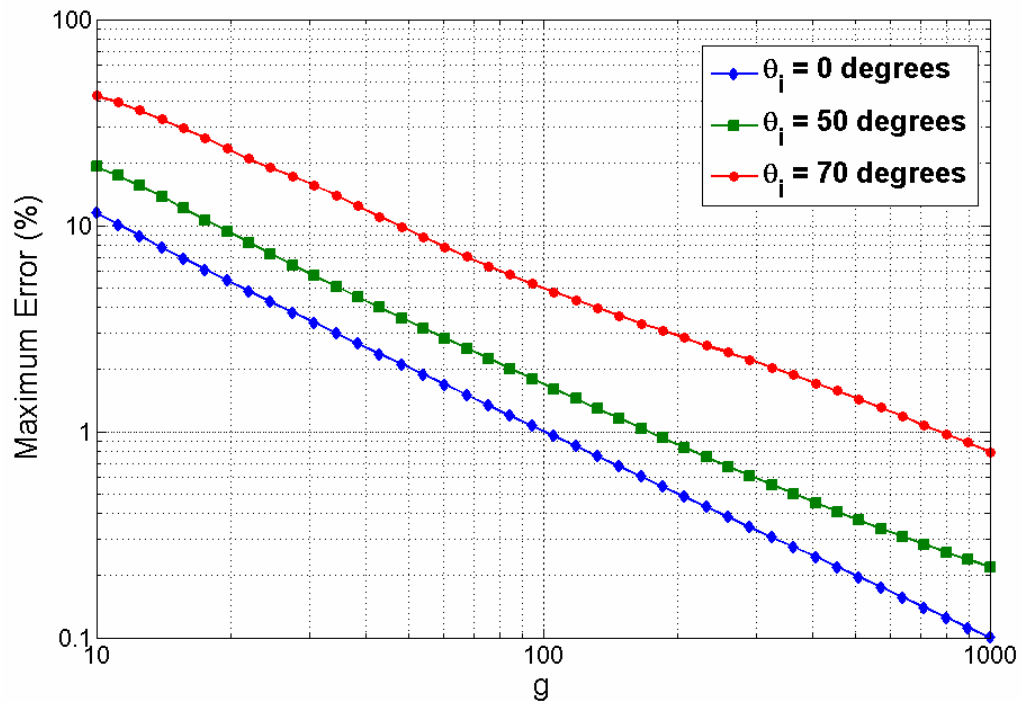


Figure 4-22: Maximum error between the general MBK solution and the MBK very rough approximation as a function of  $g$  for  $\theta_i = 0^\circ$ ,  $50^\circ$ , and  $70^\circ$

We can see from Figure 4-22 that the relationship between the maximum error and  $g$  is basically an inverse power law relationship, as the error for each incident angle is nominally a straight line when plotted in a log-log format. We also see that the maximum error for larger incident angles can be much greater than the error for smaller incident angles. Determining the value of  $g$  for which the very rough surface approximation is valid again depends on how much error can be tolerated. If your tolerance was 1%, then for normal incidence, the very rough approximation could be used when  $g \approx 100$ . For a 70 degree incident angle, however, a tolerance of 1% would require that the very rough surface approximation be used only when  $g > 800$ .

## **CHAPTER 5: GENERALIZED HARVEY-SHACK SURFACE SCATTER THEORY**

In the previous chapter, a modification to the Beckmann-Kirchhoff scattering theory was found to more accurately predict surface scatter than the original Beckmann-Kirchhoff theory for rough surfaces, while at the same time yielding results comparable to the Rayleigh-Rice theory for smooth surfaces, even at large incident and scattering angles. The modified theory as presented in chapter four is only applicable to surfaces with Gaussian autocovariance functions, however, and while it can be further modified to allow surfaces with other autocovariance functions, it is not all that straightforward to do so. In addition, the fact that the modification is empirical is less than completely satisfying. Therefore, we will now turn our attention to the Harvey-Shack surface scatter theory and attempt to generalize it to overcome some of its key limitations.

### **5.1 The Original Harvey-Shack Theory**

As discussed in chapter two, the original Harvey-Shack theory uses a linear systems approach to predict scatter from surface roughness. It assumes that the scattering surface can be described by a surface transfer function,  $H$ , given by

$$H_s(\hat{x}, \hat{y}) = \exp\left\{-(4\pi \hat{\sigma}_s)^2 \left[1 - C_s(\hat{x}, \hat{y}) / \sigma_s^2\right]\right\}, \quad (5.1)$$

where as before  $\hat{\sigma}_s$  is the RMS roughness, the “hats” indicate scaling by the wavelength, and  $C_s$  is the surface autocovariance function. The transfer function can also be written

in the form

$$H_s(\hat{x}, \hat{y}) = A + B G(\hat{x}, \hat{y}), \quad (5.2)$$

where

$$A = \exp\left[-(4\pi\hat{\sigma}_s)^2\right], \quad (5.3)$$

$$B = 1 - \exp\left[-(4\pi\hat{\sigma}_s)^2\right], \quad (5.4)$$

and

$$G(\hat{x}, \hat{y}) = \frac{\exp\left[(4\pi)^2 \hat{C}(\hat{x}, \hat{y})\right] - 1}{\exp\left[(4\pi\hat{\sigma}_s)^2\right] - 1}. \quad (5.5)$$

The scattering distribution, which Harvey called the Angle Spread Function (ASF), is given by the Fourier transform of the transfer function:

$$ASF(\alpha, \beta) = \mathcal{F}\{H_s(\hat{x}, \hat{y})\} = A\delta(\alpha, \beta) + S(\alpha, \beta), \quad (5.6)$$

where

$$S(\alpha, \beta) = B \mathcal{F}\{G(\hat{x}, \hat{y})\}. \quad (5.7)$$

We can see from equation 5.6 that the *ASF* is the sum of a delta function at the location of specular reflection and a scattering function that surrounds it. The percentage of the total power in the specular reflection is given by  $A$ , and the percentage of the total power in the scattering function is given by  $B$ , also known as the total integrated scatter (*TIS*).

The derivation of the original Harvey-Shack theory contained no explicit smooth surface approximations. It did, however, have limitations. These are notably: i) It is a scalar theory and therefore does not account for polarization effects, ii) It is limited to small incident and scattering angles, and iii) It does not account for the redistribution of

energy from evanescent to propagating waves. The third limitation has already been addressed by the non-paraxial scalar diffraction theory developed in chapter three. The Harvey-Shack formulation is an application of that theory, and a renormalization constant, analogous to  $K$  in equation 3.29, can therefore be implemented in the scattering theory. The first two limitations will be addressed in the following development.

## 5.2 The Modified Harvey-Shack Formulation

In the development of the original Harvey-Shack theory, an assumption was made about the random component of the pupil function described by equation 2.97. The random phase variations introduced upon reflection from the scattering surface were assumed to be given by

$$\phi(\hat{x}, \hat{y}; 0) = (2\pi / \lambda) OPD = 4\pi \hat{h}(\hat{x}, \hat{y}; 0), \quad (5.8)$$

where  $\hat{h}$  is the height variation of the random rough surface scaled by the wavelength of light. Equation 5.8 corresponds to the phase variations that would be introduced onto a wavefront striking the surface at normal incidence. This assumption limits the theory to both very small incident and scattering angles.

Figure 5-1 shows a ray incident upon a scattering surface at an arbitrary angle of incidence  $\theta_i$ . The optical path difference of a ray reflected from the surface in the specular ( $\theta_0 = -\theta_i$ ) direction is given by

$$OPD = (\cos \theta_i + \cos \theta_o) h(\hat{x}, \hat{y}; 0) = 2 \cos \theta_i h(\hat{x}, \hat{y}; 0), \quad (5.9)$$

and the corresponding phase variation is given by

$$\phi(\hat{x}, \hat{y}) = (2\pi / \lambda) OPD = 4\pi \cos \theta_i \hat{h}(\hat{x}, \hat{y}; 0). \quad (5.10)$$

Provided that the scattering angles are small relative to the angle of specular reflection, the phase function of equation 5.10 describes the phase variations introduced upon reflection from a scattering surface for a wavefront incident at an arbitrary angle.

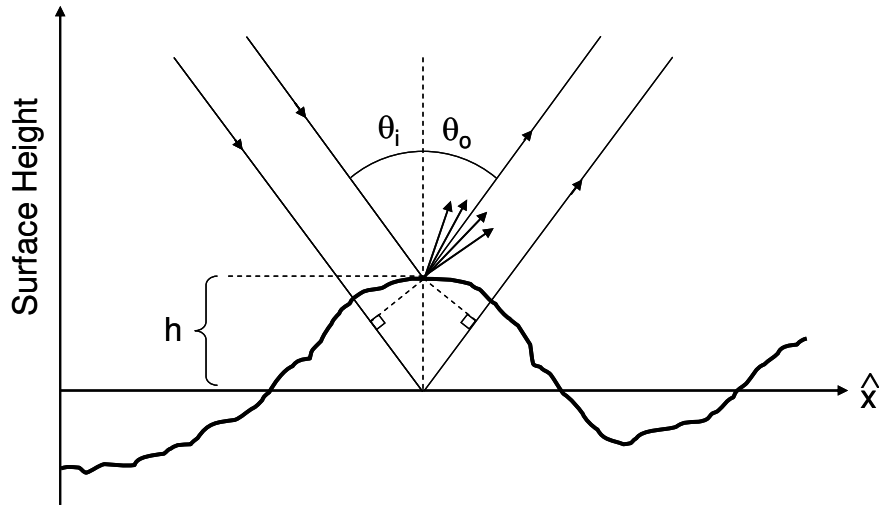


Figure 5-1: Illustration of the OPD for a specularly reflected ray

In the late 1980s, equation 5.10 was used to modify the original Harvey-Shack theory to account for the extremely large incident angles inherent to grazing incidence X-ray telescopes [54]. This resulted in a system transfer function given by

$$H_s(\hat{x}, \hat{y}; \varphi) = \exp \left\{ - \left( 4\pi \sqrt{2} \sin \varphi \hat{\sigma}_s \right)^2 \left[ 1 - C_s \left( \hat{x}, \frac{\hat{y}}{\sin \varphi} \right) / \sigma_s^2 \right] \right\}, \quad (5.11)$$

where  $\varphi$  is the grazing angle, which is the complement to the incident angle  $\theta_i$ . The factor of  $\sqrt{2}$  is due to reflection from two mirrored surfaces. This modified transfer function is in actuality a one-parameter family of surface transfer functions. The scattering process can no longer be considered shift-invariant with respect to incident angle, as a different transfer function is required for each incident angle. This does not diminish the usefulness of the theory, however. It is quite analogous to the common practice of applying linear systems theory to characterize imaging systems exhibiting field-dependent aberrations, where a different modulation transfer function is used for multiple field angles.

The transfer function in equation 5.11 was later adapted [112] to predict scattering for a single scattering surface for non-grazing incidence, where the transfer function was given as

$$H_s(\hat{x}, \hat{y}) = \exp \left\{ - \left( 4\pi \cos \theta_i \hat{\sigma}_s \right)^2 \left[ 1 - C_s \left( \hat{x}, \frac{\hat{y}}{\cos \theta_i} \right) / \sigma_s^2 \right] \right\}. \quad (5.12)$$

This form of the transfer function is incorrect, however, due to the scaling of  $\hat{y}$  by the cosine of the incident angle in the autocovariance function  $C_s$ . For grazing incidence applications, this scaling was done to calculate the scattering distribution not in a hemisphere centered about the scattering surface, but at the focal plane of the grazing-incidence telescope. The autocovariance function in equations 5.11 and 5.12 is



not given in terms of the coordinates of the scattering surface, but in a rotated coordinate system where  $\hat{x} = \hat{x}$  and  $\hat{y} = \hat{y} / \cos \theta_o$ . For the usual scattering geometry, the correct form of the modified transfer function for an arbitrary incident angle is therefore given by

$$H_s(\hat{x}, \hat{y}) = \exp \left\{ - (4\pi \cos \theta_i \hat{\sigma}_s)^2 \left[ 1 - C_s(\hat{x}, \hat{y}) / \sigma_s^2 \right] \right\}. \quad (5.13)$$

This can again be written in the form

$$H_s(\hat{x}, \hat{y}) = A + B G(\hat{x}, \hat{y}), \quad (5.14)$$

where

$$A = \exp \left[ - (4\pi \cos \theta_i \hat{\sigma}_s)^2 \right], \quad (5.15)$$

$$B = 1 - \exp \left[ - (4\pi \cos \theta_i \hat{\sigma}_s)^2 \right], \quad (5.16)$$

and

$$G(\hat{x}, \hat{y}) = \frac{\exp \left[ (4\pi \cos \theta_i)^2 \hat{C}(\hat{x}, \hat{y}) \right] - 1}{\exp \left[ (4\pi \cos \theta_i \hat{\sigma}_s)^2 \right] - 1}. \quad (5.17)$$

A wavefront incident on the scattering surface at an angle  $\theta_i$  is equivalent to introducing a linear phase shift across the pupil. Assuming the plane of incidence to be the x-z plane, this will cause a shift of the scattering function in direction cosine space of  $\alpha - \alpha_o$ , where  $\alpha_o = \sin \theta_o$ . The ASF is therefore given by the Fourier transform of the transfer function in equation 5.13 (or 5.14) multiplied by the linear phase shift:

$$ASF(\alpha, \beta) = \mathcal{F} \{ H_s(\hat{x}, \hat{y}) \exp(-i2\pi\alpha_o\hat{x}) \} = A\delta(\alpha - \alpha_o, \beta) + S(\alpha - \alpha_o, \beta). \quad (5.18)$$

where 
$$S(\alpha - \alpha_o, \beta) = B \mathfrak{F}\{G(\hat{x}, \hat{y}) \exp(-i2\pi\alpha_o \hat{x})\}. \quad (5.19)$$

This is again the sum of a delta function at the location of the specular direction surrounded by a scattering function,  $S$ , where the total power in the specular reflection is given by  $A$ , the percentage of total power in the scattering function ( $TIS$ ) is given by  $B$ , and  $A + B = 1$ .

If any portion of the scattering function  $S$  in equation 5.18 falls outside of the unit circle in direction cosine space, it will need to be truncated and renormalized to account for conservation of energy. This is accomplished in the same manner as was done for diffraction in section 3.3 of chapter three. Similar to equation 3.29, the renormalization constant,  $K$ , for the scattering function is given by

$$K = \frac{\int_{\alpha=-\infty}^{\infty} \int_{\beta=-\infty}^{\infty} ASF(\alpha, \beta) d\alpha d\beta}{\int_{\alpha=-1}^1 \int_{\beta=-\sqrt{1-\alpha^2}}^{\sqrt{1-\alpha^2}} ASF(\alpha, \beta) d\alpha d\beta}. \quad (5.20)$$

The numerator in equation 5.20 is simply equal to unity, however. The normalization constant can therefore be written as

$$K = \frac{1}{\int_{\alpha=-1}^1 \int_{\beta=-\sqrt{1-\alpha^2}}^{\sqrt{1-\alpha^2}} ASF(\alpha, \beta) d\alpha d\beta}, \quad (5.21)$$

and the angle spread function is then given by

$$ASF'(\alpha, \beta) = K \mathfrak{F}\{H_s(\hat{x}, \hat{y}) \exp(-i2\pi\alpha_o \hat{x})\}. \quad (5.22)$$

Recall from section 2.2.4 that the ASF is a *normalized radiance* function. We can therefore convert the angle spread function to intensity by using equation 2.96. The scattered intensity is therefore given by

$$I(\alpha, \beta) = P_i \text{ASF}(\alpha, \beta) \cos \theta_s . \quad (5.23)$$

### 5.2.1 Smooth Surface Approximation

We will now compare the original and modified Harvey-Shack theories to each other and with the well-established Rayleigh-Rice theory for smooth surfaces. Although it is not necessary, it will be useful to make a smooth surface approximation to the Harvey-Shack theories to aid in the comparison.

A smooth surface implies that the roughness is small compared to the wavelength of light. If we let  $\hat{\sigma}_s \ll \lambda$  in equations 5.3-5.5 for the original Harvey-Shack theory, we obtain

$$A \approx 1 - [4\pi\hat{\sigma}_s]^2 , \quad (5.24)$$

$$B \approx [4\pi\hat{\sigma}_s]^2 , \quad (5.25)$$

and

$$G(\hat{x}, \hat{y}) = C_s(\hat{x}, \hat{y}) / \sigma_s^2 . \quad (5.26)$$

Using equation 5.7, the scattering function is then given by

$$S(\alpha, \beta) = \frac{16\pi^2}{\lambda^2} \mathcal{F}\{C_s(\hat{x}, \hat{y})\} . \quad (5.27)$$

After a change of variables from  $(\hat{x}, \hat{y})$  to  $(x, y)$ , and recognizing that the autocovariance function  $C_s$  and the surface power spectral density (PSD) constitute a Fourier transform pair, the scattering function can be written in terms of scattering angles as

$$S_{OHS}(\theta_s, \phi_s; \theta_i) = \frac{16\pi^2}{\lambda^4} \text{PSD}(f_x, f_y), \quad (5.28)$$

where

$$f_x = \frac{\sin \theta_s \cos \phi_s - \sin \theta_i}{\lambda}, \quad f_y = \frac{\sin \theta_s \sin \phi_s}{\lambda}. \quad (5.29)$$

From equation 5.23 the scattered intensity for the original Harvey-Shack (OHS) theory is therefore given by

$$I_{OHS}(\theta_s, \phi_s; \theta_i) = P_i \left( \frac{16\pi^2}{\lambda^4} \right) \cos \theta_s \text{PSD}(f_x, f_y). \quad (5.30)$$

Similarly, the intensity for the modified Harvey-Shack (MHS) theory for smooth surfaces is given by

$$I_{MHS}(\theta_s, \phi_s; \theta_i) = P_i \left( \frac{16\pi^2}{\lambda^4} \right) \cos^2 \theta_i \cos \theta_s \text{PSD}(f_x, f_y). \quad (5.31)$$

Recall from equation 2.39 that the intensity (normalized by incident power) for the Rayleigh-Rice (RR) theory, assuming a perfect conducting surface and TE polarization, is given by

$$I_{RR}(\theta_s, \phi_s; \theta_i) = P_i \left( \frac{16\pi^2}{\lambda^4} \right) \cos \theta_i \cos^2 \theta_s \text{PSD}(f_x, f_y). \quad (5.32)$$

Comparing equation 5.30 with 5.31, we can see that the original Harvey-Shack and the modified Harvey-Shack theories are only strictly equal for normal incidence. They should give similar results, however, for paraxial incident angles when  $\cos \theta_i \approx 1$ . Comparing both versions of the Harvey-Shack theory to the Rayleigh-Rice theory, we can see that all three should agree fairly well when both the incident and scattering angles are paraxial, for which  $\cos \theta_i, \cos \theta_s \approx 1$ . For larger incident angles, the original Harvey-Shack will predict both a higher peak and larger TIS than either the modified Harvey-Shack or the Rayleigh-Rice theories. For all incident angles, the modified Harvey-Shack and Rayleigh-Rice theories are equal at the location of specular reflection where  $\cos \theta_i = \cos \theta_s$ . They should agree fairly well elsewhere provided that the spread of the scattering function around the specular beam is small.

For comparison purposes, we will assume the scattering surface to have a Gaussian autocovariance function of the form

$$C_s(x, y) = \sigma_s^2 \exp \left[ -\frac{x^2 + y^2}{\ell_c^2} \right]. \quad (5.33)$$

The *PSD* is then given by

$$PSD(f_x, f_y) = \pi \sigma_s^2 \ell_c^2 \exp \left[ -\pi^2 \ell_c^2 (f_x^2 + f_y^2) \right], \quad (5.34)$$

where  $\ell_c$  is the correlation length, and  $f_x, f_y$  are given by equation 5.29. To calculate the intensity for the three theories, equation 5.34 is substituted into equations 5.30, 5.31, and 5.32. For smooth surfaces, the RMS roughness only affects the magnitude of the

scattering function, not its shape. Therefore we will only use one roughness scale,  $\sigma_s / \lambda = 0.02$ , when calculating scatter for smooth surfaces.

Figure 5-2 shows a comparison of the original and modified Harvey-Shack theories with the Rayleigh-Rice theory for a surface with the autocovariance function given in equation 5.33. The incident angle is zero degrees and the ratio of the correlation length to the wavelength of light ( $\ell_c/\lambda$ ) is five. The original and modified Harvey-Shack theories are exactly equal for normal incidence as discussed above. The ratio of  $\ell_c/\lambda$  determines the angular spread of the scattering function and, in the case of Figure 5-2, the spread is narrow enough that the Harvey-Shack theories and Rayleigh-Rice theories yield virtually identical results.

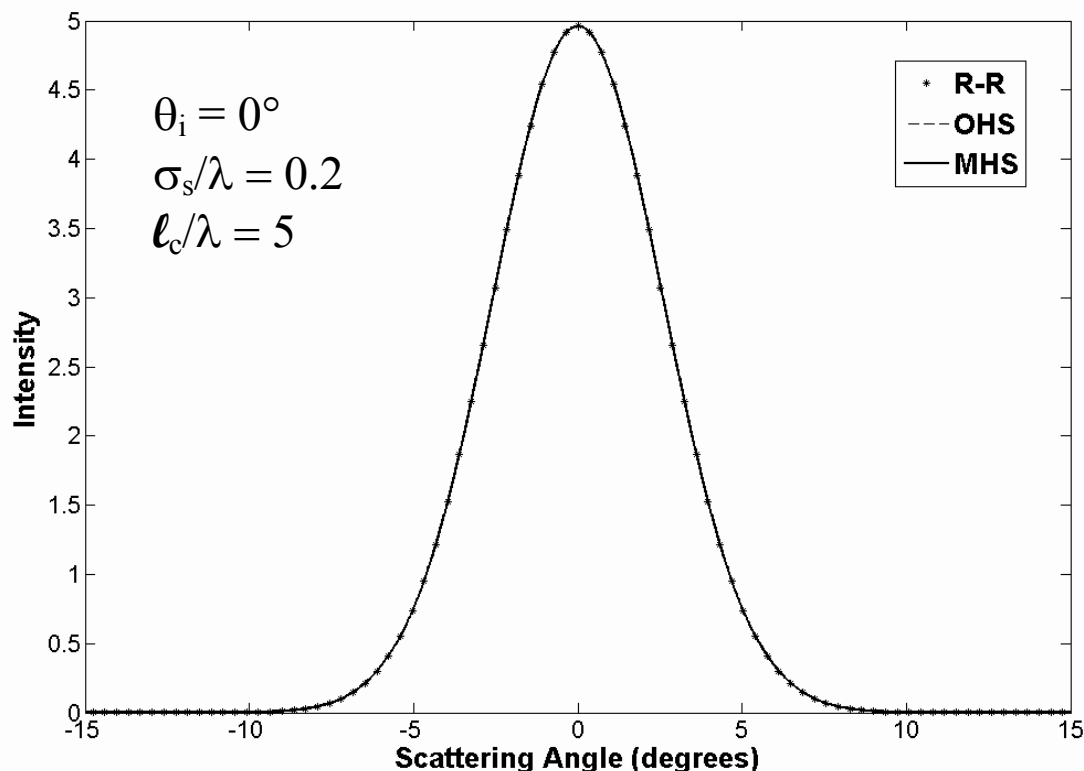


Figure 5-2: OHS and MHS compared to RR for  $\theta_i = 0^\circ$  and  $\ell_c/\lambda = 5$

In Figure 5-3, the incident angle is again zero degrees, but  $\ell_c/\lambda$  has been decreased by a factor of ten to 0.5. This results in a much wider angular spread of the scattering function than in Figure 5-2, and the Harvey-Shack theories depart from the Rayleigh-Rice theory at larger scattering angles. The original and modified Harvey-Shack theories still yield identical results since the light is normally incident on the scattering surface.

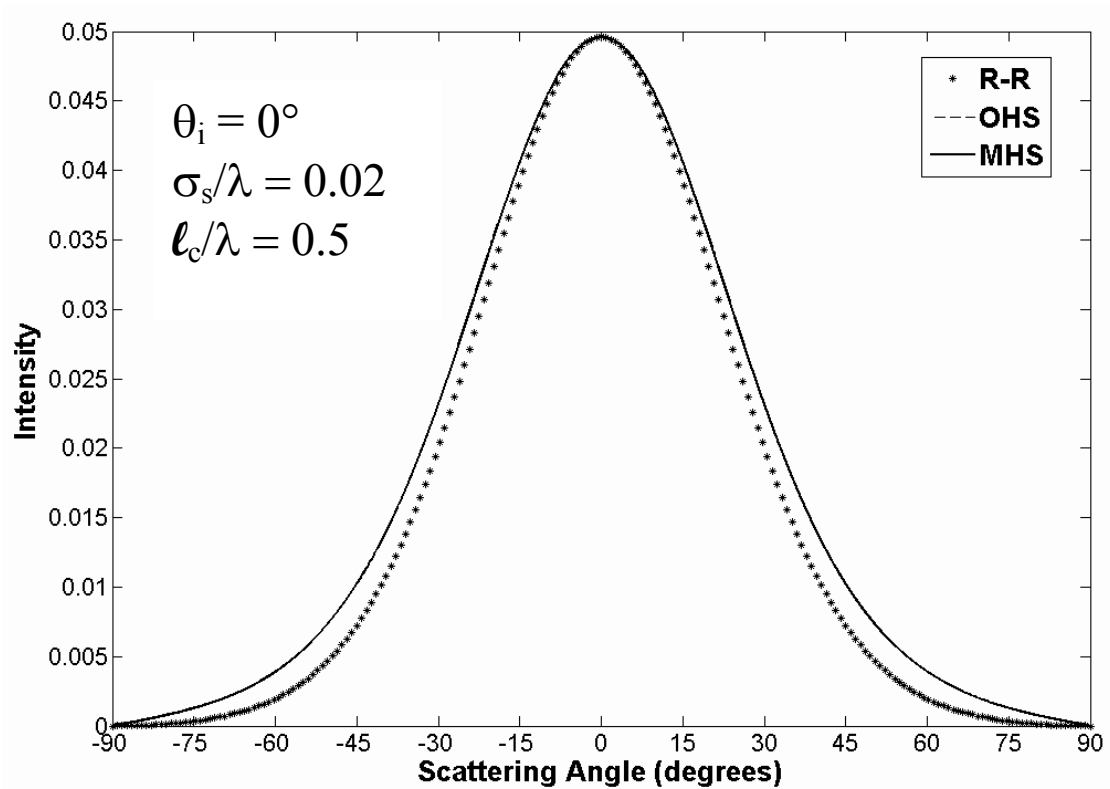


Figure 5-3: OHS and MHS compared to RR for  $\theta_i = 0^\circ$  and  $\ell_c/\lambda = 0.5$

In Figure 5-4,  $\ell_c/\lambda$  has again been set to five, resulting in a small angular spread of the scattering function. The incident angle has been increased slightly to five degrees.

The agreement between the three theories is still good; however the original Harvey-Shack theory deviates slightly from the other two theories near the location of the specular reflection.

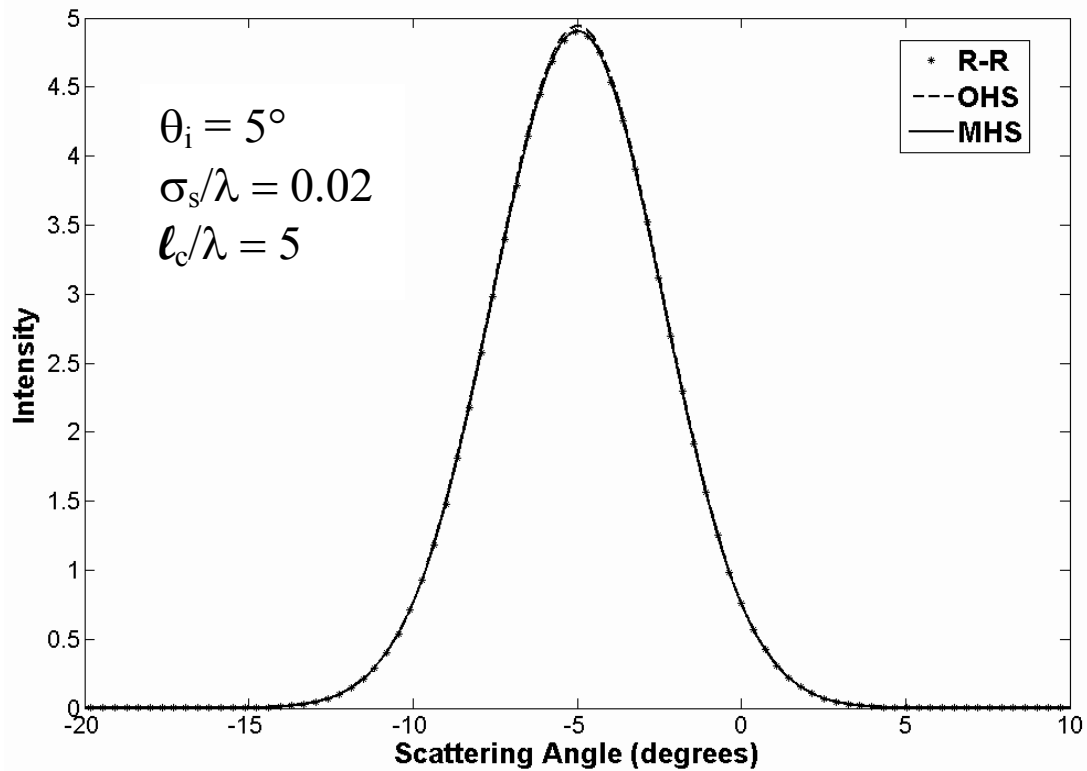


Figure 5-4: OHS and MHS compared to RR for  $\theta_i = 5^\circ$  and  $\ell_c/\lambda = 5$

In Figure 5-5,  $\ell_c/\lambda$  has been kept at five, but the incident angle has been increased to 40 degrees. The agreement between the modified Harvey-Shack and Rayleigh-Rice theories is still generally good. The original Harvey-Shack theory departs drastically from the other two theories. From equation 5.25, the original Harvey-Shack theory



predicts that 6.32% of the total energy is contained in the scattering function, while both the modified Harvey-Shack and Rayleigh-Rice theories predict that the scattering function contains 3.71% of the total energy. The departure will only get worse with increasing incident angle, as the original Harvey-Shack theory will continue to predict a *TIS* of 6.32%, regardless of what the incident angle is, while the *TIS* predicted by the modified Harvey-Shack and Rayleigh-Rice theories will continue to decrease with increasing incident angle.

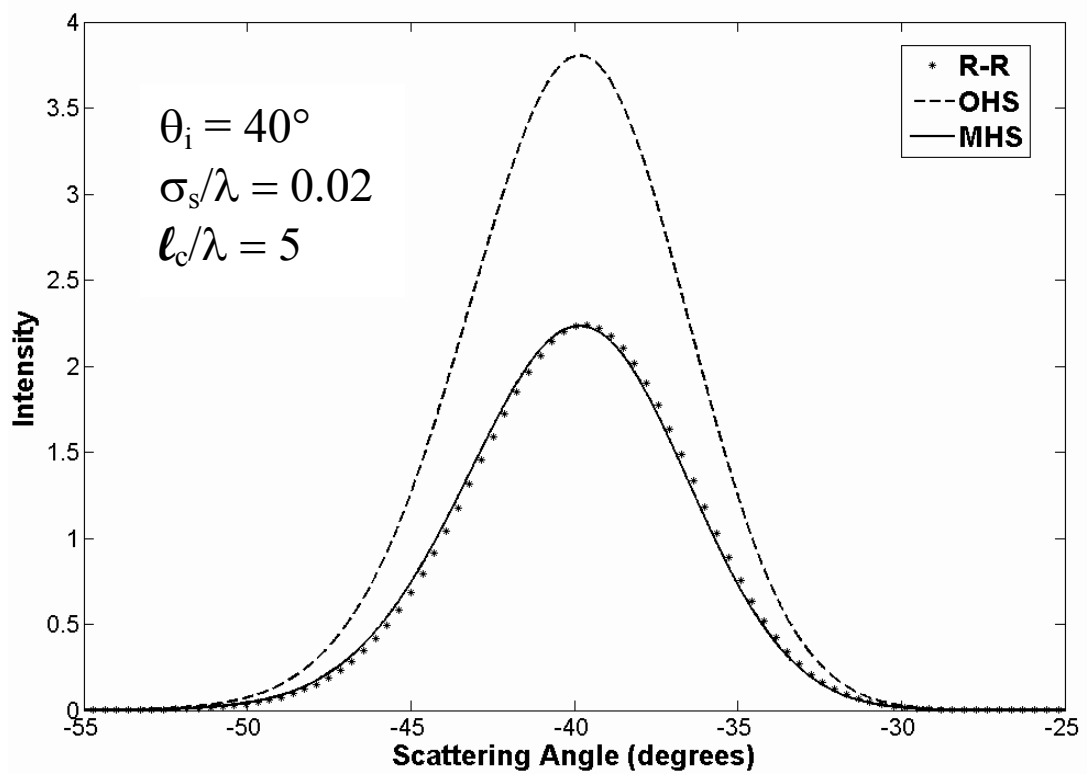


Figure 5-5: OHS and MHS compared to RR for  $\theta_i = 40^\circ$  and  $\ell_c/\lambda = 5$

The modified Harvey-Shack theory is obviously a large improvement over the original Harvey-Shack theory whenever the incident angle is not small. Therefore, we will continue to compare only the modified Harvey-Shack theory with the Rayleigh-Rice theory. In Figures 5-6, 5-7, and 5-8 the two theories are compared for incident angles of 20, 50, and 70 degrees and  $\ell_c/\lambda$  ratios of 1, 5, 10, and 40.

For an incident angle of 20 degrees in Figure 5-6, the only significant departure of the modified Harvey-Shack theory from the Rayleigh-Rice theory occurs for  $\ell_c/\lambda = 1$ , when the angular spread of the scattering function is almost 80 degrees. Even then, the departure is not severe.

For an incident angle of 50 degrees in Figure 5-7, the modified Harvey-Shack theory departs slightly from the Rayleigh-Rice theory for  $\ell_c/\lambda = 5$ , where the scattering function is roughly 20 degrees wide. For  $\ell_c/\lambda = 1$ , the departure is quite severe.

In Figure 5-8, where the incident angle is 70 degrees, there is only good agreement between the two theories when  $\ell_c/\lambda = 40$ , where the width of the scattering function is about 6 degrees. For all of the other  $\ell_c/\lambda$  ratios, the modified Harvey-Shack theory departs significantly from the Rayleigh-Rice theory.

The two theories should agree when the angular spread of the scattering function is small. For small incident angles, the modified Harvey-Shack theory is fairly accurate even for very wide scattering functions. The restriction on the angular spread becomes more severe with increasing incident angle, however, and for a given surface, the theory may work well for smaller incident angles but may break down at larger incident angles.

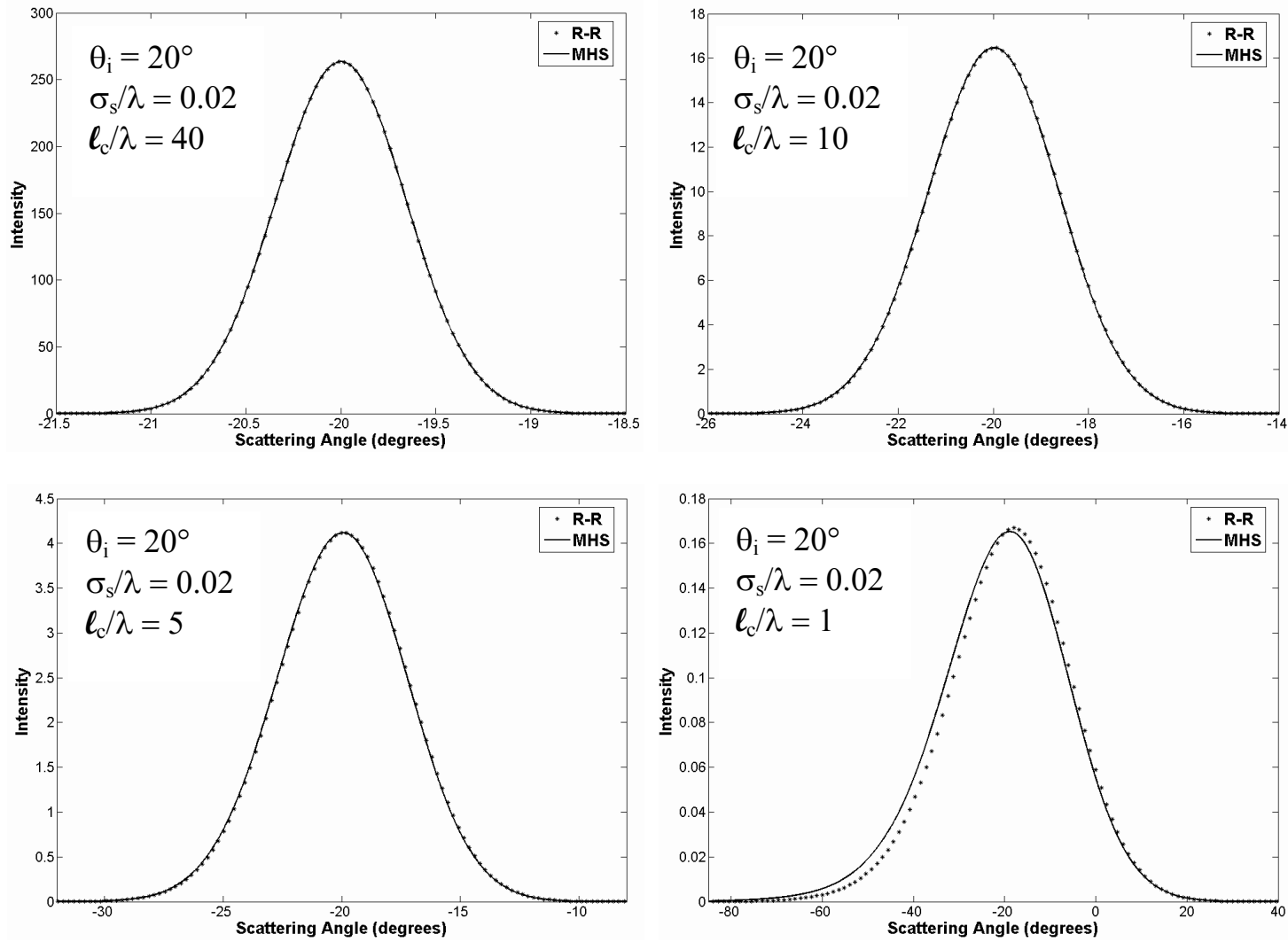


Figure 5-6: MHS compared to RR for  $\theta_i = 20^\circ$  and  $\ell_c/\lambda = 40, 10, 5$ , and 1

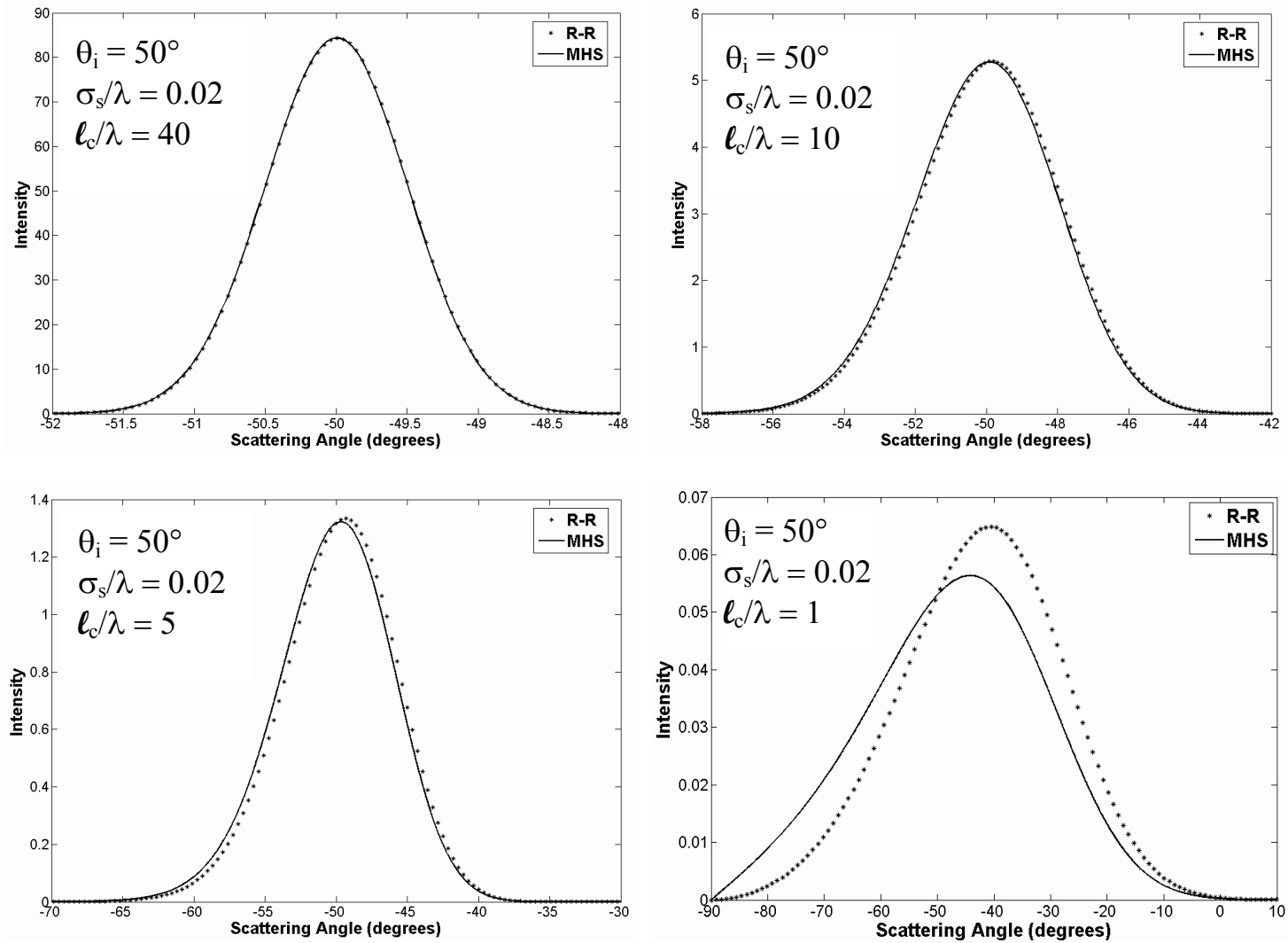


Figure 5-7: MHS compared to RR for  $\theta_i = 50^\circ$  and  $\ell_c/\lambda = 40, 10, 5$ , and 1

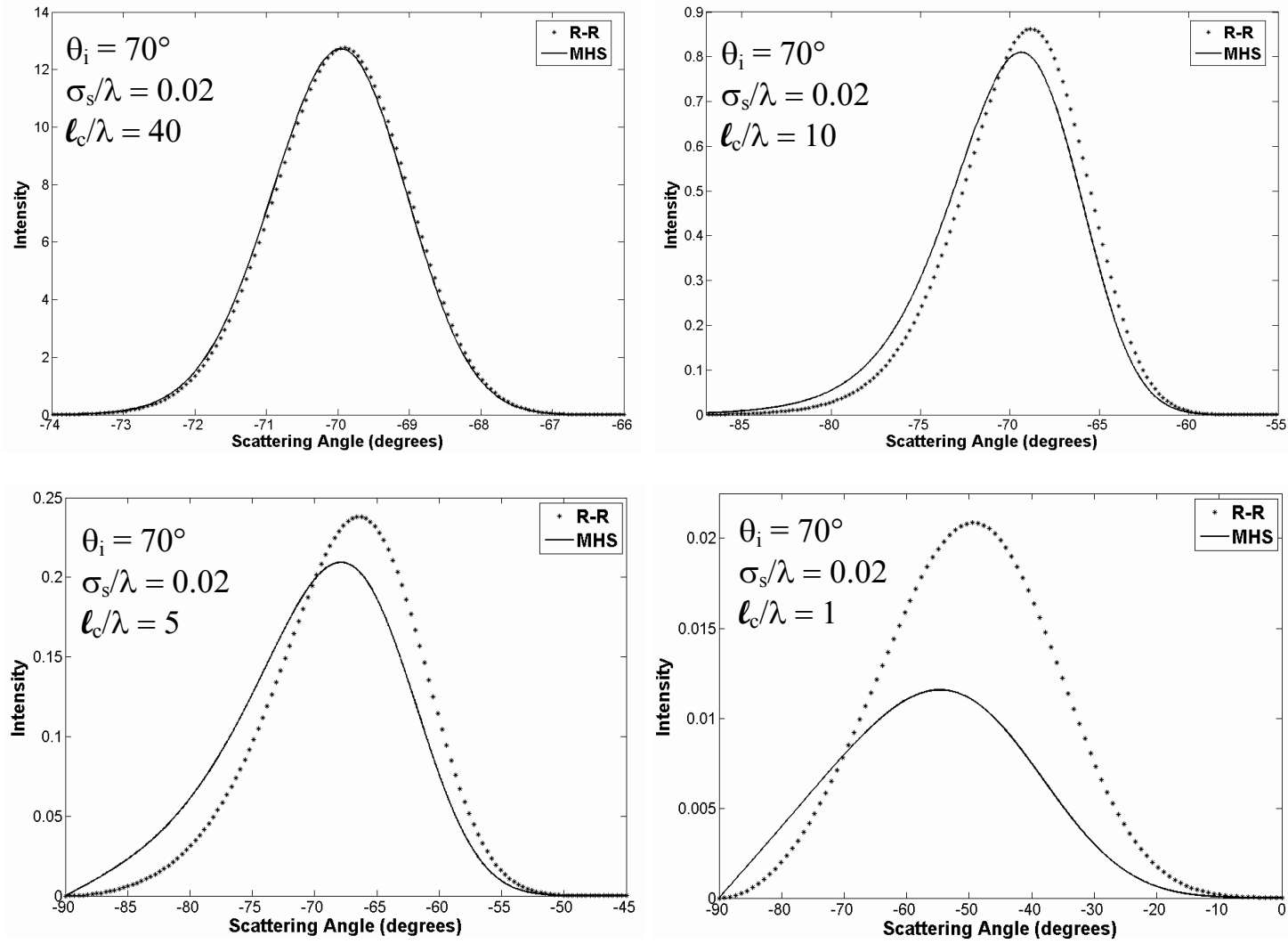


Figure 5-8: MHS compared to RR for  $\theta_i = 70^\circ$  and  $\ell_c/\lambda = 40, 10, 5$ , and 1

### 5.2.2 Rough Surfaces

For rough surfaces, a numerical solution to equation 5.18 (or 5.22) will most likely be required. This is easily accomplished with computational software, such as MATLAB®, which is what we will use to perform the calculations using the built-in FFT routine.

Given the *ACV* function of a surface, as well as the wavelength of light, the surface transfer function of equation 5.13 or 5.14 is calculated first. If the *ACV* of the surface is not known, but the *PSD* is, the *ACV* can be calculated from the *PSD* since the two constitute a Fourier transform pair. Care must be taken, however, since the *PSD* is usually known only over some band-limited region. Fitting the *PSD* to some functional form can be useful in these cases to allow extrapolation beyond the known portion of the *PSD*.

Figure 5-9 shows the surface transfer function for the O'Donnell-Mendez surface [110] discussed in chapter four. In this case  $\lambda = 10.6 \mu\text{m}$ ,  $\theta_i = 70^\circ$ ,  $\sigma_s = 2.27 \mu\text{m}$ , and  $\ell_c = 20.9 \mu\text{m}$ . As seen in the figure, the transfer function consists of the sum of a constant and a bell-shaped function.

We next use equation 5.18 to calculate the angle spread function which is shown in Figure 5-10. The constant portion of Figure 5-9 will Fourier transform into a delta function in the location of specular reflection, while the bell-shaped function will Fourier transform into the scattering function. The peak of the transfer function is unity, and therefore from the central ordinate theorem of Fourier transform theory [1], the volume

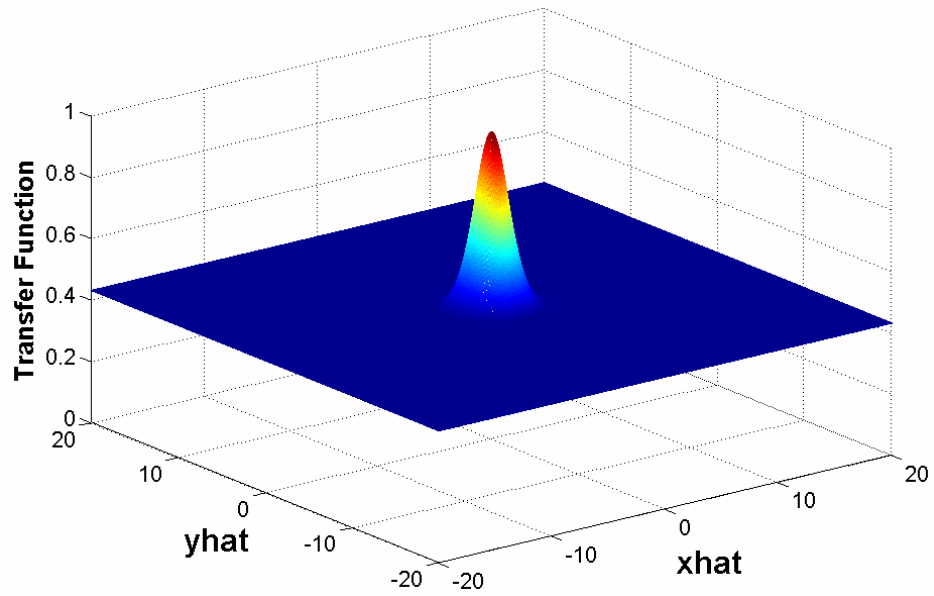


Figure 5-9: MHS surface transfer function for a scattering surface with a Gaussian  $ACV$  function.  $\lambda = 10.6 \mu\text{m}$ ,  $\theta_i = 70^\circ$ ,  $\sigma_s = 2.27 \mu\text{m}$ ,  $\ell_c = 20.9 \mu\text{m}$ .

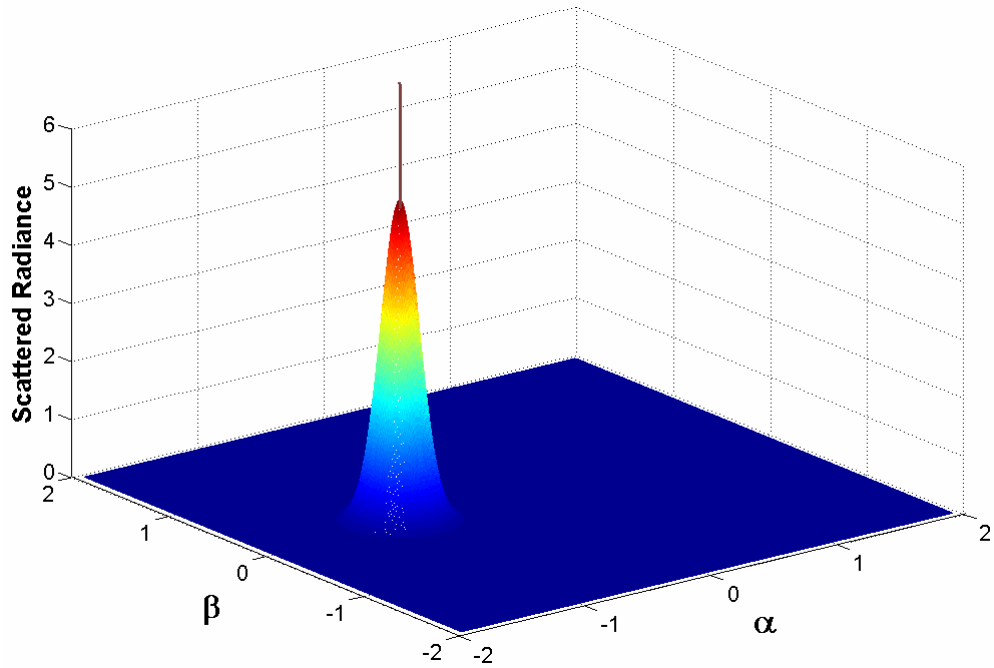


Figure 5-10: The  $ASF$  calculated by taking the Fourier transform of the transfer function in Figure 5-9

under its Fourier transform (the *ASF*) will also be unity. The constant portion of the transfer function determines the percentage of the total power that resides in the specular portion of the *ASF*, given by  $A$  in equation 5.15. The percentage of the total power in the scattering function is then given by  $B = 1 - A$ . For this specific case,  $B = 0.571$ .

Any portion of the *ASF* that falls outside of the unit circle in direction cosine space is not real and does not propagate. The *ASF* then needs to be truncated at the unit circle and renormalized according to equations 5.21 and 5.22. This renormalization redistributes the energy from that portion of the scattering function that falls outside the unit circle back into both the real part of the scattering function and the specularly reflected light. Figure 5-11 shows the result of this truncation and renormalization for the *ASF* of Figure 5-10. For this situation, the renormalization factor  $K$  is equal to 1.244.

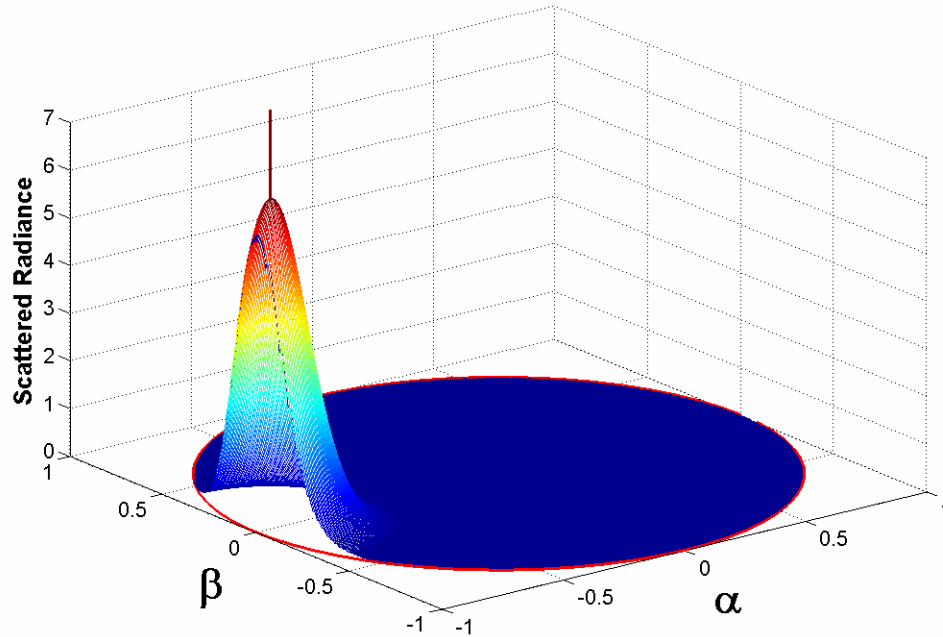


Figure 5-11: Truncated and renormalized *ASF* of Figure 5-10



Figure 5-12 shows a profile of the diffusely scattered portion of the *ASF* along the plane of incidence both before and after the truncation and renormalization is performed. The specular reflection has been omitted. The two profiles differ in magnitude by a factor of  $K = 1.244$ , as calculated from equation 5.21. When plotted as a function of direction cosines, the scattering function as predicted by the modified Harvey-Shack theory is symmetrical about the location of specular reflection.

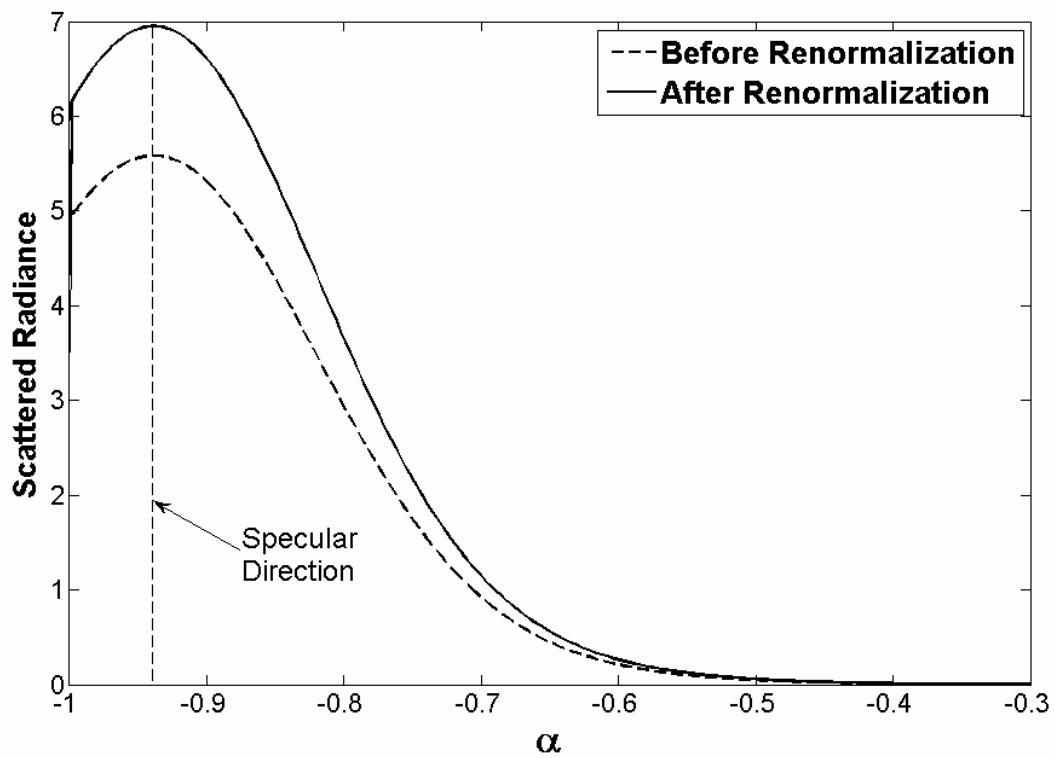


Figure 5-12: Plane-of-incidence profile of the diffusely scattered portion of the *ASF* in Figure 5-10 both before and after renormalization.

The scattered intensity can be calculated from the *ASF* using equation 5.23. Figure 5-13 shows a profile of the scattered intensity in the plane-of-incidence as a function of scattering angle for the diffusely scattered portion of the *ASF* of Figure 5-10. The scattered intensity is highly asymmetrical about the direction of specular reflection, and the peak of the scattered intensity is shifted inside of the specular reflection. The shift is due to the multiplication of the radiance by a cosine of the scattering angle to convert it to intensity. The asymmetry is due to both the cosine and the fact that it is plotted as a function of scattering angle instead of the direction cosine of that angle.

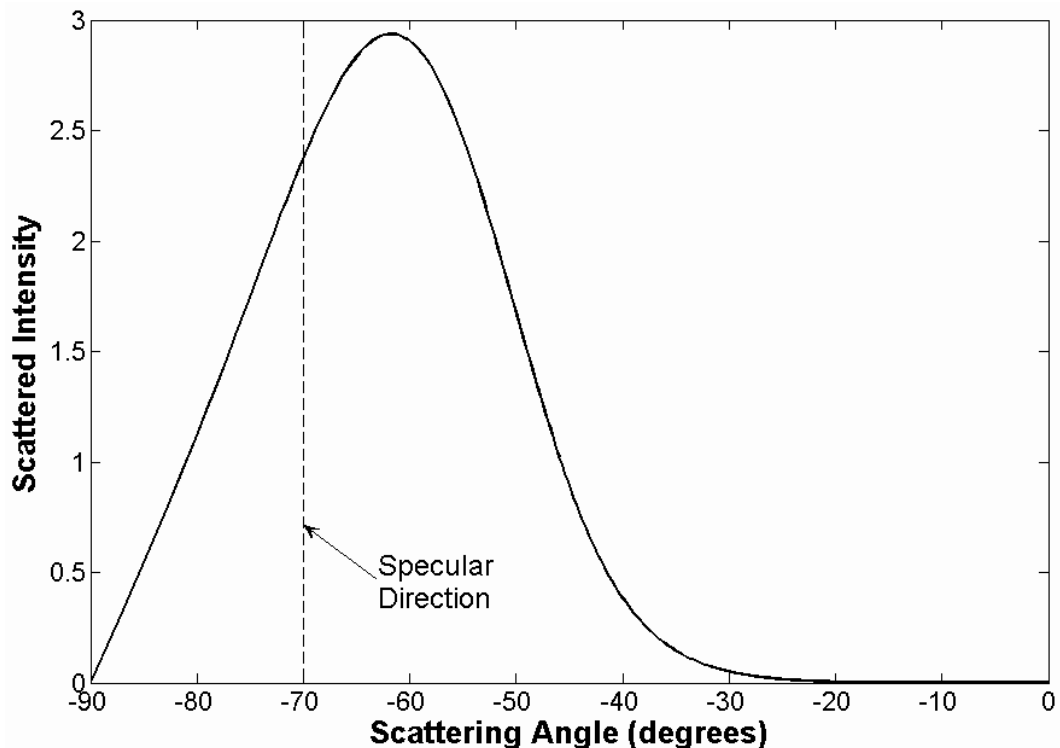


Figure 5-13: Scattered intensity in the plane of incidence as a function of scattering angle for the diffusely scattered portion of the *ASF* of Figure 5-10

A comparison of scattered intensity predicted by the original and modified Harvey-Shack theories is shown in Figure 5-14 for the O'Donnell-Mendez surface with a wavelength of 10.6  $\mu\text{m}$  at incident angles of 0, 20, 50, and 70 degrees. Experimental data taken from [110] for 20 and 70 degrees is also plotted for comparison. For incident radiation with a wavelength of 10.6  $\mu\text{m}$ ,  $\sigma_s/\lambda = 0.214$ , and this surface can be considered moderately rough. Since we only know the profile of the scattered intensity from the experimental data, we are not able to calculate its volume to scale it to the theoretical predictions. The peak of the experimental data was therefore normalized to the peak of the modified Harvey-Shack prediction.

For normal incidence in Figure 5-14, the original and modified Harvey-Shack theories give the same result. This will always be the case, regardless of how rough the surface is. For normally incident 10.6  $\mu\text{m}$  radiation, both theories predict that all of the light will be diffusely scattered, and there will therefore be no specular reflection.

For a 20 degree incident angle, both theories still predict that all of the light will be diffusely scattered. The original Harvey-Shack theory predicts a smaller peak and a slightly wider scattering function. The modified Harvey-Shack theory gives a fairly good fit to the experimental data for this small incident angle, even though the scattering function has an angular spread of roughly 80 degrees.

For a 50 degree incident angle, the disagreement between the theories is far more pronounced. The peak of the original Harvey-Shack prediction is about half of the modified Harvey-Shack peak, and the angular spread is larger. In addition, the original Harvey-Shack theory still predicts a *TIS* of 1, while the *TIS* from the modified Harvey-Shack theory drops slightly to 0.942.

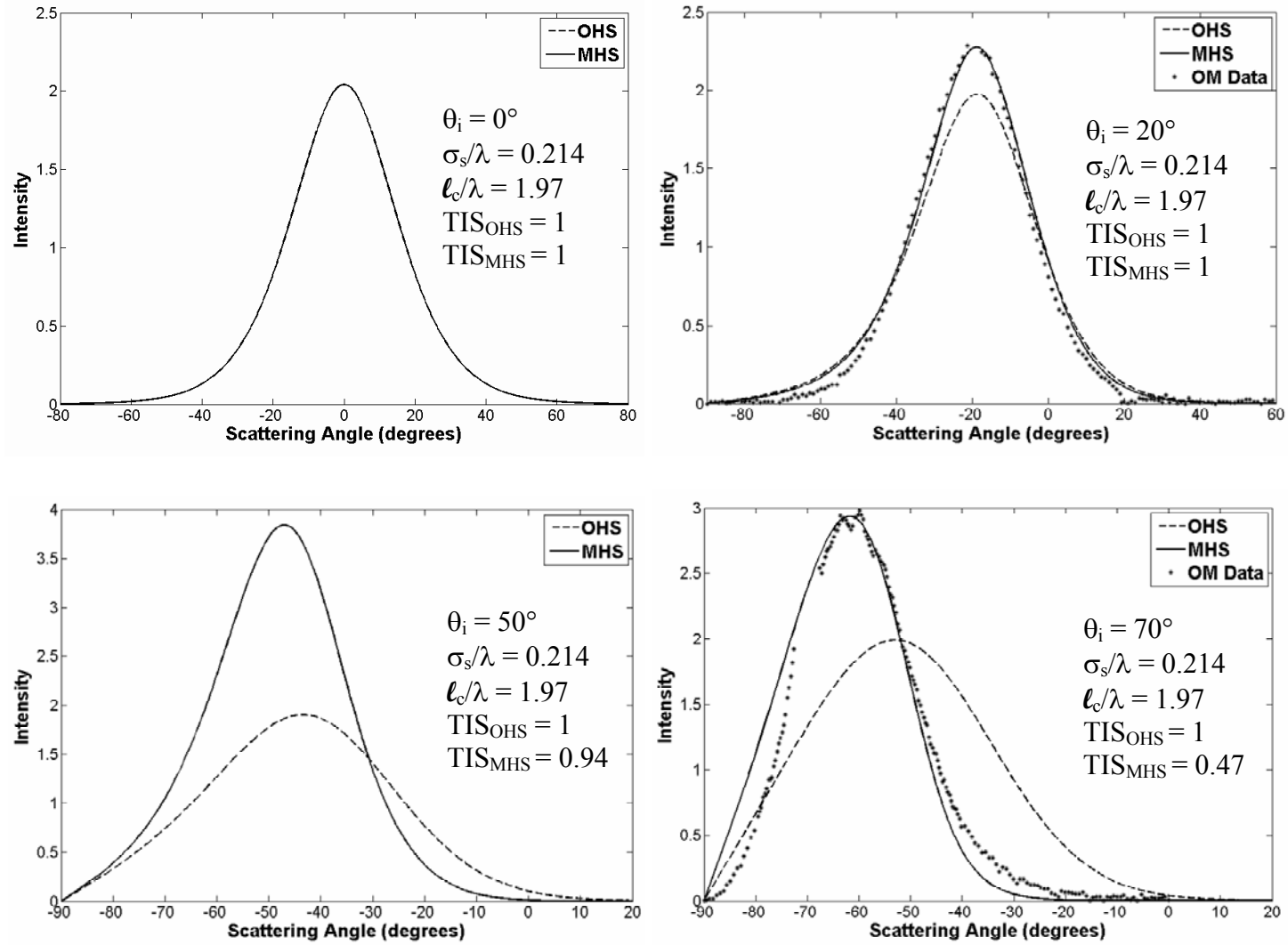


Figure 5-14: MHS compared to OHS and OM experimental data for  $\sigma_s/\lambda = 0.214$ ,  $\ell_c/\lambda = 1.97$ , and  $\theta_i = 0^\circ, 20^\circ, 50^\circ$ , and  $70^\circ$

For the 70 degree incident angle in Figure 5-14, the disagreement between the original and modified Harvey-Shack theories is worse still. The peak of the original theory is once again smaller than the modified theory, and the angular spread wider. In addition, while both theories predict that the peak of the scattering function is shifted from the specular direction, the original theory predicts a larger shift. Even more significant is that the original Harvey-Shack theory continues to predict that all of the light will be diffusely scattered, while the modified Harvey-Shack theory predicts that the *TIS* will drop to 0.465 for this incident angle. Comparing the theories with the experimental data, it is once again obvious that the modified Harvey-Shack theory is a vast improvement over the original theory, especially at large incident angles. Even so, the agreement of the modified theory with the experimental data is far from ideal. This is understandable, however, as it can not be expected to work well with such wide angle scattering at large incident angles.

In Figure 5-15, we are once again comparing the original and modified Harvey-Shack theories with experimental data for the O'Donnell-Mendez surface, this time for visible light at 0.6328  $\mu\text{m}$ . At this wavelength,  $\sigma_s/\lambda = 3.59$ , and the surface can be considered very rough. Both the original and modified theories predict that all of the light will be diffusely scattered, with no specular reflection. The disagreement between the theories is once again quite severe, however, with the original theory having a much smaller peak and a much larger angular spread. The modified theory may be an improvement, but its agreement with the data is still not very good. The peak of the modified theory is once again shifted inside of the specular direction, but in this case the data does not exhibit the same shift. The slope of the scattering function in the

backwards scattering direction is also much steeper for the modified Harvey-Shack prediction than it is for the experimental data. Once again, the inaccuracy of the theory should not be surprising, since the assumption of small angle scattering has been violated.

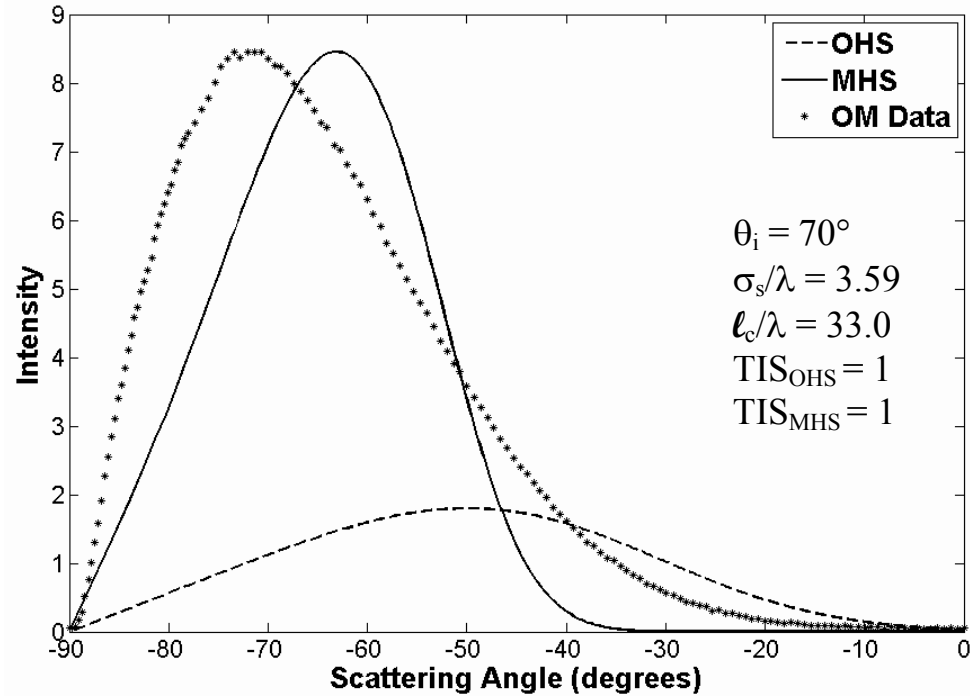


Figure 5-15: MHS compared to OHS and OM experimental data for  $\sigma_s/\lambda = 3.59$ ,  $l_c/\lambda = 33.0$ , and  $\theta_i = 70^\circ$

### 5.3 The Generalized Harvey-Shack Formulation

The modified version of the Harvey-Shack theory was clearly an improvement over the original Harvey-Shack theory, especially for anything larger than paraxial incident angles. However, the restriction of small angular spread of the scattering function, which becomes more stringent at large incident angles, is very limiting. We

will remove this limitation in the following development by generalizing the Harvey-Shack theory for large incident and scattering angles.

Figure 5-16 illustrates radiation incident on a scattering surface at an arbitrary incident angle,  $\theta_i$ . It is obvious from examining the figure that the optical path difference introduced upon reflection depends not just on the surface height and incident (and specular) angle, but also on the scattering angle  $\theta_s$ . The OPD can be written as

$$OPD = (\cos \theta_i + \cos \theta_s) h(\hat{x}, \hat{y}; 0). \quad (5.35)$$

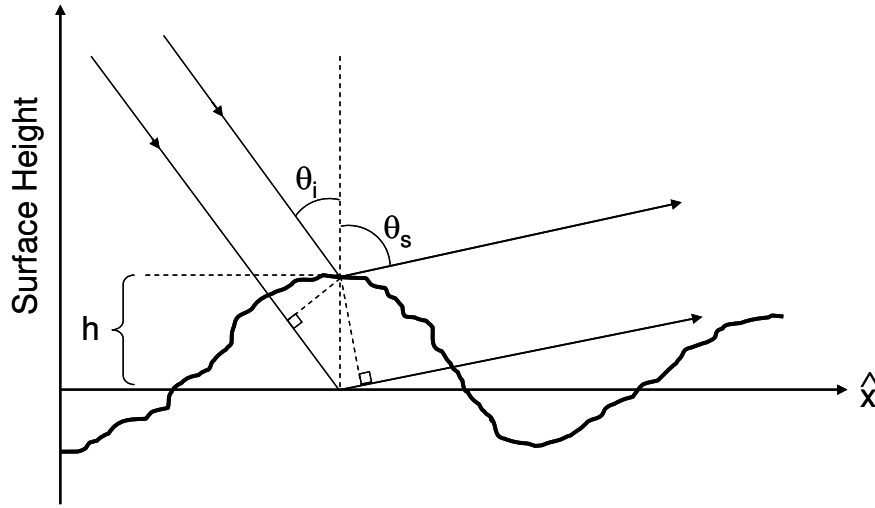


Figure 5-16: Illustration of the OPD for a ray scattered at an arbitrary angle  $\theta_s$

The random phase variation of the reflected wavefront can therefore be written as

$$\phi(\hat{x}, \hat{y}) = (2\pi / \lambda) OPD = 2\pi(\gamma_i + \gamma_s) \hat{h}(\hat{x}, \hat{y}; 0), \quad (5.36)$$

where  $\gamma_i = \cos \theta_i$  and  $\gamma_s = \cos \theta_s$  . (5.37)

If we return to the derivation of the original Harvey-Shack theory which was summarized in chapter two, we can use equation 5.36 to rewrite the random component of the pupil function given by equation 2.97 as

$$P_R(\hat{x}, \hat{y}; 0) = a_s(\hat{x}, \hat{y}; 0) \exp \left[ i 2 \pi (\gamma_i + \gamma_s) \hat{h}(\hat{x}, \hat{y}; 0) \right] . \quad (5.38)$$

Substituting equation 5.38 into equation 2.97, and completing the derivation as before results in a surface transfer function given by

$$H_S(\hat{x}, \hat{y}; \gamma_i, \gamma_s) = \exp \left\{ - \left[ 2 \pi \hat{\sigma}_s (\gamma_i + \gamma_s) \right]^2 \left[ 1 - C_s(\hat{x}, \hat{y}) / \sigma_s^2 \right] \right\} . \quad (5.39)$$

This generalized Harvey-Shack transfer function is in reality a two-parameter family of surface transfer functions. A different transfer function is required for each incident *and* scattering angle. The angle spread function is given by

$$ASF(\alpha_s, \beta_s) = \mathcal{F} \left\{ H_S(\hat{x}, \hat{y}; \gamma_i, \gamma_s) \exp(-i 2 \pi \alpha_o \hat{x}) \right\} \Big|_{\alpha=\alpha_s, \beta=\beta_s} . \quad (5.40)$$

Equation 5.40 corresponds to the light scattered in the  $\alpha_s, \beta_s$  direction. The direction cosines  $\alpha_s$  and  $\beta_s$  are related to  $\gamma_s$  by

$$\gamma_s = \sqrt{1 - \alpha_s^2 - \beta_s^2} . \quad (5.41)$$

As before, the surface transfer function can be written in the form

$$H_S(\hat{x}, \hat{y}; \gamma_i, \gamma_s) = A + B G(\hat{x}, \hat{y}; \gamma_i, \gamma_s) , \quad (5.42)$$



where 
$$A = \exp \left\{ - \left[ 2\pi (\gamma_i + \gamma_s) \hat{\sigma}_s \right]^2 \right\}, \quad (5.43)$$

$$B = 1 - \exp \left\{ - \left[ 2\pi (\gamma_i + \gamma_s) \hat{\sigma}_s \right]^2 \right\}, \quad (5.44)$$

and 
$$G(\hat{x}, \hat{y}; \gamma_i, \gamma_s) = \frac{\exp \left\{ \left[ 2\pi (\gamma_i + \gamma_s) \right]^2 \hat{C}(\hat{x}, \hat{y}) \right\} - 1}{\exp \left[ 2\pi (\gamma_i + \gamma_s) \hat{\sigma}_s \right]^2 - 1}. \quad (5.45)$$

The *ASF* can then be written as

$$ASF(\alpha_s, \beta_s) = \left[ A \delta(\alpha - \alpha_o, \beta) + S(\alpha - \alpha_o, \beta) \right] \Big|_{\alpha=\alpha_s, \beta=\beta_s}, \quad (5.46)$$

where 
$$S(\alpha - \alpha_o, \beta) = B \mathcal{F} \left\{ G(\hat{x}, \hat{y}; \gamma_i, \gamma_s) \exp(-i2\pi\alpha_o\hat{x}) \right\}. \quad (5.47)$$

Equations 5.40 and 5.46 indicate that for a given incident angle, a different Fourier transform needs to be performed in order to calculate the *ASF* for each scattering angle. This process can be avoided if the Fourier transform can be solved analytically. When this is the case,  $\gamma_s$  is just treated as a constant since it is not a function of the variables of integration  $\hat{x}$  and  $\hat{y}$ . When a numerical solution is required, multiple transforms will indeed have to be performed in order to calculate the entire angle spread function.

Since the delta function in equation 5.46 is equal to zero except when  $\alpha = \alpha_o$ , equation 5.43 corresponds to the percentage of the total power that resides in the specularly reflected light when  $\gamma_i = \gamma_s$ .  $A$  is then given by

$$A = \exp\left\{-\left[4\pi\gamma_i\hat{\sigma}_s\right]^2\right\}. \quad (5.48)$$

This is the same value predicted by the modified Harvey-Shack theory. The percentage of the total power that is diffusely scattered is therefore given by

$$B = 1 - A = 1 - \exp\left\{-\left[4\pi\gamma_i\hat{\sigma}_s\right]^2\right\}. \quad (5.49)$$

Once the *ASF* is known over the entire observation hemisphere, equation 5.21 can be used to renormalize the *ASF* to unit volume and thus ensure conservation of energy.

### 5.3.1 Smooth Surface Approximation

For smooth surfaces, we will compare the predictions of the generalized Harvey-Shack theory to both the modified Harvey-Shack theory and the well-established Rayleigh-Rice scattering theory. When the roughness of a surface is small compared to the wavelength of incident light, we can again make an approximation to the surface transfer function. Letting  $\hat{\sigma}_s \ll \lambda$  in equations 5.43-5.45 yields

$$A \approx 1 - \left[2\pi\hat{\sigma}_s(\gamma_i + \gamma_s)\right]^2, \quad (5.50)$$

$$B \approx \left[2\pi\hat{\sigma}_s(\gamma_i + \gamma_s)\right]^2, \quad (5.51)$$

and

$$G(\hat{x}, \hat{y}) = C_s(\hat{x}, \hat{y}) / \sigma_s^2. \quad (5.52)$$

Using equation 5.47, the scattering function can be written as

$$S(\alpha, \beta) = \frac{4\pi^2}{\lambda^2} (\gamma_i + \gamma_s)^2 \mathcal{F}\{C_s(\hat{x}, \hat{y})\}. \quad (5.53)$$

Writing this in integral form gives

$$S(\alpha, \beta) = \frac{4\pi^2}{\lambda^2} (\gamma_i + \gamma_s)^2 \int_{-\infty}^{\infty} \int_{-\infty}^{\infty} C_s(\hat{x}, \hat{y}) \exp[-i2\pi(\alpha\hat{x} + \beta\hat{y})] d\hat{x}d\hat{y}. \quad (5.54)$$

Performing a change of variables from  $(\hat{x}, \hat{y})$  to  $(x, y)$  yields

$$S(\alpha, \beta) = \frac{4\pi^2}{\lambda^2} (\gamma_i + \gamma_s)^2 \frac{1}{\lambda^2} \int_{-\infty}^{\infty} \int_{-\infty}^{\infty} C_s(x, y) \exp[-i2\pi(f_x x + f_y y)] dx dy. \quad (5.55)$$

The integral in 5.55 is the Fourier transform of the autocovariance function  $C_s(x, y)$ , which is simply the power spectral density of the surface. The scattering function for the generalized Harvey-Shack (GHS) theory can therefore be written in terms of spherical angles as

$$S_{GHS}(\theta_s, \phi_s; \theta_i) = \frac{4\pi^2}{\lambda^4} (\cos \theta_i + \cos \theta_s)^2 \text{PSD}(f_x, f_y), \quad (5.56)$$

where from the grating equation

$$f_x = \frac{\sin \theta_s \cos \phi_s - \sin \theta_i}{\lambda}, \quad f_y = \frac{\sin \theta_s \sin \phi_s}{\lambda}. \quad (5.57)$$

Using equation 5.23, we can write the diffusely scattered intensity as

$$I_{GHS}(\theta_s, \phi_s; \theta_i) = P_i \frac{4\pi^2}{\lambda^4} (\cos \theta_i + \cos \theta_s)^2 \cos \theta_s \text{PSD}(f_x, f_y). \quad (5.58)$$

Recall from equation 5.31 that the scattered intensity predicted by the modified Harvey-Shack (MHS) theory for a perfectly conducting smooth surface is given by

$$I_{MHS}(\theta_s, \phi_s; \theta_i) = P_i \left( \frac{16\pi^2}{\lambda^4} \right) \cos^2 \theta_i \cos \theta_s \text{PSD}(f_x, f_y), \quad (5.59)$$

and from equation 5.32 the scattered intensity predicted by the Rayleigh-Rice (RR) theory for a perfectly conducting smooth surface and TE polarization is given by

$$I_{RR}(\theta_s, \phi_s; \theta_i) = P_i \left( \frac{16\pi^2}{\lambda^4} \right) \cos \theta_i \cos^2 \theta_s \text{PSD}(f_x, f_y). \quad (5.60)$$

Comparing equations 5.58, 5.59, and 5.60 we can see that all three equations are approximately equal for small incident and scattering angles when  $\cos \theta_i \approx \cos \theta_s \approx 1$ . All three equations should be exactly equal when  $\theta_s = \theta_i$ , or when  $\theta_s = \theta_o$  since  $\cos \theta_i = \cos \theta_o$ .

To compare the modified and generalized Harvey-Shack theories with the Rayleigh-Rice theory, we will again assume a scattering surface with the Gaussian autocovariance function in equation 5.33. The *PSD* is then given by equation 5.34. The ratio of the RMS surface roughness to the wavelength will again be assumed to be 0.02.

Figure 5-17 shows a comparison of the three theories for normal incidence and an  $\ell_c/\lambda$  ratio of five. The angular spread of the scattering function is less than 20 degrees wide, which for normal incidence is relatively small. For this set of parameters, all three theories yield virtually identical results.

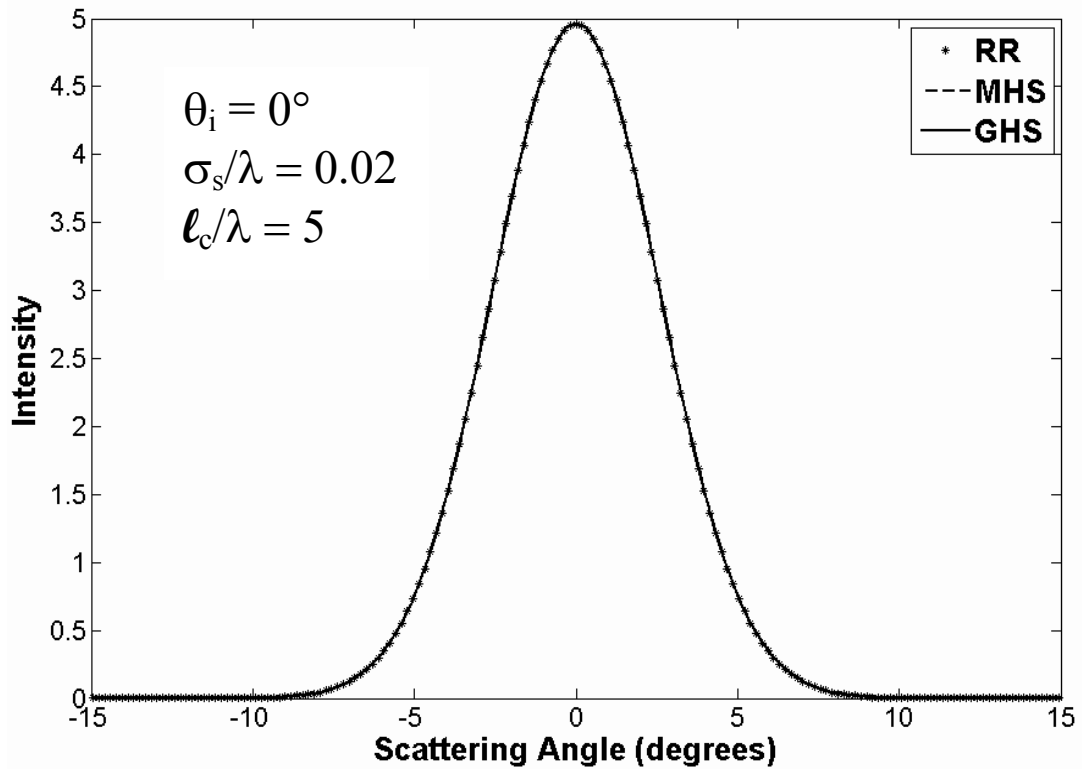


Figure 5-17: GHS and MHS compared to RR for  $\theta_i = 0^\circ$  and  $\ell_c/\lambda = 5$

In Figure 5-18, the angle of incidence has been kept at 0 degrees, but the ratio of  $\ell_c/\lambda$  has been decreased by a factor of ten to 0.5. This results in a much larger angular spread of the scattering function, and the modified Harvey-Shack theory departs from the Rayleigh-Rice prediction at larger scattering angles. The generalized Harvey-Shack theory, however, agrees quite well with the Rayleigh-Rice theory even at large scattering angles.

In Figures 5-19, 5-20, and 5-21, the modified Harvey-Shack, generalized Harvey-Shack, and Rayleigh-Rice theories are compared for incident angles of 20, 50, and 70 degrees and  $\ell_c/\lambda$  ratios of 10, 5, 1, and 0.5.

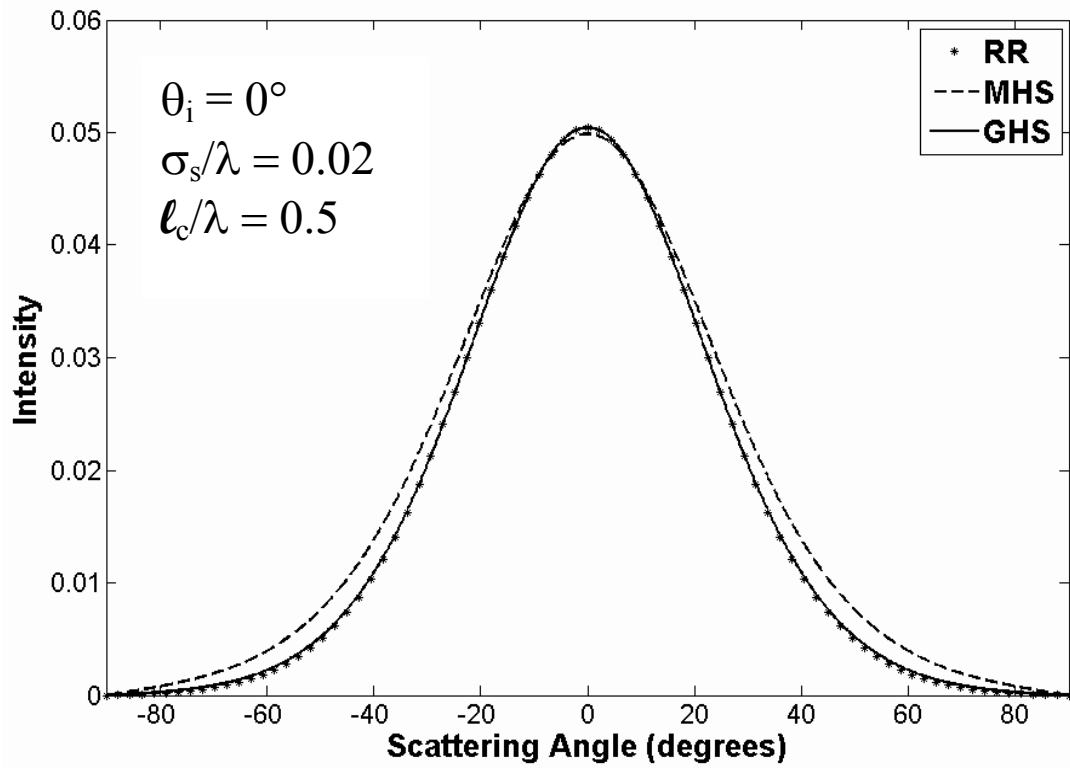


Figure 5-18: GHS and MHS compared to RR for  $\theta_i = 0^\circ$  and  $\ell_c/\lambda = 0.5$

For the 20 degree incident angle in Figure 5-19, the three theories agree extremely well for  $\ell_c/\lambda = 10$  and  $\ell_c/\lambda = 5$  for which the scattering function is relatively narrow. For  $\ell_c/\lambda = 1$  and  $\ell_c/\lambda = 0.5$ , the generalized Harvey-Shack and Rayleigh-Rice theories continue to agree quite well, while the modified Harvey-Shack theory departs from the other two. The only noticeable departure of the generalized Harvey-Shack from the Rayleigh-Rice occurs at the larger negative scattering angles for  $\ell_c/\lambda = 0.5$ , and even this is relatively minor.

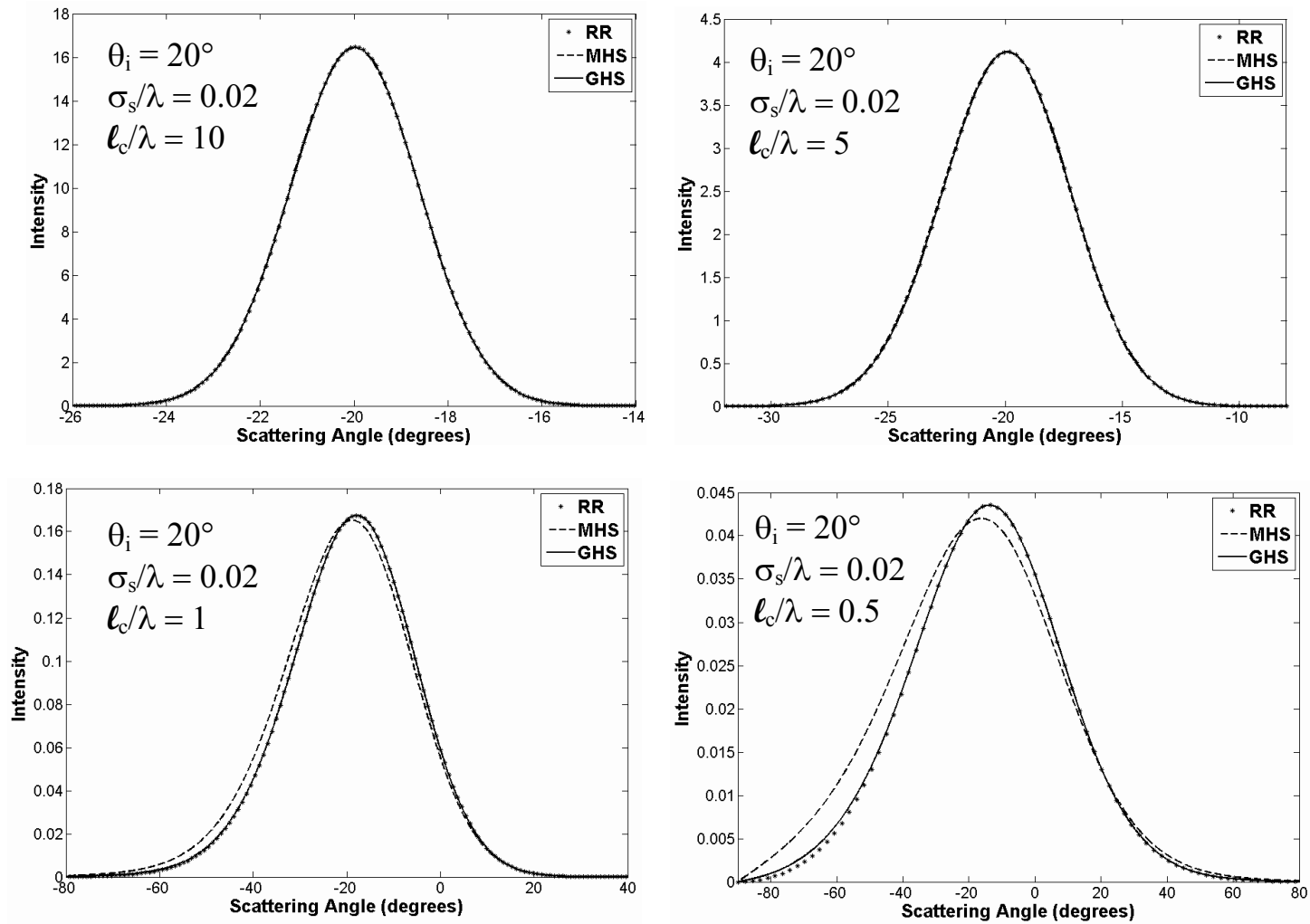


Figure 5-19: GHS and MHS compared to RR for  $\theta_i = 20^\circ$  and  $\ell_c/\lambda = 10, 5, 1$ , and  $0.5$

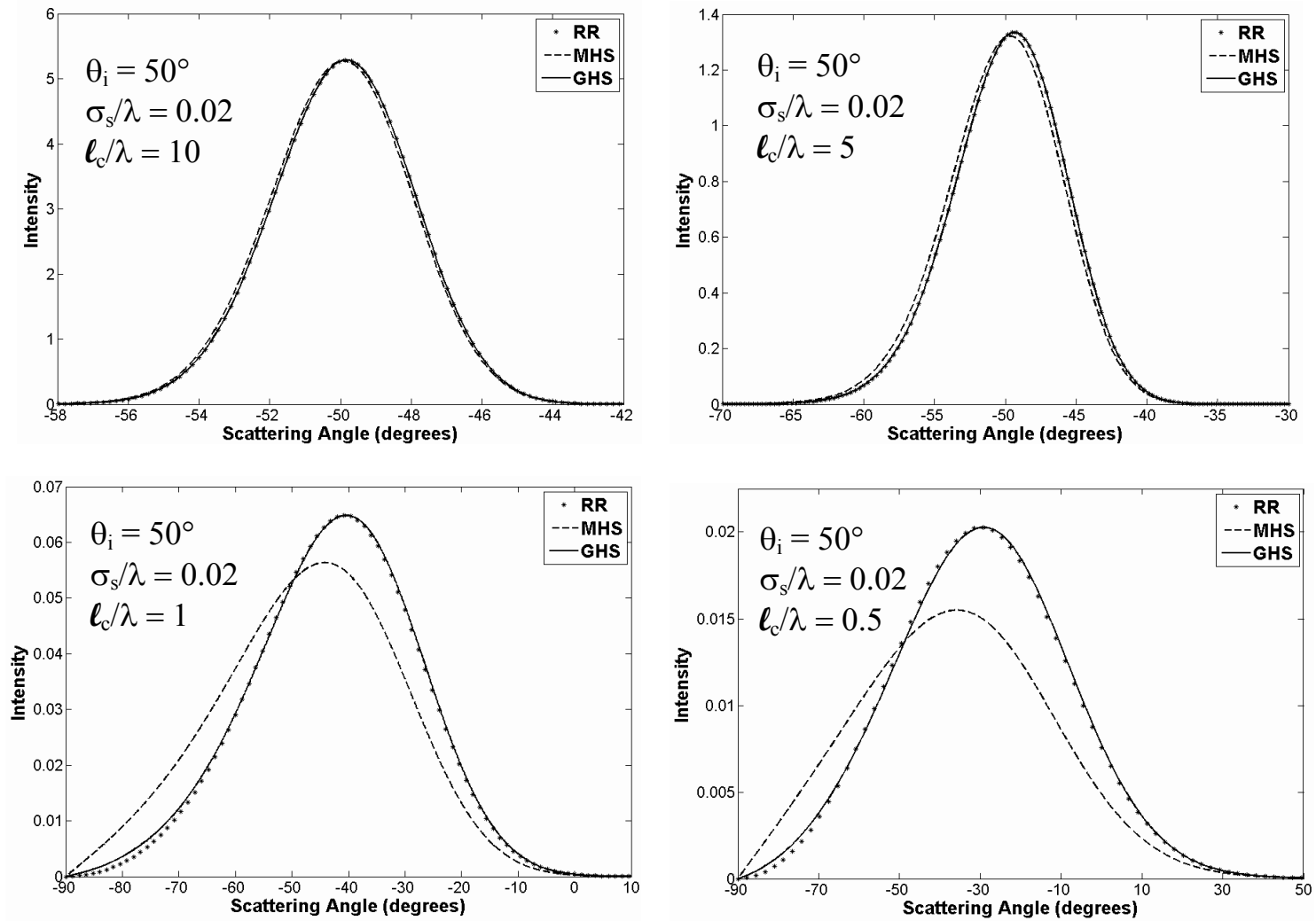


Figure 5-20: GHS and MHS compared to RR for  $\theta_i = 50^\circ$  and  $\ell_c/\lambda = 10, 5, 1$ , and  $0.5$



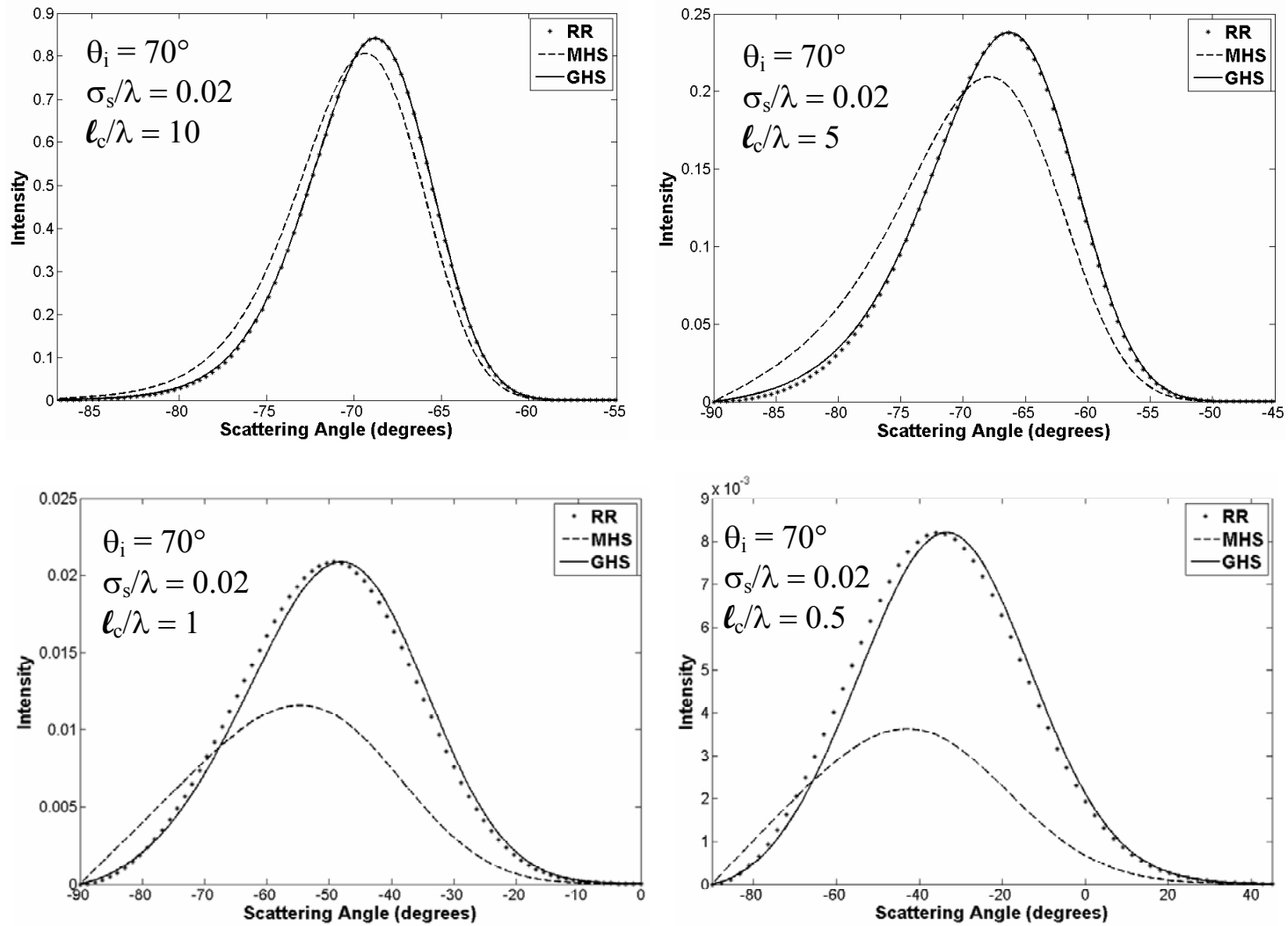


Figure 5-21: GHS and MHS compared to RR for  $\theta_i = 70^\circ$  and  $\ell_c/\lambda = 10, 5, 1$ , and  $0.5$

For the 50 degree incident angle in Figure 5-20, the modified Harvey-Shack theory is just beginning to depart from the other two when  $\ell_c/\lambda = 10$  and  $\ell_c/\lambda = 5$ . For the other two  $\ell_c/\lambda$  values, the departure of the modified Harvey-Shack theory is quite drastic. The generalized Harvey-Shack theory, on the other hand, agrees very well with the Rayleigh-Rice theory for all values of  $\ell_c/\lambda$ . The only departure again comes for the larger negative scattering angles for both  $\ell_c/\lambda = 1$  and  $\ell_c/\lambda = 5$ .

For the 70 degree incident angle in Figure 5-21, the modified Harvey-Shack theory departs significantly from the other two theories for all values of  $\ell_c/\lambda$ . The generalized Harvey-Shack theory and Rayleigh-Rice theory agree very well for  $\ell_c/\lambda = 10$  and  $\ell_c/\lambda = 5$ . For both  $\ell_c/\lambda = 1$  and  $\ell_c/\lambda = 0.5$ , the two theories depart slightly. The shapes of the scattering function predicted by both theories are virtually identical; however the generalized Harvey-Shack result is shifted slightly towards zero degrees. Despite this discrepancy, the agreement is still quite good.

Most optical surfaces do not have a Gaussian autocovariance function and *PSD*. They instead tend to have a *PSD* with an inverse power law falloff at larger spatial frequencies. A sufficiently general model for this behavior is the abc or K-correlation model [46,113] The autocovariance function is given by

$$C_s(r) = (2\pi)^{1/2} \frac{a}{b} \frac{2^{-c/2}}{\Gamma(c/2)} \left(\frac{2\pi r}{b}\right)^{(c-1)/2} \mathcal{K}_{(c-1)/2}\left(\frac{2\pi r}{b}\right), \quad (5.61)$$

where a, b, and c are fitting parameters,  $\mathcal{K}_{(c-1)/2}$  is the modified Bessel function of the second kind [114], and  $r = \sqrt{(x^2 + y^2)}$ . The two-dimensional PSD is the Fourier

transform of equation 5.61 and is given by

$$PSD(f_x, f_y) = \frac{1}{2\sqrt{\pi}} \frac{\Gamma[(c+1)/2]}{\Gamma(c/2)} \frac{ab}{[1+b^2(f_x^2 + f_y^2)]^{(c+1)/2}}. \quad (5.62)$$

The parameters  $a$  and  $b$  are usually expressed in units of  $\text{\AA}^2\text{-}\mu\text{m}$  and  $\mu\text{m}^{-1}$ , while the parameter  $c$  is unitless. If  $c$  is greater than 1, the  $PSD$  will have a finite volume equal to the square of the RMS roughness given by

$$\sigma_s^2 = \frac{\sqrt{\pi}}{c-1} \frac{\Gamma[(c+1)/2]}{\Gamma(c/2)} \frac{a}{b}. \quad (5.63)$$

The intensity predicted by the generalized Harvey-Shack and Rayleigh-Rice theories for the K-correlation model can be calculated by substituting equation 5.62 into equations 5.58 and 5.60, respectively. Figure 5-22 shows a comparison of the two theories for a surface with a K-correlation  $PSD$  with  $a = 1.5\text{E}5$ ,  $b = 300$ ,  $c = 1.4$ , and incident radiation with a wavelength of  $0.6328 \mu\text{m}$  for incident angles of 0, 20, 50, and 70 degrees.

For all four angles of incidence in Figure 5-22, the biggest disagreement between the two theories occurs at the larger scattering angles. Note however that the intensity is plotted on a log scale. The majority of the power is contained in near-specular region, and very little is contained out at the larger angles. The differences between the two theories are therefore relatively minor, and the agreement can still be considered very good. This disagreement will be explored further in section 5.3.3 when we discuss the inverse scattering problem.

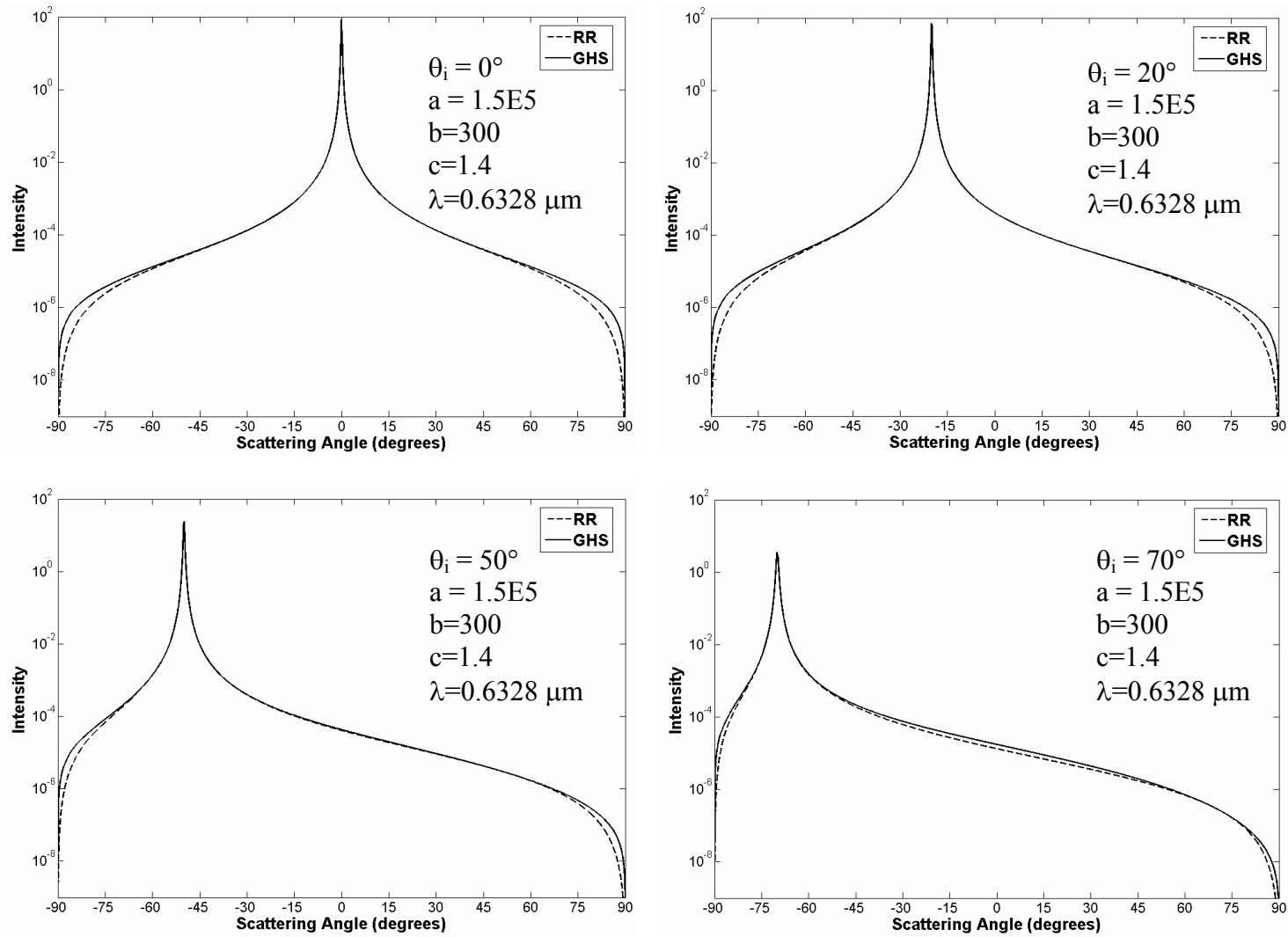


Figure 5-22: GHS and RR for a K-Correlation PSD with  $a = 1.5E5$ ,  $b = 300$ ,  $c = 1.4$ ,  $\lambda = 0.6328 \mu\text{m}$  for  $\theta_i = 0^\circ$ ,  $20^\circ$ ,  $50^\circ$ , and  $70^\circ$

### 5.3.2 Quasi-Vectorizing The Harvey-Shack Theory For Smooth Surfaces

One of the limitations of the original Harvey-Shack theory is the fact that since it is a scalar theory, it is unable to account for polarization effects. This is still true for the generalized Harvey-Shack theory presented in the last section. All of the comparisons we have made so far have assumed that the scattering surface is perfectly conducting and that the incident light was TE polarized. The angle spread function was derived to be independent of any material effects of the scattering surface. The *ASF* is not a quantity that can in reality be measured, however. Intensity is the quantity that is actually measured in practice, and when it is it will include the effects of both material properties (reflectance) and polarization.

The intensity for a non-perfectly conducting smooth surface as predicted by the generalized Harvey-Shack theory is given by:

$$I_{GHS}(\theta_s, \phi_s; \theta_i) = P_i R \frac{4\pi^2}{\lambda^4} (\cos \theta_i + \cos \theta_s)^2 \cos \theta_s \text{PSD}(f_x, f_y), \quad (5.64)$$

where  $R$  is the reflectance of the scattering surface. From equation 2.39, the intensity for the Rayleigh-Rice theory can be written as

$$I_{RR}(\theta_s, \phi_s; \theta_i) = P_i Q \frac{16\pi^2}{\lambda^4} \cos \theta_i \cos^2 \theta_s \text{PSD}(f_x, f_y), \quad (5.65)$$

where  $Q$  is the polarization dependent reflectance of the surface given by equations 2.44 through 2.52.

We have already shown in the previous section that apart from some small discrepancies at large scattering angles, equations 5.64 and 5.65 give virtually identical results for perfectly conducting (i.e.,  $R = Q = 1$ ) surfaces and TE polarized radiation. Therefore, we will quasi-vectorize the generalized Harvey-Shack theory for smooth surfaces by replacing the reflectance  $R$  in equation 5.64 with the polarization dependent reflectance  $Q$  of the Rayleigh-Rice theory. This will then allow us to account for polarization effects with the generalized Harvey-Shack theory, at least for smooth surfaces.

### 5.3.3 Inverse Scattering For Smooth Surfaces

Thus far in this chapter, we have discussed the prediction of surface scatter from known surface roughness in the form of the power spectral density or autocovariance function of a surface. It is often desirable to solve the inverse problem: calculation of surface roughness from scattering measurements. The first attempt at solving the inverse scattering problem was most likely that of Bennett and Porteus [115] based on the scalar theory of Davies [2]. The Rayleigh-Rice vector theory is the most widely used method of performing inverse scattering from smooth surfaces, and has been discussed in detail by Stover [3].

For smooth, clean, front-surface reflecting surfaces, the *PSD* of a surface is related to the scattering *BRDF* using the Rayleigh-Rice theory by

$$BRDF_{RR}(\theta_s, \phi_s; \theta_i) = Q \left( \frac{16\pi^2}{\lambda^4} \right) \cos \theta_i \cos \theta_s \text{PSD}(f_x, f_y), \quad (5.66)$$

where, once again,  $f_x$  and  $f_y$  are related to the incident and scattering angles by

$$f_x = \frac{\sin \theta_s \cos \phi_s - \sin \theta_i}{\lambda}, \quad f_y = \frac{\sin \theta_s \sin \phi_s}{\lambda}. \quad (5.67)$$

Using the generalized Harvey-Shack theory, the relationship between the  $BRDF$  and the surface  $PSD$  is given by

$$BRDF_{GHS}(\theta_s, \phi_s; \theta_i) = Q \left( \frac{4\pi^2}{\lambda^4} \right) (\cos \theta_i + \cos \theta_s)^2 \text{PSD}(f_x, f_y), \quad (5.68)$$

where  $f_x$  and  $f_y$  are given by equation 5.67, and we have used the polarization-dependent surface reflectance as discussed in section 5.3.2.

Given a measured  $BRDF$ , we can therefore invert equations 5.66 or 5.68 and solve for the  $PSD$ . The  $PSD$  determined by this procedure will actually be a bandwidth-limited portion of the actual surface  $PSD$ ; the frequency limits will depend on both the wavelength of light and the incident angle as can be seen from equation 5.67. The maximum frequency at which the  $PSD$  can be determined will increase with increasing angle of incidence and decreasing wavelength. This is useful in that the  $PSD$  calculated from scattering measurements for a given wavelength and angle of incidence can then be used to calculate angle-limited scattering from different wavelengths and angles of incidence. In addition, if the  $PSD$  is well behaved, it can be fit with an analytical function and extrapolated to higher frequencies so that scattering can be calculated for both larger and smaller wavelengths and angles of incidence.

It is important to realize, however, that not all surfaces will scale with wavelength in the manner described. Some may scale correctly over a limited wavelength region, while some may not scale correctly at all. Surfaces that do not scale correctly at a certain wavelength most likely do not meet the requirements of being smooth, clean, and front-surface reflecting at that wavelength, even though they may meet these requirements at other wavelengths.

As an example of the inverse scattering process, we will use a measured scattering *BRDF* from a molybdenum mirror surface to calculate the surface *PSD*. We will then use that *PSD* to predict the *BRDF* at different angles of incidence and compare it to experimental measurements. All of the *BRDF* and reflectance measurements for this mirror surface were performed and provided to us by John Stover of The Scatterworks [116].

The measured *BRDF* for the molybdenum mirror for an incident angle of  $-5$  degrees, a wavelength of  $0.488\mu\text{m}$ , and TE polarization in the plane of incidence is shown in Figure 5-23. Note that the sharp drop in the curve occurs when the detector passes through the incident beam. The *BRDF* spans several orders of magnitude and is fairly symmetric about the location of specular reflection.

The reflectance of the molybdenum mirror is shown in Figure 5-24. The reflectance was measured at three different angles and a polynomial fit to the data was then performed, with the assumption that the reflectance goes to unity at 90 degrees. The equation of the polynomial fit is given in the figure.



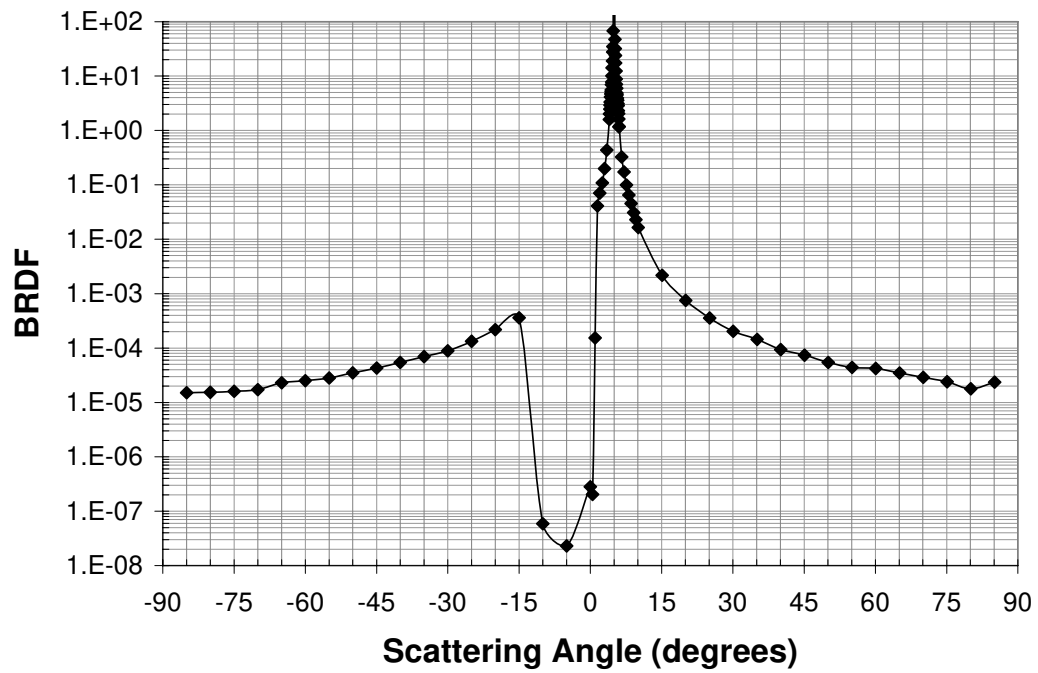


Figure 5-23: Measured  $BRDF$  of molybdenum mirror for  $\theta_i = -5^\circ$  and  $\lambda = 0.488 \mu\text{m}$

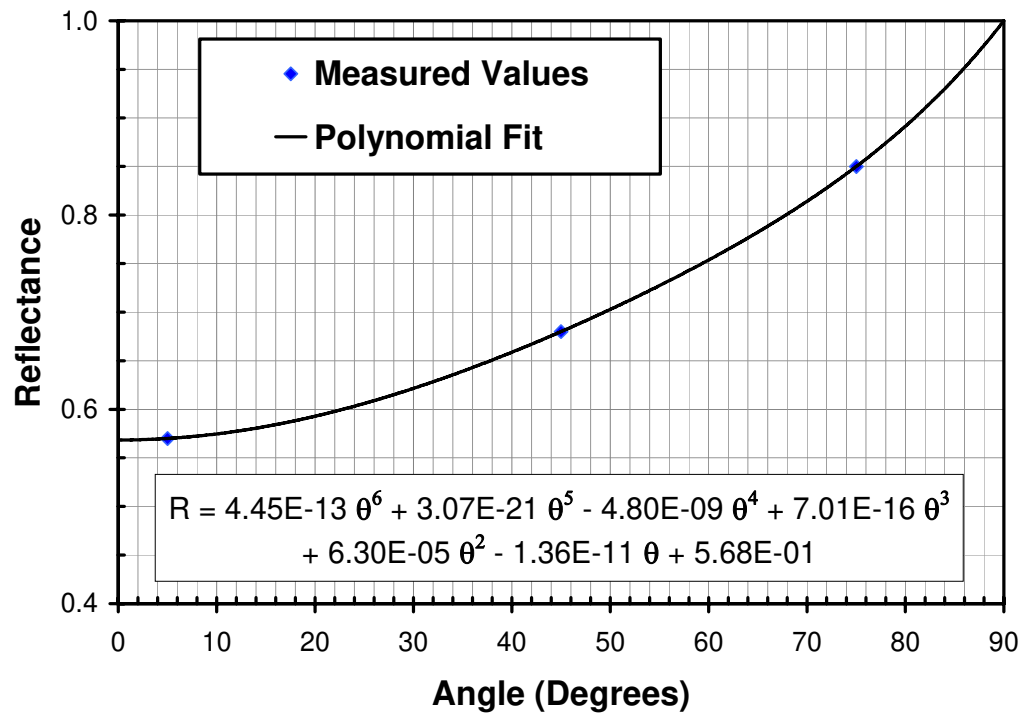


Figure 5-24: Reflectance of the molybdenum mirror as a function of angle

The *PSD* of the mirror can now be calculated from the *BRDF* in Figure 5-23 through the use of equation 5.66 for the Rayleigh-Rice theory or equation 5.68 for the generalized Harvey-Shack theory. In order to do so, we need to know the polarization dependent reflectance,  $Q$ . For TE polarized incident radiation and measurement in the plane of incidence,  $Q$  is given by [3]

$$Q(\theta_o, \theta_s) = \sqrt{R(\theta_o)R(\theta_s)}, \quad (5.69)$$

where  $R(\theta_o)$  is the reflectance in the specular direction and  $R(\theta_s)$  is the reflectance in the scattered direction. These reflectance values can be calculated through the use of the polynomial equation given in Figure 5-24.

The *PSD* predicted using equation 5.66 for the Rayleigh-Rice theory is shown in Figure 5-25, and the generalized Harvey-Shack prediction from equation 5.68 is shown in Figure 5-26. Both theories predict a *PSD* that appears linear when plotted on a log-log scale, and the agreement between the two is excellent up until a frequency of  $1 \mu\text{m}^{-1}$ . Beyond that point, the Rayleigh-Rice prediction demonstrates a sharp up-turn. The generalized Harvey-Shack prediction has a very slight up-turn at the end, but it is not nearly as drastic as that of the Rayleigh-Rice theory. It is possible that this up-turn is due to particulate scattering, where light scattering off of particles either in the air or on the surface itself dominates the surface scattering. This does not explain the difference between the two theories, however. Recall from section 5.3.1 that intensity predictions for the Rayleigh-Rice and generalized Harvey-Shack theories tend to disagree only at large scattering angles. This disagreement becomes even more apparent when comparing

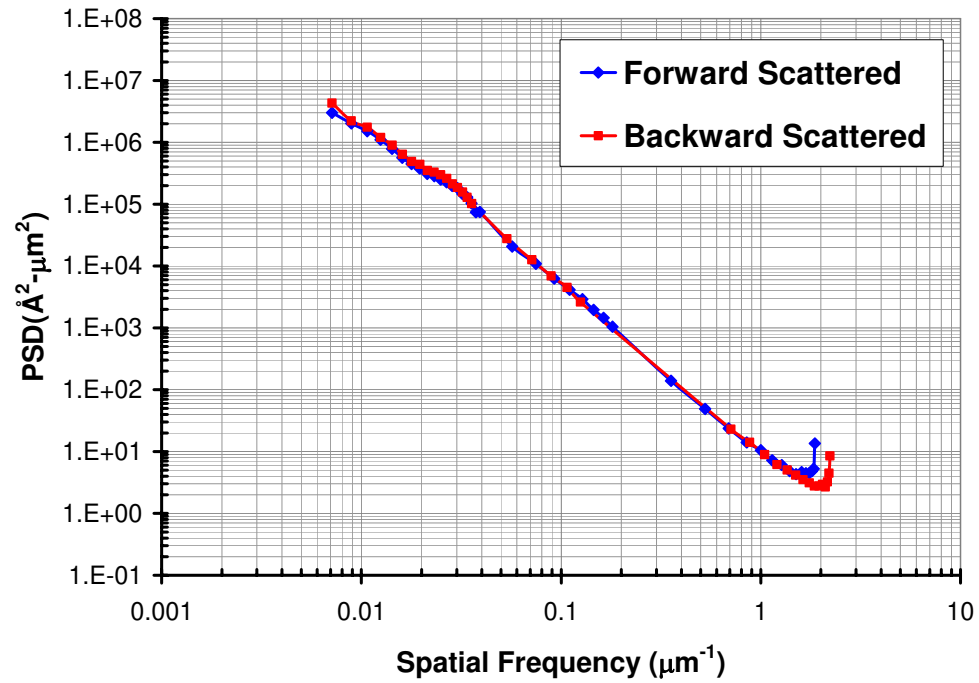


Figure 5-25: Predicted *PSD* of the molybdenum mirror using the Rayleigh-Rice theory and measured *BRDF* data for  $\theta_i = -5^\circ$  and  $\lambda = 0.488 \mu\text{m}$

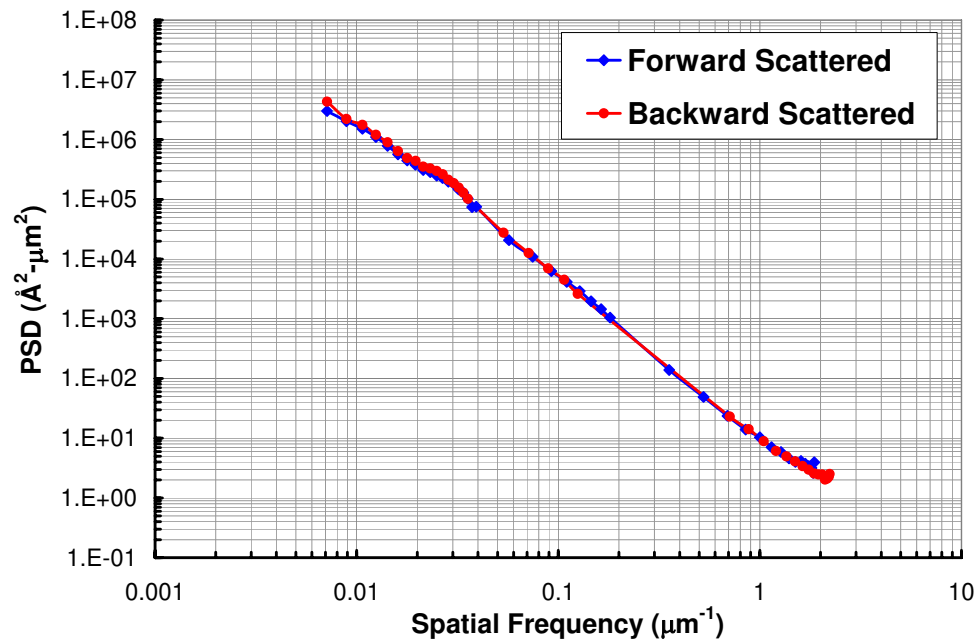


Figure 5-26: Predicted *PSD* of the molybdenum mirror using the generalized Harvey-Shack theory and measured *BRDF* data for  $\theta_i = -5^\circ$  and  $\lambda = 0.488 \mu\text{m}$

the  $BRDF$ s predicted by the two theories. Figure 5-27 shows predicted  $BRDF$ s for a surface with a K-correlation  $PSD$  given by equation 5.62 with  $a = 1.5E5$ ,  $b = 300$ ,  $c = 1.4$ , and incident radiation with a wavelength of  $0.6328 \mu\text{m}$  for normal incidence. The agreement between the two theories is extremely good until approximately  $\pm 60$  degrees. After that, the Rayleigh-Rice prediction begins dropping sharply to zero, while the generalized Harvey-Shack maintains a steady rate of decrease and has a non-zero value at  $\pm 90$  degrees.

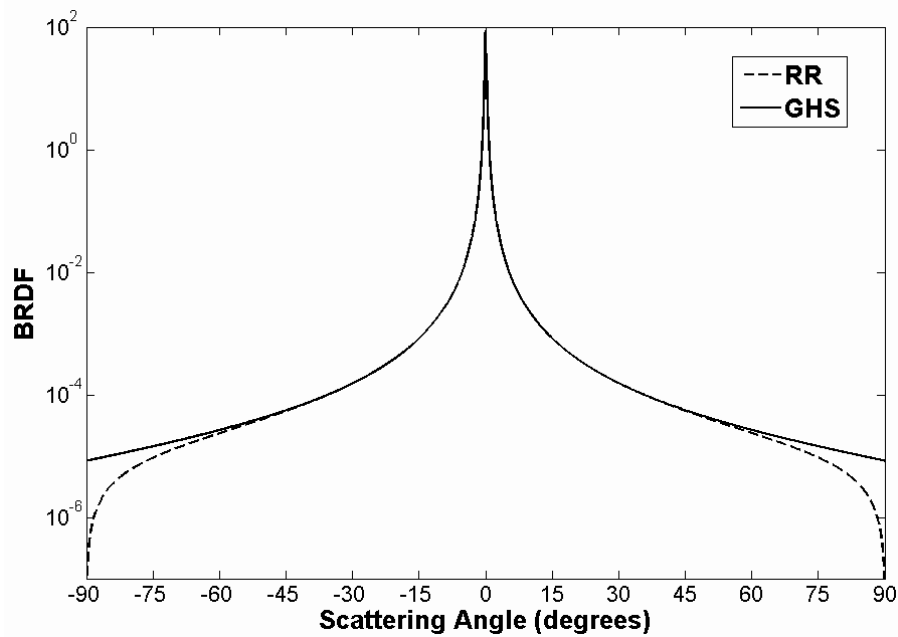


Figure 5-27: GHS and RR predictions of  $BRDF$  for a K-Correlation  $PSD$  with  $a = 1.5E5$ ,  $b = 300$ ,  $c = 1.4$ , and  $\lambda = 0.6328 \mu\text{m}$  for normal incidence.

The fact that the  $BRDF$  predicted by the Rayleigh-Rice theory drops to zero at  $\pm 90$  degrees is a direct consequence of the factor  $\cos\theta_s$  in equation 5.66. The Rayleigh-Rice theory predicts that *all*  $BRDF$ s go to zero at  $\pm 90$  degrees. The  $BRDF$  is a

radiance distribution, and while intensity must tend to zero at  $\pm 90$  degrees, there is no requirement that radiance do so. We know, for instance, that the radiance of a Lambertian surface is a constant as a function of angle, and is therefore discontinuous at  $\pm 90$  degrees. We are therefore skeptical of the Rayleigh-Rice *BRDF* prediction at large scattering angles.

Figure 5-28 again shows the generalized Harvey-Shack prediction of the *PSD* of the molybdenum mirror, but with the addition of a K-correlation fit to the predicted *PSD*. The parameters of the K-correlation *PSD* are shown on the figure. We will use this fit to predict the scattered *BRDF* for incidence angles of 5, 45, and 75 degrees.

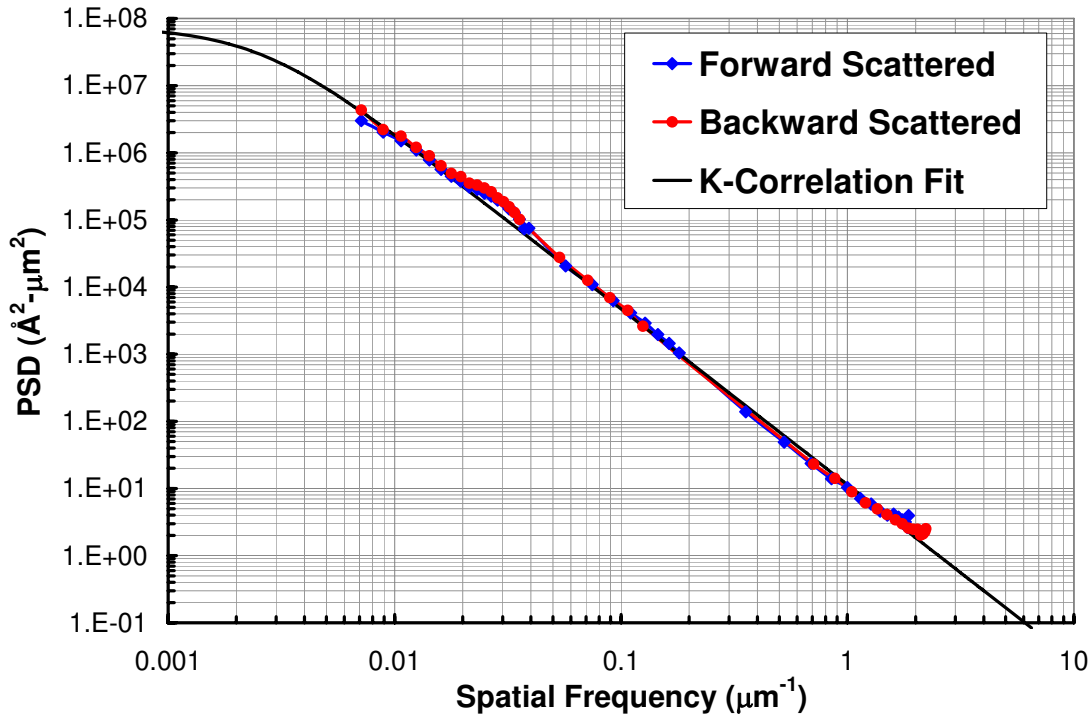


Figure 5-28: K-correlation fit to the *PSD* prediction shown in Figure 5-26

Figure 5-29 shows a comparison of the Rayleigh-Rice and generalized Harvey-Shack  $BRDF$  predictions with experimental data for an incident angle of  $-5$  degrees and a wavelength of  $0.488\text{ }\mu\text{m}$ . The two theories agree extremely well out to scattering angles of around 60 degrees. At larger angles, the generalized Harvey-Shack prediction seems to agree better with the measured data. As previously stated, the  $BRDF$  may be dominated by particulate scattering at large scattering angles, so this agreement may simply be fortuitous.

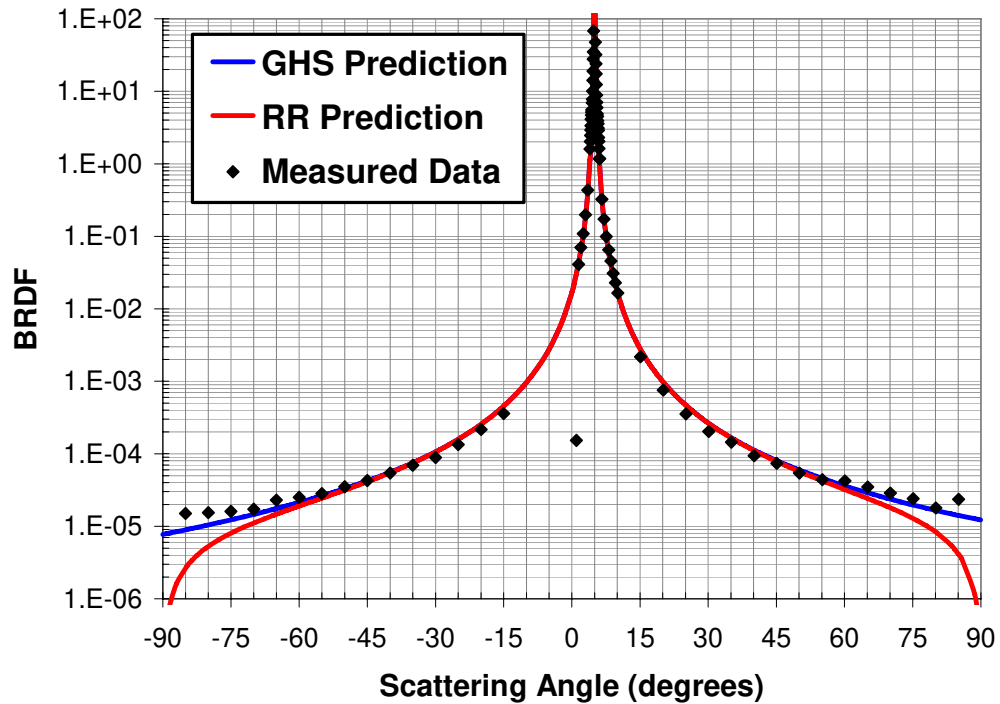


Figure 5-29: GHS and RR predictions of the  $BRDF$  for the molybdenum mirror compared to experimental data for  $\theta_i = -5^\circ$  and  $\lambda = 0.488$

Figure 5-30 shows a comparison of the two theories with experimental data for an incident angle of  $-45$  degrees and a wavelength of  $0.488\text{ }\mu\text{m}$ . The two theories agree extremely well with each other in the backscattered portion of the  $BRDF$ , again until approximately  $-60$  degrees, and both theories agree very well with the data out to  $-24$  degrees, or approximately  $70$  degrees from the location of specular reflection. Beyond that, both theories depart from the data, and this again may be due to the domination of particulate scatter at angles far from the specular direction. This does not explain the disagreement in the forward direction, however. The data at larger scattering angles in the forward direction does not tend to zero as predicted by the Rayleigh-Rice theory, but instead seems to more closely follow the generalized Harvey-Shack prediction.

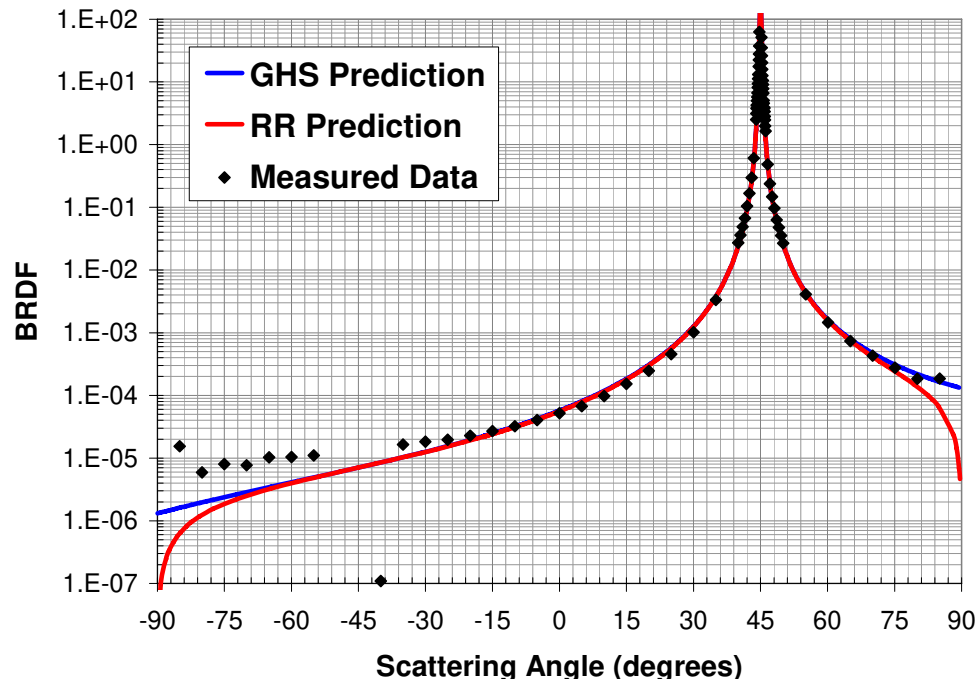


Figure 5-30: GHS and RR predictions of the  $BRDF$  for the molybdenum mirror compared to experimental data for  $\theta_i = -45^\circ$  and  $\lambda = 0.488$

Figure 5-31 shows a comparison of the two theories with experimental data for an incident angle of  $-75$  degrees and a wavelength of  $0.488\text{ }\mu\text{m}$ . The two theories agree very well with each other near the specular beam and out to approximately  $-80$  degrees in the backscattered portion of the *BRDF*; however there is a discrepancy between the two theories for angles between  $-75$  and  $+75$  degrees. Comparing equations 5.66 and 5.68, we can see that the two theories are only strictly equal when the scattering angle is equal to either the incident or specular angle. As the distance between the incident and specular angle increases, the disagreement between the two theories will increase at points in between those two angles. The two theories agree well with the data between  $15$  and  $80$  degrees, but they again disagree substantially at large negative scattering angles. Once again, this may be due to the dominance of particulate scatter.

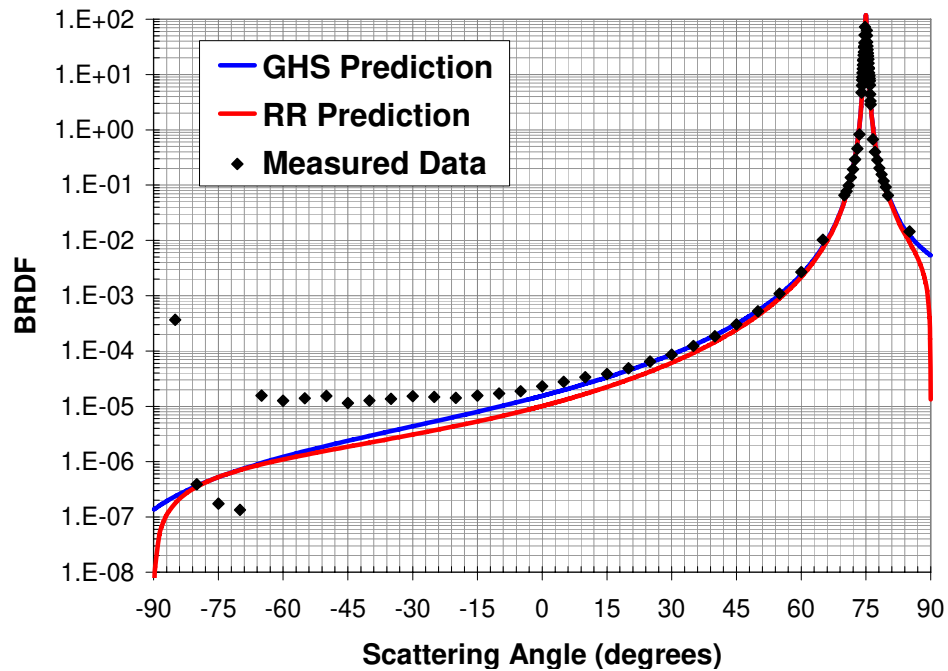


Figure 5-31: GHS and RR predictions of the *BRDF* for the molybdenum mirror compared to experimental data for  $\theta_i = -75^\circ$  and  $\lambda = 0.488$



### 5.3.4 Numerical Calculations For Rough Surfaces

When the roughness of a scattering surface is not small compared to the wavelength of the incident radiation, we cannot use the approximations of section 5.3.1. If no other approximations can be made that will result in an analytical solution of equation 5.40, numerical methods will be required to compute the scattered light distribution.

Recall that the surface transfer function for the generalized Harvey-Shack theory is given by

$$H_S(\hat{x}, \hat{y}; \gamma_i, \gamma_s) = \exp \left\{ - \left[ 2\pi \hat{\sigma}_s (\gamma_i + \gamma_s) \right]^2 \left[ 1 - C_s(\hat{x}, \hat{y}) / \sigma_s^2 \right] \right\}, \quad (5.70)$$

where  $\gamma_i = \cos \theta_i$  and  $\gamma_s = \sqrt{1 - \alpha_s^2 - \beta_s^2} = \cos \theta_s$ . (5.71)

The angle spread function, which consists of both the specular reflection and the diffusely scattered light distribution, is given by

$$ASF(\alpha_s, \beta_s) = \mathcal{F} \left\{ H_S(\hat{x}, \hat{y}; \gamma_i, \gamma_s) \exp(-i2\pi\alpha_o\hat{x}) \right\} \Big|_{\alpha=\alpha_s, \beta=\beta_s}, \quad (5.72)$$

where  $\alpha_o = \sin \theta_o$  and  $\gamma_s = \sqrt{1 - (\alpha_s^2 + \beta_s^2)}$ . (5.73)

When numerical solutions of equation 5.72 are required, the parameters  $\gamma_i$  and  $\gamma_s$  have to be specified before performing the Fourier transform. Calculating the scattering distribution over the entire observation space for a given angle of incidence will therefore

require a different transfer function and Fourier transform calculation for every scattering angle.

Direction cosine space is a very convenient space in which to perform the necessary calculations, as the entire observation hemisphere can be reduced to a circle with unit radius in the  $\alpha, \beta$  plane. Figure 5-32 shows a grid of discrete values in the  $\alpha, \beta$  plane along with the unit circle representing all space. This unit circle corresponds to  $\theta_s = 90^\circ$  for all values of  $\phi_s$  in the spherical coordinate system.

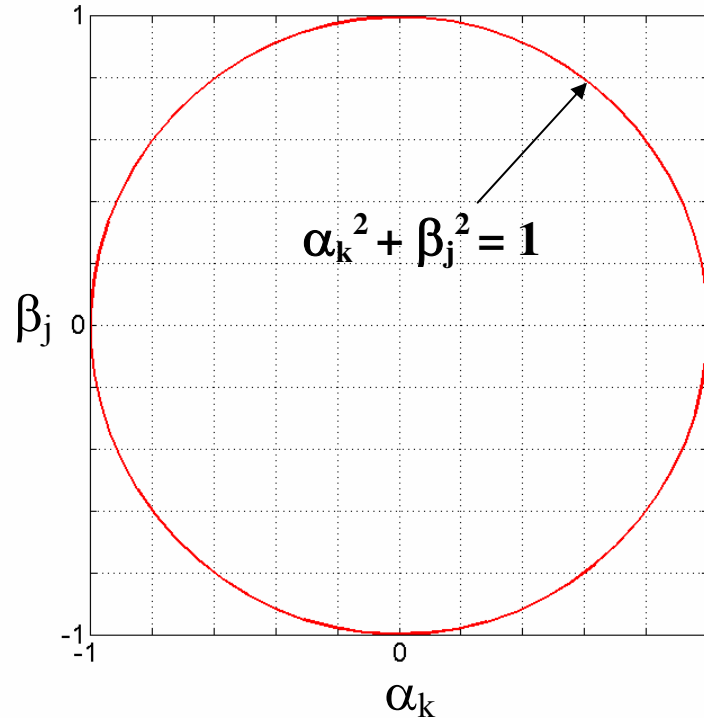


Figure 5-32: Grid of  $\alpha, \beta$  values with unit circle representing the observation space

It is straightforward to create a grid like the one shown in Figure 5-32 in MATLAB® as a two dimensional array and then perform the calculation of the  $ASF$ , given by equation 5.72, for each point in the array. For points that lie outside of the unit circle, we can simply assign a value of zero to the  $ASF$ , since  $\gamma_s$  is not a real number at those locations. The calculation of the entire  $ASF$  can be written as

$$ASF_{jk}(\alpha, \beta) = K \sum_j \sum_k ASF(\alpha_k, \beta_j), \quad (5.74)$$

where 
$$ASF(\alpha_k, \beta_j) = \mathcal{F} \left\{ H_s(\hat{x}, \hat{y}; \gamma_i, \gamma_{jk}) \exp(i2\pi\alpha_o \hat{x}) \right\} \Big|_{\alpha_s=\alpha_k, \beta_s=\beta_j}, \quad (5.75)$$

$$\gamma_{jk} = \sqrt{1 - \alpha_k^2 - \beta_j^2}, \quad (5.76)$$

and  $K$  is the renormalization constant given by equation 5.21.

As an example of the process, we will calculate the scattering of the O'Donnell-Mendez surface discussed previously. The Gaussian autocovariance function of this surface is given by equation 5.33 with  $\sigma_s = 2.27 \mu\text{m}$  and  $\ell_c = 20.9 \mu\text{m}$ . We will assume that the incident radiation has a wavelength  $10.6 \mu\text{m}$ , and that the angle of incidence is 45 degrees ( $\alpha_o = -\sqrt{2}/2$ ,  $\gamma_i = \sqrt{2}/2$ ).

We first set up a two-dimensional square array of size  $N^2$  for the  $ASF$ . Each array location corresponds to points in the  $\alpha, \beta$  plane, where  $\alpha$  and  $\beta$  are one-dimensional arrays of length  $N$ ;  $\alpha$  varies from -1 to 1, while  $\beta$  varies from 1 to -1. The first location in the  $ASF$  array ( $j = 1, k = 1$ ) corresponds to  $\alpha = -1, \beta = 1$ . The last location in the  $ASF$  array ( $j = N, k = N$ ) corresponds to  $\alpha = 1, \beta = -1$ .

We will let  $N=101$ , so that the  $ASF$  is a square array of  $101 \times 101$  locations. We first set  $k = 1$ , which corresponds to  $\alpha = -1$ , and we set  $j = 1$  which corresponds to  $\beta = 1$ . For these values,  $\gamma_{jk}$  is a complex number since that location lies outside of the unit circle. We therefore assign a value of zero to the  $ASF$  at that location. We then continue to loop through values of  $j$  and  $k$ . At each step we calculate equation 5.75 if the location lies inside the unit circle, or we assign a value of zero to the  $ASF$  if the location lies outside the unit circle.

For example, when  $k = 7$  and  $j = 51$ ,  $\alpha_k = -0.88$  and  $\beta_j = 0$ . We use these values of  $\alpha$  and  $\beta$  to calculate  $\gamma_{jk}$  in equation 5.76. We can then calculate the corresponding surface transfer function, which is shown in Figure 5-33.

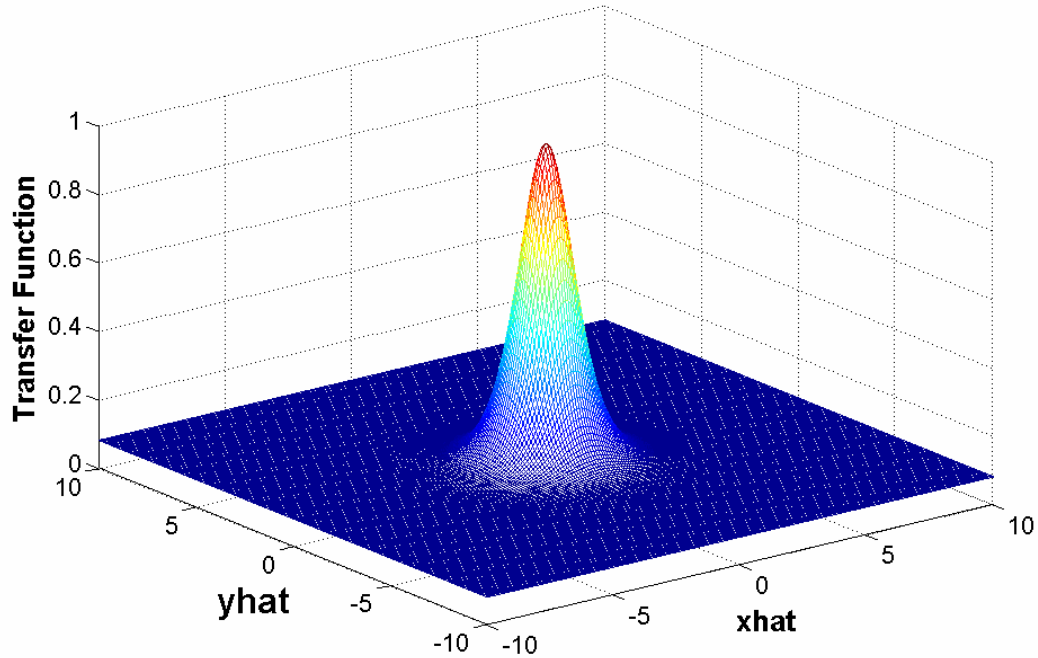


Figure 5-33: GHS surface transfer function for a surface with a Gaussian  $ACV$  function.  $\lambda = 10.6 \mu\text{m}$ ,  $\sigma_s = 2.27 \mu\text{m}$ ,  $\ell_c = 20.9 \mu\text{m}$ ,  $\theta_i = 45^\circ$ ,  $\alpha_s = -0.88$ ,  $\beta_s = 0$

Once the surface transfer function has been calculated, it can be used in equation 5.75. The Fourier transform of the surface transfer function yields a two-dimensional array, which will be referred to as the intermediate *ASF*. From this array, we extract only the *one data point* that corresponds to  $\alpha_j, \beta_k$ . The intermediate ASF for the surface transfer function of the current example is shown in Figure 5-34. Only the value corresponding to  $\alpha = -0.88, \beta = 0$  will be retained in the final ASF. A profile of this intermediate ASF along the  $\beta = 0$  axis is shown in Figure 5-35. The single data point to be extracted is circled.

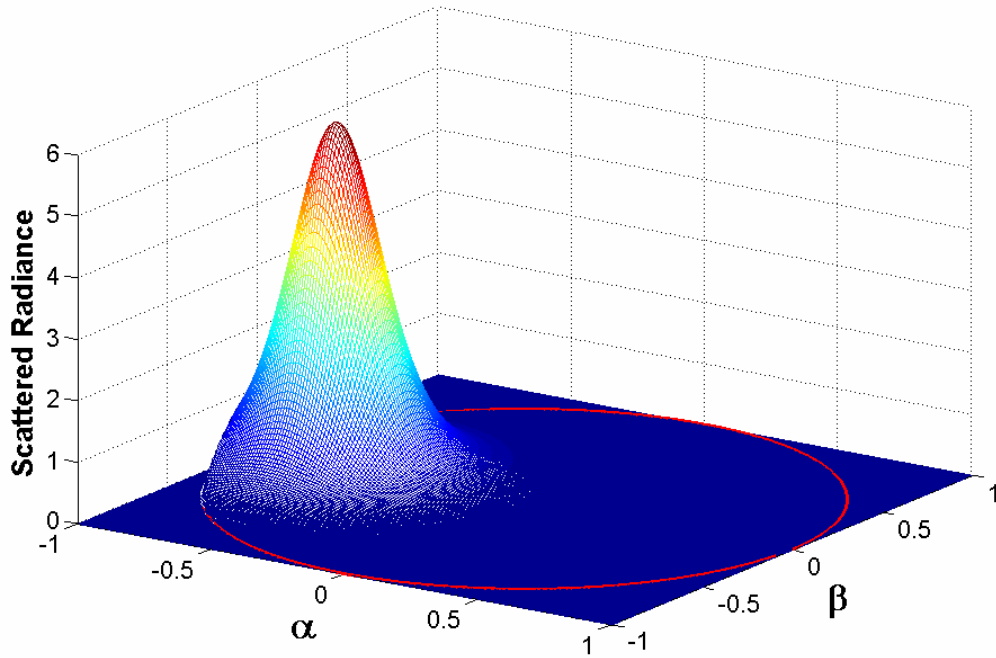


Figure 5-34: Intermediate *ASF* calculated from the surface transfer function in Figure 5-33 where  $\alpha_s = -0.88, \beta_s = 0$ .

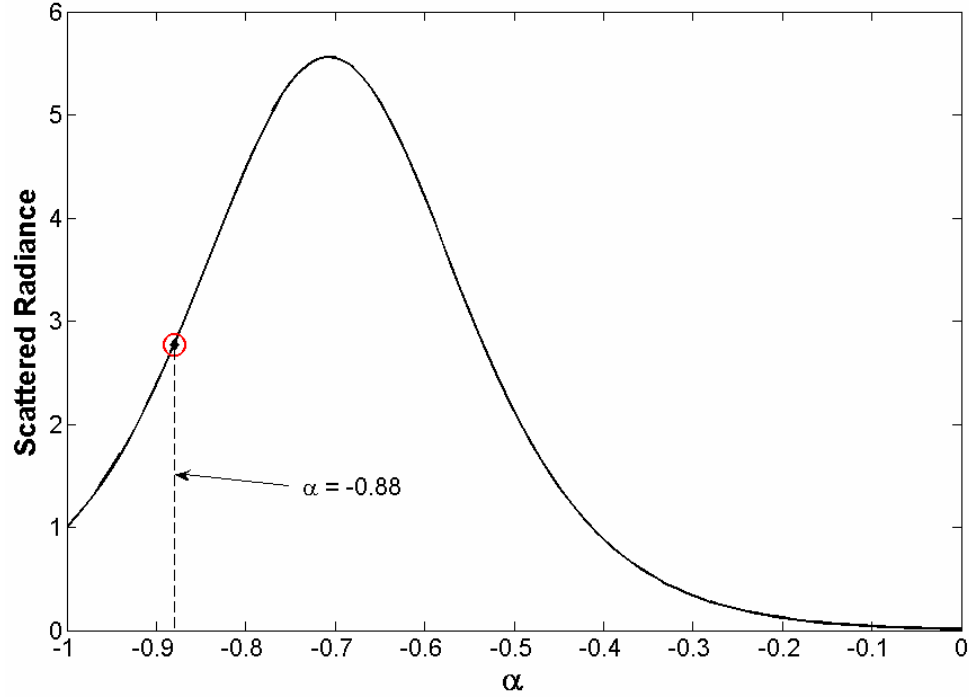


Figure 5-35: One-dimensional profile along the  $\beta=0$  axis for the intermediate *ASF* of Figure 5-34. The single data point being extracted is circled.

This procedure is repeated as we continue to loop through  $j$  and  $k$ . The final *ASF* function is made up of the array summation of the single data points extracted at each step. The single data point extracted in the example above will be the  $k=7$ ,  $j=51$  element of the two-dimensional final *ASF* array. The final *ASF* for this example is shown in Figure 5-36, and a profile in the plane-of-incidence ( $\beta=0$ ) is shown in Figure 5-37. The intensity can be calculated by using equation 5.23.

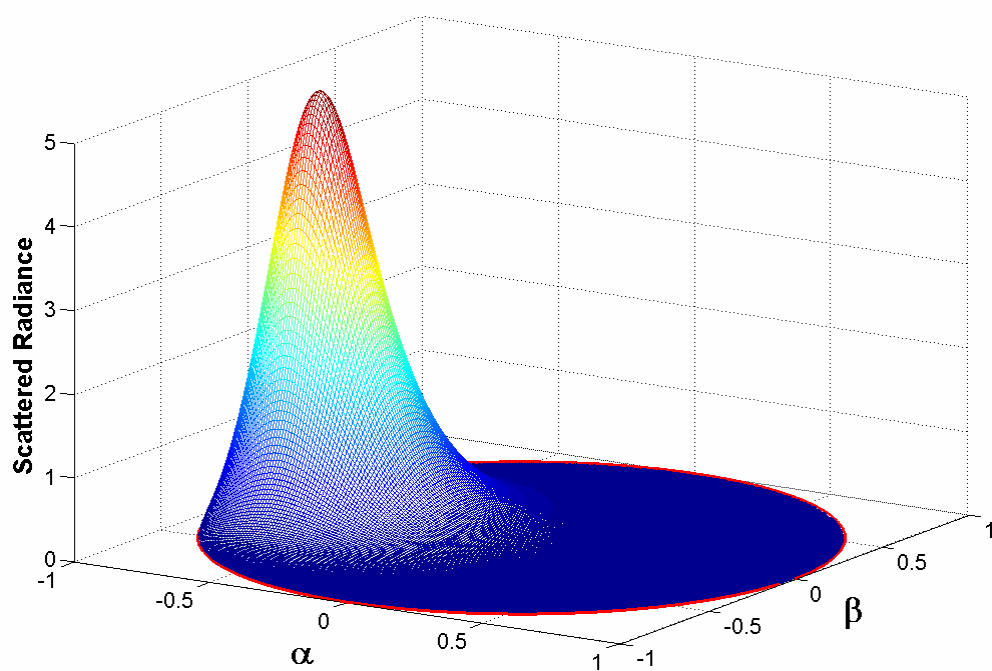


Figure 5-36: Final *ASF* predicted by the GHS theory for a surface with a Gaussian *ACV* function.  $\lambda = 10.6 \mu\text{m}$ ,  $\sigma_s = 2.27 \mu\text{m}$ ,  $\ell_c = 20.9 \mu\text{m}$ , and  $\theta_i = 45^\circ$ .

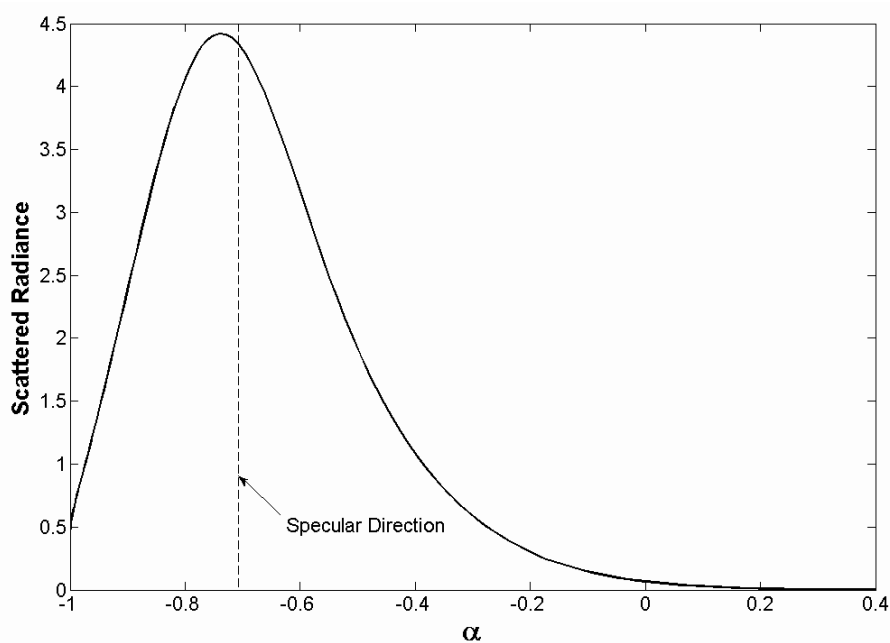


Figure 5-37: Profile of the *ASF* in Figure 5-36 in the plane-of-incidence.

The process described above is computationally intensive, since for each scattering angle we have to perform a two-dimensional discrete Fourier transform of the transfer function, extract the one data point corresponding to that scattering angle and then repeat the process for all other scattering angles. If the surface roughness is isotropic, the surface transfer function will be rotationally symmetric, and the two-dimensional Fourier transform in equation 5.75 reduces to a Hankel transform. Since the Hankel transform operation is one-dimensional, this can help to reduce the computation time significantly. The process is still the same, except at each step a numerical Hankel transform is performed, yielding the radial profile of the circularly symmetric intermediate *ASF*. Using this profile, it is a simple matter to use a one-dimensional interpolation to obtain the one point corresponding to  $\alpha_k, \beta_j$ . For the rough surface scattering predictions that follow, we utilized a quasi-discrete Hankel transform algorithm based on a Fourier-Bessel series expansion [117].

Using the procedure for the generalized Harvey-Shack theory outlined above we have performed scattering predictions for the O'Donnell-Mendez scattering surface. A comparison of the scattered intensity predicted by the modified Harvey-Shack theory and the generalized Harvey-Shack theory is shown in Figure 5-38 for the O'Donnell-Mendez surface with a wavelength of 10.6  $\mu\text{m}$  at incident angles of 0, 20, 50, and 70 degrees. Experimental data taken from [110] for 20 and 70 degrees is also plotted for comparison. For radiation with a wavelength of 10.6  $\mu\text{m}$ , the surface can be considered moderately rough since  $\sigma_s/\lambda = 0.214$ . It will also produce fairly wide angle scatter since  $\ell_c/\lambda = 1.97$ .



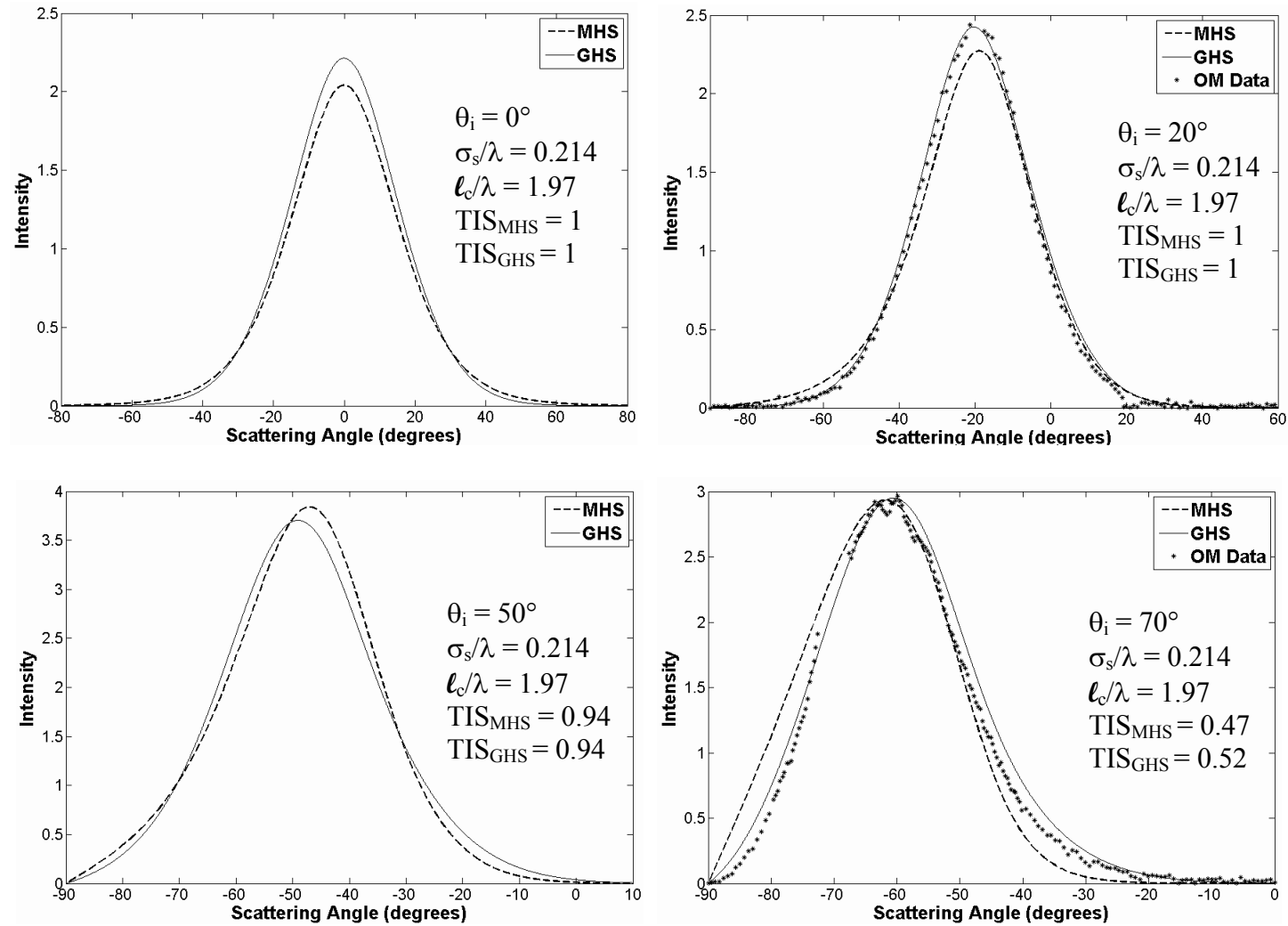


Figure 5-38: GHS compared to MHS and OM experimental data for  $\sigma_s/\lambda = 0.214$ ,  $\ell_c/\lambda = 1.97$ , and  $\theta_i = 0^\circ$ ,  $20^\circ$ ,  $50^\circ$ , and  $70^\circ$

For normal incidence in Figure 5-38, both the modified Harvey-Shack theory and the generalized Harvey-Shack theory predict that all of the light is diffusely scattered ( $TIS = 1$ ). The generalized Harvey-Shack prediction is slightly higher and narrower than the modified Harvey-Shack prediction, however.

For the 20 degree angle of incidence in Figure 5-38, both theories again predict that all of the light is diffusely scattered. The peak of the generalized Harvey-Shack prediction is again higher and slightly narrower than the modified Harvey-Shack peak. The agreement between the two theories is better on the right hand side of the peak than it is on the left hand side. The generalized Harvey-Shack provides much better agreement with the experimental data.

For the 50 degree angle of incidence in Figure 5-38, both theories predict that there will be a small specular peak, but that 94% of the power will still reside in the diffusely reflected light. The agreement between the two theories is reasonably good, although there is some asymmetry since the two theories cross each other on both sides of the peak. The peak of the modified Harvey-Shack theory is actually higher than that of the generalized Harvey-Shack prediction for this incident angle, and shifted more towards zero degrees.

For the 70 degree angle of incidence in Figure 5-38, the disagreement between the two theories is more pronounced. The generalized Harvey-Shack theory predicts a  $TIS$  of 0.52 as opposed to the  $TIS$  of 0.47 predicted by the modified Harvey-Shack theory. The two theories disagree significantly on both sides of the peak. Although not perfect, the generalized Harvey-Shack theory is a better fit to the experimental data than the modified Harvey-Shack theory.

In Figure 5-39, we compare the modified and generalized Harvey-Shack theories with experimental data for the O'Donnell-Mendez surface for light with a wavelength of  $0.6328\text{ }\mu\text{m}$ . For this wavelength, the surface can be considered very rough since  $\sigma_s/\lambda = 3.59$ , and both theories predict that all of the light will be diffusely scattered. The disagreement between the two theories is substantial, however. The peak of the modified Harvey-Shack theory is shifted substantially from the peak of the generalized Harvey-Shack theory and is also about 40% higher. The shapes of the two profiles are also quite different. The agreement between the generalized Harvey-Shack theory and the experimental data is excellent, especially considering how rough the surface is.

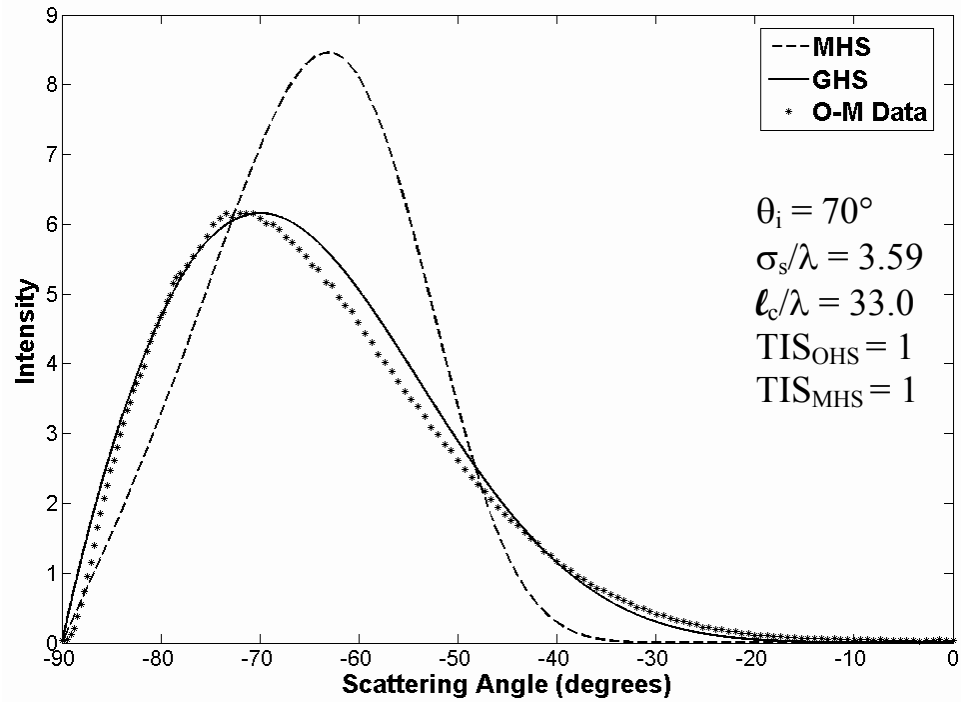


Figure 5-39: GHS compared to MHS and OM experimental data for  $\sigma_s/\lambda = 3.59$ ,  $\ell_c/\lambda = 33.0$ , and  $\theta_i = 70^\circ$

### 5.3.5 Comparison With The Modified Beckman-Kirchhoff Theory

Both the modified Beckmann-Kirchhoff theory of chapter four and the generalized Harvey-Shack theory presented in this chapter yield excellent agreement with the Rayleigh-Rice theory for scattering from smooth surfaces. In addition, both theories provide very good agreement with measured experimental data for both moderately rough and very rough surfaces. We will therefore perform a direct comparison of the two theories and determine exactly how well they agree with each other.

Recall from equation 4.11 that for smooth or moderately rough surfaces with a Gaussian autocovariance function, the radiance predicted by the modified Beckmann-Kirchhoff theory is given by

$$L(\theta, \phi) = K \frac{\pi \ell_c^2 \exp(-g)}{A_s} \sum_{m=1}^{\infty} \frac{g^m}{m!m} \exp\left(-\frac{v_{xy}^2 \ell_c^2}{4m}\right), \quad (5.77)$$

where

$$g = \left(\frac{2\pi\sigma_s}{\lambda}\right)^2 (\cos\theta_i + \cos\theta_s)^2 \quad (5.78)$$

and

$$v_{xy} = \left(\frac{2\pi}{\lambda}\right) \sqrt{\sin^2\theta_i - 2\sin\theta_i \sin\theta_s \cos\phi_s + \sin^2\theta_s}. \quad (5.79)$$

From equation 4.13, the radiance predicted by the modified Beckmann-Kirchhoff theory for very rough surfaces with a Gaussian *ACV* is given by

$$L(\theta, \phi) = K \frac{\pi \ell_c^2}{A_s g} \exp\left(-\frac{v_{xy}^2 \ell_c^2}{4g}\right), \quad (5.80)$$

where  $g$  and  $v_{xy}$  are again given by equations 5.78 and 5.79 respectively.

Before proceeding to make comparisons of the modified Beckmann-Kirchhoff and generalized Harvey-Shack theories, we need to first verify that we are comparing the same quantities. From equation 2.115, we know that the Harvey-Shack  $ASF$  is a *normalized* radiance function given by

$$ASF = L \frac{A_s}{P}, \quad (5.81)$$

where  $L$  is the radiance,  $A_s$  is the illuminated area of the scattering surface and  $P$  is the total power. For the modified Beckmann-Kirchhoff theory, we equated the right sides of equations 5.77 and 5.80 to radiance. However, the derivation of the original Beckmann-Kirchhoff theory assumed a unit amplitude plane wave incident on the scattering surface. In order to account for anything other than unit amplitude incident radiation, equations 5.77 and 5.80 are more accurately described as radiance normalized by the total power. Therefore, when we compare the two theories we will use the quantity in equation 5.81 and call it the  $ASF$  for both theories. Also note that equations 5.77 and 5.80 only represent the diffuse part of the scattering distribution. Thus, we will only compare the diffusely scattered portion of the  $ASF$  for the two theories.

As a starting point, we will compare the two theories for a moderately rough surface with a Gaussian ACV function. We let  $\ell_c = 2$ ,  $\sigma_s = 0.1$ ,  $\lambda = 0.6328$ , and  $\theta_i = 50^\circ$ . This is indeed a moderately rough surface since  $g \approx 2.66$ , and we can use equation 5.77 with an appropriate number of terms to calculate the modified Beckmann-Kirchhoff result. The generalized Harvey-Shack prediction is calculated using the numerical process outlined in section 5.3.4. The results are shown in Figure 5-40.

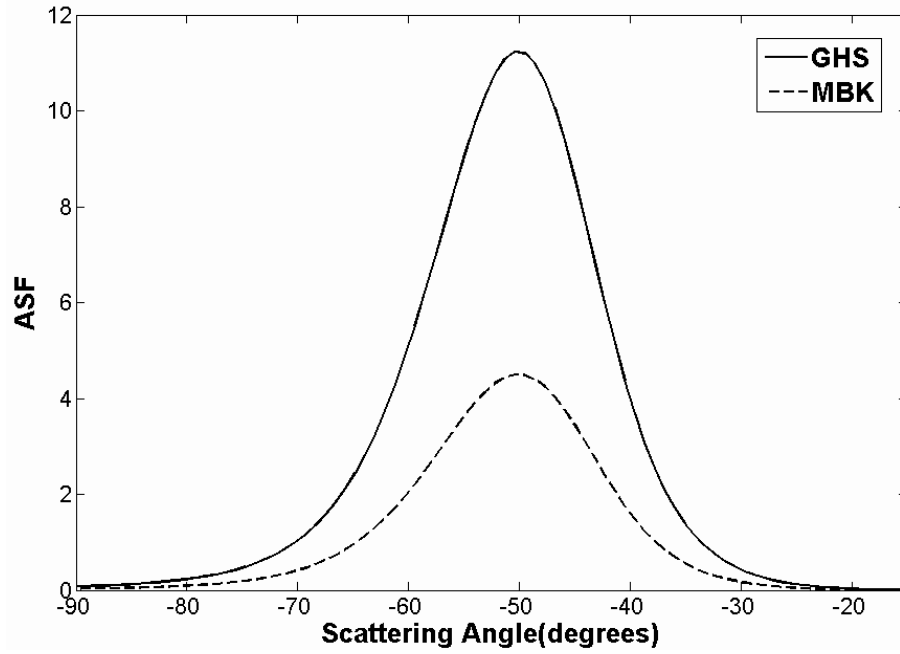


Figure 5-40: GHS and MBK scattering functions compared for a moderately rough surface with a Gaussian  $ACV$  function.  $\ell_c = 2$ ,  $\sigma_s = 0.1$ ,  $\lambda = 0.6328$ , and  $\theta_i = 50^\circ$

As Figure 5-40 shows, the scattering function predicted by the modified Beckmann-Kirchhoff theory has a much lower peak. Comparison of the numerical results shows that the generalized Harvey-Shack prediction is higher by a factor of  $1/\lambda^2$ . When the modified Beckmann-Kirchhoff prediction is divided by  $\lambda^2$ , the two results are identical as shown in Figure 5-41.

If we let  $\ell_c = 20$ ,  $\sigma_s = 2.74$ ,  $\lambda = 0.6328$ , and  $\theta_i = 50^\circ$ , the surface can be classified as very rough since  $g \approx 2000$ . We can therefore use equation 5.80 to calculate the modified Beckmann-Kirchhoff result. The generalized Harvey-Shack prediction is again calculated using the numerical process outlined in section 5.3.4. A comparison of the two theories for this surface is shown in Figure 5-42.

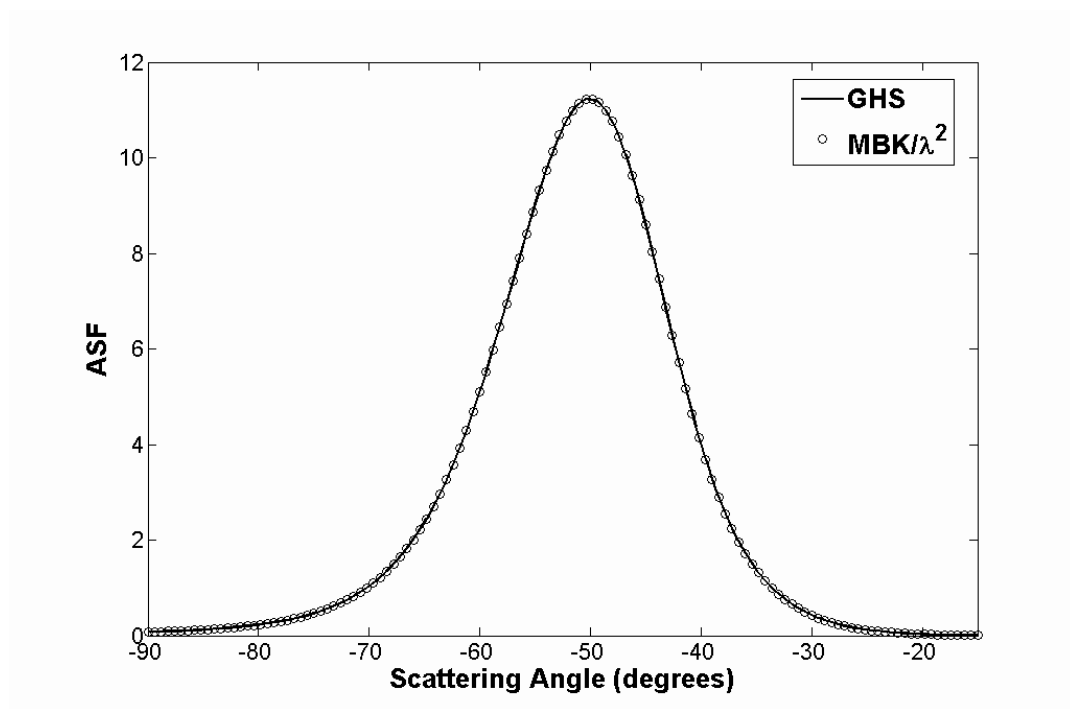


Figure 5-41: The same comparison as Figure 5-40, except that the MBK result has been divided by  $\lambda^2$

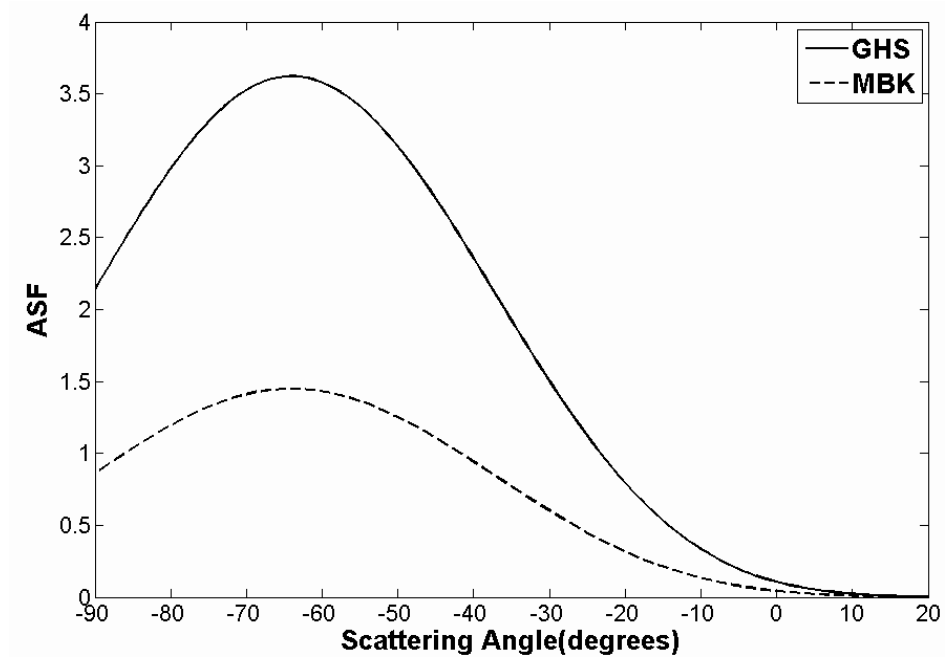


Figure 5-42: GHS and MBK angle spread functions compared for a very rough surface with a Gaussian  $ACV$  function.  $\ell_c = 20$ ,  $\sigma_s = 2.74$ ,  $\lambda = 0.6328$ , and  $\theta_i = 50^\circ$

As seen in Figure 5-42, the modified Beckmann-Kirchhoff prediction has a much lower peak. After investigating the numerical results, the generalized Harvey-Shack *ASF* was once again found to be higher by a factor of  $1/\lambda^2$ . When the modified Beckmann-Kirchhoff result is divided by  $\lambda^2$ , the two predictions are identical as shown in Figure 5-43.

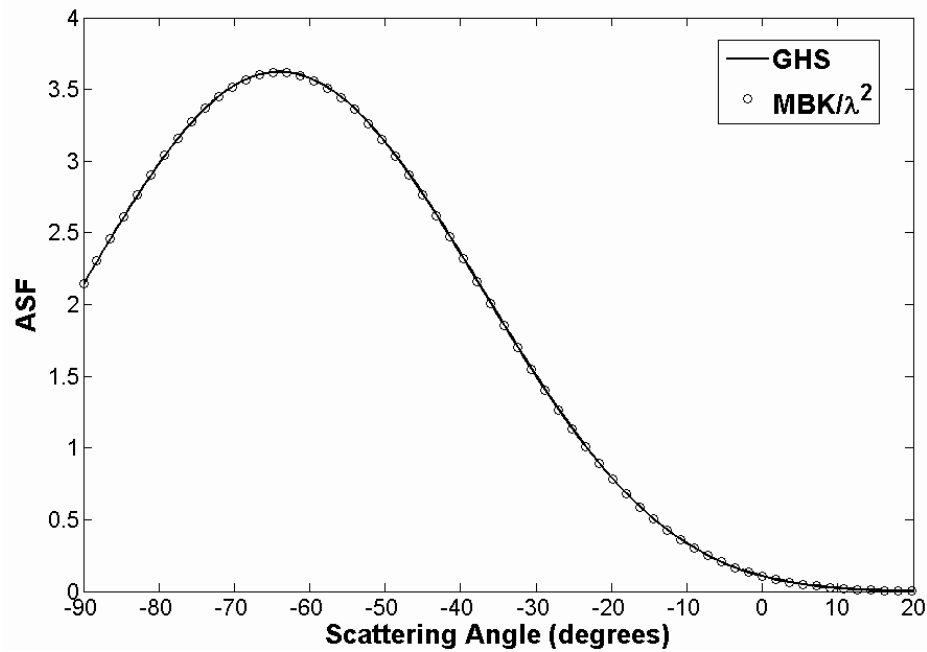


Figure 5-43: The same comparison as Figure 5-42, except that the MBK result has been divided by  $\lambda^2$

The discrepancy between the two theories was investigated for numerous cases with different roughness values and wavelength. The modified Beckmann-Kirchhoff result was either higher or lower than the generalized Harvey-Shack result; however the difference was always a factor of  $1/\lambda^2$ .



For smooth surfaces, we can actually obtain an analytical solution for both the modified Beckmann-Kirchhoff theory and the generalized Harvey-Shack theory in order to compare the two. For smooth surfaces,  $g \ll 1$  and we can use equation 5.77 to write the diffusely scattered portion of the *ASF* for the modified Beckmann Kirchhoff theory as

$$S_{MBK}(\theta, \phi) = K \frac{\pi \ell_c^2 g}{A_s} \exp\left(-\frac{v_{xy}^2 \ell_c^2}{4m}\right). \quad (5.82)$$

Using equations 5.78 and 5.79, as well as equations 3.15, equation 5.82 can be rewritten in terms of direction cosines as

$$S_{MBK}(\alpha, \beta) = K \frac{4\pi^3 \ell_c^2 \sigma_s^2 (\gamma_i + \gamma_s)^2}{\lambda^2} \exp\left\{-\frac{\pi^2 \ell_c^2}{\lambda^2} [(\alpha_s - \alpha_o)^2 + \beta_s^2]\right\}. \quad (5.83)$$

From equations 5.56, 5.57, and 5.34, as well as equations 3.15, the generalized Harvey-Shack scattering function can be written in terms of direction cosines as

$$S_{GHS}(\alpha, \beta) = K \frac{4\pi^3 \ell_c^2 \sigma_s^2 (\gamma_i + \gamma_s)^2}{\lambda^4} \exp\left\{-\frac{\pi^2 \ell_c^2}{\lambda^2} [(\alpha_s - \alpha_o)^2 + \beta_s^2]\right\}. \quad (5.84)$$

Comparing equations 5.83 and 5.84, we can see that for smooth surfaces, the modified Beckmann-Kirchhoff and generalized Harvey-Shack scattering theories are indeed identical except for the extra  $\lambda^2$  in the denominator of the generalized Harvey-Shack equation. We also note the the generalized Harvey-Shack result has the correct units of 1/Sr, while the modified Beckmann-Kirchhoff result does not.

To understand why, apart from the  $\lambda^2$  discrepancy, the two theories predict the same results, we need to look back further in the derivation of the Beckmann-Kirchhoff theory. The equations for smooth, moderately rough, and very rough surfaces are all approximations to the general solution given by equation 2.71 for isotropic roughness:

$$\langle \rho \rho^* \rangle = \frac{2\pi F^2}{A} \int_0^\infty J_0(v_{xy}\tau) \chi_2(v_z, -v_z; \tau) \tau d\tau, \quad (5.85)$$

where  $\chi_2$  is the characteristic function of a joint probability distribution, and  $F^2$  is the geometrical factor, which was discarded in the modified Beckmann-Kirchhoff theory. The quantity on the right side of 5.85, without the geometrical factor, was equated to radiance in the modified Beckmann-Kirchhoff theory. However, as per the previous discussion in this section, it will now be equated to radiance normalized by the total power. Using equation 5.81, we can therefore write the general solution of the modified Beckmann-Kirchhoff theory as

$$ASF_{MBK}(v_{xy}) = 2\pi \int_0^\infty J_0(v_{xy}\tau) \chi_2(v_z, -v_z; \tau) \tau d\tau. \quad (5.86)$$

If we assume the surface height has a Gaussian distribution, equation 5.86 can be rewritten with the help of equation 2.79 as

$$ASF_{MBK}(v_{xy}) = 2\pi \int_0^\infty J_0(v_{xy}\tau) \exp[-g(1-C(\tau))] \tau d\tau, \quad (5.87)$$

where  $g$  is given by 5.78 and  $C$  is the correlation coefficient, which is related to the surface autocovariance function  $C_s$  by [90]

$$C = \frac{C_s}{\sigma_s^2}. \quad (5.88)$$

Using equations 5.78, 5.88, and the fact that  $\gamma = \cos\theta$ , equation 5.87 can be rewritten as

$$ASF_{MBK}(v_{xy}) = 2\pi \int_0^\infty J_0(v_{xy}\tau) \exp \left\{ - \left[ \left( \frac{2\pi\sigma_s}{\lambda} \right) (\gamma_i + \gamma_s) \right]^2 \left[ 1 - \frac{C_s(\tau)}{\sigma^2} \right] \right\} \tau d\tau. \quad (5.89)$$

Examining equation 5.89, we see that the modified Beckmann-Kirchhoff scattering distribution is given by the Hankel transform of an exponential function that is *exactly equal to the generalized Harvey-Shack surface transfer function*, except that the spatial variables are not scaled by the wavelength.

We can therefore understand why the two theories produce nearly identical results. However, we still need to account for the difference of the factor  $1/\lambda^2$ . Equation 5.89 can be written more generally for surfaces whose roughness may not be isotropic as a two-dimensional Fourier transform given by [118]

$$ASF_{MBK}(v_x, v_y) = \int_{-\infty}^{\infty} \int_{-\infty}^{\infty} \exp \left[ -i(v_x x + v_y y) \right] H_s(x, y; \gamma_i, \gamma_s) dx dy, \quad (5.90)$$

where

$$H_s(x, y) = \exp \left\{ - \left[ \left( \frac{2\pi\sigma_s}{\lambda} \right) (\gamma_i + \gamma_s) \right]^2 \left[ 1 - \frac{C_s(x, y)}{\sigma^2} \right] \right\}. \quad (5.91)$$

With the help of equation 5.79, as well as equations 3.15, equation 5.90 can be rewritten as

$$ASF_{MBK}\left(\frac{\alpha_s}{\lambda}, \frac{\beta_s}{\lambda}\right) = \int_{-\infty}^{\infty} \int_{-\infty}^{\infty} \exp\left\{-i2\pi\left[\frac{(\alpha - \alpha_o)}{\lambda}x + \frac{\beta}{\lambda}y\right]\right\} H_s(x, y; \gamma_i, \gamma_s) dx dy. \quad (5.92)$$

The  $ASF$  from the generalized Harvey-Shack theory is given from equation 5.40 as

$$ASF_{GHS}(\alpha_s, \beta_s) = \int_{-\infty}^{\infty} \int_{-\infty}^{\infty} \exp\left\{-i2\pi[(\alpha - \alpha_o)\hat{x} + \beta\hat{y}]\right\} H_s(\hat{x}, \hat{y}; \gamma_i, \gamma_s) d\hat{x} d\hat{y}, \quad (5.93)$$

where  $H_s(\hat{x}, \hat{y}; \gamma_i, \gamma_s)$  is given by 5.91 with the spatial variables  $x$  and  $y$  scaled by the wavelength.

Examining equations 5.92 and 5.93, we see that for the modified Beckmann-Kirchhoff equation, the Fourier transform variables are  $(x, y)$  and  $(\alpha/\lambda, \beta/\lambda)$ , while the Fourier transform variables for the generalized Harvey-Shack equation are  $(\hat{x}, \hat{y})$  and  $(\alpha, \beta)$ . We can put the modified Beckmann-Kirchhoff result in the same “space” as the generalized Harvey-Shack result by performing a change of variables on equation 5.92, letting  $\hat{x} = x/\lambda$ ,  $\hat{y} = y/\lambda$ . When we do so, equation 5.92 can be rewritten as

$$ASF_{MBK}(\alpha_s, \beta_s) = \lambda^2 \int_{-\infty}^{\infty} \int_{-\infty}^{\infty} \exp\left\{-i2\pi[(\alpha - \alpha_o)\hat{x} + \beta\hat{y}]\right\} H_s(\hat{x}, \hat{y}; \gamma_i, \gamma_s) d\hat{x} d\hat{y}. \quad (5.94)$$

Comparing equations 5.93 and 5.94, we can see that the two equations indeed differ only by a factor  $\lambda^2$ . From equation 3.27, the total power is given by

$$P_T = A_s \int_{\alpha=-1}^1 \int_{\beta=-\sqrt{1-\alpha^2}}^{\sqrt{1-\alpha^2}} L(\alpha, \beta) d\alpha d\beta . \quad (5.95)$$

Using equation 5.81, we can therefore write equation 5.95 as

$$1 = \int_{\alpha=-1}^1 \int_{\beta=-\sqrt{1-\alpha^2}}^{\sqrt{1-\alpha^2}} ASF(\alpha, \beta) d\alpha d\beta . \quad (5.96)$$

Therefore, the volume of the *ASF* integrated over  $\alpha, \beta$  must be equal to unity.

Since the peak value of  $H_s$  in equation 5.93 is by definition unity, the Fourier transform of  $H_s$  must have unit volume, and thus the volume of the *ASF* given by equation 5.93 will be unity, satisfying equation 5.96. By the same argument, the volume of the *ASF* given by equation 5.94 would be equal to  $\lambda^2$ , and equation 5.96 would not be satisfied. The modified Beckmann-Kirchhoff result is only wrong in that we have incorrectly defined it radiometrically. What we had equated to radiance in chapter four, and to *ASF* previously in this section should actually be defined as  $ASF * \lambda^2$ .

Based on the above discussion, the modified Beckmann-Kirchhoff equations used to predict the diffusely scattered light for a surface with a Gaussian autocovariance function are given by

$$ASF(\theta_s, \phi_s) = \frac{K \pi \ell_c^2 \exp(-g)}{\lambda^2} \sum_{m=1}^{\infty} \frac{g^m}{m! m} \exp\left(-\frac{v_{xy}^2 \ell_c^2}{4m}\right) \quad (5.97)$$

for smooth or moderately rough surfaces, and

$$ASF(\theta_s, \phi_s) = K \frac{\pi \ell_c^2}{\lambda^2 g} \exp\left(-\frac{v_{xy} \ell_c^2}{4g}\right) \quad (5.98)$$

for very rough surfaces, with  $g$  and  $v_{xy}$  given by equations 5.78 and 5.79 respectively.

We have shown in this section that the modified Beckmann-Kirchhoff theory and the generalized Harvey-Shack theory are identical. Scattering predictions using equations 5.78 and 5.79 will be entirely consistent with numerical solutions using equation 5.93, provided that equations 5.78 and 5.79 are used in their proper domain of validity as discussed in chapter four.

## **CHAPTER 6: SUMMARY AND CONCLUSIONS**

In this dissertation, the Harvey-Shack linear-systems treatment of surface scatter theory has been generalized to account for large incident and scattering angles through the application of non-paraxial scalar diffraction theory. The result of this generalization is a new definition of the surface transfer function which is in reality a two-parameter *family* of surface transfer functions, one for each incident *and* scattering angle. This new surface scatter model is able to provide excellent agreement with the Rayleigh-Rice theory for smooth surfaces with large incident and scattering angles. In addition, when compared to previously measured experimental data, this new model was shown to predict scattering from rough surfaces at large incident and scattering angles with greater accuracy than the classical Beckmann-Kirchhoff is able to provide. While it can be computationally intensive for rough surfaces, this new model retains the intuitive nature of the original Harvey-Shack theory due to its linear-systems approach to the problem of surface scattering.

### **6.1 Dissertation Summary**

In chapter one of this dissertation, the concept of surface scattering was introduced, and the motivations and goals for the dissertation were discussed. Our two main motivations were the need to be able to predict surface scatter in optics applications and the inability of the currently widespread models (Rayleigh-Rice,

Beckmann-Kirchhoff, and Harvey-Shack) to do so in many situations because of their limited range of applicability. The goal was to develop a surface scatter model that would incorporate the advantages of each of the three theories while extending the range of applicability to rougher surface and larger incident and scattering angles. This goal has been accomplished.

In chapter two, a historical background of both scalar diffraction theory and surface scattering theories was presented, with particular emphasis on previous work in the area of non-paraxial scalar theory, as well as fairly extensive detail of both the Beckmann-Kirchhoff and Harvey-Shack scattering theories. This detail was necessary to provide the context and background for the new developments in the following chapters.

In the first part of chapter three, a linear-systems formulation of *non-paraxial* scalar diffraction theory was developed. By incorporating proper radiometric terminology and choosing an appropriate parameter space, it was shown that *diffracted radiance* is shift-invariant in direction cosine space and therefore the fundamental quantity predicted by scalar diffraction theory. The proper application of Parseval's theorem allows the theory to model the redistribution of energy from evanescent waves to propagating waves, ensuring conservation of energy.

In the second part of chapter three, some common misconceptions due to paraxial Fourier treatments of sinusoidal phase gratings were discussed. The new non-paraxial theory was then applied to these gratings and used to explain their wide-angle behavior. Finally, the non-paraxial theory was used to predict TE diffraction efficiencies for a perfectly conducting sinusoidal phase grating. These results were then compared to the efficiencies predicted by paraxial scalar theories and a rigorous vector treatment. It was



shown that the non-paraxial theory is a great improvement over the paraxial scalar treatments in the range of  $\lambda/d$  values for which scalar theory is generally thought to be invalid. There was some disagreement between the paraxial and non-paraxial scalar theories in the “paraxial regime”, however, and further rigorous numerical simulations or experimental measurements are needed to investigate this.

In chapter four, the insight and understanding of non-paraxial scalar diffraction obtained in the previous chapter was utilized to make an empirical modification to the classical Beckmann-Kirchhoff scattering theory for surfaces with Gaussian autocovariance functions. This modified Beckmann-Kirchhoff model was shown to agree with the Rayleigh-Rice theory for smooth surfaces with large incident and scattering angles, while at the same time agreeing with experimental rough surface measurements at large incident and scattering angles. In both cases, the modified Beckmann-Kirchhoff theory was shown to be a vast improvement over the classical Beckmann-Kirchhoff theory. A study on the appropriate use of each of the closed-form solutions of the modified theory with regard to the amount of roughness was also performed. An equation for the number of terms that need to be used for moderately rough surfaces was found, and the choice of a proper “break point” between the smooth regime and the moderately rough regime, as well as between the moderately rough regime and the very rough regime, was discussed.

In the first part of chapter five, a study of the modified Harvey-Shack theory was performed. This variation of the Harvey-Shack theory was originally derived for grazing incidence telescope applications, and was here adapted to non-grazing incidence. The modified Harvey-Shack theory was shown to agree with the Rayleigh-Rice theory for

arbitrary incident angles *only* when the spread of the scattering function around the specular direction is small. This was not a great surprise, as this was the condition under which it was derived. However, this was the first time such a study has been performed. The modified Harvey-Shack theory was shown to be a vast improvement over the original Harvey-Shack theory, however, as the original theory is only valid for small (paraxial) angles of incidence and small scattering angles.

In the second part of chapter five, the Harvey-Shack theory was generalized to account for large incident and scattering angles. This was shown to lead to a new two-parameter family of surface transfer functions, one for each incident and scattering angle. This new model agrees well with the Rayleigh-Rice theory for smooth surfaces with large incident and scattering angles, and also provides good agreement with experimental data from rough surfaces at large incident and scattering angles. A smooth-surface approximation to and a quasi-vectorizing of the generalized Harvey-Shack scattering theory also provides an improved *BRDF* model for solving the inverse scattering problem to obtain surface characteristics from measured *BRDF* data. Finally it was shown that the modified Beckmann-Kirchhoff model and the generalized Harvey-Shack theory are in fact identical.

## **6.2 Areas For Future Work**

There are three areas that are easily identifiable as directions in which to proceed from the work presented in this dissertation.

The first involves the sinusoidal phase grating. It was pointed out that there is some disagreement between the *paraxial* and *non-paraxial* scalar treatments in what is known as the “paraxial regime”. It is obvious from the efficiency plots for various values of  $h/d$  that the paraxial theory will not *always* be valid in what is labeled the “paraxial regime”, since as  $h/d$  is increased, more and more energy is spread out to higher diffracted orders. It is therefore not clear if the disagreement for lower  $h/d$  values is due to our method of redistributing the energy from evanescent orders to propagating orders. This merits further investigation, either through comparisons with calculations from a rigorous vector treatment, or through comparisons with experimental measurements. In addition, our results are only valid for TE polarization. A quasi-vectorizing of the non-paraxial model may be possible, but this also requires further investigation.

The second area involves the numerical computation of scattering using the generalized Harvey-Shack theory. Since a different Fourier transform is required for every scattering angle of interest, the computation time can be substantial. This was alleviated to some extent by assuming isotropic roughness and implementing a numerical Hankel transform routine. Further research into increasing the computational efficiency, either through analytical approximations or more efficient numerical methods, would be useful and perhaps extend the range of applications to which the model can be applied.

Finally, an extensive experimental study of scattering from various rough surfaces over a range of incident angles, scattering angles, wavelengths, and polarizations with which to compare the generalized Harvey-Shack theory would be extremely useful in further quantifying its range of validity.

## LIST OF REFERENCES

- [1] J. D. Gaskill, *Linear Systems, Fourier Transforms, and Optics*. New York: Wiley, 1978.
- [2] H. Davies, "The reflection of electromagnetic waves from a rough surface", *Proceedings of the IEE* **101**, pp. 209-214, 1954.
- [3] J. C. Stover, *Optical scattering, measurement and analysis*, 2nd ed. Bellingham, WA: SPIE Optical Engineering Press, 1995.
- [4] T. M. Elfouhaily and C. A. Guerin, "A critical survey of approximate scattering wave theories from random rough surfaces", *Waves in Random Media* **14**, p. R1-R40, 2004.
- [5] R. Cecchini and G. Pelosi, "Diffraction: the first recorded observation", *IEEE Antennas and Propagation Society Magazine* **32**, pp. 27-30, 1990.
- [6] R. Hooke, *Micrographia*. Project Gutenberg (eBook), 2005  
<http://www.gutenberg.org/etext/15491>
- [7] J. H. Marsh, "Optical Sciences in Scotland", in *15th annual meeting of IEEE Lasers and Electro-Optics Society*, **1**, pp. 9-10, 2002.
- [8] H. W. Turnbull, "James Gregory (1638-1675)", Address at the Tercentenary of the birth of James Gregory, University of St. Andrews, Scotland, 1938  
[http://www-history.mcs.st-andrews.ac.uk/Extras/Turnbull\\_address.html](http://www-history.mcs.st-andrews.ac.uk/Extras/Turnbull_address.html)
- [9] B. B. Baker and E. T. Copson, *The Mathematical Theory of Huygens' Principle*, 2nd ed. Oxford: Clarendon Press, 1949.
- [10] I. Newton, *Opticks*. New York: Dover, 1952.
- [11] T. Young, *Miscellaneous Works of the Late Thomas Young*. London: John Murray, 1855.
- [12] A. J. Fresnel, *Oeuvres completes d'Augustin Fresnel*. Paris: Imprimerie imperiale, 1866.
- [13] J. W. Goodman, *Introduction to Fourier Optics*, 2nd ed. New York: McGraw-Hill, 1996.
- [14] G. R. Kirchhoff, "Zur theorie der lichtstrahlen", *Annalen der Physik und Chemie* **18**, pp. 663-695, 1883.

- [15] A. Sommerfeld, "Mathematische Theorie der Diffraction", *Mathematische Annalen* **47**, pp. 317-374, 1896.
- [16] A. Sommerfeld, *Optics. Lectures on Theoretical Physics*. New York: Academic Press, 1954.
- [17] H. G. Booker and P. C. Clemmow, "The concept of an angular spectrum of plane waves and its relation to that of polar diagrams and aperture distribution", *Proceedings of the IEE* **3**, pp. 11-17, 1950.
- [18] P. C. Clemmow, *The Plane Wave Spectrum Representation of Electromagnetic Fields*. New York: Wiley-IEEE Press, 1996.
- [19] J. A. Ratcliffe, "Some Aspects of diffraction theory and their application to the ionosphere," in *Reports on Progress in Physics*. A. C. Strickland, Ed. London: The Physical Society, 2006.
- [20] J. E. Harvey, "Fourier treatment of near-field scalar diffraction theory", *American Journal of Physics* **47**, pp. 974-980, 1979.
- [21] J. E. Harvey, "Light Scattering Characteristics of Optical Surfaces." PhD Dissertation, University of Arizona, (1976).
- [22] J. E. Harvey and R. V. Shack, "Aberrations of diffracted wave fields", *Applied Optics* **17**, pp. 3003-3009, 1978.
- [23] Lord Rayleigh, *The Theory of Sound*, 2nd ed. London: Macmillan & Company, 1896.
- [24] Lord Rayleigh, "Polish", *Nature* **64**, pp. 385-388, 1901.
- [25] Lord Rayleigh, "On the dynamical theory of gratings", *Proceedings of the Royal Society* **A79**, pp. 399-416, 1907.
- [26] T. K. Chenmoganadam, "On the specular reflection from rough surfaces", *Physical Review* **13**, pp. 96-101, 1919.
- [27] U. Fano, "The theory of anomalous diffraction gratings and of quasi-stationary waves on metallic surfaces (Sommerfeld's waves)", *Journal of the Optical Society of America* **31**, pp. 213-222, 1941.
- [28] S. O. Rice, "Reflection of electromagnetic waves from slightly rough surfaces", *Communications in Pure and Applied Mathematics* **4**, pp. 351-378, 1951.
- [29] S. O. Rice, *Reflection of EM from Slightly Rough Surfaces*. New York: Interscience, 1963.

- [30] D. E. Barrick and W. H. Peake, "Scattering from sufraces with different roughness scales: Analysis and Interpretation," Battelle Memorial Institute, BAT-197-A-10-3, 1967.
- [31] D. E. Barrick, "Rough Surfaces," in *Radar Cross Scection Handbook*. e. a. G.T.Ruck, Ed. New York: Plenum Press, 1970, pp. 671-772.
- [32] C. I. Beard, "Coherent and incoherent scattering of microwaves from the ocean", *IRE Transactions on Antennas and Propagation* **9**, pp. 470-483, 1961.
- [33] I. M. Fuks, "Theory of radio wave scattering at a rough sea surface", *Soviet Radiophysics* **9**, pp. 513-519, 1966.
- [34] W. H. Peake, "Theory of radar return from terrain", *IRE National Conventional Record* **7**, pp. 27-41, 1959.
- [35] G. R. Valenzuela, "Depolarization of EM waves by slightly rough surfaces", *IEEE Transactions on Antennas and Propagation* **15**, pp. 552-557, 1967.
- [36] G. R. Valenzuela, "Scattering of electromagnetic waves from a tilted slightly rough surface", *Radio Science* **13**, p. 1057, 1968.
- [37] F. B. Daniels, "A theory of radar reflection from the moon and planets", *Journal of Geophysical Research* **66**, pp. 1781-1788, 1961.
- [38] J. V. Evans and G. H. Petengill, "The scattering behavior of the moon at wavelengths of 3.6, 68, an 784 centimeters", *Journal of Geophysical Research* **68**, pp. 423-447, 1993.
- [39] T. Hagafors, "Effects of structure size on moon and earth radar returns at various angles", *Journal of Geophysical Research* **69**, pp. 3779-3784, 1964.
- [40] E. L. Church and J. M. Zavada, "Residual surface roughness of diamond-turned optics", *Applied Optics* **14**, pp. 1788-1795, 1975.
- [41] E. L. Church, H. A. Jenkinson, and J. M. Zavada, "Measurement of the finish of diamond-turned metal surfaces by differential scattering", *Optical Engineering* **16**, pp. 360-374, 1977.
- [42] E. L. Church, H. A. Jenkinson, and J. M. Zavada, "Relationship between surface scattering and microtopographic features", *Optical Engineering* **18**, pp. 125-136, 1979.
- [43] E. L. Church, "Fractal Surface Finish", *Applied Optics* **27**, pp. 1518-1526, 1988.

- [44] E. L. Church, P. Z. Takacs, and T. A. Leonard, "The prediction of BRDFs from surface profile measurements", in *Scatter From Optical Components*, J. C. Stover, Ed., Proceedings of SPIE **1165**, pp. 136-150, 1989.
- [45] E. L. Church and P. Z. Takacs, "Subsurface and volume scattering from smooth surfaces", in *Scatter from Optical Components*, J. C. Stover, Ed., Proceedings of SPIE **1165**, pp. 31-41, 1989.
- [46] E. L. Church and P. Z. Takacs, "The optimal estimation of finish parameters", in *Optical Scatter: Applications, Measurement, and Theory*, J. C. Stover, Ed., Proceedings of SPIE **1530**, pp. 71-78, 1991.
- [47] L. M. Brekhovskikh, "The diffraction of waves from a rough surface: 2. Applications of the general theory (in Russian)", *Journal of Experimental and Theoretical Physics* **23**, pp. 289-304, 1952.
- [48] L. M. Brekhovskikh, "The diffraction of waves by a rough surface: 1. General theory (in Russian)", *Journal of Experimental and Theoretical Physics* **23**, pp. 275-288, 1952.
- [49] M. A. Isakovich, "Wave scattering from a statistically rough surface (in Russian)", *Journal of Experimental and Theoretical Physics* **23**, pp. 305-314, 1952.
- [50] C. Eckart, "The scattering of sound from the sea surface", *Journal of the Acoustical Society of America* **25**, pp. 66-570, 1953.
- [51] P. Beckmann and A. Spizzichino, *The scattering of electromagnetic waves from rough surfaces*. Oxford: Pergamon Press; distributed in the Western Hemisphere by Macmillan, New York, 1963.
- [52] F. E. Nicodemus, "Reflectance nomenclature and directional reflectance and emissivity", *Applied Optics* **9**, pp. 1474-1475, 1970.
- [53] J. E. Harvey, "Surface scatter phenomena: a linear, shift-invariant process", in *Scatter From Optical Components*, J. C. Stover, Ed., Proceedings of SPIE **1165**, pp. 87-99, 1989.
- [54] J. E. Harvey, E. C. Moran, and W. P. Zmek, "Transfer function characterization of grazing incidence optical systems", *Applied Optics* **27**, pp. 1527-1533, 1988.
- [55] P. Glenn, P. Reid, A. Slomba, and L. P. Van Speybroeck, "Performance prediction of AXAF technology mirror assembly using measured mirror surface errors", *Applied Optics* **27**, pp. 1539-1543, 1988.

- [56] J. E. Harvey and P. L. Thompson, "Generalized Volter type I design for the Solar X-Ray Imager (SXI)", in *X-Ray Optics, Instruments, and Missions II*, R. B. Hoover and A. B. Walker II, Eds., Proceedings of SPIE **3766**, pp. 173-183, 1999.
- [57] J. Shen and A. A. Maradudin, "Multiple scattering of waves from random rough surfaces", *Physical Review B* **22**, pp. 4234-4240, 1980.
- [58] D. P. Winebrenner and A. Ishimaru, "Application of the phase perturbation technique to randomly rough surfaces", *Journal of the Optical Society of America A* **2**, pp. 2285-2294, 1985.
- [59] D. P. Winebrenner and A. Ishimaru, "Investigation of a surface field perturbation technique for scattering", *Radio Science* **20**, pp. 161-170, 1985.
- [60] A. G. Voronovich, "Small-slope approximation in wave scattering from rough surfaces", *Soviet Physics - JETP* **62**, pp. 65-70, 1985.
- [61] A. G. Voronovich, "Non-classical approaches in the theory of wave scattering from rough surfaces," in *Mathematical and Numerical Aspects of Wave Propagation*. J. A. DeSanto, Ed. Philadelphia: SIAM, 1998.
- [62] K. M. Watson, "A transport-equation description of nonlinear ocean surface wave interactions", *Journal of Fluid Mechanics* **70**, pp. 815-826, 1975.
- [63] J. W. West, "A new numerical method for surface hydrodynamics", *Journal of Geophysical Research* **92**, pp. 803-824, 1987.
- [64] D. M. Milder, "The effects of truncation on surface-wave Hamiltonians", *Journal of Fluid Mechanics* **216**, pp. 249-262, 1990.
- [65] D. M. Milder, "An improved formalism for wave scattering from rough surfaces", *Journal of the Acoustical Society of America* **89**, pp. 529-541, 1991.
- [66] D. M. Milder, "An improved formalism for electromagnetic scattering from a perfectly conducting surface", *Radio Science* **31**, pp. 1369-1376, 1996.
- [67] R. A. Smith, "The operator expansion formalism for electromagnetic scattering from rough dielectric surfaces", *Radio Science* **31**, pp. 1377-1385, 1996.
- [68] A. K. Fung and G. W. Pan, "An integral equation method for rough surface scattering", Proceedings of the International Symposium on Multiple Scattering of Waves in Random Media and Random Surfaces pp. 701-714, 1986.
- [69] A. K. Fung and G. W. Pan, "A scattering model for perfectly conducting random surface: I. Model", *International Journal of Remote Sensing* **8**, pp. 1579-1593, 1987.



- [70] G. W. Pan and A. K. Fung, "A scattering model for perfectly conducting random surface: II. Range of Validity", *International Journal of Remote Sensing* **8**, pp. 1595-1605, 1987.
- [71] A. K. Fung, Z. Li, and K. S. Chen, "Backscattering from a randomly rough dielectric surface", *IEEE Transactions on Geoscience and Remote Sensing* **30**, pp. 356-369, 1992.
- [72] E. L. Dereniak, L. G. Brod, and J. Hubbs, "Bidirectional transmittance distribution function measurements on ZnSe", *Applied Optics* **21**, pp. 4421-4425, 1982.
- [73] F. O. Bartell, E. L. Dereniak, and W. L. Wolfe, "The theory and measurement of bidirectional reflectance distribution function (BRDF) and bidirectional transmittance distribution function (BTDF)", in *Radiation Scattering in Optical Systems I*, W. H. Hunt, Ed., Proceedings of SPIE **257**, pp. 154-160, 1980.
- [74] T. A. Leonard and M. Pantoliano, "BRDF round robin", in *Stray Light and Contamination in Optical Systems*, R. P. Breault, Ed., Proceedings of SPIE **987**, pp. 226-235, 1988.
- [75] ASTM Standard E1392-90, *Standard Practice for Angle Resolved Optical Scatter Measurements of Specular or Diffuse Surfaces*. Philadelphia: American Society for Testing and Materials, 1991.
- [76] G. S. Agarwal, "Interaction of electromagnetic waves at rough dielectric surfaces", *Physical Review B* **15**, pp. 2371-2383, 1977.
- [77] J. M. Elson and R. H. Ritchie, "Diffuse scattering and surface-plasmon generation by photons at a rough dielectric surface", *Physica Status Solidi B* **62**, p. 461, 1974.
- [78] J. M. Elson, "Light scattering from semi-infinite media for non-normal incidence", *Physical Review B* **12**, pp. 2541-2542, 1975.
- [79] J. M. Elson, "Theory of light scattering from a rough surface with an inhomogeneous dielectric permittivity", *Physical Review B* **30**, pp. 5460-5480, 1984.
- [80] C. Lopez, F. J. Yndurain, and N. Garcia, "Iterative series for calculating the scattering of waves from a hard corrugated surface", *Physical Review B* **18**, pp. 970-972, 1978.
- [81] A. A. Maradudin and D. L. Mills, "Scattering and absorption of electromagnetic radiation by a semi-infinite medium in the presence of surface roughness", *Physical Review B* **11**, pp. 1392-1415, 1975.

- [82] M. Nieto-Vesperinas and N. García, "A detailed study of the scattering of scalar waves from random rough surfaces", *Optica Acta* **28**, pp. 1651-1672, 1981.
- [83] M. Nieto-Vesperinas, "Depolarization of electromagnetic waves scattered from slightly rough random surfaces: a study by means of the extinction theorem", *Journal of the Optical Society of America* **72**, pp. 539-547, 1982.
- [84] R. K. Rosich and J. R. Wait, "A general perturbation solution for reflection from two-dimensional periodic surfaces", *Radio Science* **12**, pp. 719-729, 1977.
- [85] J. P. Rossi and D. Maystre, "A perturbation theory for scattering from three-dimensional rough surfaces", *Journal of Optics* **18**, pp. 219-228, 1978.
- [86] P. C. Waterman, "Symmetry, unitarity, and geometry in electromagnetic scattering", *Physical Review D* **3**, pp. 825-839, 1971.
- [87] D. R. Jackson, D. P. Winebrenner, and A. Ishimaru, "Comparison of perturbation theories for rough surface scattering", *Journal of the Acoustical Society of America* **83**, pp. 961-969, 1988.
- [88] M. Nieto-Vesperinas, *Scattering and Diffraction in Physical Optics*. New York: Wiley-Interscience, 1991.
- [89] L. Tsang and J. A. Kong, *Scattering of Electromagnetic Waves, Advanced Topics*. New York: Wiley-Interscience, 2001.
- [90] P. Beckmann and A. Spizzichino, *The scattering of electromagnetic waves from rough surfaces*. Norwood, MA: Artech House, 1987.
- [91] A. Papoulis, *Probability, Random Variables, and Stochastic Processes*. New York: McGraw-Hill, 1965.
- [92] J. J. Muray, F. E. Nicodemus, and I. Wunderman, "Proposed supplement to the SI nomenclature for radiometry and photometry", *Applied Optics* **10**, pp. 1465-1468, 1971.
- [93] R. W. Boyd, *Radiometry and the Detection of Optical Radiation*. New York: Wiley, 1983.
- [94] E. L. Dereniak and G. D. Boreman, *Infrared Detectors and Systems*. New York: Wiley, 1996.
- [95] H. F. Davis, *Vector Analysis*. Boston: Allyn and Bacon, Inc., 1961.
- [96] D. A. Gremaux and N. C. Gallager, "Limits of scalar diffraction theory for conducting gratings", *Applied Optics* **32**, pp. 1048-1053, 1993.

- [97] E. G. Loewen and E. Popov, *Diffraction Gratings and Applications*. New York: Marcel Dekker, 1997.
- [98] D. A. Pommet, M. G. Moharam, and E. B. Grann, "Limits of scalar diffraction theory for diffractive phase elements", *Journal of the Optical Society of America A* **11**, pp. 1827-1834, 1994.
- [99] R. Petit, *Electromagnetic Theory of Gratings*. New York: Springer-Verlag, 1980.
- [100] J. M. Bennett and L. Mattsson, *Introduction to Surface Roughness and Scattering*, 2nd ed. Washington D.C.: Optical Society of America, 1999.
- [101] J. E. Harvey and E. A. Nevis, "Angular grating anomalies: effect of fine beam size upon wide-angle diffraction phenomena", *Applied Optics* **31**, pp. 6783-6788, 1992.
- [102] R. W. Wood, "On a remarkable case of uneven distribution of light in a diffraction grating spectrum", *Philosophical Magazine* **4**, pp. 396-410, 1902.
- [103] J. E. Harvey and C. L. Vernold, "Description of diffraction behavior in direction cosine space", *Applied Optics* **37**, pp. 8158-8160, 1998.
- [104] D. Maystre, "Rigorous vector theories of diffraction gratings," in *Progress in optics XXI*. E. Wolf, Ed. New York: Elsevier Science, 1984.
- [105] M. Born and E. Wolf, *Principles of Optics*, 7th ed. New York: Cambridge University Press, 1999.
- [106] T. K. Gaylord and M. G. Moharam, "Analysis and applications of optical diffraction by gratings", *Proceedings of SPIE* **73**, pp. 894-937, 1985.
- [107] C. V. Raman and N. S. N. Nath, "The diffraction of light by high frequency sound waves", *Proceedings of the Indian Academy of Sciences* **2**, pp. 406-413, 2006.
- [108] C. Palmer, *Diffraction Grating Handbook*, 4th ed. New York: Richardson Grating Laboratory, 2000.
- [109] A. Hessel and A. A. Oliner, "A new theory of Wood's anomalies on optical gratings", *Applied Optics* **4**, pp. 1275-1297, 1965.
- [110] K. A. O'Donnell and E. R. Mendez, "Experimental study of scattering from characterized random surfaces", *Journal of the Optical Society of America A* **4**, pp. 1194-1205, 1987.
- [111] C. L. Vernold and J. E. Harvey, "A modified Beckmann-Kirchhoff scattering theory", in *Scattering and Surface Roughness II*, Z.-H. Gu and A. A. Maradudin, Eds., *Proceedings of SPIE* **3426**, pp. 51-56, 1998.

- [112] J. E. Harvey, C. L. Vernold, A. Krywonos, and P. L. Thompson, "Diffracted radiance: a fundamental quantity in non-paraxial scalar diffraction theory", *Applied Optics* **38**, pp. 6469-6481, 1999.
- [113] J. M. Elson, J. M. Bennett, and J. C. Stover, "Wavelength and angular dependence of light scattering from beryllium: comparison of theory and experiment", *Applied Optics* **32**, pp. 3362-3376, 1993.
- [114] M. Abramowitz and I. A. Stegun, *Handbook of Mathematical Functions*. New York: Dover, 1965.
- [115] H. E. Bennett and J. O. Porteus, "Relationship between surface roughness and specular reflectance at normal incidence", *Journal of the Optical Society of America* **51**, pp. 123-129, 1961.
- [116] J. C. Stover, Private Communication, 2005.
- [117] M. Guzar-Sicairos and J. C. Gutierrez-Vega, "Computation of quasi-discrete Hankel transforms of integer order for propagating optical wave fields", *Journal of the Optical Society of America A* **21**, pp. 53-58, 2004.
- [118] R. Piessens, "The Hankel Transform," in *The Transforms and Applications Handbook*, 2nd ed. A.D. Poularikas, Ed. Boca Raton, FL: CRC Press, 2000.